U.PORTO
FEUP FACULDADE DE ENGENHARIA
UNIVERSIDADE DO PORTO

Damage and fracture in advanced composite laminates: thin-ply and nanoengineered composites

Carolina Furtado Pereira da Silva

Thesis submitted to the Faculty of Engineering of the University of Porto - FEUP
in partial fulfilment of the requirements for the degree of
Doctor in Mechanical Engineering

Supervisors
Prof. Dr. Pedro Manuel Ponces Rodrigues de Castro Camanho
Prof. Dr. Brian L. Wardle

Programa Doutoral em Engenharia Mecânica (PRODEM)
Departamento de Engenharia Mecânica (DEMec)
Faculdade de Engenharia (FEUP)
Universidade do Porto (UP)

Porto, January 2020

Acknowledgements

I take this opportunity to express my gratitude to Prof. Pedro P. Camanho and Prof. Brian L. Wardle for the opportunity, for taking the time to share their expertise and for all the support and encouragement without which this work would not have been possible.

I gratefully acknowledge the financial support provided by the Portuguese Government's Fundação para a Ciência e a Tecnologia, under grant SFRH/BD/115859/2016 and the project MITP-TB/PFM/0005/2013. I would also like to acknowledge the institutional support of INEGI, LAETA and the MIT-Portugal Program.

I would like to thank my colleagues at University of Porto, Dr. Albertino Arteiro, Dr. Fermin Otero, Rodrigo Tavares, Martim Salgado, Luís Pereira, Giuseppe Corrado, Tobias Laux and Dr. Fujian Zhuang and at the MIT, Dr. Estelle Kalfon-Cohen, Xinchen Ni, Nathan Fritz, Reed Kopp, and Jeonyoon Lee for their feedback, cooperation and friendship.

Furthermore, I would like to thank Dr. Carlos Sarrado, Prof. Albert Turon, Prof. Josep Costa, Prof. José Xavier, Dr. Patrick Gray, Dr. Peter Linde, Dr. Giuseppe Catalanotti and Dr. Albertino Arteiro for their guidance and all their help in the development of this work.

Finally, I special thanks to my friends, my parents and my family.

Abstract

The main objective of this work is to contribute to the development of a new generation of advanced composite structures with improved mechanical properties over the current state-of-the-art composite materials used in the aeronautical industry. This requires on one hand the development of analysis models to predict the mechanical behaviour of conventional and non-conventional composite laminates, and on the other hand, the detailed analysis of the mechanical behaviour of materials manufactured using new technologies. Improved models to predict failure of composite coupons are proposed to contribute to the reduction of the certification time and cost associated with the introduction of new materials and structures in the aeronautical industry. A ply-level finite element modelling methodology to simulate composite laminates at the coupon level suitable for industrial use is proposed and validated for various material systems and test cases with increasing levels of structural complexity. A very good agreement is found between the predictions and the experimental ultimate strengths, oftentimes within the standard error of the tests, and in a time frame compatible with industry requirements.

The numerical analyses are complemented by a fast-analysis analytical model to predict the notched strength of multidirectional laminates based on three ply properties is proposed and validated. Relative errors around or below 10% are obtained for all the laminates and open-hole geometries analysed. The model is successfully coupled with statistical tools required to consider the variability of the material and geometrical parameters that determine statistically based design allowables.

The analysis models developed not only contribute to a faster and less expensive product development, but are also fundamental to study new, non-conventional composite materials.

The two recently developed technologies addressed in this thesis are: i) the use of thin-ply laminates, based on tow-spreading techniques, at the structural level for high-end applications; and ii) the reinforcement of the interfaces of thin-ply prepreg systems with carbon nanotubes. One notion that has hampered the use of thin-ply laminates (thickness lower than $100\mu m$) in high-end applications, is the general perception that thin plies have lower fracture toughness associated with longitudinal failure than the conventionally used standard thickness plies (thickness around $150\mu m$). This topic is addressed in a rigorous manner, coupling experimental and numerical analysis, based on previously developed models, to show that the intralaminar fracture toughness of the 0° plies is not ply thickness dependent.

A broad study of the structural performance of laminates, of the same fibre-resin system, made from unidirectional tapes, non-crimp fabrics and spread-tow fabrics of different ply thicknesses under various loading configurations is performed. A thorough study on the mechanical behaviour of these materials and their failure

processes is performed and an overall improvement of the material behaviour with the decrease of ply thickness is observed.

Finally, nanoengineered thin-ply composites are analysed by combining thin-ply materials with vertically aligned carbon nanotubes in the interfaces, (termed "nanostitching"). The fracture properties of the nano-reinforced interfaces are improved, however, as the crack bifurcates to the intralaminar region regardless of the test configuration, only the improvement related to the initiation fracture toughness can be measured. Improvements in the design strengths of structures whose main failure mechanisms is the onset of delamination can be obtained using this type of nano-reinforcement.

Resumo

Este trabalho tem como principal objetivo contribuir para o desenvolvimento de uma nova geração de materiais compósitos com um comportamento mecânico superior ao comportamento dos materiais compósitos de última geração atualmente utilizados pela indústria aeronáutica. Isso requer, por um lado, o desenvolvimento de modelos de análise capazes de prever o comportamento mecânico de laminados compósitos convencionais e não convencionais e, por outro lado, a análise detalhada do comportamento mecânico de materiais fabricados com base nestas novas tecnologias.

Neste trabalho, propõe-se uma estratégia de modelação, baseada no método dos elementos finitos, adequada à simulação do comportamento elástico e inelástico de detalhes estruturais fabricados com materiais compósitos. A estratégia é validada para vários tipos de detalhes estruturais e sistemas materiais e verifica-se a existência de uma boa correlação entre os resultados experimentais e numéricos, sendo os tempos de computação compatíveis com os requisitos impostos para o seu uso em contexto industrial.

Propõe-se também um modelo analítico capaz de prever a tensão de rotura de laminados multidirectionais na presença de entalhes a partir de apenas três propriedades materiais. O modelo é validado para várias geometrias e sistemas materiais, obtendo-se erros relativos entre os resultados experimentais e as previsões abaixo de 10% para todos os laminados e geometrias analisadas. O modelo analítico proposto é combinado com ferramentas estatísticas de forma a considerar a variabilidade associada às propriedades materiais e à geometria dos detalhes estruturais, permitindo a quantificação da incerteza associada às tensões de rotura estimadas analiticamente. Os modelos de análise propostos contribuem não só para um desenvolvimento mais rápido e económico de estruturas aeronáuticas, mas são também fundamentais para o desenvolvimento de novos materiais compósitos não convencionais.

Duas tecnologias recentemente desenvolvidas são abordadas nesta tese: i) o uso de laminados ultra-finos a nível estrutural para aplicações de alto desempenho; e ii) o reforço das interfaces de sistemas pré-impregnados com nanotubos de carbono. A tenacidade à fratura longitudinal das camadas ultra-finas (com espessura inferior a $100\mu m$) tem sido considerada inferior à das camadas de espessura convencional (espessura em torno de $150\mu m$). Esta noção tem atrasado o uso de laminados ultra-finos em aplicações estruturais já que é considerado que uma menor tenacidade à fratura longitudinal confere a estes materiais um comportamento mais frágil e desta forma menos desejável. Este tema é abordado de forma rigorosa, combinando análises experimentais e numéricas, com base nos modelos de análise desenvolvidos, tendo sido demonstrado que a tenacidade à fratura intralaminar das camadas a 0°

de facto não depende da espessura da camada.

É também realizado um estudo experimental detalhado focado no comportamento mecânico de laminados multidirecionais fabricados com camadas unidirecionais, têxteis e tecidos "não entrelaçados" do mesmo sistema material e com diferentes espessuras de camada. É observada uma melhoria geral do comportamento mecânico dos laminados com a diminuição da espessura da camada.

Por fim, é investigada a influência do uso de nanotubos de carbono alinhados verticalmente como reforço das interfaces de laminados compósitos ultra-finos na sua tenacidade interlaminar. Verifica-se que, usando as configurações de teste normalizadas, apenas é possível medir o aumento da tenacidade interlaminar associada ao valor de iniciação de propagação da fenda, já que a presença dos nanotubos de carbono promove a bifurcação da fenda para a região intralaminar logo após o início da sua propagação.

Contents

List of Figures

List of Tables

List of symbols

Chapter 3

$\mathbf{1}$	Identity tensor
$\mathbf{a}$	Preferred direction
$\mathbf{A}$	Structural tensor - characteristic direction of a transversely isotropic material
$\mathbf{C_0}$	Undamaged stiffness tensor
d	Damage variable associated to interface failure
d_i	Scalar damage variables associated with ply failure
E_1, E_2	Longitudinal and transverse Young's moduli
f_{fxc}	Internal frictional parameter under longitudinal compression
F_i	Damage activation function for direction i
f_{XT}, f_{XC}	Long. tensile and compressive stress at inflection point
f_{XC}^{ef}	Effective longitudinal compression strength ratio at the inflection point
G_{12}	In-plane shear modulus
$\mathcal{G}$	Complementary free energy density
$\mathcal{G}_{1+}$, $\mathcal{G}_{1-}$	Fracture toughness for longitudinal tension and compression
$\mathcal{G}_{1-}^{ef}$	Effective longitudinal compressive fracture toughness
$\mathcal{G}_{2+}$, $\mathcal{G}_{2-}$	Mode I fracture toughness for transverse tension and compression
$\mathcal{G}_6$	Mode II fracture toughness
$\mathcal{G}_6^{ef}$	Effective fracture toughness for in-plane shear
$\mathcal{G}_{Ic}$, $\mathcal{G}_{IIc}$	Mode I and mode II fracture toughness
$\mathcal{G}_{IIc}^{ef}$	Effective fracture toughness
$\mathbf{H}$	Lamina compliance tensor
I_1, I_2, I_3	Invariants of transversely-isotropic composite materials
$\mathbf{K}$	Diagonal stiffness matrix
K, K_N, K_{sh}	Penalty stiffness
K_β	Mode-dependent interfacial stiffness
K_P	Shear incremental stiffness under plastic flow
r_d	Elastic domain threshold function
r_i	Elastic domain threshold in the direction i

S_L, S_T	In-plane and transverse shear strengths
S_L^{ef}	Artificial in-plane shear strength
S_{LP}	Shear stress that activates plastic flow
X_T, X_C	Longitudinal tensile and compressive strengths
Y_{BT}, Y_{BC}	Biaxial transverse tensile and compressive strengths
Y_T, Y_C	Transverse tensile and compresive strengths
α_0	Fracture angle of the UD ply subjected to transv. compression
α_i	Yield surface parameters
α_{ii}, β_{ii}	Coefficients of thermal and hygroscopic expansion
β	Local mixed mode ratio
$\boldsymbol{\Delta}$	Relative displacement
$\boldsymbol{\Delta}^{de}$, $\boldsymbol{\Delta}^{di}$	Elastic and inelastic part of the relative displacement
Δ^o, Δ^f	Displacement jumps under mixed-mode conditions
ΔT, ΔM	Temperature and moisture content variations
$\boldsymbol{\epsilon}$	Strain tensor
$\boldsymbol{\varepsilon}_e$	Elastic strains
η	Mixed-mode interaction parameter
η_G	Internal frictional parameter under in-plane shear
η^L, η^T	Longitudinal and transverse frictional coefficient
λ	Mixed-mode norm of the displacement jump
μ	Friction coefficient
ν_{12}	Poisson's ratio
ϕ	Friction function
ϕ_i	Loading function associated with the direction i
φ	Misalignment angle
φ^C	Misaligned angle at failure of a UD ply under longitudinal compression
ψ	Angle of the kinking plane
$\boldsymbol{\sigma}$	Stress tensor
$\tilde{\boldsymbol{\sigma}}$	Effective (undamaged) stress tensor
$\tilde{\boldsymbol{\sigma}}^p$	Plasticity inducing stresses
$\tilde{\boldsymbol{\sigma}}^r$	Reaction stresses
τ	Homogenized interface traction
τ^d	Damaged component of the interface traction
τ^u	Undamaged component of the interface traction
$\tilde{\tau}^L_{\text{eff}}$, $\tilde{\tau}^T_{\text{eff}}$	Effective in-plane and transverse shear shear strengths
τ_n	Strength under pure mode I
τ_{sh}	Strength under pure mode II
θ	Sliding angle

Chapter 4

$\mathbf{A}$, $\mathbf{D}$	In-plane and flexural laminate stiffness matrix
$\acute{E}$	Equivalent modulus of the laminate
E_1, E_2	Longitudinal and transverse Young's moduli
E_1^*, E_2^*	Trace-normalized Young's moduli
E_x, E_y	Laminate Young's modulus in the x- and y-directions
$E_x^{(i)}$, $E_y^{(i)}$	Young's modulus in the x- and y- directions of sub-laminate (i)
E_x^*, E_y^*	Trace-normalized laminate Young's moduli
G_{12}	Shear modulus
G_{12}^*	Trace-normalized shear modulus
G_{xy}	Laminate shear modulus
$G_{xy}^{(i)}$	Shear modulus of the sub-laminate (i)
G_{xy}^*	Trace-normalized laminate shear modulus
$\mathcal{G}_I(a)$	Mode I Energy Release Rate
$\mathcal{G}_{Ic}$	Energy dissipated per unit area
$\mathcal{K}_I(a)$	Mode I Stress Intensity Factor
$\mathcal{K}_{Ic}^{(0)}$	Fracture toughness of a sub-laminate of 0° plies
$\mathcal{K}_{Ic}^{(i)}$	Fracture toughness of the sub-laminate (i)
$\mathcal{K}_{Ic}^{L}$	Fracture toughness of the laminate
K_T	Stress concentration factor of a plate with a centre hole
K_T^{∞}	Stress concentration factor of na infinite plate with centre hole
l	Crack length at failure
l_{fpz}	Length of the fracture process zone
P_{10}	10^{th} percentile value
$\mathbf{Q}$	Plane stress stiffness matrix in the material coordinate system system
$\overline{\mathbf{Q}}$	Plane stress stiffness matrix in the laminate coordinate system system
$\mathbf{Q}^*$	Trace-normalized plane stress stiffness matrix
R	Radius of the hole
$\mathcal{R}(\Delta a)$	$\mathcal{R}$-curve
$\mathcal{R}_{SS}$	Steady-state value of the fracture toughness
s	Standard deviation
Tr	Trace
$t^{(i)}$	Thickness of sub-laminate (i)
t^L	Laminate thickness
W	Width of the specimen
X^L	Laminate unnotched strength
$\bar{x}$	Mean value
χ^0	Orthotropy correction factor of the of 0° plies

$\chi^{(i)}$	Orthotropy correction factor of the sub-laminate (i)
ν_{12}	Poisson's coefficient
ν_{12}^{*}	Trace-normalized Poisson's coefficient
ν_{xy}, ν_{yx}	Laminate Poisson's ratios
$\nu_{xy}^{(i)}$, $\nu_{yx}^{(i)}$	Poisson's ratios of sub-laminate (i)
ν_{xy}^{*}	Trace-normalized laminate Poisson's coefficient
$\Omega_0^{(i)}$	Stress ratio
ρ	In-plane orthotropy parameter of the laminate
$\rho^{(i)}$	In-plane orthotropy parameter of the sub-laminate (i)
$\bar{\sigma}^0$	Remote failure stress of a sub-laminate of 0° plies
$\bar{\sigma}^{(i)}$	Remote failure stress of the sub-laminate (i)
$\bar{\sigma}^{\infty}$	Remote stress
$\sigma_{xx}(0,\, y)$	Stress distribution along the x- direction
ζ, η	Fitting parameters of the $\mathcal{R}$-curve

Chapter 5

a, a_0	Crack length, initial value of the crack length
A, C	Fitting parameter used in the linear regression I and II
$\acute{E}$	Equivalent modulus
E_1, E_2	Longitudinal and transverse Young's moduli
E_f	Longitudinal Young's modulus of the fibres
E_m	Young's modulus of the matrix
f_{fxc}	Internal frictional parameter under longitudinal compression
f_{XT}, f_{XC}	Long. tensile and compressive stress at inflection point
G_{12}	In-plane shear modulus
$\mathcal{G}_{1+}$, $\mathcal{G}_{1-}$	Fracture toughness for longitudinal tension and compression
$\mathcal{G}_{2+}$, $\mathcal{G}_{2-}$	Mode I fracture toughness for transverse tension and compression
$\mathcal{G}_6$	Mode II fracture toughness
$\mathcal{G}_{Ic}$, $\mathcal{G}_{IIc}$	Mode I and mode II fracture toughness
$\mathcal{G}_I$	Energy release rate in mode I
$\mathcal{G}^d$	Energy dissipated due to in-plane shear damage
$\mathcal{G}^p$	Plastic work due to in-plane shear plasticity
h	Thickness of the laminate
h_0	Thickness of the 0° plies
I_3	Third invariant of transversely-isotropic composite materials
K_P	Shear incremental stiffness under plastic flow
K	Penalty stiffness
$\mathcal{K}_I$	Stress intensity factor

l	Half length of the specimen
l_{fpz}	Length of fracture process zone
M, N	Fitting parameter used in the bilogarithmic regression fit
$\mathcal{R}_0(\Delta a)$	$\mathcal{R}$-curve for the 0° ply
$\mathcal{R}(\Delta a)$	$\mathcal{R}$-curve of the laminate
$\mathcal{R}_{ss}$	Steady-state value of fracture toughness
S_L, S_T	In-plane and transverse shear strengths
S_{LP}	Shear stress that activates plastic flow
S_L^{is}	In-plane shear in-situ strength
V_f	Fibre volume fractions
w	Half of the width of the specimen
X_T, X_C	Longitudinal tensile and compressive strengths
Y_T, Y_C	Transverse tensile and compresive strengths
Y_{BT}, Y_{BC}	Biaxial transverse tensile and compressive strengths
Y_C^{is}	Transverse compression *in-situ* strength
Y_T^{is}	Transverse tension *in-situ* strength
α_0	Fracture angle of the UD ply subjected to transv. compression
α, α_0	Shape parameter, initial value of the shape parameter
β	Parameter used in the $\mathcal{R}$-curve fit
Δa	Crack increment
η_G	Internal frictional parameter under in-plane shear
η	Mixed-mode interaction parameter
κ	Correction factor
κ_0	Correction factor κ for $\alpha = \alpha_0$
$\acute{\kappa}_0$	Derivative of the correction factor κ for $\alpha = \alpha_0$
μ	Friction coefficient
$\mathbf{\Phi}$	Matrix for the polynomial fitting
ρ	In-plane orthotropy parameter
$\overline{\sigma}$	Ultimate nominal stress
$\overline{\sigma}^{\infty}(w)$	Size effect law
τ_n	Strength under pure mode I
τ_{sh}	Strength under pure mode II

Chapter 6

E_x, E_y	Laminate Young's moduli
G_{xy}	Laminate shear modulus
K_T	Stress concentration factor
K_T^{∞}	Stress concentration factor of an infinite plate with a centre hole

L	Length of the specimen
M	Geometrical parameter
P	Maximum load
R, D	Hole radius and diameter
R_K	Finite width correlation factor
t	Thickness of the specimen
W	Width of the specimen
X_L^T, X_L^C	Unnotched tensile and compressive strengths
η	Notch sensitivity ratio
ν_{xy}	Laminate Poisson's ratio
σ^{br}	Bearing stress
σ_N	Normalized strength
$\overline{\sigma}_N$	Normalized notched strength
$\overline{\sigma}^T$, $\overline{\sigma}^C$	Notched tensile and compressive strengths

Chapter 7

a_0	Initial crack length
b	Width of the specimen
c	Lever arm length
E_1, E_2	Longitudinal and transverse Young's moduli
$\mathcal{G}_{1+}$, $\mathcal{G}_{1-}$	Fracture toughness for longitudinal tension and compression
$\mathcal{G}_{2+}$, $\mathcal{G}_{2-}$	Mode I fracture toughness for transverse tension and compression
$\mathcal{G}_6$	Mode II fracture toughness
$\mathcal{G}_{Ic}$, $\mathcal{G}_{IIc}$	Mode I and mode II fracture toughness
h	Half thickness of the specimen
J	J-integral
K_P	Shear incremental stiffness under plastic flow
K	Penalty stiffness
L	Length of the specimen
P	Applied load
p	p-value
S_L, S_T	In-plane and transverse shear strengths
S_{LP}	Shear stress that activates plastic flow
X_T, X_C	Longitudinal tensile and compressive strengths
Y_T, Y_C	Transverse tensile and compressive strengths
Y_{BT}, Y_{BC}	Biaxial transverse tensile and compressive strengths
α	Level of significance
τ_n	Strength under pure mode I

τ_{sh}	Strength under pure mode II
θ	Rotation angle on the load introduction points

List of abbreviations

A-CNT	Aligned Carbon Nanotubes
BEA	Bearing
C3D8R	8-node linear brick reduced integration element
CAI	Compression After Impact
CFRP	Carbon Fibre Reinforced Polymer
CMH-17	Composite Material Handbook
CNT	Carbon Nanotube
COH3D8	8-node three-dimensional cohesive element
CVD	Chemical Vapour Deposition
DCB	Double Cantilever Beam
DENT	Double Edge Notched Tension
DIC	Digital Image Correlation
ECDF	Empirical Cumulative Distribution Function
ENF	End Notched Flexure
ERR	Energy Release Rate
FAW	Fibre Areal Weight
FE	Finite Element
FFM	Finite Fracture Mechanics
FHC	Filled Hole compression
FWC	Finite-Width Correction
ILSS	Interlaminar Shear Strength
LEFM	Linear Elastic Fracture Mechanics
LPT	Laminated Plate Theory
LVI	Low Velocity Impact
MCS	Monte Carlo Simulations
MWCNT	Single-Walled Carbon Nanotubes
NCF	Non-crimp fabric
OHC	Open-hole Compression

OHT	Open-hole Tension
PSC	Plain Strength Compression
PST	Plain Strength Tension
REA	Representative Elementary Area
$\mathcal{R}$-curve	Crack resistance curve
RTM	Resin Transfer Moulding
RVE	Representative Volume Element
SBS	Short Beam Shear
SEM	Scanning electron microscope
STF	Spread tow fabric
SWCNT	Single-Walled Carbon Nanotubes
UC	Unnotched compression
UD	Unidirectional
UQ&M	Uncertainty Quantification and Management
UT	Unnotched tension
VA-CNT	Vertically Aligned Carbon Nanotubes
VARTM	Vacuum Assisted Resin Transfer Moulding

Part I

Introduction

Chapter 1

Introduction

Advanced polymer matrix composites result from the combination of a polymeric thermoset or thermoplastic polymer resin and either short er continuous reinforcing fibres. These materials started being exploited in the 20^{th} century with the appearance of glass fibre and quickly gained visibility. The aerospace industry was the key driver of the use of polymer matrix components for structural and non-structural applications, however, their use has gained a more widespread acceptance, and other industries, such as the automotive, boating and sports equipment industries have shown great interest in the technology.

Emerging technologies for structural applications have been addressed in more detail in the past decade and researchers, academic and industrial alike, have been seeking different or complementing characteristics with each one. Some of these tecnhologies are the following:

- Thermoplastic based composites, where continuous fibres are bound by high performance thermoplastic resins, have gained some visibility in recent years as new manufacturing techniques that allow their effective processing have been developed. Researches have been looking for the improved toughness over thermoset based composites, virtual eternal shelf-life, recyclability, and reduced manufacturing/maintenance cost.

- Fibre hybrid composites, where different types of fibres are combined in the same laminate, have improved design freedom, reduced cost if high- and low-grade fibres are combined and have the potential to yield more ductile and tough materials, improving the low crash-worthiness generally associated with composite materials.

- Thin-ply laminates, made from plies 2-6 times thinner than conventional grade plies, have improved design freedom, potential to yield lighter structures, delayed onset of damage and consequent improved fatigue life.

- Nano-reinforced composite laminates, where carbon nanotubes are used alongside microscale fibres, have the potential to result in materials with improved strength and toughness by the improvement of matrix related properties and improved multifunctionality, taking advantage of the high thermal and electrical conductivity of carbon nanotubes.

The introduction of new materials in an industrial context relies, not only on the understanding of their behaviour, but also on the definition of computational

strategies to assist in their design, definition of new design rules and standardization of efficient manufacturing procedures compatible with the given technology. This thesis will focus on some of the presented emerging technologies and the advanced computational methods to predict and understand the behaviour of these materials.

1.1 Motivation and objectives

The main objective of this work is to contribute to the development of a new generation of advanced composite structures with improved properties over the current state-of-the-art composite materials used in the aeronautical industry. On one hand, through the development of analysis models to predict the mechanical behaviour of composite laminates, and on the other hand, through the detailed analysis of the mechanical behaviour of materials manufactured using promising technologies recently developed.

With the development of analysis models to predict failure of composite laminates, the author intends to push the boundaries of simulation of fracture of composite materials, and to contribute to the reduction of the certification time and cost associated with the introduction of new materials and structures in the aeronautical industry. This process relies on the development of advanced numerical and analytical models, definition of standard modelling strategies and proper material definition.

It is clear that the introduction of new materials implies the comprehensive understanding of their mechanical behaviour. The recent development of tow-spreading techniques, which are able to produce thin plies, with thickness comprised between 20μm and 100μm, motivated the study of the effect of ply thickness on the ply properties and the structural behaviour of laminates that use thinner plies as building blocks. Two promising recently developed technologies based on these techniques were selected and are addressed in this thesis: the use of thin-ply laminates at the structural level for high-end applications, and the reinforcement of the interfaces of thin-ply prepreg systems with carbon nanotubes. The technologies selected have dissimilar levels of maturity and distinct timelines for their potential integration in an industrial context, being the latter in a lower technology readiness level.

Regarding the mechanics of thin-ply laminates, the author intends to address two topics that still require further research. On one hand, one notion that has hampered the use of thin-ply laminates in high-end applications, is the general perception that thin plies have lower fracture toughness associated with longitudinal failure than the conventionally used intermediate grade plies. With this work, the author intends to clarify the effect of ply thickness on the intralaminar fracture toughness in a consistent and scientifically rigorous manner. On the other hand, even though several experimental studies on the structural behaviour of thin-ply laminates have been made, no direct comparison on the effect that the use of different types of geometry reinforcement has on the damage mechanisms that dominate failure and strength of multidirectional laminates and structural components has been made. Part of the work developed here dedicated to this study.

The combination of thin-ply laminates with nano-stitched interfaces based on carbon nanotubes has great potential to yield improved polymer-based composite materials with improved properties and multifunctionality. However, comprehensive studies still need to be conducted to assess the advantages of such a material system

and to understand what are mechanisms that control their failure. The objective of this work is to further develop this technology, identify potential applications and develop numerical tools to predict the behaviour of nanoengineered materials.

1.2 Thesis layout

This thesis is divided in five parts. In Part II, the state-of-the-art and literature review is presented. This chapter is divided in two sections. The first is dedicated to the spread-tow thin-ply technology, where the mechanical performance and damage mechanisms typically observed in thin-ply laminates are addressed. The second is dedicated to the study of nano-reinforced composite materials with focus on the combination of unidirectional prepregs with vertically aligned carbon nanotubes in the interfaces.

In Part III of this thesis, two analysis models to predict the failure of composite laminates are presented in detail. In Chapter 3, a ply-level finite element modelling methodology to simulate composite laminates at coupon level compatible with industrial requirements is proposed. Different material systems of interest to the aeronautical community and test cases with increasing levels of complexity are addressed. The proposed methodology is used throughout the remaining part of the work to clarify experimental observations and predict ultimate failure of composite components.

Even though finite element models to simulate failure of composite laminates are particularly powerful solutions given their flexibility, their computational complexity and cost still limits their use, particularly as a preliminary design tool. Considering this limitation, a fast-analysis analytical model to predict the notched strength of multidirectional laminates is proposed and validated in Chapter 4. The proposed analytical framework is also coupled with statistical tools required to consider the variability of the material and geometrical parameters and propagate this uncertainty to the notched and unnotched strengths.

Part IV of this thesis focuses on the mechanics of thin-ply composite laminates. Two topics are addressed: on one hand, given the contradictory opinions found in literature, an experimental/numerical study on the effect of the ply thickness on the fracture toughness associated with tensile fibre failure is presented in Chapter 5. On the other hand, a comprehensive study of the structural performance of equivalent multidirectional laminates made from unidirectional tapes, non-crimp fabrics and spread-tow fabrics of different ply thicknesses is presented in Chapter 6. Structural details corresponding to unnotched specimens, notched specimens, and bolted connections are analysed to clarify the effect of ply thickness, to elucidate on the effect of selective ply thickness hybridization and to understand the effect of the type of geometry reinforcement on the damage mechanisms that dominate failure and strength of multidirectional laminates.

In Part V, the combination of thin plies with carbon nanotubes is explored. In Chapter 7, a methodology to characterize nano-reinforced interfaces is proposed and a numerical study on the effect of nano-reinforcing the interfaces of a panel with a co-cured stiffener is performed.

Finally, the main conclusions of the work carried out and potential research topics related to the developed work are presented in Part VI.

Part II

State-of-art and literature review

Chapter 2

State-of-art and literature review

2.1 Spread tow thin-ply laminates

Conventional composite laminates are made of plies with fibre areal weight (FAW) higher than 100 g/m^2. Recently, a new generation of composite materials has been introduced in the market: thin-ply composites. This type of material is made out of plies with FAW below 100 g/m^2 and as low as 30g/m^2. The plies are produced by a method known as spread tow thin-ply technology where large fibre tows are continuously spread to a flat thinner tape. The spreading machines are typically equipped with an air duct and a vacuum system. As the tow passes through the air duct, it is sagged down, which causes the fibres to separate from each other. The tows are continuously and stably spread and since the air flow is relatively low, the fibres remain undamaged. This method allows the production of thin tapes that can then be used to produce unidirectional plies and thin fabrics [6]. The morphology, design opportunities and mechanical performance of thin-ply composite laminates will be discussed in the following sections.

2.1.1 Reinforcement geometry

Different types of ply reinforcement can currently be manufactured based on the spread tow thin-ply technology:

- Unidirectional tapes (UD) are continuous fibre tapes/plies (Fig. 2.1a) and are the type of reinforcement more commonly used.

- Non-crimp fabrics (NCFs) are multiaxial fabrics made up of continuous fibre unidirectional plies (0°, 90°, ±45°) that are mechanically sewn together (Fig. 2.1b). The polymeric knitting threads do not provide additional reinforcement but hold the yarns in place prior to the infusion of resin. This type of multi-angle ply construction is considered to have similar behaviour to UD tapes and increased mechanical performance compared to woven fabrics. Since multiple (typically two) angle plies are sewn together, prepreg handling during lay-up is easier than when UD prepreg tapes are used and the lay-up process is more efficient.

- Spread-tow fabrics (STFs) are produced by interlacing spread tow tapes (Fig. 2.1c). The thinner the tapes, the smaller the waviness in both the 0° and 90° directions caused by the weaving architecture (crimp angle). The result is a

reinforcement with the mechanical performance similar to a cross-plied UD and the ease of handling of a fabric.

Experimental studies to assess the effect of ply thickness on the mechanical performance of composite structures based on these three thin-ply technologies have been performed. UD tapes have been studied in Refs. [1, 2, 6, 19], NCFs in Refs. [18, 19, 24], and STFs in Refs. [19, 24]. However, the performance of the different types of reinforcement have not been compared since the different types of reinforcement are supplied by distinct manufacturers, which in turn, generally develop and supply prepregs based on different resins, reinforcing fibres and sizings.

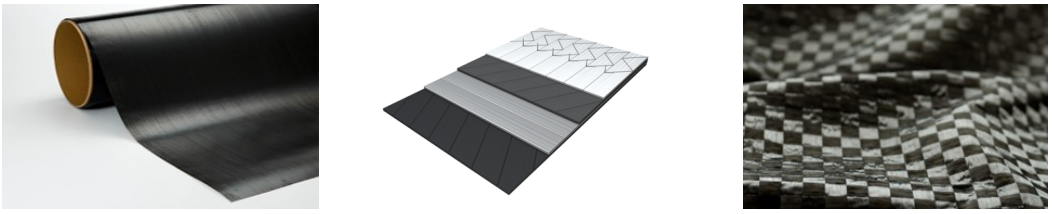

(a) (b) (c)

Figure 2.1: Types of spread tow ply reinforcement: a) unidirectional tapes, b) non-crimp fabrics and c) spread tow fabrics

2.1.2 Design space

The use of thin plies offer some advantages and opportunities in terms of design. First of all, the design constrains such as quasi-isotropy or symmetry can be met with less total laminate thickness and, therefore, weight can be saved. Moreover, the constrain that laminates should be symmetric can be relaxed for laminates manufactured with plies that are thin enough to minimize warpage. This constraint is mostly a manufacturing constrain: unsymmetric laminates generally exhibit curvature after curing because of the residual stresses developed during cool-down [25]. However, the residual stresses that cause curvature are a function of the components of the extension-bending coupling matrix, which depend on the ply thickness. For sufficiently thin-plies the components of the coupling matrix will be insignificant and therefore will not cause noticeable bending of the laminates. This opens the potential to use thin-plies in continuous automatic layup. Since more plies can be stacked together for the same laminate thickness, the design freedom is improved, and, for example, smaller mismatch angles (angles between adjacent plies) can be used, which is shown to improve the interfacial fracture resistance [1].

2.1.3 Microstructure

Thin-ply laminates have slightly different microstructure than conventional grade laminates as a direct consequence of the manufacturing process. In spread tow thin-ply technology, the large fibre tows are continuously spread to a flat thinner tape until a desired ply thickness is achieved. Since the plies are thinner, the resin flows better between the fibres and, since the bundles are smaller, the fibres are better dispersed throughout the laminate, which results in a more homogeneous material than conventional laminates. Amacher et al. [1] analysed the morphology of thin

($30g/m^2$), intermediate ($100g/m^2$) and thick ($300g/m^2$) laminates and concluded that for the thinnest plies, the microstructure is significantly more homogeneous up to the point that it becomes difficult to identify the interfaces between the plies (see Fig. 2.2). Also, non-crimp fabric thin-ply laminates have smaller crimp angles and resin pockets than thick-ply laminates, and therefore, the regions where damage is prone to appear and propagate from are smaller (see Fig. 2.3).

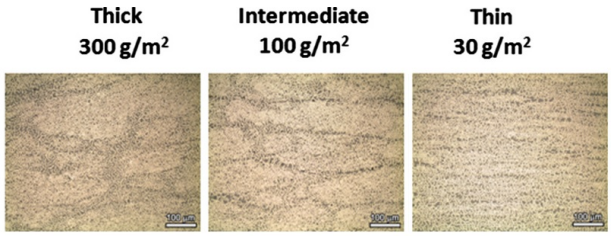

Figure 2.2: Microstructure of unidirectional laminates for different ply thickness [1]

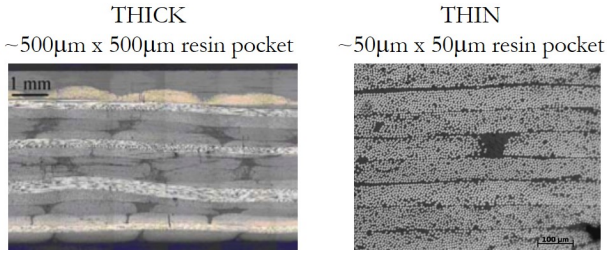

Figure 2.3: Microstructure and size of the resin pockets on unidirectional laminates with different ply thickness

The uniformity and homogeneous morphology characteristic of thin-ply laminates has consequences in terms of mechanical performance. Amacher et al. [1] measured the elastic and ply strengths of three grades of the same material system: thin (0.03mm), intermediate (0.1mm) and thick (0.3mm). No significant differences between the different lamina level properties was observed except for the longitudinal compression strength, which was around 20% higher for thinnest configuration compared to the thick configurations. The longitudinal compression strength was found to be higher for thinner plies as a consequence of the uniformity of the plies as shown in Fig. 2.2. The difference in morphology originates from the tow spreading process involved in the production of the prepregs. The tows are spread until the desired thickness is obtained and, therefore, the thinner the plies, the more spread and consequently more homogeneous and less prone to fibre micro buckling and fibre kinking the plies become.

The homogeneous morphology characteristic of thin-ply laminates influences not only the longitudinal compression strength but also the mode I fracture toughness as first suggested by Arteiro [24] and confirmed by Frossard et al. [2]. Frossard et al. [2] assessed the influence of ply thickness on the mode I fracture toughness by testing DCB specimens made with 0.03mm, 0.075mm and 0.150mm thick plies. It was observed that, even tough the energy release rate (ERR) at crack initiation is nearly identical regardless of the ply thickness, the ERR at steady-state of the thin laminate (0.03mm) and intermediate (0.075mm) were around 60% and 40% lower

than that of the thicker laminate (0.150mm), respectively. As shown in Fig. 2.4, the thinner the plies, the less wavy the crack plane is and, therefore, the less prone to promote fibre bridging the material becomes.

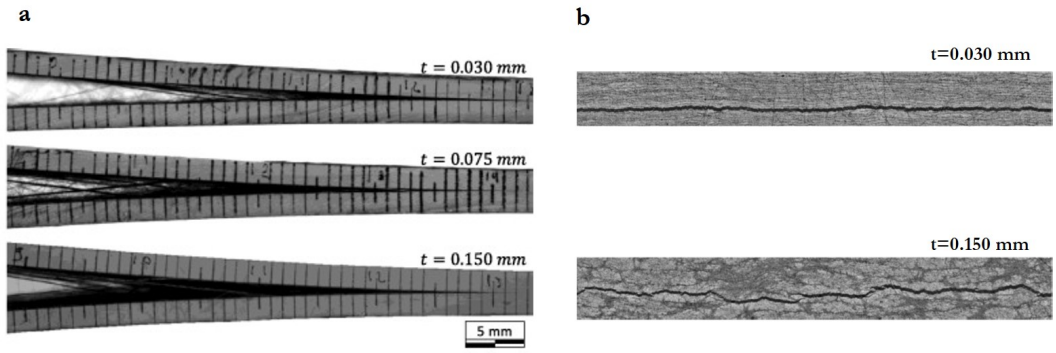

Figure 2.4: Side views (left) and cross sections (right) of specimens with different ply thicknesses exhibiting different fibre bridging intensities [2]

2.1.4 Mechanical performance

It has been shown by means of acoustic emission [1, 6, 26], X-ray photos and C-scan images [6], and also by observation of damage modes of failed specimens [1, 6, 18, 19] that thin-ply laminated composites can suppress microcracking, delamination and splitting damage under general loading conditions. This strengthening effect that inhibits the excessive growth of cracks in off-axis plies within a laminate is a consequence of the *in-situ* effect, which gains additional importance for thin-ply laminates. The *in-situ* effect is characterized an increase in transverse and shear strengths when a ply is constrained by plies with different fibre orientations in a laminate. This strengthening effect is a consequence of the constraining effect imposed by the neighbouring plies, which increases with the decrease of ply thickness. This effect was first detected experimentally for transverse tension and in-plane shear by Parvizi et al. [27], and further analysed by other authors [28–33]. More recently, using micro-mechanical modelling, Arteiro et al. [4] demonstrated that the transverse compressive strength also depends on the ply thickness. The increase in ply strength with ply thinness is one of the reasons why subcritical matrix cracking is delayed or suppressed in thin-ply laminates.

To evaluate the mechanical response of ultra-thin plies, and to assess the effect of ply thickness on the mechanical response of laminated composites under tension [3] and compression [4], Arteiro and co-authors [3, 4] developed a micro-mechanical finite element model consisting on a representative volume element of a 90° ply with thickness between 0.02mm and 0.140mm in between two homogenised 0° plies. Arteiro and co-authors [3, 4] observed that the damage mechanisms and damage distribution vary with the ply thickness: the thinner the plies the more the dispersed damage and the higher the applied displacement required to propagate a crack all way though the thickness, as shown in Figs. 2.5 and 2.6. For ultra-thin plies under tensile loading [3], suppression of transverse cracking is clearly observed. e.g. in tension loading, for an applied strain of 2% the cracks did not propagate through the thickness, which means that ply failure was not detected. Note that,

such applied strain is higher than the maximum elongation allowed by the fibres which suggests that, in a laminated composite with sufficiently thin plies, tensile transverse cracks in the 90° plies would be completely suppressed. In brief, for sufficiently thin-plies, failure is controlled by fibre failure since damage in off-axis plies is suppressed up to the point just before failure.

As any change in material behaviour, damage suppression has implications on the mechanical performance of composite structures, on the design constrains and on the performance prediction tools. Extensive experimental programs have been carried out to evaluate the performance of thin-ply laminates compared to laminates made out of conventional thick plies for different types of loading, geometries and structural details to understand the advantages and disadvantages of this new type of material Ref. [1, 6, 18, 19, 24, 26, 37, 39]. Some of these studies are summarized in the following sections.

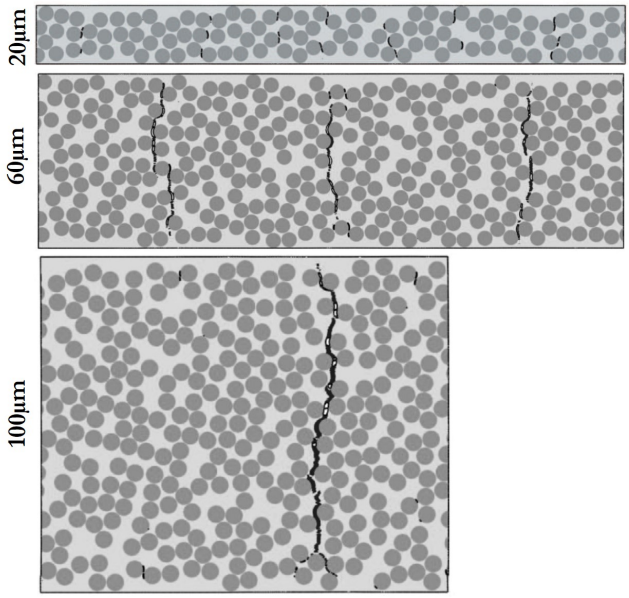

Figure 2.5: Contour plots of the matrix damage variable on an RVE of a 0.020, 0.06 and 0.100mm thick 90° ply of a sublaminate with 0° outer plies under transverse tension for an applied strain of 1.2%. [3]

2.1.4.1 Unnotched strength

In general, thin-ply laminates show enhanced ultimate plain strength [1, 6, 19]. Unlike thick-ply composites, which show damage due to microcracks and delamination before final failure, little severe damage before failure was detected in thin-ply composites. In fact, as reported by Sihn et al.[6] and Amacher et al. [1], the response of thin-ply laminates loaded in tension remains linear up to failure and no damage was detected by acoustic emission up to 97% of the ultimate failure for the 0.03mm thick ply laminate [1]. This indicates that the onset of damage is delayed until the point just before failure.

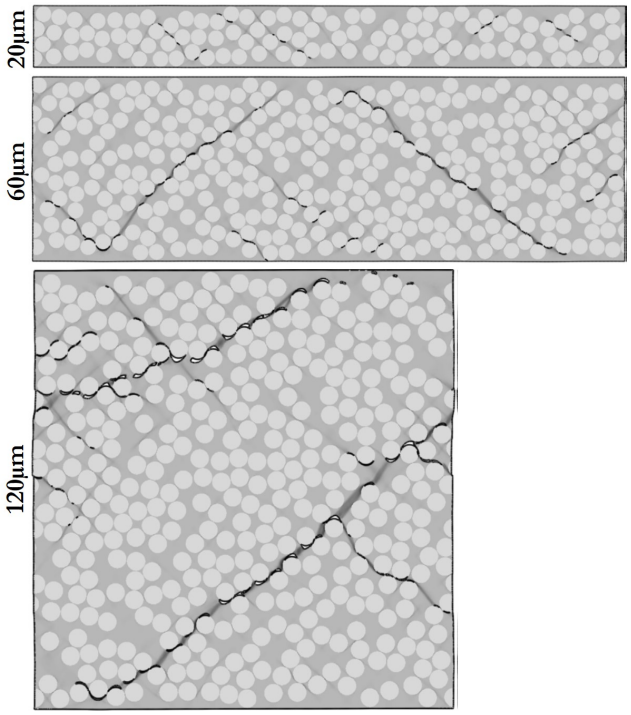

Figure 2.6: Contour plots of the matrix damage variable on an RVE of a 0.020, 0.06 and 0.120mm thick 90° ply of a sublaminate with 0° outer plies under transverse compression for an applied strain of 2.5%. [4]

2.1.4.2 Notched strength

Any structure inevitably has weak points as a consequence of the presence of a geometrical discontinuities or discrete damage. For this reason, it is important to evaluate the performance of composite structures in the presence of stress concentrations both under tension and compression. With the development of thin-ply laminates, it became crucial to study the effect of ply thickness on the notched strength of composite laminates. Some of the studies recently performed and their conclusions are summarized below.

2.1.4.2.1 Tension

Green et al. [34] and Wisnom et al. [35] studied the effect of ply thickness on the tensile strength of notched composites of conventional grade composite materials. They concluded that, if the laminates have sufficiently thin plies, failure is fibre dominated without extensive delamination and damage of the off-axis plies. If the plies are too thick, failure is matrix dominated: damage propagates from the off-axis plies to the interfaces causing delamination to spread across the width and the length of the specimens. For intermediate thick plies, conventionally used, the damage mechanisms combine fibre failure with some delamination around the notch.

These studies regard the effect of ply thickness on damage onset and propagation of laminates with ply thickness higher than the conventional grade, however, the development of spread thin-ply technology required the need to analyse the damage mechanisms associated with failure of notched thin-ply structures. Sihn et al. [6] performed tests to evaluate the performance of tow-spread thin-ply laminated

composites including open-hole tension tests on a quasi-isotropic layups. Amacher et al. [1] also investigated the influence of ply thickness on thin-ply laminates on open-hole specimens. In both studies [1, 6], the load-displacement curves were obtained and acoustic emission was used to detect first ply failure. The recorded load displacement curves of thin-ply laminates were shown to be linear up to failure and the first ply failure detected by acoustic emission was recorded for loads very close to ultimate failure of the specimens.

Arteiro and co-authors [18, 20] studied the notched performance of thin-ply laminates and Furtado et al. [19] compared the performance of notched thin-ply and conventional intermediate grade laminates. The authors [18–20] evaluated subcritical damage near the notched by analysing the onset and propagation of cracks in the outer surfaces using Digital Image Correlation. Using thin-ply laminates the load displacement curves were shown to be linear up to failure and nearly no surface cracks were detected before ultimate failure, which indicates that damage extension is very limited up to final failure.

From these studies [1, 6, 18–20] it was concluded that, the thinner the plies, the higher the stress at which the first ply fails but the lower the ultimate strength of the specimen. i.e. the thinner the plies, the less damage propagation there is and the more catastrophic and premature ultimate failure will be. While subcritical damage and damage propagation before final failure is usually a disadvantage because it leads to degradation of the material and can eventually contribute to delamination growth, for notched structures loaded in tension, it is actually beneficial. As schematically shown in Fig. 2.7, while in conventional thick laminates, splitting and matrix cracking appear at the vicinity of the notches, allowing stress relaxation in that area to occur, in thin-ply laminates, this blunting mechanism is inhibited, which means that stress concentration around the notch is not relaxed until final premature brittle failure of the structure. This disadvantage has been pointed out as one of the main obstacles to the introduction of thin plies in a large scale.

Furtado et al. [19] introduced the concept of ply-hybridization where both thin and intermediate grade plies of the same material system are combined in the same laminate. The open-hole tension strength of thin, intermediate grade and hybrid layups was evaluated and compared. Two types of hybridization were studied: uniform combination of thin and conventional plies resulted in a hybrid laminate with intermediate notched response and a selective hybridisation, where thin off-axis plies are combined with thicker 0° plies, resulted in a globally enhanced notched behaviour without compromising the unnotched response. This work clearly showed how ply-level hybridisation, when designed to trigger specific damage mechanisms, can be used to improve the notched response of composite laminates, thus overcoming one of the main disadvantages of thin-ply laminates.

2.1.4.2.2 Compression

As in tensile loading, different damage modes can be observed in compression depending on the ply thickness. For sufficiently thin plies, failure is brittle and dominated by fibre kinking. Since there is not severe microcraking, the stress is the 0° plies increases until fibre kinking is triggered. For sufficiently thick plies failure is dominated by delamination: matrix damage develops and propagates to the interfaces and eventually across the width and length of the specimens. Since the stress is redistributed due to matrix dominated mechanisms, the 0° plies might not even

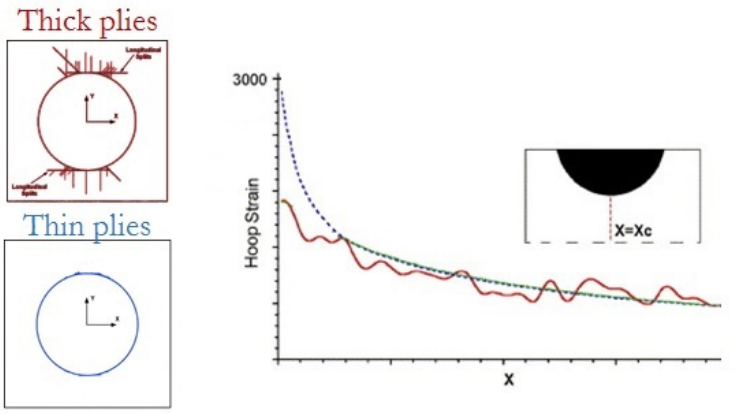

Figure 2.7: Schematic representation of the strain distribution and damage around the hole for thick and thin-ply laminates loaded in tension (modified from [5])

fail. For intermediate ply thicknesses, the failure mode is a combination of both damage mechanics: some matrix cracking propagates to the interfaces causing local delamination growth but does not spread enough to inhibit kinking failure of the 0° plies. [36]

Lee and Soutis [36] evaluated the notched strength of open-hole compression of two quasi-isotropic laminates, one fabricated with blocked standard thick plies and other with distributed standard thick layers. The authors concluded that the strength of the laminate with blocked plies was higher than the one with dispersed plies, because the first layup allowed a more effective stress redistribution around the hole due to the development of split cracks at the vicinity of the hole delaying final kinking failure of the 0° plies. Note that this study addressed the effect of ply thickness on the notched strength but the minimum ply thickness used was 0.125mm that does not qualify as a thin ply.

Yokozeki et al. [26] studied the performance of thin-ply laminates compared to standard laminates under open-hole compression and concluded that thin-ply laminates performed better under this type of loading possibly because they may have superior resistance to delamination growth and higher compressive stability compared to the standard grade laminates.

Amacher et al. [1] also investigated the influence of ply thickness on the open-hole compressive strength and concluded that thin-ply laminates have improved resistance over standard and thick-ply laminates. The onset of damage was detected by acoustic emission and a delay of 17% on the onset of damage was reported for the thin-ply laminate. The thin-ply laminate failed by fibre kinking, while the thick ply laminate failed by a combination of intralaminar cracking in the 45° plies, fibre kinking and delamination.

Arteiro [24] also investigated the effect of ply thickness on the notched compressive strength. Quasi-isotropic open-hole specimens made from 160g/m^2 and 240g/m^2 spread tow fabrics (STF) were tested under compression. The thinner 160 g/m^2 STF exhibited higher compressive strength than the high-grade 240g/m^2 STF. This was attributed to a better uniformity of the spread-tow yarns, lower fibre waviness and smaller crimp angles characteristic of thinner plies. Thin plies were considered able to delay micro-instabilities in the fibre direction, allowing the

longitudinal yarns to carry higher loads.

In brief, thin-ply laminates are more homogeneous and have higher compressive strength and therefore, are expected to have higher compressive strength in the presence of stress concentrations. Moreover, the use of thin plies delays subcritical damage that suppresses the development of extensive matrix damage and delamination and increases the compressive stability of the laminates [1, 24, 26]. However, as for notched structures loaded in tension, the delay on damage onset might inhibit stress redistribution around the notch and lead to premature brittle failure of the structures [36]. Nevertheless, an increase of the notched compressive strength compared to the conventional grade materials has generally been reported.

2.1.4.3 Bearing resistance

Amacher et al.[1] studied the performance of thin-ply composites in comparison to conventional and thick-ply laminates under bearing loading conditions. Single-shear bearing tests were performed to the three configurations under room temperature and hot-wet conditions. The thinner the plies, the higher the bearing strength, especially under hot-wet conditions. The reduction of ply thickness affected the failure modes: while the failure of thick-ply laminates was matrix-dominated with extensive delamination growth, especially under hot-wet conditions, thin-ply laminates failed by local shearing and crushing of the composite in a small area under the bolt head and no delamination was observed.

2.1.4.4 Low velocity impact and compression after impact

Low Velocity Impact (LVI) events are particularly dangerous for composite structures and can lead to unexpected catastrophic failure. After impact, the structure may present nearly invisible superficial damage but present severe internal damage and extensive delamination and consequently have greatly reduced strength when compared to a pristine structure. For this reason, it is important to understand and to be able to predict the effect of impact loading on the ultimate strength of composite laminates. The design strengths regarding damage resistance and damage tolerance under impact loadings are usually determined using Low Velocity Impact panels (LVI), which are then compressed (CAI-Compression After Impact).

There is no clear consensus of the effect of ply thickness on the damage tolerance but, generally speaking, thicker plies seem to lead to larger internal delaminated areas while thinner plies present more fibre breakage after a low velocity impact event. Moreover, equal or higher compression strengths after impact are generally obtained when thinner plies are used.

Sihn et al. [6] evaluated the performance of thin-ply laminates under impact loading by performing low velocity impact followed by compression after impact tests. The overall sizes of the delamination damage were similar for thin and thick specimens. All the panels buckled in compression after impact tests. Thin-ply specimens buckled at higher applied stress than thick-ply specimens which suggests that thin-ply laminates have higher resistance to damage propagation after impact loading.

Yokozeki et al. [26] performed low velocity impact followed by compression after impact tests on conventional and thin-ply quasi-isotropic laminates. Even tough the projected delamination areas were very similar, the thin-ply laminate had

a slightly higher CAI strength and superior resistance against delamination.

Saito et al. [37] performed low velocity impact followed by compression after impact tests on quasi-isotropic manufactured with 38μm and 147μm thick prepregs. The thinner configuration exhibit 23% higher CAI strength. The authors observed that transverse cracks decreased drastically in thin-ply laminates and delamination was localized in a specific interface and was largely extended. As proposed by Kawabe et al. [38], the higher compression after impact strength of thin plies was attributed to the better fibre alignment and uniformity of the plies which gives better load carrying capability to the laminates and hampers the development of microbucking in the 0° plies.

Amacher et al. [1] performed low velocity impact tests to thin (30g/m^2), intermediate (100g/m^2) and thick-ply (300g/m^2) laminates and also identified a significant change of failure mode when decreasing ply thickness. For thick plies, delamination was predominant. For the intermediate-ply laminate both delamination and 0° fibre fracture on the outer ply was identified. For the thin-ply laminate, the impact damage was characterized by a large translaminar crack that developed along the width of the specimen. Compression after impact was not performed in this study.

2.1.4.5 Fatigue resistance

Composite structures are frequently exposed to cyclical loading. When composite structures are cyclically loaded and unloaded, transverse cracks that appear in the free-edges or in points of stress concentration propagate and can lead to delamination growth over time. This process can lead to the degradation of the structures, severely compromising their performance, and potentially leading to their premature collapse. Given the issues related to the fatigue behaviour of composite materials, many authors have studied the behaviour of thin-plies under cyclical loading, anticipating that the damage suppression capability of this type of material would have positive consequences on their fatigue life.

Nishikawa et al. [39] investigated the fatigue behaviour of a spread-tow plain-woven carbon fibre epoxy system under tension-tension fatigue. The internal damage was observed using an optical microscope. The experimental results showed that the fatigue crack onset and propagation was constrained in spread tow plain-woven laminates and that their fatigue life was longer than those of conventional plain-woven laminates.

Sihn et al. [6] also studied the performance of notched thin-ply laminates under fatigue loading. Tension-tension and open-hole tension fatigue tests were performed to thin and thick-ply quasi-isotropic and hard laminates. Damage extension was observed using X-ray imaging. After fatigue loading, extensive free-edge delamination was observed in quasi-isotropic thick-ply laminates. Additionally, transverse cracking and fibre splitting in the 0° and 45° plies near the hole was detected for both quasi-isotropic and hard thick-ply laminates while thin-ply laminates showed almost no subcritical damage (see Fig. 2.8). It was concluded that thin-ply laminates have superior fatigue life either in notched and unnotched structures.

Yokozeki et al. [26] studied the performance of thin-ply laminates compared to standard laminates by testing both configurations under tension-tension loading and reported that thin-ply laminates exhibited superior fatigue life in addition to static

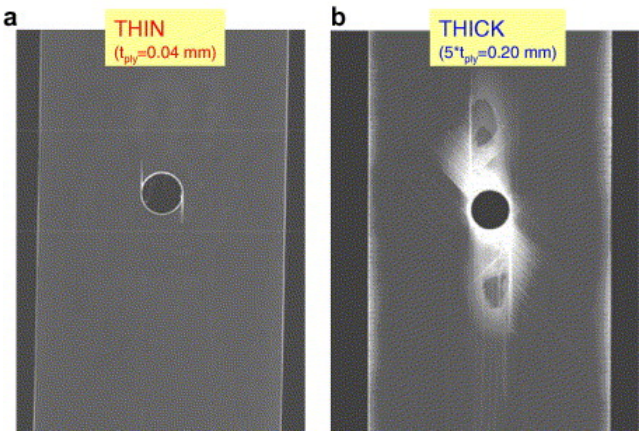

Figure 2.8: X-ray images of hard (a) thin- and (b) thick-ply specimens after 73,000 cycles of open-hole tensile fatigue loading at 70% stress level of ultimate static strength [6]

strength compared to the standard grade laminates. Free-edge delamination was observed in both configurations, however, the thin-ply laminates were less susceptible to propagation of the free-edge delaminations, and therefore, exhibited superior fatigue life compared to the standard grade laminates.

Amacher et al. [1] investigated the influence of ply thickness on fatigue life of notched structures by testing thin ($30g/m^2$) and thick-ply ($300g/m^2$) laminates under open-hole tension fatigue loading. The damage extension was characterized using ultrasonic C-Scans. The thick-ply laminate exhibited progressive damage accumulation by delamination and transverse and shear cracking of the off-axis plies, which led to failure after a reduced number of cycles. Thin-ply laminates failed in a very reduced number of cycles for loading conditions where the maximum stress was above the onset of damage (around 90% the maximum strength), but exhibited a quasi infinite life under fatigue with no damage growth and propagation for loadings with lower maximum applied stress.

Following the work of Amacher et al. [1], Furtado et al. [19] also investigated damage propagation under open-hole tension fatigue loading. The specimens were subjected to 50000 cycles and the fatigue life was assessed by analysing the stiffness reduction, which was assumed to be related to the damage propagation within the specimens. Even though the number of cycles was not high enough to cause specimen failure, the thin-ply laminate had slower and less pronounced damage propagation than the conventional grade laminate.

In summary, fatigue life of thin-ply laminates is improved over that of conventional laminates since microcracking and delamination is delayed or suppressed in this type of material and consequently, damage propagation is slower and less pronounced.

2.1.5 Analysis models

The prediction of the ultimate failure of composite laminates generally relies on finite element models that use the ply as the building block. Mesomodels that treat the composite lamina or sub-laminate as a homogeneous material and describe the possible failure mechanisms in composite laminates and their interactions have

been proposed throughout the years [40–51] and are usually combined with cohesive models developed to simulate delamination onset and propagation [52–54]. These are particularly powerful solutions given their flexibility to predict the material behaviour of different laminates, geometries and loading conditions.

Since that, for the same thickness, thin-ply laminates can accommodate significantly more plies than conventional grade laminates, numerical modelling of thin-ply laminates using the ply as a building block can be rather impractical, given the discretization required and consequent high computational expense. Moreover, since thin-ply laminates exhibit significantly reduced subcritical damage and delamination when compared to conventional grade laminates, macroscopic models formulated at the laminate level can potentially be used to predict failure of this type of material. Recently, Reinoso et al. [55], proposed the use of phase-field methods to predict the mechanical response of thin-ply laminates. The method had been developed and proved suitable for triggering brittle fracture events in solids [56, 57], and was first applied to composite laminates in Ref. [55]. The authors used the model to predict the ultimate strength of thin-ply specimens under open-hole tensile loading, adopting a homogenized constitute response at the laminate level, and achieved very good accuracy between the experimental and numerical results.

Phase-field models are a promising methodology in the context of thin-ply laminates, however, issues related to mesh dependency, sensitivity to the characteristic length used to regularize the localized failure, ability to account for material orthotropy, among others, need to be addressed so their use can be extended to more general loading conditions and scenarios.

Macro-mechanical analytical models have also been developed to predict the performance of composite laminates under different geometries and loading conditions. Despite being simple tools, they have proven extremely accurate and can, therefore, be used for material selection and as base for geometry/layup optimization. In general, analytical models assume that the effect of a three dimensional stress fields at the vicinity of notches or edges can be neglected, and that the damage mechanisms can be lumped up into a through the thickness macrocrack. These hypothesis hold more true for thin-ply laminates than for conventional grade laminates for which the models were proposed. Therefore, they should not only be applied to thin-ply laminates, but used more confidently with this type material.

The classical lamination theory allied with a failure criteria and the last-ply-failure method, can be used to predict the laminate strength. Many failure criteria for laminates composites have been developed over the years. Stress- [58–62] and strain-based [60] failure criteria are simple and easy to implement, however, lack accuracy as they are purely empirical. For this reason, the definition of more physically-based and accurate failure criteria have been an important research subject over the last few years [11, 16, 63–67]. This method to predict laminate failure is a very simplified approach as the degradation factors are empirically derived and damage interaction and delamination propagation are not taken into account, but it is a very efficient method. Amacher et al. [1] suggests that no ply degradation method is necessary to predict failure of ultra thin-ply laminates and that only failure criteria to predict failure under longitudinal tension and compression are needed, since these laminates are able to suppress microcracking and delamination up to the point just before failure, which indicates that all the plies are able to carry load until the 0° plies fail.

Analytical models to predict the notched strength of composite laminates have been proposed over the years e.g. the Point Stress [68], the Average Stress [68], the Inherent Flaw [69] and the Finite Mechanics model [70]. The Point Stress model, the Average Stress model are stress-based criteria: the first one predicts failure when the stress in a point at a given distance from the notch reaches the material's unnotched strength, and the second predicts failure when the average stress from the notch tip up to a characteristic distance reaches the material's unnotched strength. These models rely on calibration from a baseline specimen to calculate the "characteristic distance", thus adding unnecessary costs to the predictions. Moreover, since this calibration is not physically based, the predictions tend to be inaccurate for geometries different from the one used for calibration. The Finite Fracture Mechanics model [70] enriches the Average Stress model, including a energy-based criteria to the stress criteria already defined, thus, not requiring model calibration. Crack propagation is predicted when both stress-based and energy-based criteria are satisfied and that failure occurs by the propagation of kinematically admissible cracks with finite length, i.e. failure is predicted if when two conditions are simultaneous met: i) the average stress ahead of the crack tip until the crack length l reaches the material unnotched strength and ii) the energy needed to propagate the crack the distance l is equal to the fracture toughness of the material.

Using the finite fracture mechanics model proposed by Camanho et al. [70] the ultimate strength of notched composites that exhibits brittle failure can be predicted fast and accurately. The Finite Fracture Mechanics model has been used to predict the failure stress of composite structures with open-holes or cracks loaded in tension [19, 70, 71] and compression [71] and to predict the large damage capability of notched composites [20] with errors below 10%. Given the brittle failure characteristic of thin-ply laminates, predictions are generally more accurate for this type of material.

2.1.6 Concluding remarks

Thin-ply laminates offer a large set of advantages over conventional grade laminates both in terms of design space and mechanical performance. The enhanced mechanical performance of thin-ply composites is due to the delayed onset of damage exhibited by these materials. In general, thin-ply composites exhibit an enhanced unnotched strength, higher compressive notched strength, better resistance under fatigue loadings and, if designed to trigger specific damage mechanisms, enhanced tensile notched strength. Despite the large number of studies previously conducted on thin-ply laminates, no studies regarding the effect of different type of geometry reinforcements available (i.e. UD, NCF and SFT) have been performed, since the different types of reinforcement are supplied by distinct manufacturers, which in turn, generally develop and supply prepregs based on different resins, reinforcing fibres and sizings.

Given the simpler damage mechanisms and clear crack propagation typically observed in thin-ply laminates, analytical models developed to predict the strength of laminated composites have proven extremely accurate when applied to this type of material. Since the models are simple to implement and provide fast predictions, they can be used as material selection and layup optimization tools, which are of extreme use in an industrial context and can largely reduce certification costs.

Even tough analytical models are quite useful due to their efficiency, their applicability is limited to relatively simple geometries and to very well defined crack planes. To predict the general response of composite materials for more complex structures and loading conditions, constitutive models that account for matrix damage and fibre breakage have been developed and applied to finite element codes. Since that, for the same thickness, thin-ply laminates can accommodate significantly more plies than conventional grade laminates, numerical modelling of thin-ply laminates using the ply as a building block can be rather impractical, given the discretization required and consequent high computational expense. Since thin-ply laminates exhibit significantly reduced subcritical damage and delamination when compared to conventional grade laminates, macroscopic models formulated at the laminate level can potentially be used to predict failure of this type of material.

Even though the mechanical performance of thin-ply laminates has been thoroughly studied, there are still many opportunities to fully exploit the characteristics of thin plies and to explore their applicability, e.g. explore the improved design space by reducing mismatch angles, dropping design constrains or attempting to meet them with less total thickness. These opportunities have been on hold since these initial studies required the laminates produced to be directly comparable so that the difference in damage mechanics could be correctly assessed. It is also important to note that the design constrains and design rules for composite materials were proposed based on the mechanical behaviour of conventional grade composite laminates. The introduction of thin-ply laminates at the industrial level, would perhaps require or, at least, benefit from their review.

2.2 Nanoreinforced composite materials

2.2.1 Carbon Nanotubes

Carbon nanotubes (CNTs) are graphene sheets rolled into a hollow cylinder organized in a hexagonal mesh [72, 73]. CNTs exist in two different basic forms: Single-Walled (SWCNTs) have diameters between 0.5 and 2nm and Multi-Walled (MWCNTs), which can have two or more van der Waals bonded cylindrical walls and have diameters from 2-50nm. SWCNT are generally more resistant and stiff than MWCNTs. Schematic representations of both forms are presented in Fig. 2.9.

CNTs exhibit high strength and stiffness in the axial direction and outstanding flexibility in the transverse direction. The modulus of elasticity in the highest quality CNT reaches values in the order of 1TPa [74]. Tensile strengths of 63GPa in MWCNT and about 100GPa in SWCNT were reported. Molecular dynamics simulations suggest that CNTs break at applied strains up to 15% and at tensile stresses of 65 to 93GPa and that in compression they tend to buckle.

One of the most relevant properties in CNT is its thermal stability under reaction conditions and specific heat. Researches show that the CNT have a high thermal stability up to 2800^{o}C and a high thermal conductivity, reaching values between 2800 to 6000WK^{-1}m^{-1} at room temperature. This conductivity is comparable to the best known conductors, as is the case of graphite and diamond [75].

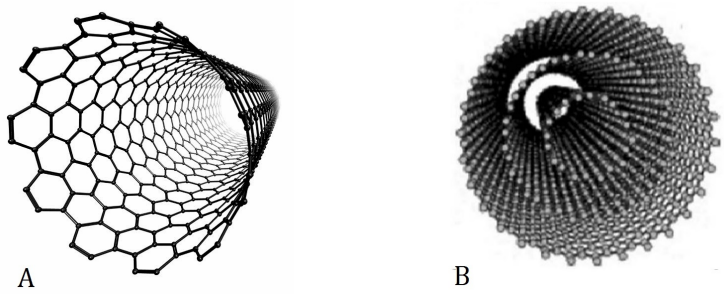

Figure 2.9: A) Single-Walled Carbon Nanotube B) Multi-Walled Carbon Nanotube

2.2.2 Toughening mechanisms in polymer nanocomposites

Non-conventional composite materials reinforced by carbon nanotubes have been studied and their potential to answer the challenges faced by the aeronautical industry has been exploited throughout the last decades. However, only very recently has nanotechnology become a useful tool to improve the performance of polymers by designing their structures at the nanoscale leading to improvements of the mechanical properties, in terms of stiffness, strength and toughness.

The source of this outstanding potential of nanomodified polymers arises from the energy dissipating mechanisms. Quaresimin et al. [76] suggests that there should be a distinction based on the scale of the reinforcement mechanisms responsible for the improvement of mechanical performance in nanocomposites:

- micro-mechanisms (related with the presence of agglomerates or large particles) e.g. crack deflection, crack pinning, micro-cracking and matrix deformation.

- nano-mechanisms (related with the presence of well dispersed and distributed nano-fillers) e.g. debonding, plastic void growth and pull-out. The nano-mechanisms are different according to the type of filler used. Since this work will focus on the use of carbon nanotubes, this review will also focus on this type of nano-reinforcement.
  CNT pull-out and bridging are the most commonly reported reinforcement mechanism of CNT in thermosets. Plastic void growth after pull-out can also be considered a toughening mechanism, however, Hsieh et al. [77] concluded that the contribution of such mechanism can be neglected. Fig. 2.10 shows a schematic representation of the possible toughening fracture mechanisms of CNTs:

  (a) intact multiwalled CNT;
  (b) matrix/CNT debonding caused by a weak interface;
  (c) CNT breakage caused by a strong interface;
  (d) bridging of the inner walls and breakage of the outer walls (sword pull-out);
  (e) partial bridging and debonding.

These mechanisms were also reported experimentally by Cooper et al. [78] by detaching single carbon nanotubes from a polymer matrix. From this experimental procedure, the separation stresses were obtained and the toughening mechanisms were observed, which included the previously mentioned CNT pullout (partial or complete), bending or breakage of CNT, and unsheathing of inner from outer tube layers.

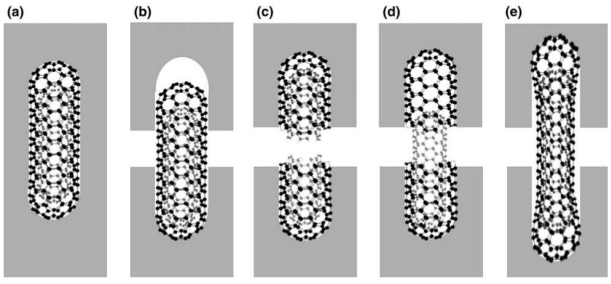

Figure 2.10: Schematic representation of the possible fracture mechanisms of CNTs [7]

The inclusion of CNT in polymer matrices can, in fact, increase the toughness of the bulk polymer, however, this possible enhancement is largely dependent on the dispersion, CNT aspect ratio and CNT/polymer interface properties, which are parameters difficult to control. In fact, the idea to use CNT for structural benefit of composite materials has received considerable attention but researchers have struggled with the sometimes unexpected challenges that the implementation of such an idea represents. Early challenges focused on dispersion of nanotubes in polymers, which is limited by the high surface to volume ratios of CNT that increase resin viscosity and limit processability. Recent challenges focus on organization, i.e. controlling the alignment of nanotubes relative to each other and relative to other reinforcements present in the material system. In fact, isotropic behaviour resulting from randomly mixed reinforcement have given way to more complex nano-structures

where, either the nanotubes are oriented in a preferred direction in a reinforced polymer or in a preferred direction and a specific location such as around the fibres or between the ply interfaces in a composite laminate.

2.2.3 Carbon nanotube reinforced composite laminates

Interest has been growing in the development of nanostructured composite materials, where nanoparticles such as carbon nanotubes are used alongside microscale fibre composite laminates. The main idea behind the combination is to improve the matrix dominated properties of traditional composites. In fact, carbon nanotubes introduce additional energy dissipating mechanisms that have the potential to enhance the toughness of the matrix and therefore they can be used to improve the interfacial and transverse properties of composite laminates.

The combination of carbon nanotubes into composite laminates has mainly been attempted by either adding them to the matrix, to the interfaces or to attach them directly in the fibres. The most common process to incorporate carbon nanotubes in the manufacturing process is by mixing the carbon nanotubes in the matrix, followed by infusion or impregnation of the primary fibres by the modified matrix. This process is simple and fairly compatible with standard industrial lines, however, is limited to very low loading fractions of carbon nanotubes because the resin viscosity greatly increases by the addiction of carbon nanotubes, limiting the processability of the matrix. Resin transfer moulding (RTM) [7, 79, 80] and vacuum assisted resin transfer moulding (VARTM) [81–86] are typical methods used in the resin infusion process for producing nanoreinforced composite laminates. The main problem with these approaches is associated with the high viscosity of the modified resin, which can cause incomplete infusion. Moreover, CNT tend to agglomerate and when infused they might not be able to penetrate the laminate and get deposited on the surface. The higher the carbon nanotube loading, the more difficult the manufacturing process becomes. These problems with processability have been the main reason why the inclusion of CNT has failed to deliver the expected improvement in mechanical performance. However, some success has been obtained in improving the electrical and thermal conductivity and thermal degradation resistance because, these properties are drastically changed even for very low percentages of CNTs. [87–94]

Nonetheless, success in increasing the mechanical performance of composite laminates using nano-modified resins has been reported by some authors. It has been reported that the in-plane properties are not significantly affected by the inclusion of nanotubes while the matrix dominated properties are highly superior when the reinforcement is present. 8%-30% improvements have been reported on the interlaminar shear strength evaluated by means of short beam shear testing [7, 80, 81, 85]. Delamination resistance has been evaluated by means of double cantilever beam [80, 84, 95–98] and end-notch flexure tests [80, 95, 96] and increases in fracture toughness up to 100% have been reported.

To mitigate the processing problems associated with the impregnation of nano-modified resins and to further improve the mechanical performance of nanoengineered composite materials, more advanced methods have been developed to incorporate nanotubes as through-the-thickness reinforcement.

Arai et al. [99] used nanofiber/epoxy interlayers between the plies and deter-

mined the mode I and mode II interlaminar fracture toughness of the new material systems. The experimental results showed that the mode I and mode II interlaminar fracture toughnesses for hybrid laminates were 1.5 and 2-3 times greater than base CFRP laminates, respectively.

Some authors developed techniques to grow CNT directly on carbon fibres [100–105]. Even though the dispersion of nanotubes is good and the radial distribution of the carbon nanotubes helps the impregnation process through capillary effect, there is usually a degradation of the carbon fibre strength due to conditions they are exposed to during CNT growth [106–108].

Garcia et al. [109] developed a technique to produce CNT reinforced composite materials by growing carbon nanotubes on the surface of woven cloths. It was observed that the carbon nanotubes grow long, aligned and densely packed radially around the fibres. After carbon nanotube growth, the cloth was impregnated with epoxy resin and hand layed-up into a laminate. Short beam shear tests were performed to the reinforced and unreinforced to compare their interlaminar shear strength. The experimental results showed that the reinforced laminate had 70% higher interfacial strength than the unreinforced laminate.

Garcia et al. [8] proposed the incorporation of vertically aligned carbon nanotubes in the ply interfaces to increase the interlaminar fracture toughness of composite laminates. Since the work regarding the effect of the presence of CNTs on the mechanical behaviour of composite laminates presented in this thesis will mainly focus on this technology, the manufacturing process and the experimental results obtained up to date will be reported in the following section.

2.2.3.1 Nanostitched composite laminates

Recently, composite laminates composed of carbon fibre-epoxy plies nanostitched together with vertically aligned carbon nanotube arrays have been developed [8]. A schematic representation of a nano-stitched composite interface is shown in Fig. 2.11. It was shown that this innovative process guarantees a good dispersion of carbon nanotubes and improves both interlaminar and intralaminar composite strength and toughness and significantly increases the electrical and thermal conductivity, allowing the possibility of creating not only a new generation of mechanically enhanced composite materials but also of multifunctional structures [8, 110–112]. In the following sections, the manufacturing process used to produce aligned carbon nanotubes arrays and how to incorporate them in the interface of carbon fibre composite laminates will be explained. Furthermore, recent experimental results that demonstrate the potential benefits to improve the mechanical performance of CFRP of such a technology will be reported.

2.2.3.1.1 Manufacturing process

Aligned Carbon Nanotubes (A-CNT) can be produced by chemical vapour deposition (see Fig. 2.12). In this process, a hydrocarbon vapor at atmospheric pressure passes through a tubular reactor heated at temperatures from 600°C to 1200°C where a catalyst material is present. This catalyst acts as a substrate and triggers the decomposition of the hydrocarbon, forming CNTs on its surface. The length of the CNT arrays can be controlled by changing the cycle time. A reduction

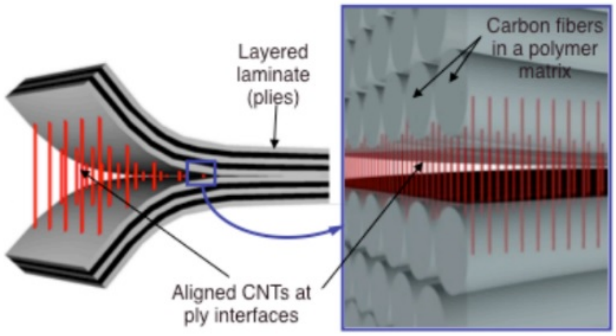

Figure 2.11: Schematic representation of a nano-stitched composite interface [8]

cycle is applied to reduce the attachment of the CNT forest and the substrate and allow a better transferring process [8]. After cooling, the CNT forests are removed from the reactor. The CNTs can then be transferred to the interface of a prepreg during stacking.

After a careful investigation to determine the causes of non-uniform heights and morphologies of CNT forests of successive growths, Lewis [110] proposed the following CNT growing cycle:

1. **Bake out:** This is a cleaning procedure which should be done periodically or even after every growth cycle to eliminate excessive humidity and amorphous carbon present inside the furnace: the furnace is heated to 740°C while open to the air to remove any of the contaminants from previous growth cycles. The temperature is maintained for 3 minutes before cool down.

2. **Load and Purge:** The Si wafers are inserted on the quartz tube, the tube is sealed and the furnace lid is closed. When the furnace temperature drops from the bake-out temperature to 165±10°C, the growth cycle is initiated. All lines are purged at 400sccm [1] for one minute, then the tube is purged with helium at 2000sccm for five minutes to ensure an inert environment.

3. **Growth Cycle:**

   (a) **Catalyst anneal:** 600ppmv [2] water is introduced into the furnace by bubbling helium through a water bath. The temperature of the furnace is increased up to 680°C and maintained for 8 minutes.

   (b) **Growth:** Ethylene is turned on at 400sccm for a time period specified by the desired height of the forest. During this step the hydrogen flows at 1040sccm.

   (c) **Delamination:** While hydrogen and water continue to flow, ethylene is turned off and helium is turned on at 500sccm for 30 seconds. This step makes the delamination of the CNT forest easier.

4. **Cool-down:** The furnace is shut off once the delamination step is complete. Hydrogen is also shut off and the furnace is allowed to cool under helium and

[1] sccm: standard cubic centimetres per minute
[2] ppmv: parts per million volume

water. Once the furnace temperature drops to 550-600°C, the water is shut off. Once the furnace temperature reaches 225°C, the helium is shut off and the process is considered finished.

5. **Chip Removal:** The tube is opened and the chips removed as soon as the process is finished.

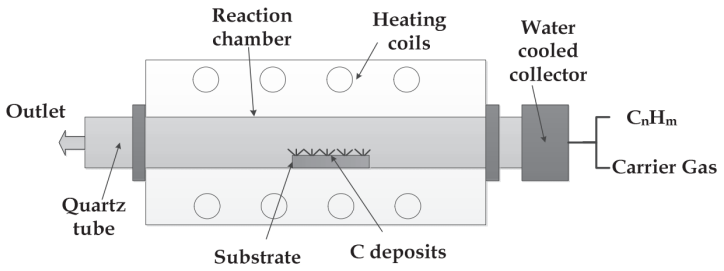

Figure 2.12: Schematic representation of the Chemical Vapor Deposition process [9]

Some techniques have been proposed to transfer the CNT into the prepreg material by Garcia et al. [8], Falzon et al. [10] and Lewis [110]. The CNT forests can be transferred attaching the prepreg to a cylinder and rolling it while pressing it across the Si substrate containing the CNT as proposed by Garcia et al. [8] (Fig. 2.13). Falzon et al. [10] transfered the CNT forests to the prepreg by inverting the silicon wafer, so that the top of the CNT forest was in direct contact with the prepreg, and applying load with a weight as shown in Fig. 2.14. The weights were kept below 500g to maintain the CNT alignment. At room temperature the forests would not be well transferred to the prepreg, and for high applied temperature and load, the CNT forest would completely penetrate inside the ply and, as a result, the silicon wafer came into contact with the prepreg which made it difficult to remove. A careful selection of the combination of applied load, loading time and temperature should be made for each prepreg system. Lewis [110] proposed two transferring methods. In the first, the temperature of the prepreg is increased to make it tacky, the silicon wafer is inverted onto the prepreg and pressure is applied to the ply using a roll. In the second, the prepreg is heated to a slightly higher temperature but no pressure is applied to the wafer. The two methods yield different A-CNT morphologies in the composite: since pressure is applied, the first method compresses the forest to a 5μm thick band, while in the second method, the original CNT height is better preserved. However, despite the difference is morphology, no difference in the mechanical behaviour between the two transferring processes was reported [110].

2.2.3.1.2 Mechanical performance

Vertically aligned carbon nanotubes have been successfully introduced in the interlaminar region of unidirectional laminates as explained in the previous section and many studies to evaluate the mechanical performance of composites with CNTs have been conducted [8, 10, 110, 111].

Garcia et al. [8] conducted an experimental program to assess the influence of including CNT in the interface on the mode I and mode II interlaminar fracture

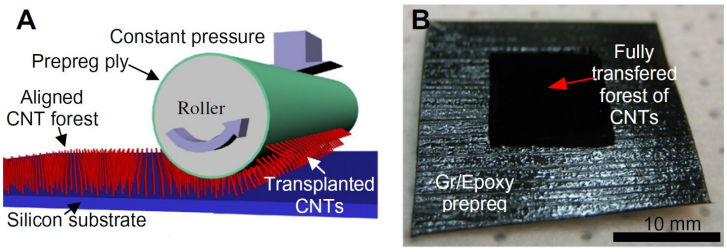

Figure 2.13: Transfer of vertically aligned CNT to prepreg: (A) Schematic representation of the transfer process; (B) Fully transferred CNT forest [8]

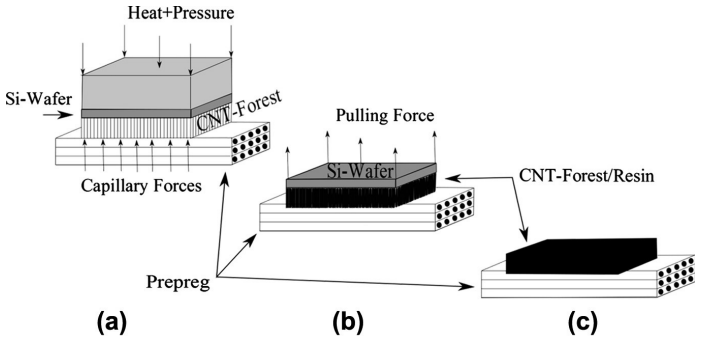

Figure 2.14: Transplantation of CNT forest (a) heat and pressure applied to silicon substrate (b) removal of the substrate after the cool down period and (c) transplanted CNT forest infused with resin through capillary action and partially inserted into the prepreg. [10]

toughness. Double cantilever beam (DCB) and four point bending tests on end notched flexure (4ENF) tests were performed in a unidirectional CFRP reinforced with 60-150μm high CNT arrays. In this preliminary study, it was concluded that the inclusion of CNT does not influence the resulting thickness of the specimens after curing and that the mode I and mode II fracture toughness were improved by a scale of 1.5-2.5 and 3 times, respectively, by the inclusion of CNTs. This improvement was thought to a be a consequence of both interlayer toughening through plastic deformation and crack bridging. In fact, SEM analyses of the fracture surface of reinforced DCB specimens showed z-oriented CNTs on both the crack surfaces suggesting bridging of the crack by the aligned CNTs.

Falzon et al. [10] also compared the fracture toughness of nano-stitched and unreinforced interfaces by performing DCB and ENF tests and determining the mode I and mode II $\mathcal{R}$-curves, respectively. Mode I tests showed an increase in the average fracture toughness between 31%-61%, and mode II tests showed an increase of 161% but with a very large scatter in the results.

In both studies [8, 10], an unexpected negative slope on the mode I $\mathcal{R}$-curve for the CNT reinforced interfaces was observed. Garcia et al. [8] attributed this phenomenon to the side-by-side placement of the CNT forest patches and suggest that a more consistent manufacturing process should be used to fabricate the specimens. However, Falzon et al. [10] did not place the CNT side-to-side but reported the same trend. The reason for a reduction of fracture toughness with crack propagation is, therefore, not properly explained but can simply be a consequence of the data reduction method used. The ASTM standards [113, 114] are based on Linear Elastic Fracture Mechanics (LEFM) which main hypothesis is that the non-

linear deformation at the crack front is small in comparison to any of the specimen's dimensions. The method has been largely applied to fibre reinforced polymers, however, the fracture process zone of nano-reinforced interfaces might be too large to be well characterized using the standard method. J -integral closed-form solutions for interlaminar fracture tests have been proposed for mode I [115–118], mode II [119–122] and mixed mode [123–126] but, to the author's knowledge, never applied to nano-reinforced composite laminates.

Lewis [110] performed short beam shear tests [127] to study the influence of nano-stitching on the interlaminar shear strength (ILSS). Quasi-isotropic laminates reinforced with 5-65μm CNT in every interface were tested. Even though samples with seven different CNT heights were tested, no relevant difference is shown between the experimental results for the reinforced samples because regardless of the initial height, the forests were compressed to around $5\mu m$ in the interface. The average improvement in ILSS over the unreinforced baseline was 8.75±0.5%. However, SBS specimens should fail in the interfaces so that the test is considered valid and while the unreinforced specimens failed properly, the reinforced specimens failed with multiple cracks through both interlaminar and intralaminar regions, especially when the CNT transferring method used did not involve applying pressure. This suggests that, the CNT reinforcement was effective enough to deviate delamination propagation to within the plies, even though this results in a very limited strength improvement.

Lewis [110] also evaluated the fatigue behaviour of nano-stitched interfaces, loading SBS specimens in fatigue bending. Specimens were cycled to failure at peak loads of 60-90% of the reference static ILSS. Over all load levels, the nano-stitched coupons exhibited a 3.2 times longer fatigue life than the unreinforced coupons.

Other forms of through thickness reinforcement that rely on bridging as the main toughening mechanism such as stitching, z-pinning and weaving have proved to increase the through-thickness properties, however, the in-plane properties usually decrease due to damage and misalignment of the reinforcing fibres caused by the reinforcement. Following Garcia et al. [8], Guzmán de la Villoria et al. [111] carried out an experimental campaign to prove that the nano-reinforcement did not have such degrading effect due to the un-obstructive nature of the interface reinforcement in the adjacent plies. The experimental campaign was based on the subcomponent level and included open-hole compression, bolt bearing and L-shape tests.

For bolt-bearing, the major reported improvement was not the increase in ultimate failure but the delay/suppression of subcritical interlaminar damage giving the material a 30% increase in the load corresponding to damage onset (first load drop). For open-hole compression, both a 14% increase of ultimate strength and the suppression of subcritical damage near the hole was reported. For the L-shapes tested, the reported improvement was also the suppression of subcritical damage which resulted in a 26% increase in the ultimate deflection of the specimen and a correspondent 30.7% increase in the energy required to break the specimen.

The experimental campaign reported in Ref. [111] suggests that the in-plane properties are not degraded by the presence of CNT in the interfaces and actually benefit from their presence. Their presence contributes to the suppression of interlaminar damage in some loading cases, lay-ups and geometries and can result in the improvement of the strength used to design them and to the ultimate failure of the components.

2.2.3.1.3 Multifunctionality

Besides improving the overall mechanical performance by increasing the interfacial toughness and helping to suppress interfacial subcritical damage, it is possible to take advantage of the exceptional electrical and thermal conductivity of CNT to increase the multifunctionally of the composite structures. The thermal conductivity of CNT has been especially explored to produce microheater films [128–143]. It has been shown that CNT based heaters can reach very high temperatures, however, the lack of alignment of the CNT compromised the heat transfer and their mechanical performance and therefore, recent work has focused on microheaters made from aligned CNT networks.

Guzmán de Villoria [144] showed that aligned CNT networks in composite structures allow very efficient heating. This characteristic can be used to detect damage or manufacturing defects by ohmically heating the part and using thermographic imaging to detect damage or even to de-ice composite structures. The appearance of ice on aerodynamic surfaces has to be avoided because it increases weight and drag and therefore reduces the performance of the structure. By incorporating CNT on the surface of the structure and using them as resistive heater, the ice-formation can be eliminated, avoiding the need for the commonly used de-icing fluids.

The thermal conductivity of CNT can be especially useful in the curing process of polymer composites. Since CNTs are able to efficiently conduct heat, the curing process is more homogeneous, which is especially interesting for thicker components, where the degrees of curing tend to be different in the middle and in the surface of the structure and the residual stresses tend to be high. Another way to take advantage of the thermal conductivity of CNT is to use them as a heater to cure the part where they are introduced [145]. This process has recently been called "out-of-oven curing" where, not an autoclave nor an oven are required to cure the part. This has already been attempted and the degree of cure was comparable to that of laminates cured using conventional oven based techniques, which is a very promising preliminary result. Moreover, it is important to note that the efficiency of such a curing process is a lot higher than autoclave curing since it is not necessary to waste energy heating the whole chamber, but only to heat the part itself. Also, the maximum possible temperature reached was higher than 500°C which is high enough to eventually use this technique to process high processing thermoplastic polymers such as PAN, PEEK and PEKK.

2.2.4 Analysis models

Several studies have been conducted on modelling of nanotube reinforced polymers, but only a small number of studies have addressed modelling of CNT reinforced composite materials.

2.2.4.1 Analytical models

The general concept to estimate the fracture energy of nanotube-modified epoxies has been to assume that the fracture toughness of the matrix is not affected by the presence of the carbon nanotubes and that the fracture toughness enhancement results from additional dissipative mechanisms such as nanotube breakage,

pull-out, sword-in-sheath, debonding and void growth after debonding, depending on the author. Not only the dissipation mechanics considered differ from model to model but also the assumed geometry of the nanotubes, orientation, length and position distributions vary. The energy associated with each of these mechanisms have generally been predicted assuming that classical mechanics are valid at the nanoscale and by using extensions of the models proposed for short fibre composites.

Tong et al. [146] and Blanco et al. [112] proposed analytical models for the Mode I interlaminar fracture of laminated composites reinforced with aligned nanotubes. Similar hypothesis were considered: the nanotubes are perpendicularly embedded into the matrix rich region at the interface between plies and when delamination occurs, the nanotubes bridged the crack increasing the fracture toughness due to frictional sliding of the CNTs during pullout [78, 147] and during sword-in-sheath pullout where the outer shell of a multi-walled CNT remains attached to the polymer and the inner tube pull out of this outer tube [148, 149].

The concept of critical length applied to nanotube pull-out introduced by Wichmann et al. [150] was used by Mirjalili et al. [151, 152]. The critical length is a threshold that distinguishes two possible bridging scenarios: nanotube pull-out and nanotube breakage. It can be computed from a force balance on a single nanotube and its interfacial bonding with the polymer chains, i.e.

$$l_c = \frac{\sigma_u}{\tau} r \tag{2.1}$$

where l_c is the critical length, r is the nanotube radius, σ_u is the nanotube ultimate strength and τ is the interfacial shear stress between the nanotube and the polymer. Mirjalili et al. [151, 152] suggests that nanotube pull-out will occur when its length is smaller than the critical length otherwise both rupture and pull-out will occur because the embedded length might be lower than the critical length, which will lead to nanotube pull-out of the shorter embedded end [153]. Two extensions of the model were proposed [153]: the first assumes that the nanotubes are aligned and perpendicular to the crack plane and the second assumes that the nanotubes are randomly oriented and that only those with orientated between 50° and 90° with the crack plane, have a contribution to the enhancement of the fracture toughness.

Wagner et al. [154] focused on the nanotube pull-out mechanism. Nanocomposite toughness is quantified through a reanalysis for nanotubes of the Cottrell-Kelly-Tyson model where the concept of critical length is modified for hollow tubes or fibres.

Hsieh et al. [77] considered nanotube debonding, nanotube pull-out and plastic void growth of the epoxy matrix to be the most important toughening mechanisms of nanotube modified epoxies. The model indicated that the debonding and pull-out contribute significantly to the increase in toughness, but the contribution of void growth is not significant.

Chen et al. [155] studied the effect of nanotube curvature on nanocomposite toughness by considering a matrix crack bridged by curved nanotubes. If the strength of the nanotubes were uniform, all nanotubes would either break or pull-out. These are extreme cases, that do not represent well the crack bridging effect. In fact, as the crack opens and/or propagates under load and the bridging nanotubes pull out of the crack face, the nanotubes may break, most likely at the most defective region along their length than at the point of maximum stress, i.e., the crack plane.

For this reason, Chen et al. considered the strength along the length and between nanotubes to follow a Weibull distribution as proposed in Refs. [156–161].

Menna et al. [162] proposed a micromechanical model, based on analytical framework developed for classical short fibre composites, to determine the enhancement of mode I fracture toughness due to nanotube pull-out and fracture. The proposed model is developed for nano-reinforced composites that contain nanotubes with known length and orientation distributions rather than assuming they are constant. Menna et al. [162] used the Weibull distribution to describe the length distribution and the orientation distribution proposed by Fu et al. [163] for misaligned short fibres, however other distributions can be used. Moreover, the position of the centre of gravity of nanotube relatively to the crack plane is assumed to follow a uniform distribution. When a nanotube is embedded between two halves of a crack, it will pullout when the length of the shorter embedded end is less than its critical length. In this case, only the shorter embedded end pulls-out and the other remains embedded. Note that the embedded length varies with the orientation, length and the position of the nanotube, which follow statistical distributions. When both the embedded lengths are longer than the nanotube than the critical length, the nanotube will break instead of pulling out. Accounting for the waviness of the nanotubes and the altered matrix morphology and toughness due to the presence of nanotubes could improve this model.

All these studies focused on the toughening mechanisms of carbon nanotubes under mode I loading but, to the author's knowledge, the mechanicsms under mode II and mixed mode loadings have not been yet examined.

2.2.4.2 Finite element models

It is generally agreed that, due to the very different scales of the constituents in nano-reinforced composite laminates, a wide range of modelling tools and simulation techniques from quantum mechanics to continuum mechanics can be used to predict their behaviour [164, 165]. In comparison, Quantum Mechanics describes the matter at the subatomic level, Molecular Dynamics describes the matter in terms of atoms, molecules and chemical bonds and is able to predict its molecular structure and behaviour [166], while continuum mechanics describe the matter as a continuous medium [167–169]. Recently, multiscale modelling techniques which incorporate multiple simulation techniques into a single algorithm are being developed to relate material structure to macroscopic material behaviour. Multiscale simulation is a challenging research area because i) quantum and molecular level simulations are extremely computationally expensive; ii) the types of simulation require very different assumptions and approaches that might not be compatible, and iii) are generally mastered by different people.

The mechanics of nanotubes might be only physically well described by Molecular Dynamics, which is a very powerful tool to understand the damage mechanisms at the nanoscale and, even though the insight of the behaviour of carbon nanotubes will certainly induce changes and improvements in the construction of higher scale models, describing composite laminates with Molecular Dynamics is very inconvenient and inefficient.

The introduction of vertically aligned carbon nanotubes in the interlaminar region of unidirectional laminates has consequences in terms of mechanical perfor-

mance as explained in Section 2.2.3.1.2. The simulation of such modified interfaces has, to the author's knowledge never been attempted. Their simulation could possibly be based on cohesive zone models [170–183] or constitutive models developed to predict matrix plasticity and fracture [184–190] modified to account for the additional toughening dissipation mechanisms that CNTs introduce to the material such as, CNT pull-out, breakage, debonding and void growth. However, evaluating these damage mechanisms and understanding them so that they can be taken into account at the macroscale is a difficult process due to the scale at which it is happening. Because the effective use of composites rely on the ability to predict its performance, new models for CNT reinforced interfaces should be developed.

2.2.5 Concluding remarks

Non-conventional composite materials reinforced by nanotubes have been studied and their potential to answer the challenges faced by the aeronautical industry have been exploited. The most popular strategy followed to include carbon nanotubes in CFRP has been to mix them in the matrix as an attempt to increase the toughness of the composite structure and its conductivity. However, many difficulties have been faced mainly due to the increase in resin viscosity when introducing CNTs, which limits the processability. Additionally, the increase in viscosity results in low volume fractions, and agglomeration of the carbon nanotubes, which leads to poor dispersion in the matrix. Recently, composite laminates composed of carbon fibre-epoxy plies nano-stitched together with vertically aligned carbon nanotube arrays have been developed. It has been shown that this innovative process guarantees a good dispersion of carbon nanotubes and improves both interlaminar toughness [8, 10], intralaminar [8, 110, 111] strength and significantly increases the electrical and thermal conductivity, allowing the possibility of creating not only a new generation of mechanically enhanced composite materials but also of multifunctional structures.

The fracture toughness of CNT reinforced interfaces has been assessed using standard ASTM testing [8, 10], which are based on the Linear Elastic Fracture Mechanics. The main hypothesis is that the damage zone at the crack front is small in comparison to any of the specimen's dimensions. However, the fracture process zone of nano-reinforced interfaces might be too large to be well characterized using the standard method and alternative data reduciton methods should be used instead [115–125].

Analytical models to estimate the fracture energy of nanotube-modified epoxies have been proposed mostly assuming that the classical mechanics proposed for short fibre composites are valid at the nanoscale [77, 112, 146, 151, 152, 154, 155, 162]. They generally assume that the fracture toughness enhancement results from additional dissipative mechanisms such as nanotube breakage, pull-out, sword-in-sheath, debonding and void growth after debonding. Depending on the model, different geometry of the nanotubes, orientation, length and position distributions are assumed. The energy associated with each of these mechanisms have generally been predicted assuming that classical mechanics are valid at the nanoscale and by extensions of the models proposed for short fibre composites.

It is of general agreement that due to the very different scales of the constituents in nano-reinforced composite laminates multiscale models that combine

a very wide range of modelling tools and simulation techniques from quantum mechanics to structural mechanics are ideal to predict the behaviour of nano-reinforced composite laminates [164, 165]. However, multiscale modelling techniques is an extremely challenging research area and while Molecular Dymanics is a very powerful tool to understand the damage mechanisms at the nanoscale, describing composite laminates at this scale is very inconvenient and inefficient. New, more efficient models for CNT reinforced interfaces should be developed possibly from the modification of cohesive zone models [170–183] or constitutive models developed to predict matrix plasticity and fracture [184–190].

Part III

Analysis models to predict failure of composite laminates

Chapter 3

Simulation of fracture in laminated polymer composites: building-block validation

The design of composite structures is based on testing and simulation of composite coupons that represent structural details under simple loading scenarios, following an approach known as the building block approach [191]. This process ensures that a deep understanding of the structural behaviour under simple loading conditions is gained at the early stages of the design process, consequently mitigating the risk associated with the design of complex structures that usually have strict certification and safety requirements. The experimental determination of these design parameters is an inherently costly and time-consuming process, and consequently delays both the introduction of the new materials addressed in the previous chapters and the design of new structures, two aspects that are critical for the competitiveness of the aeronautical industry. The development of numerical models to complement, or potentially replace, the purely experimental determination of the design parameters is, therefore, of key importance. Numerical solutions based on analytical [15, 16, 69, 70, 192–194] and finite elements models at the meso- and macroscale [40–51, 55] have been proposed; however, their use is still not widespread since the models are generally not implemented in commercially available software and/or their validation has not gained widespread acceptance for material systems of interest.

Finite element models to simulate failure of composite laminates using the ply as a building block have been proposed by several authors [40–51]. These are particularly powerful solutions given their flexibility to estimate the material behaviour of different laminates, geometries and loading conditions. However, their efficient use relies not only on the accuracy of the predictions of the ultimate failure loads, but also on the time frame in which these predictions are obtained. The time required to run the numerical models should be compatible with the requirements from industry. Moreover, it is important that the models rely on physically based material properties that can be determined following well-defined test methods and rely as little as possible on numerical calibration.

The objective of the work presented in this chapter is to develop and implement a methodology to simulate composite laminates at coupon level compatible with industrial requirements. The model should be able to predict the strength of different structural details without changing its formulation or required material properties. The model is based on the continuum damage model proposed by Maimí et al. [47–49] and the cohesive zone model proposed by Turon et al. [195] and Alfano et al. [196]. The models were modified (as described in later sections) from

their original versions to improve their ability to accurately predict damage initiation and evolution under general loading conditions while maintaining the model complexity and, therefore, the computational cost. The current work serves as basis for modelling more complex geometries [197–199] and can potentially be used for the generation of statistically based design allowables for the most simple test cases when allied with powerful statistical tools.

3.1 Modelling strategy

The modelling strategy proposed in this work is presented in the following sections. The continuum damage model for the ply and respective improvements proposed are detailed in Section 3.1.1 and the cohesive zone model for the interface proposed here is presented in Section 3.1.2.

3.1.1 Continuum damage model for the ply

Maimí et al. [47–49] proposed a continuum damage model to predict the onset and accumulation of intralaminar damage mechanisms in laminated composites. Generally speaking, the formulation of the continuum damage model starts by the definition of a potential (the complementary free energy density) as a function of damage variables associated to the different failure modes. It is also necessary to define the damage activation functions, i.e. the conditions that lead to the onset of inelastic response, and the damage evolution functions. The model was developed assuming that the out-of-plane stresses are too small to promote damage and, therefore, damage is activated only by the in-plane components of the stress tensor. This assumption is not suitable for test cases where the triaxiality of the stresses is not negligible. In this chapter, the model was modified to improve its ability to accurately predict damage initiation and evolution under general load conditions without increasing the model complexity and, therefore, the computational cost. These modifications are reported in the following sections, with full details of the original model available in Refs. [47–49].

3.1.1.1 Constitutive model

The scalar function corresponding to the ply complementary free energy density, accounting for the different longitudinal Young's moduli in tension and compression reads:

$$\begin{aligned}\mathcal{G} = \frac{\langle\sigma_{11}\rangle^2}{2(1-d_1)E_1} + \frac{\langle-\sigma_{11}\rangle^2}{2(1-d_1)E_{1c}} + \frac{\sigma_{22}^2}{2(1-d_2)E_2} + \frac{\sigma_{33}^2}{2(1-d_3)E_2} + \\ + \frac{\sigma_{12}^2}{2(1-d_6)G_{12}} + \frac{\sigma_{23}^2}{2(1-d_4)G_{23}} + \frac{\sigma_{13}^2}{2(1-d_5)G_{12}} - \\ - \nu_{12}\left(\sigma_{22}+\sigma_{33}\right)\left(\frac{\langle\sigma_{11}\rangle}{E_1} + \frac{\langle-\sigma_{11}\rangle}{E_{1c}}\right) - \frac{\nu_{23}}{E_2}\sigma_{22}\sigma_{33} + \\ + (\alpha_{11}\sigma_{11} + \alpha_{22}\left(\sigma_{22}+\sigma_{33}\right))\Delta T + (\beta_{11}\sigma_{11} + \beta_{22}\left(\sigma_{22}+\sigma_{33}\right))\Delta M \end{aligned} \tag{3.1}$$

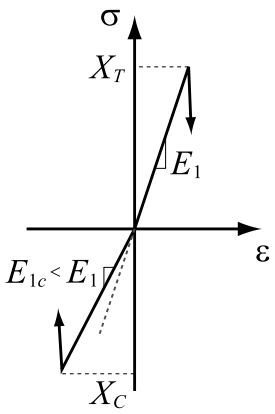

Figure 3.1: Longitudinal nonlinear ply behaviour in tension and compression.

where σ_{ij} are the components of the stress tensor, d_i are the scalar damage variables, E_1 and E_{1c} are respectively the longitudinal tensile and compressive Young's moduli, E_2 is the transverse Young's modulus, G_{12} is the shear modulus, ν_{12} is the Poisson's ratio, α_{ii} $(i = 1, 2)$ are the coefficients of thermal expansion, β_{ii} $(i = 1, 2)$ are the coefficients of hygroscopic expansion, ΔT is the temperature variation, ΔM is the variation in moisture content, and $\langle \bullet \rangle$ stands for the Macaulay brackets, which return the argument $\bullet$ if positive, and zero otherwise. The previous equation results in a non-linear behaviour in tension and compression if $E_1 \neq E_{1c}$ — see Fig. 3.1.

The strain tensor reads:

$$\boldsymbol{\epsilon} = \frac{\partial \mathcal{G}}{\partial \sigma} = \mathbf{H} : \sigma + \alpha \Delta T + \beta \Delta M \tag{3.2}$$

where $\mathbf{H}$ is the lamina compliance tensor:

$$\mathbf{H} = \frac{\partial^2 \mathcal{G}}{\partial \sigma^2} = \begin{bmatrix} H_{11} & H_{12} & H_{13} & 0 & 0 & 0 \\ H_{12} & H_{22} & H_{23} & 0 & 0 & 0 \\ H_{13} & H_{23} & H_{33} & 0 & 0 & 0 \\ 0 & 0 & 0 & H_{44} & 0 & 0 \\ 0 & 0 & 0 & 0 & H_{55} & 0 \\ 0 & 0 & 0 & 0 & 0 & H_{66} \end{bmatrix} \tag{3.3}$$

where

$$\begin{aligned} &H_{11} = \tfrac{1}{(1-d_1)|\sigma_{11}|}\left(\tfrac{\langle \sigma_{11} \rangle}{E_1} + \tfrac{\langle -\sigma_{11} \rangle}{E_{1c}}\right) \quad ; \quad H_{22} = \tfrac{1}{(1-d_2)E_2}; \\ &H_{33} = \tfrac{1}{(1-d_3)E_2} \quad ; \quad H_{44} = \tfrac{1}{(1-d_6)G_{12}}; \\ &H_{55} = \tfrac{1}{(1-d_5)G_{12}} \quad ; \quad H_{66} = \tfrac{1}{(1-d_4)G_{23}}; \\ &H_{12} = -\tfrac{\nu_{12}}{|\sigma_{11}|}\left(\tfrac{\langle \sigma_{11} \rangle}{E_1} + \tfrac{\langle -\sigma_{11} \rangle}{E_{1c}}\right) \quad ; \quad H_{13} = -\tfrac{\nu_{12}}{|\sigma_{11}|}\left(\tfrac{\langle \sigma_{11} \rangle}{E_1} + \tfrac{\langle -\sigma_{11} \rangle}{E_{1c}}\right); \\ &H_{23} = -\tfrac{\nu_{23}}{E_2} \end{aligned} \tag{3.4}$$

To account for closure of longitudinal and transverse cracks under load reversal, four damage variables associated with longitudinal (d_{1+} and d_{1-}) and transverse (d_{2+} and d_{2-}) damage are considered to define the d_1 and d_2:

$$d_1 = d_{1+}\frac{\langle\sigma_{11}\rangle}{|\sigma_{11}|} + d_{1-}\frac{\langle-\sigma_{11}\rangle}{|\sigma_{11}|} \tag{3.5}$$

$$d_2 = d_{2+}\frac{\langle\sigma_{22}\rangle}{|\sigma_{22}|} + d_{2-}\frac{\langle-\sigma_{22}\rangle}{|\sigma_{22}|} \tag{3.6}$$

Since shear damage represents transverse cracks which do not close under shear stresses, only one variable is considered for shear damage (d_6). The damage variables d_3, d_4 and d_6 read:

$$d_3 = 1 - (1 - d_{1-})(1 - d_{2-}) \quad ; \quad d_4 = d_6 \quad ; \quad d_5 = d_{1+} \tag{3.7}$$

3.1.1.2 Damage activation functions

The continuum damage model predicts four intralaminar failure mechanisms: longitudinal tensile failure (F_{1+}), longitudinal compressive failure (F_{1-}), transverse failure where the crack plane is perpendicular to the mid-plane of the laminate (F_{2+}), and transverse failure where the crack plane is not perpendicular to the mid-plane of the laminate (F_{2-}) [48]. The respective activation functions are defined as:

$$\begin{aligned} F_{1+} &= \phi_{1+} - r_{1+} \leq 0 \quad ; \quad F_{1-} = \phi_{1-} - r_{1-} \leq 0 \\ F_{2+} &= \phi_{2+} - r_{2+} \leq 0 \quad ; \quad F_{2-} = \phi_{2-} - r_{2-} \leq 0 \end{aligned} \tag{3.8}$$

The four loading functions, ϕ_i ($i = 1+, 1-, 2+, 2-$), define the failure surfaces, and are established in terms of strain tensor, using an approximation of the LaRC03-04 failure criteria [64] that will be discussed later in Section 3.1.1.4.1. For the sake of completeness, the loading functions are reported below. Refs. [47–49] include full details on definition of the loading functions and their physical meaning. The material properties of the ply are defined in Appendix A. The loading functions read:

$$\phi_{1+} = \frac{E_1}{X_T}\varepsilon_{11} \tag{3.9a}$$

$$\phi_{2+} = \begin{cases} \sqrt{\left(1 - \frac{\mathcal{G}_{2+}}{\mathcal{G}_6}\right)\frac{\tilde{\sigma}_{22}}{Y_T} + \left(\frac{\mathcal{G}_{2+}}{\mathcal{G}_6}\right)\left(\frac{\tilde{\sigma}_{22}}{Y_T}\right)^2 + \left(\frac{\tilde{\sigma}_{12}}{S_L}\right)^2} & \text{if} \quad \tilde{\sigma}_{22} \geq 0 \\ \frac{1}{S_L}\left\langle|\tilde{\sigma}_{12}| + \eta^L\tilde{\sigma}_{22}\right\rangle & \text{if} \quad \tilde{\sigma}_{22} < 0 \end{cases} \tag{3.9b}$$

$$\phi_{1-} = \frac{\left\langle\left|\tilde{\sigma}^R_{12}\right| + \eta^L\tilde{\sigma}^R_{22}\right\rangle}{S_L} \tag{3.9c}$$

$$\phi_{2-} = \sqrt{\left(\frac{\tilde{\tau}^T_{\text{eff}}}{S_T}\right)^2 + \left(\frac{\tilde{\tau}^L_{\text{eff}}}{S_L}\right)^2} \quad \text{if} \quad \tilde{\sigma}_{22} < 0 \tag{3.9d}$$

The effective (undamaged) stress tensor, $\tilde{\boldsymbol{\sigma}}$, is a function of the undamaged stiffness tensor, $\mathbf{C_0}$, and of the elastic strains $\boldsymbol{\varepsilon}_e$:

$$\tilde{\boldsymbol{\sigma}} = \mathbf{C}_0 : \boldsymbol{\varepsilon}_e \tag{3.10}$$

The components of the effective stress tensor in the coordinate system associated with the rotation of the fibres are calculated as:

$$\tilde{\sigma}_{22}^R = \tilde{\sigma}_{11} \sin^2 \varphi^C + \tilde{\sigma}_{22} \cos^2 \varphi^C - 2 \left|\tilde{\sigma}_{12}\right| \sin \varphi^C \cos \varphi^C \tag{3.11a}$$

$$\tilde{\sigma}_{12}^R = (\tilde{\sigma}_{22} - \tilde{\sigma}_{11}) \sin \varphi^C \cos \varphi^C + \left|\tilde{\sigma}_{12}\right| \left(\cos^2 \varphi^C - \sin^2 \varphi^C\right) \tag{3.11b}$$

where the misaligned angle at failure of a unidirectional (UD) ply subjected to uniaxial longitudinal compression, φ^C, is given by:

$$\varphi^C = \arctan\left(\frac{1 - \sqrt{1 - 4\left(S_L/X_C + \eta^L\right) S_L/X_C}}{2\left(S_L/X_C + \eta^L\right)}\right) \tag{3.12}$$

The effective shear strengths, $\tilde{\tau}_{\text{eff}}^T$ and $\tilde{\tau}_{\text{eff}}^L$ are given by:

$$\tilde{\tau}_{\text{eff}}^T = \left\langle -\tilde{\sigma}_{22} \cos(\alpha_0) \left(\sin(\alpha_0) - \eta^T \cos(\alpha_0) \cos(\theta)\right)\right\rangle \tag{3.13a}$$

$$\tilde{\tau}_{\text{eff}}^L = \left\langle \cos(\alpha_0) \left(\left|\tilde{\sigma}_{12}\right| + \eta^L \tilde{\sigma}_{22} \cos(\alpha_0) \sin(\theta)\right)\right\rangle \tag{3.13b}$$

where the longitudinal and transverse frictional coefficients, η^L and η^T, respectively, read:

$$\eta^L \approx -\tfrac{S_L \cos(2\alpha_0)}{Y_C \cos^2 \alpha_0} \quad ; \quad \eta^T = -\tfrac{1}{\tan(2\alpha_0)} \tag{3.14}$$

the transverse shear strength, S_T is approximated by:

$$S_T = Y_C \cos(\alpha_0) \left[\sin(\alpha_0) + \frac{\cos(\alpha_0)}{\tan(2\alpha_0)}\right] \tag{3.15}$$

and the sliding angle, θ is given by:

$$\theta = \arctan\left(\frac{-\left|\tilde{\sigma}_{12}\right|}{\tilde{\sigma}_{22} \sin(\alpha_0)}\right) \tag{3.16}$$

The elastic domain thresholds, r_i $(i = 1+, 1-, 2+, 2-)$ are related to the damage variables by the damage evolution laws. r_i take the initial value 1 when the material is undamaged and increase as damage evolves. The elastic domain thresholds read:

$$r_{1+} = \max\left\{1, \max_{s=0,t}\left\{\phi_{1+}^s\right\}, \max_{s=0,t}\left\{\phi_{1-}^s\right\}\right\} \tag{3.17a}$$

$$r_{1-} = \max\left\{1, \max_{s=0,t}\left\{\phi_{1-}^s\right\}\right\} \tag{3.17b}$$

$$r_{2+} = \max\left\{1, \max_{s=0,t}\left\{\phi_{2+}^s\right\}, \max_{s=0,t}\left\{\phi_{2-}^s\right\}\right\} \tag{3.17c}$$

$$r_{2-} = \max\left\{1, \max_{s=0,t}\left\{\phi_{2-}^s\right\}\right\} \tag{3.17d}$$

3.1.1.3 Uniaxial response

To accurately capture the mechanical response of an UD composite lamina before and after initiation of the different failure modes, a different stress-strain response is considered for each damage mechanism (Fig. 3.2):

- Under longitudinal tensile loading, a linear-elastic response followed by a bi-linear softening law after longitudinal tensile damage initiation is assumed — Fig. 3.2A.
- Following the experimental findings of Moran et al. [200], under longitudinal compressive loading the initially linear-elastic response (preceding kink band formation) is followed by linear softening, corresponding to the propagation of a kink band, until reaching a plateau, corresponding to kink band broadening at constant stress — Fig. 3.2B.
- The transverse tensile and compressive stress-strain relations are represented by a linear softening law following an initially linear-elastic response — Fig. 3.2C.
- Finally, under in-plane shear, a nonlinear elasto-plastic response is assumed, represented by a reduced slope in the stress-strain curve to account for the inelastic response caused by plastic deformation, followed by a linear softening law — Fig. 3.2D.

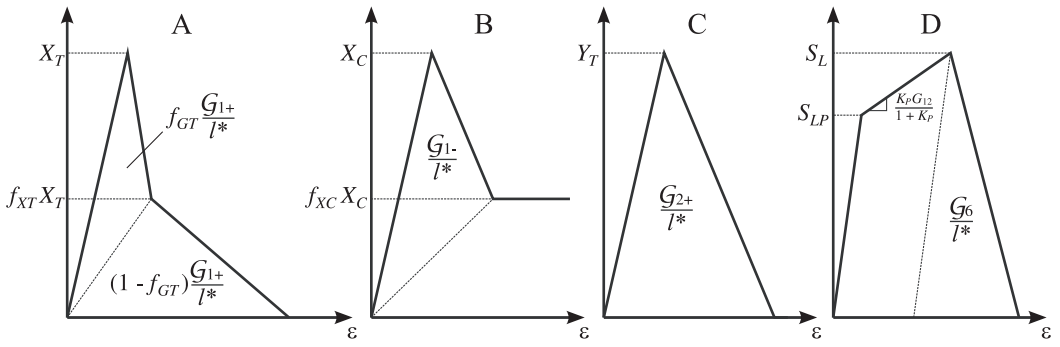

Figure 3.2: Uniaxial response in A) longitudinal tension, B) longitudinal compression, C) transverse tension or compression and D) in-plane shear.

To ensure correct energy dissipation during damage propagation and to avoid mesh-size dependency of the numerical solution, the slopes of the softening laws are determined as a function of the fracture toughness $\mathcal{G}_c$ associated with each failure mechanism ($\mathcal{G}_{1+}$, $\mathcal{G}_{1-}$, $\mathcal{G}_{2+}$ / $\mathcal{G}_{2-}$, and $\mathcal{G}_6$ — see Fig. 3.2), and as a function of the characteristic length l^* of the finite elements [201]. Since quadrangular elements are used, a damage mode independent element characteristic length is defined.

3.1.1.4 Effect of though-the-thickness stress

The three modifications related to the effect of pressure on damage onset and propagation proposed in this work are reported hereafter. A damage activation function for longitudinal compression that accounts for the effect of though-thickness

stresses based on the 3D failure criteria proposed by Camanho et al. [11] is proposed in Section 3.1.1.4.1 and engineering solutions to account for ii) the effect of pressure on the longitudinal compression and iii) in-plane shear fracture toughness are proposed in Sections 3.1.1.4.2 and 3.1.1.4.3, respectively.

3.1.1.4.1 Damage activation function for longitudinal compression

The model proposed in Refs. [47–49] assumed that the out-of-plane stress components are negligibly small to promote damage, and therefore only the in-plane stress components of the stress tensor activate damage. However, this assumption is not suitable for test cases where the triaxiality of the stress state is not negligible. Therefore, to improve the ability to accurately predict damage initiation and evolution in 3D test cases, the model initially proposed in Refs. [47–49] was modified to include a 3D invariant-based failure criterion for fibre kinking (Fig. 3.3) [11]. This failure criterion is used to define an artificial in-plane shear strength S_L^{ef}, which represents the effect of hydrostatic pressure on the shear response of the polymer matrix [202–204]. S_L^{ef} is determined imposing that, at failure, the 2D damage activation function [48] is equal to the activation function from the 3D invariant-based failure criterion [11]:

$$\frac{\left\langle \left| \tilde{\sigma}_{12}^R \right| + \eta^L \tilde{\sigma}_{22}^R \right\rangle}{S_L} = \alpha_1 I_1 + \alpha_2 I_2 + \alpha_3 I_3 + \alpha_{32} I_3^2 \tag{3.18}$$

and solving for the in-plane shear strength, S_L. The 2D damage activation function (left-hand side of Eq. (3.18)), is defined in Section 3.1.1.2. The 3D invariant-based failure criterion for fibre kinking (right-hand side of Eq. (3.18)) is defined by the set of invariants:

$$I_1 = \frac{1}{2} \mathrm{tr} \left(\tilde{\boldsymbol{\sigma}}^p \right)^2 - \mathbf{a} \left(\tilde{\boldsymbol{\sigma}}^p \right)^2 \mathbf{a} \tag{3.19a}$$

$$I_2 = \mathbf{a} \left(\tilde{\boldsymbol{\sigma}}^p \right)^2 \mathbf{a} \tag{3.19b}$$

$$I_3 = \mathrm{tr}\, \tilde{\boldsymbol{\sigma}} - \mathbf{a}\, \tilde{\boldsymbol{\sigma}}\, \mathbf{a} \tag{3.19c}$$

assuming a decomposition of the effective stress tensor $\tilde{\boldsymbol{\sigma}}$ in plasticity inducing stresses $\tilde{\boldsymbol{\sigma}}^p$ and reaction stresses $\tilde{\boldsymbol{\sigma}}^r$:

$$\tilde{\boldsymbol{\sigma}}^p = \tilde{\boldsymbol{\sigma}} - \tilde{\boldsymbol{\sigma}}^r \tag{3.20a}$$

$$\tilde{\boldsymbol{\sigma}}^r = \frac{1}{2} \left(\mathrm{tr}\, \tilde{\boldsymbol{\sigma}} - \mathbf{a}\, \tilde{\boldsymbol{\sigma}}\, \mathbf{a} \right) \mathbf{1} - \frac{1}{2} \left(\mathrm{tr}\, \tilde{\boldsymbol{\sigma}} - 3\, \mathbf{a}\, \tilde{\boldsymbol{\sigma}}\, \mathbf{a} \right) \mathbf{A} \tag{3.20b}$$

where $\mathbf{1}$ is the identity tensor and $\mathbf{A} = \mathbf{a} \otimes \mathbf{a}$ is the structural tensor that represents the intrinsic characteristic direction of the transversely isotropic material. The preferred direction $\mathbf{a}$, in the case of UD fibre-reinforced composites, coincides with the fibre direction. For the rotated fibres in the misalignment frame of a kink band, this preferred direction reads [11]:

$$\mathbf{a} = \begin{bmatrix} \cos\varphi \\ \cos\psi \sin\varphi \\ \sin\psi \sin\varphi \end{bmatrix} \tag{3.21}$$

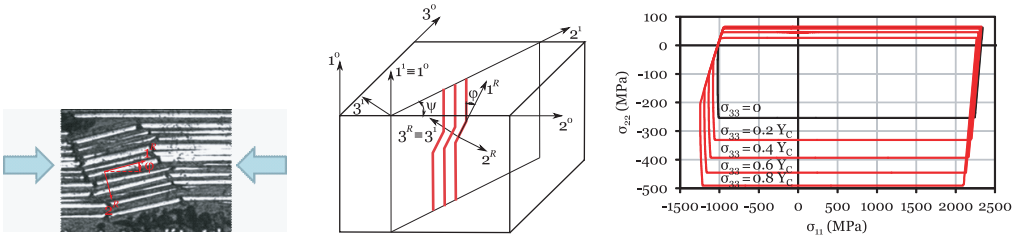

Figure 3.3: Fibre kinking kinematics and effect of through-thickness stresses predicted by a 3D invariant-based failure criterion [11].

where φ is the misalignment angle and ψ is the angle of the kinking plane (see Fig. 3.3). The parameters α_i (with $i = 1, 2, 3, 32$) are simple functions of the transverse and shear ply strengths that depend on the direction of the applied normal load through the sign of I_3 to account for the tensile/compressive strengths asymmetry:

$$\alpha_1 = \frac{1}{S_T^2} \tag{3.22a}$$

$$\alpha_2 = \frac{1}{S_L^2} \tag{3.22b}$$

$$\alpha_{32} = \begin{cases} \alpha_{32}^T = (1 - \frac{Y_T}{2Y_{BT}} - \alpha_1 \frac{Y_T^2}{4})/(Y_T^2 - 2Y_{BT}Y_T) & \text{if} \quad I_3 > 0 \\ \alpha_{32}^C = (1 - \frac{Y_C}{2Y_{BC}} - \alpha_1 \frac{Y_C^2}{4})/(Y_C^2 - 2Y_{BC}Y_C) & \text{if} \quad I_3 < 0 \end{cases} \tag{3.22c}$$

$$\alpha_3 = \begin{cases} \frac{1}{2Y_{BT}} - 2\alpha_{32}^T Y_{BT} & \text{if} \quad I_3 > 0 \\ \frac{1}{2Y_{BC}} - 2\alpha_{32}^C Y_{BC} & \text{if} \quad I_3 < 0 \end{cases} \tag{3.22d}$$

3.1.1.4.2 Softening law for longitudinal compression

In this work, the 3D invariant-based failure criterion for fibre kinking included in the damage model is also used to scale the fracture toughness for longitudinal compression ($\mathcal{G}_{1-}$) and the longitudinal compressive strength ratio at the inflection point (f_{XC}) as a function of the applied pressure (Fig. 3.4). The fracture toughness is scaled proportionally to the increase of longitudinal compressive strength:

$$\mathcal{G}_{1-}^{ef} = \mathcal{G}_{1-} \left| \frac{\bar{\sigma}_{11}}{X_C} \right|, \quad \text{if} \quad \left| \frac{\bar{\sigma}_{11}}{X_C} \right| > 1 \tag{3.23}$$

where X_C is the uniaxial longitudinal compressive strength and $\bar{\sigma}_{11}$ is the compressive strength predicted by the 3D invariant-based failure criterion for multiaxial stress states (see Fig. 3.5). The effective longitudinal compressive strength ratio at the inflection point (f_{XC}^{ef}) is:

$$f_{XC}^{ef} = \min \left\{ 1, f_{XC} \left(1 - f_{fxc} \left\langle -I_3 \right\rangle \right) \right\} \tag{3.24}$$

where $I_3 = \sigma_{22} + \sigma_{33}$ is the third invariant of the 3D invariant-based failure criterion [11] and f_{fxc} is a frictional parameter that needs to be calibrated using the experimental curves from a bearing, filled-hole compression or open-hole compression test.

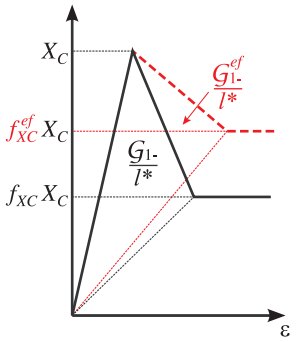

Figure 3.4: Effect of hydrostatic pressure on the longitudinal compressive response.

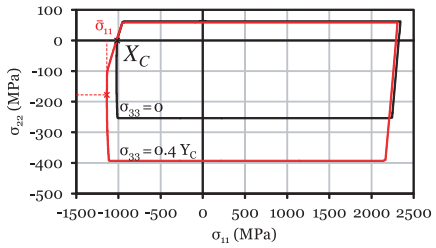

Figure 3.5: UD ply failure by fibre kinking under multiaxial stress states.

3.1.1.4.3 Fracture toughness for in-plane shear

It has been shown experimentally that through-thickness compression increases the apparent interlaminar mode II fracture toughness and delays delamination onset [205–207]. Cui et al. [208] suggested that this strengthening effect can be represented by an effective fracture toughness, $\mathcal{G}_{IIc}^{ef}$:

$$\mathcal{G}_{IIc}^{ef} = \mathcal{G}_{IIc} \left(1 - \eta_G \langle -\sigma_{33} \rangle\right) \tag{3.25}$$

where $\mathcal{G}_{IIc}$ is the mode II fracture toughness, η_G is a material dependent empirically derived enhancement factor, σ_{33} is the through-thickness stress and $\langle x \rangle$ is the Macaulay operator [208, 209]. It can be postulated that, at the ply level, applying transverse compression stress should have a similar strengthening effect since a similar fracture process occurs for transverse cracking and, therefore, the effective fracture toughness for in-plane shear can be expressed as:

$$\mathcal{G}_{6}^{ef} = \mathcal{G}_{6} \left(1 - \eta_G \langle -\sigma_{22} \rangle\right) \tag{3.26}$$

The resulting effect of this modification is shown in Fig. 3.6.

3.1.1.5 *In-situ* strengths

It is clear that a proper model formulation is fundamental to accurately predict damage onset and propagation in composite laminates, however the material properties used to populate the model also have to be accurately determined. It is particularly important to take into account that some of the ply strengths are *in-situ* properties, i.e. are a function of the ply thickness in a multidirectional laminate.

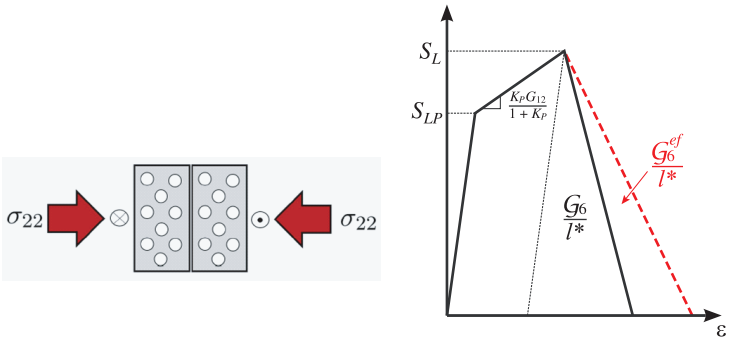

Figure 3.6: Effect of transverse compressive stresses on the longitudinal in-plane shear response.

This effect was first detected experimentally for transverse tension and in-plane shear by Parvizi et al. [27], and further analysed by other authors [3, 4, 22, 28–33, 210]. Camanho et al. [22] proposed an analytical model to predict the *in-situ* transverse tension, Y_T^{is}, and in-plane shear, S_L^{is}, strengths using Fracture Mechanics models that relate the *in-situ* properties with the fracture toughness of the material.

The calculation of the *in-situ* shear strength relies on the approximation of the non-linear shear response. The shear response is usually approximated by either the Tsai-Hahn or the Ramberg-Osgood laws. Different approximations result in different predictions of the *in-situ* strengths since, as currently derived, they are highly dependent on the shape of the stress-strain behaviour prior to failure and, therefore, highly dependent on the law used to approximate the shear response [211]. Given the high dependence of the *in-situ* shear strengths on the shear response law, adopting contradictory assumptions for the shear behaviour to derive the *in-situ* strengths and to the material constitutive model should be avoided [211]. To maintain consistency, the *in-situ* strengths should, therefore, be derived assuming the bilinear shear response implemented in the model and shown in Fig. 3.2.D. The derivation of the *in-situ* strengths was carried out and implemented during this work, and are presented in Appendix B. These properties are used in the failure criteria.

3.1.1.6 Mechanical response of the ply

The model previously described is tested in this section under three loading cases, corresponding to pure longitudinal tension/compression, transverse tension/compression and in-plane shear. As shown in Fig. 3.7, the uniaxial response of the material corresponds to the behaviour defined in Section 3.1.1.3.

3.1.2 Cohesive zone model for the interfaces between plies

The accurate simulation of failure of composite laminates requires not only the prediction of intralaminar damage, but also the prediction of delamination onset and propagation. In the framework of this work, some common problems regarding the prediction of delamination were identified. Firstly, most of the formulations are developed for pure mode loading and then extended for mixed-mode loading and are, therefore, poorly validated for mixed mode loading conditions. Secondly, in the formulation of cohesive zone models, friction is usually not accounted for. The effect

of these issues can be minimized by using engineering solutions proposed by several authors [208, 209, 212, 213]; however a rigorous cohesive zone model to simulate delamination under mixed mode loading and that accounts for the effect of friction should be used.

Based on their previous work [212], Turon et al. [195] proposed a cohesive zone model that guarantees accurate prediction of damage propagation under mixed mode loading by including a mode-dependent penalty stiffness. Alfano et al. [196] proposed an approach to combine interface damage with friction considering a linear elastic behaviour for the undamaged part and the damage evolution law proposed by Crisfield et al. [175] combined with a simple Coulomb friction law. However, any cohesive zone model and friction law can be used. The cohesive zone model proposed by Turon et al. [195] was combined with the Coulomb friction law is used in this work to simulate delamination onset and propagation.

3.1.2.1 Constitutive model

The methodology proposed by Alfano and Sacco [196], assumes that a Representative Elementary Area (REA) of the interface can be divided into an undamaged and a damaged part. The relative displacement, $\mathbf{\Delta}$, experienced in both parts is equal. The interface traction can be divided into an undamaged component, $\tau^{\mathbf{u}}$, and a damaged component, $\tau^{\mathbf{d}}$. The homogenized interface traction over the REA, τ, is given by:

$$\tau = (1-d)\tau^u + d\tau^d \tag{3.27}$$

where the term $(1-d)\tau^u$ comes from the cohesive law and the term $d\tau^d$ represents friction and contact on the damaged surface. The undamaged component follows a linear elastic law:

$$\tau^u = \mathbf{K}\mathbf{\Delta} \tag{3.28}$$

where $\mathbf{K}$ is the diagonal stiffness matrix. Following Turon et al. [195], $K_{33} = K_n$ and $K_{11} = K_{22} = K_{sh}$, hence the stiffness matrix reads:

$$\mathbf{K} = \begin{bmatrix} K_{sh} & 0 & 0 \\ 0 & K_{sh} & 0 \\ 0 & 0 & K_n \end{bmatrix} \tag{3.29}$$

The damaged component of the interface traction is computed after division of the relative displacement into an elastic part, $\mathbf{\Delta}^{de}$ and an inelastic part $\mathbf{\Delta}^{di}$. The traction in the damaged part $\tau^{\mathbf{d}}$, is related to $\mathbf{\Delta}^{de} = \mathbf{\Delta} - \mathbf{\Delta}^{di}$ as:

$$\tau^d = \begin{bmatrix} K_{sh} & 0 & 0 \\ 0 & K_{sh} & 0 \\ 0 & 0 & K_n \end{bmatrix} \begin{bmatrix} \Delta_1 - \Delta_1^{di} \\ \Delta_2 - \Delta_2^{di} \\ -\langle -\Delta_n \rangle \end{bmatrix} \tag{3.30}$$

The following friction function was introduced:

$$\phi = \mu\tau_n^d + \tau_{sh}^d \tag{3.31}$$

where μ is the friction coefficient and τ_{sh}^d is given by

$$\tau_{sh}^d = \sqrt{(\tau_1^d)^2 + (\tau_2^d)^2} \tag{3.32}$$

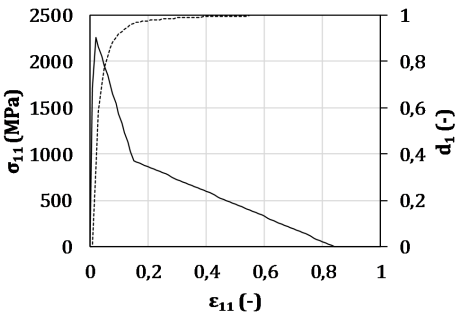

(a) Longitudinal tension

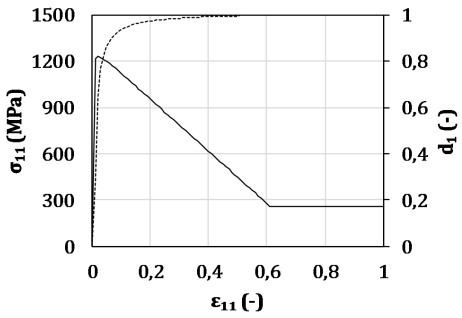

(b) Longitudinal compression

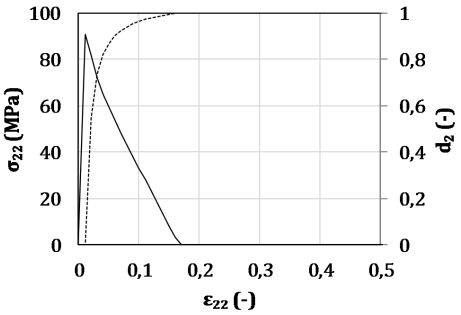

(c) Transverse tension

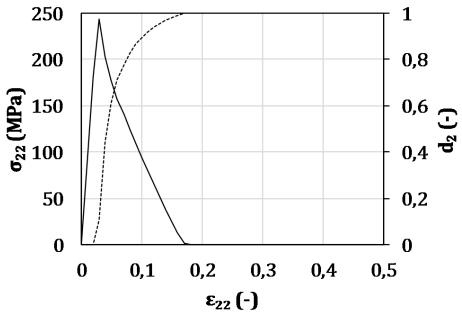

(d) Transverse compression

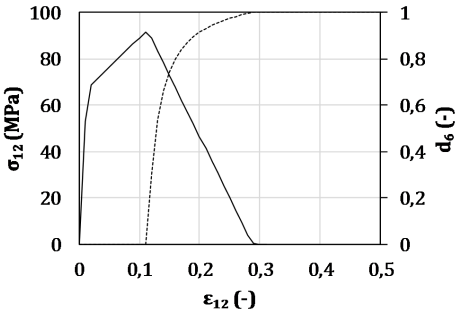

(e) In-plane shear

Figure 3.7: Mechanical response of the ply under uniaxial loading.

The evolution of $\boldsymbol{\Delta}^{\mathbf{di}}$ is assumed to be governed by the following nonassociative relationship

$$\dot{\boldsymbol{\Delta}}^{\mathbf{di}} = \dot{\lambda} \begin{bmatrix} \dfrac{\partial \phi}{\partial \tau_1^d} \\ \dfrac{\partial \phi}{\partial \tau_2^d} \\ 0 \end{bmatrix} = \dot{\lambda} \begin{bmatrix} \dfrac{\tau_1^d}{\tau_{sh}^d} \\ \dfrac{\tau_2^d}{\tau_{sh}^d} \\ 0 \end{bmatrix} \tag{3.33}$$

with the Kuhn-Tucker conditions $\dot{\lambda} \geq 0$, $\phi(\tau) \leq 0$ and $\dot{\lambda}\phi(\tau) = 0$.

3.1.2.2 Mode dependent penalty stiffness

Most of the formulations are developed for pure mode loading and then extended for mixed-mode loading and are, therefore, poorly validated for mixed mode loading conditions. Turon et al. [213] concluded that, to avoid erroneous calculation of the energy dissipation during mixed mode loading and to guarantee accurate prediction of damage propagation under mixed mode loading conditions, the relationship between the normal and shear interface stiffness (K_n and K_{sh}), the mode I and mode II fracture toughness ($\mathcal{G}_{Ic}$ and $\mathcal{G}_{Ic}$) and the normal and shear interlaminar strengths (τ_n and τ_{sh}) should be given as:

$$\frac{K_{sh}}{K_n} = \frac{\mathcal{G}_{Ic}}{\mathcal{G}_{IIc}} \left(\frac{\tau_{sh}}{\tau_n} \right)^2 \tag{3.34}$$

In their previous work, Turon et al. [213] assumed that the shear and normal penalty stiffness were equal $K_n = K_{sh}$ and therefore, the relation was imposed considering that the shear strength should not be a fully independent material property but instead a function of the fracture toughness and the normal strength:

$$\tau_{sh} = \tau_n \sqrt{\frac{\mathcal{G}_{IIc}}{\mathcal{G}_{Ic}}} \tag{3.35}$$

Note that the interface stiffness (K_n and K_{sh}) are parameters that ensure a stiff connection between the crack surfaces before crack propagation, but the fracture toughness ($\mathcal{G}_{Ic}$ and $\mathcal{G}_{IIc}$) and the interlaminar strengths (τ_n^0 and τ_{sh}^0) are properties that can be measured experimentally. For this reason, Turon et al. [195] reformulated the model assuming a dependent interface stiffness, $K_n \neq K_{sh}$, instead of dependent shear strength, $\tau_{sh} = f(\tau_n, \mathcal{G}_{IIc}, \mathcal{G}_{IIc})$:

$$K_{sh} = K_n \frac{\mathcal{G}_{Ic}}{\mathcal{G}_{IIc}} \left(\frac{\tau_{sh}}{\tau_n} \right)^2 \tag{3.36}$$

This engineering solution required the reformulation of the cohesive zone model to include the mode-dependent penalty stiffness.

To formulate the damage evolution law, the mixed-mode norms of the tractions, τ and the displacement jumps λ have to be defined. Following Refs. [214, 215], Turon et al. [195] defined the mixed-mode traction as a function of the Euclidean norm of the individual tractions along the 1, 2 and 3 directions accounting for different penalty stiffness. Under these assumptions, the mixed-mode norm of the displacement jump is redefined as:

$$\lambda = \frac{K_{sh}\Delta_{sh}^2 + K_n\Delta_n^2 - K_n\langle -\Delta_n \rangle^2}{\sqrt{K_{sh}^2\Delta_{sh}^2 + K_n^2\Delta_n^2 - K_n^2\langle -\Delta_n \rangle^2}} \tag{3.37}$$

3.1.2.3 Damage evolution law

The damage activation function is given by [195]:

$$F(\Delta) = H(\Delta) - r_d \leq 0 \tag{3.38}$$

where $H(\Delta)$ is a monotonic loading function, and r_d is the threshold function given, respectively, by:

$$H(\Delta) = \min\left(\frac{\lambda - \Delta^o}{\Delta^f - \Delta^o}, 1\right) \tag{3.39}$$

$$r_d = \max\left(1, \max_s\left[H(\Delta)\right]\right) \quad 0 < s < t \quad \forall t \tag{3.40}$$

being Δ^o and Δ^f the displacement jumps corresponding to delamination onset and propagation under mixed-mode conditions, respectively. The Benzeggagh and Kenane criterion [216] is used to define these parameters:

$$\Delta^o = \sqrt{\frac{K_n(\Delta_n^o)^2 + \left[K_{sh}(\Delta_{sh}^o)^2 - K_n(\Delta_n^o)^2\right]\beta^\eta}{K_\beta}} \tag{3.41}$$

$$\Delta^f = \frac{K_n\Delta_n^o\Delta_n^f + \left[K_{sh}\Delta_{sh}^o\Delta_{sh}^f - K_n\Delta_n^o\Delta_n^f\right]\beta^\eta}{K_\beta\Delta^o} \tag{3.42}$$

where

$$\begin{aligned} \Delta_n^o &= \tfrac{(\tau_n)^2}{K_n} \quad ; \quad \Delta_{sh}^o = \tfrac{(\tau_{sh})^2}{K_{sh}} \\ \Delta_n^f &= \tfrac{2\mathcal{G}_{Ic}}{\tau_n} \quad ; \quad \Delta_{sh}^o = \tfrac{2\mathcal{G}_{IIc}}{\tau_{sh}} \end{aligned} \tag{3.43}$$

and K_β is a mode-dependent interfacial stiffness defined as:

$$K_\beta = K_n(1-\beta) + \beta K_{sh} \tag{3.44}$$

and β is the local mixed mode ratio defined as:

$$\beta = \frac{K_{sh}\Delta_{sh}^2}{K_{sh}\Delta_{sh}^2 + K_n\langle-\Delta_n\rangle^2} \tag{3.45}$$

Finally, the damage variable is given by:

$$d = \frac{r_d\Delta^f}{r_d\Delta^f + (1-r_d)r_d\Delta^o} \tag{3.46}$$

3.1.2.4 Mechanical response of the interface

The model previously described is tested in this section using the material properties reported in Table 3.1. Three loading cases, corresponding to a) pure tension and pure shear, b) constant compressive stress followed by shear, and c) constant compressive stress followed by cyclic shear, are analysed hereafter.

(a) **Pure tension and pure shear are applied to the interface**:
The traction-displacement jump curves for pure mode I and mode II are shown in Fig. 3.8. The maximum strengths in mode I and mode II are respectively τ_n =40MPa and τ_{sh} =70MPa. The dissipated energy in pure mode I and pure

Table 3.1: Material properties of the interface.

$\mathcal{G}_{Ic}$ [N/mm]	$\mathcal{G}_{IIc}$ [N/mm]	τ_n [MPa]	τ_{sh} [MPa]	K [N/mm^3]	η [-]	μ [-]
0.75	1.5	40	70	1×10^6	1.45	0.2

mode II were calculated and found to be equal to the fracture toughness in mode I ($\mathcal{G}_{Ic}$) and mode II ($\mathcal{G}_{IIc}$), respectively, as expected.

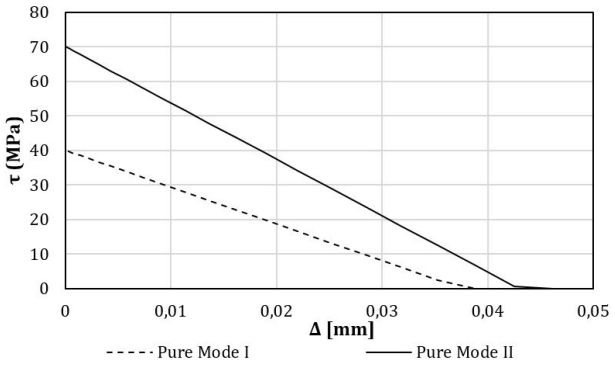

Figure 3.8: $\tau_{sh} - \Delta_{sh}$ curves for pure mode I and mode II.

(b) **The interface is subjected to constant compressive stress followed by shear displacement**
The traction-displacement jump curves for different applied compressive stresses are shown in Fig. 3.9. The mechanical response is characterized by:

(i) The interface presents a linear elastic behaviour until a stress higher that τ_{sh} is reached;

(ii) The stress continues to increase non-linearly until a maximum strength is reached;

(iii) The stress decreases until a plateau value of $\tau = \mu\sigma_n$ is reached. At this point, the element is completely damaged and can only carry load through friction.

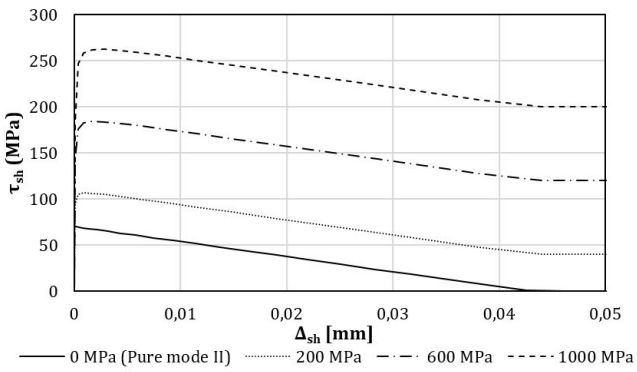

Figure 3.9: $\tau_{sh} - \Delta_{sh}$ curves for different through-thickness pressure.

(c) **The interface is subjected to constant compressive stress followed by cyclic shear loading**
The traction-displacement jump curve is shown in Fig. 3.10a. To support its interpretation, the evolution of damage and frictional sliding is shown in Fig. 3.10b. The mechanical response during the cyclic loading is characterized by the following regions:

(i) $\overline{AB}$: The interface presents a linear elastic behaviour until partial damage with frictional sliding occurs;

(ii) $\overline{BC}$: The element is unloaded with the original element stiffness and no damage propagation;

(iii) $\overline{CD}$: Frictional sliding occurs with no damage evolution;

(iv) $\overline{DE}$: Damage evolution restarts;

(v) $\overline{EF}$: The element is loaded with the original stiffness and with no damage propagation;

(vi) $\overline{FG}$: Frictional sliding occurs with no damage evolution;

(vii) $\overline{GH}$: Damage develops until the element is completely damaged and is only able to carry load though friction.

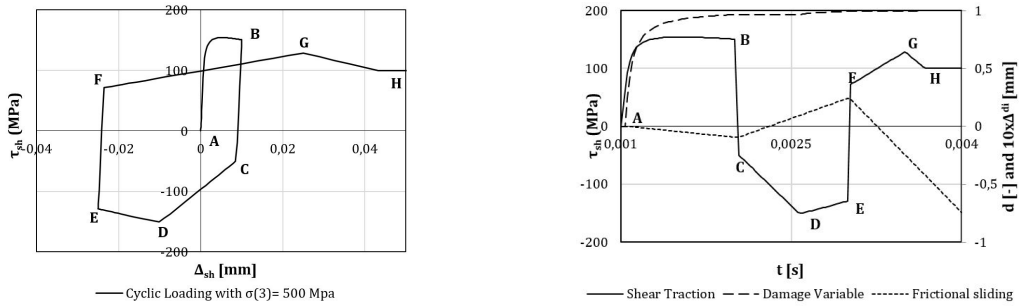

(a) τ_{sh} vs Δ_{sh} curve

(b) Damage and sliding evolution

Figure 3.10: Mechanical response of the interface during cyclic loading.

3.2 Numerical Results

Both the continuum damage model developed to simulate intralaminar damage onset and propagation in composite laminates presented in Section 3.1.1, and the cohesive zone model to simulate delamination presented in Section 3.1.2, were developed with the goal of increasing the ability of the model to accurately predict damage propagation when though-thickness stresses are not negligible, and/or under compressive loading conditions. In fact, when combined, the previous versions of the models [47–49, 215] were able to predict the in-plane mechanical behaviour of quasi-isotropic and symmetric composite laminates with good accuracy in test cases where the triaxility of stresses was fairly negligible, such as open-hole tension and open-hole compression. Camanho et al. [12] used the continuum damage model proposed in Refs. [47–49] to simulate the damage propagation in five open-hole tension tests of IM7/8552 carbon/epoxy system and obtained a maximum error of 10.5%

and a mean error of 4.2%. Bessa [14] predicted the open-hole tensile and compressive strength of IM7/8552 carbon/epoxy material system by combining the continuum damage model [47–49] and the cohesive zone model presented in Ref. [215]. For the open-hole tensile strengths, a maximum error of 11.5% and a mean error of 5.0% were obtained; for the open-hole compressive strengths, the maximum error and the mean error were of 16.5% and 11.6%, respectively. Note that relative errors between the mean strength measured experimentally and the one predicted numerically are usually considered acceptable when below 10%, hence, the predictions obtained by Bessa [14] and Camanho et al. [12] for tensile loading are particularly accurate in both studies while, the open-hole compressive strengths were slightly over-predicted [14]. This could be attributed to the fact that compressive strengths are more difficult to predict because the damage mechanisms are more complex; however, since they are remarkably consistent, i.e. the errors across the different geometries are similar, it was attributed to the inaccuracy of the experimental value available for the fracture toughness for longitudinal compression. As will be detailed in Section 3.2.4, the original versions of the models failed to deliver accurate predictions for more complex cases with significant compressive through-thickness stresses, simply because the material model for intralaminar damage was developed assuming that the components of the out-of-plane stresses are too small to affect damage, and also because the cohesive zone model was not developed accounting for frictional effects.

To validate the proposed modelling strategy, experimental results of unnotched tension/ compression, open-hole tension/ compression and filled hole compression of multidirectional laminates are compared with finite element results. Open-hole tension and compression tests were simulated to ensure that the modifications reported in Sections 3.1.1 and 3.1.2 do not affect the predictions previously obtained for these test cases [12, 14]. Filled-hole compression tests are considered the main test case to evaluate the accuracy of the modelling strategy since the pressure applied by the bolt can be significant, and therefore, accounting for the effect of friction and the effect of the through-thickness stresses in the formulation becomes more important. Filled-hole compression simulations are, therefore, analysed with more detail.

Both open-hole tension and compression Finite Element (FE) models used one 8-node linear brick reduced integration element (C3D8R) per ply thickness, t, and the plies are connected by 0.01mm thick 8-node three-dimensional cohesive element (COH3D8) user material cohesive elements. The laminate is clamped on one end while on the other a displacement (through the definition of an appropriate smooth step amplitude) is applied to all nodes at the boundary. A mesh of $0.5 \times 0.5 \times t\text{mm}^3$ is used for ply elements and $0.5 \times 0.5 \times 0.01\text{mm}^3$ for the cohesive elements (see Fig. 3.12). A similar strategy was used to model the unnotched tension and compression specimens, however, in these cases, two linear elastic regions were modelled respectively on the upper and bottom side of the specimen and were connected to the laminate in order to avoid premature failure of the elements where the boundary conditions are applied. For the unnotched tension and compression models, a mesh of $0.25 \times 0.25 \times t\text{mm}^3$ is used for ply elements and $0.25 \times 0.25 \times 0.01\text{mm}^3$ for the cohesive elements (see Fig. 3.11).

The filled hole compression model is composed by i) one bolt using of C3D8R elastic elements, ii) an upper and a lower bushing using C3D8R elastic elements, iii) the laminate. One C3D8R finite element per ply is used to simulate intralaminar damage and the plies are connected by 0.01mm thick COH3D8 user material

cohesive elements. The pre-loading of the bolt is simulated by increasing the temperature of the upper bushing. The temperature applied to the upper bushing was calibrated so that the preload of the bolt matches the experimental values. The laminate is clamped on the lower end and a smooth step is applied to the upper end of the laminate. A mesh of $0.47 \times 0.47 \times t$ mm^3 is used for ply elements and $0.47 \times 0.47 \times 0.01$mm^3 for the cohesive elements (see Fig. 3.13). The material properties of the three material systems used are presented in Tables 3.2-3.6. Nominal values without standard deviation are provided for the experimental inputs to the models. In Appendix A, the material properties are defined and the methods for their experimental determination are given.

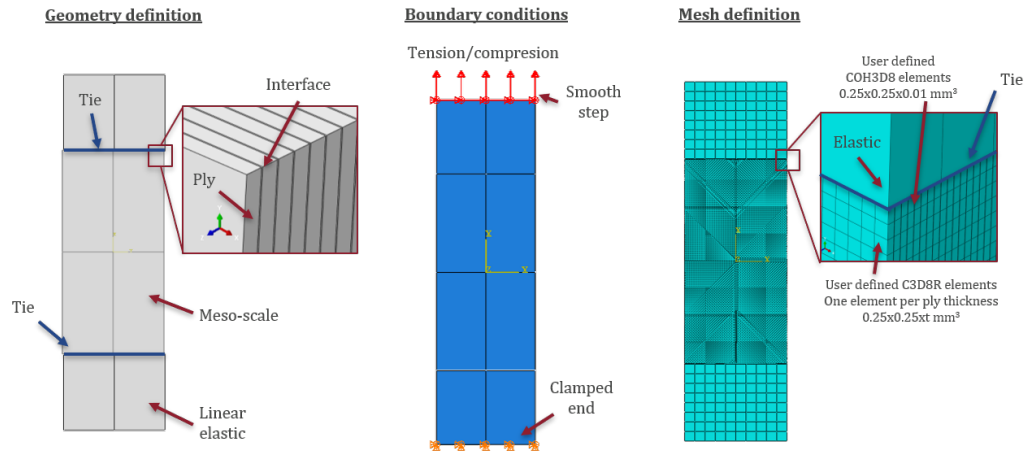

Figure 3.11: Finite element models for unnotched tension and compression.

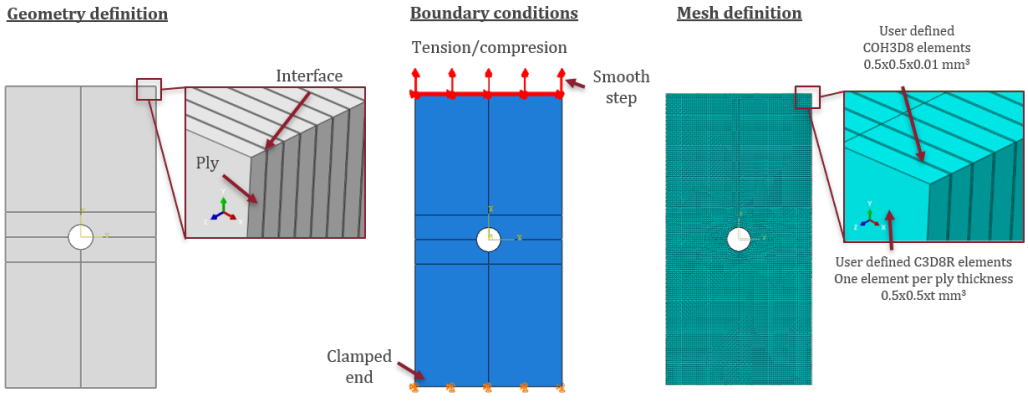

Figure 3.12: Finite element models for open-hole tension and compression.

3.2.1 Unnotched strength

Fig. 3.14 shows the experimental results for unnotched tensile and unnotched compressive strengths and the predictions obtained with the proposed modelling

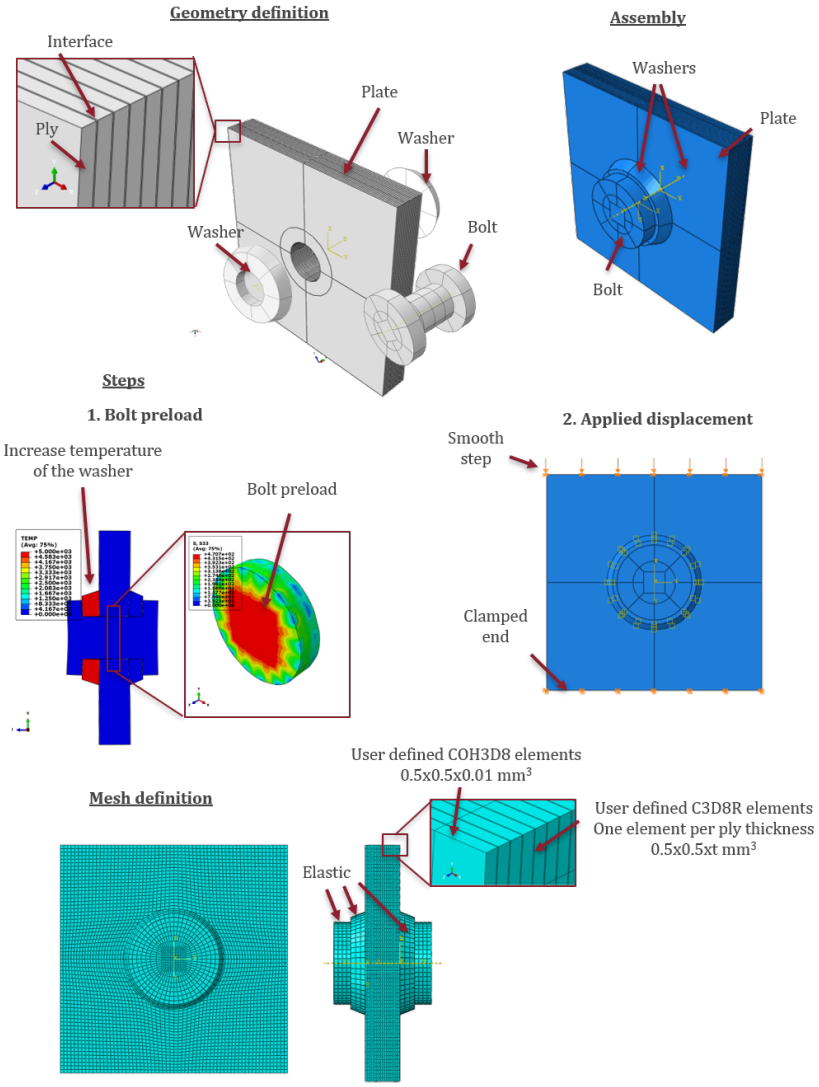

Figure 3.13: Finite element models for filled-hole compression.

strategy for a quasi-isotropic $[90/0/-45/45]_{3s}$ IM7/8552 laminate. The relative error for unnotched tensile strength is -13.1% and -4.7% for unnotched compressive strength. As shown in Figs. 3.15 and 3.16, modelled damage localizes at the 0° plies causing catastrophic failure of the specimen.

3.2.2 Open-hole tension

Figs. 3.17-3.19 show the experimental results for open-hole tensile strengths and the predictions obtained with the proposed modelling strategy for a $[90/0/-45/45]_{3s}$ IM7/8552 laminate and two quasi-isotropic T800/M21 laminates: $[90/45/0/-45]_{3s}$ (L1) and $[90_2/0_2/45_2/-45_2/90/0/45/-45]_s$ (L2). For the IM7/8552 material system, the maximum relative error is 7.9% for hole diameter $d = 8$mm while the mean error is 5.3%. For T800/M21 material system, the relative errors for the two lay-ups are below 10.7% and the mean error is 3.9%. The predictions for laminate L1 are

Table 3.2: Ply elastic properties of IM7/8552, T800/M21 and T700/M21 carbon/epoxy systems.

Elastic		IM7/8552		T800/M21		T700/M21	
E_1	(MPa)	171420	Ref. [12, 193]	172000	Ref. [217]	171200	Ref. [218]
E_{1c}	(MPa)	137136	Note (1)	137600	Note (1)	137000	Note (1)
E_2	(MPa)	9080	Ref. [12, 193]	8900	Ref. [217]	8500	Ref. [218]
G_{12}	(MPa)	5290	Ref. [12, 193]	5000	Ref. [217]	4500	Ref. [218]
ν_{12}	-	0.32	Ref. [12, 193]	0.32	Ref. [217]	0.32	Ref. [218]

(1) Assumed to be 80% of the Young's Modulus for longitudinal tension ($E_{1c} = 0.8E_1$)

Table 3.3: Ply strengths properties of IM7/8552, T800/M21 and T700/M21 carbon/epoxy systems.

Strengths		IM7/8552		T800/M21		T700/M21	
X_T	(MPa)	2323.5	Ref. [12, 193]	3039	Ref. [219]	2000	Ref. [218]
f_{XT}	(-)	0.4	Ref. [219]	0.4	Ref. [219]	0.4	Note (1)
X_C	(MPa)	1200.1	Ref. [12, 193]	1051	Ref. [220]	1300	Ref. [218]
f_{XC}	(-)	0.2	Note (2)	0.2	Note (2)	0.2	Note (3)
Y_T	(MPa)	62.3	Ref. [12, 193]	75	Ref. [219]	46	Ref. [221]
Y_C	(MPa)	253	Ref. [12, 193]	250	Ref. [219]	260	Ref. [221]
Y_{BT}	(MPa)	38.7	Ref. [11, 50]	46.5	Note (4)	28.5	Note (4)
Y_{BC}	(MPa)	600.0	Ref. [11, 50]	592.5	Note (5)	616.2	Note (5)
S_L	(MPa)	92.3	Ref. [12, 193]	95	Ref. [219]	81	Ref. [221]
S_L^P	(MPa)	66.9	Note (6)	66.9	Note (6)	50	Note (6)
K_p	(-)	0.08	Note (6)	0.09	Note (6)	0.29	Note (6)

(1) Assumed from the IM7/8552 material system
(2) Inversely identified using one OHC simulation
(3) Inversely identified using one FHC simulation
(4) The ratio Y_{BT}/Y_T was assumed to be constant and equal to $38.7/62.3 = 0.62$
(5) The ratio Y_{BC}/Y_C was assumed to be constant and equal to $600/253 = 2.37$
(6) Best fitting from the transverse shear stress-strain curve of the material

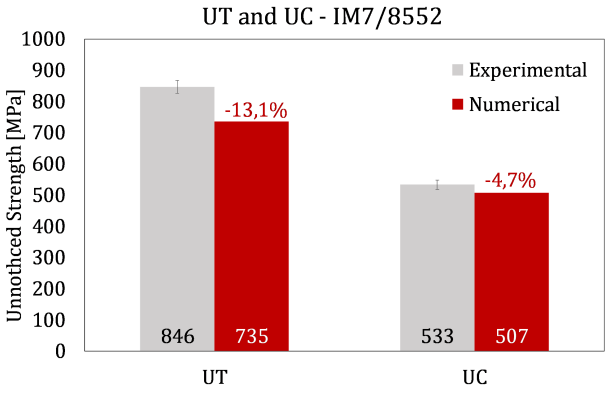

Figure 3.14: Comparison between the numerical and experimental results for the unnotched tensile and compressive strengths of an IM7/8552 carbon/epoxy quasi-isotropic laminate. The standard error related to the experimental test results is presented.

more accurate than the ones for laminate L2. Both lay-ups are quasi-isotropic, but L2 has plies with the same orientation blocked together. Having thicker 0° plies in a laminate promotes fibre splitting, which blunts the notch and improves the notched strength [13, 19, 225, 226], resulting in an apparent increase of the fracture toughness of the laminate. However, the modelling strategy used, which is not based on struc-

Table 3.4: Ply fracture toughness of IM7/8552, T800/M21 and T700/M21 carbon/epoxy systems.

Fracture		IM7/8552		T800/M21		T700/M21	
$\mathcal{G}_{2+}$	(kJ/m^2)	0.28	Ref.[12, 193]	0.228	Ref. [219]	0.35	Ref. [221]
$\mathcal{G}_{2-}$	(kJ/m^2)	1.31	Note (1)	1.0	Note (1)	2.0	Note (1)
$\mathcal{G}_6$	(kJ/m^2)	0.79	Ref.[12, 193]	0.652	Ref. [219]	1.2	Ref. [221]
$\mathcal{G}_{1+}$	(kJ/m^2)	133.3	Ref. [14]	340	Ref. [219]	133.3	Note (2)
f_{GT}	(-)	0.3	Note (3)	0.52	Ref. [219]	0.52	Note (4)
$\mathcal{G}_{1-}$	(kJ/m^2)	61	Ref. [222]	60	Note (5)	95	Note (6)

(1) $\mathcal{G}_{2-} = \mathcal{G}_6/\cos(\alpha_0)$ where $\mathcal{G}_6$ is the mode II fracture toughness and α_0 is the fracture angle of the UD ply subjected to uniaxial transverse compression (approximately 53°)
(2) Assumed from the IM7/8552 material system
(3) Inversely identified using one OHT simulation
(4) Assumed from the T800/M21 material system
(5) Inversely identified using one OHC simulation
(6) Inversely identified using one FHC simulation

Table 3.5: Ply geometric and friction parameters of IM7/8552, T800/M21 and T700/M21 carbon/epoxy systems.

Geometrical		IM7/8552		T800/M21		T700/M21	
α_0	(rad)	0.925	-	0.925	-	0.925	-
t	(mm)	0.125	-	0.125/0.184	-	0.250	-
Friction							
η_G	(MPa^{-1})	0.0035	Note (1)	0.0035	Note (1)	0.0035	Note (1)
f_{fxc}	(MPa^{-1})	0.01	Note (2)	0.01	Note (2)	0.01	Note (2)

(1) Assumed to be equal to the η parameter that accounts for the increase in interlaminar mode II fracture toughness as a function of applied through-thickness compressive stress determined for the IM7/8552 carbon/epoxy material system in Ref. [207]
(2) Inversely identified from a OHC or FHC simulation

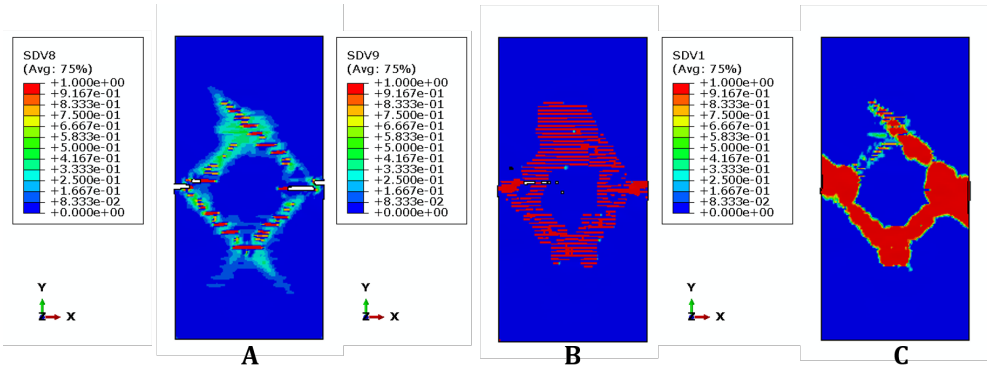

Figure 3.15: Damage extent at ultimate load in the unnotched tension simulation: A) fibre damage in a 0° ply (d_1), B) matrix damage in a 90° (d_2), C) interface damage (d). The specimen presented in this Fig. corresponds to the $[90/0/\text{-}45/45]_{3s}$ IM7/8552 laminate.

tured meshes, is likely not able to accurately predict fibre splitting in the 0° plies and to distinguish blocked 0° plies of single 0° plies. An accurate prediction of splitting would require a more refined mesh, accounting for large deformation/rotations in the model formulation [227], and the use of structured, fibre-aligned meshes where the edges of the elements follow the fibre direction [228] .

Table 3.6: Interlaminar material properties.

Elastic		IM7/8552		T800/M21		T700/M21	
K_n	(N/mm^3)	10^6	Ref. [177]	10^6	Ref. [177]	10^6	Ref. [177]
Strengths							
τ_n	(MPa)	62.3	Ref. [12, 193]	75	Ref. [219]	46	Ref. [221]
τ_{sh}	(MPa)	92.3	Ref. [12, 193]	95	Ref. [219]	81	Ref. [221]
Fracture							
$\mathcal{G}_{IC}$	(kJ/m^2)	0.28	Ref. [12, 193]	0.228	Ref. [219]	0.35	Ref. [221]
$\mathcal{G}_{IIC}$	(kJ/m^2)	0.79	Ref. [12, 193]	0.652	Ref. [219]	1.2	Ref. [221]
η_{B-K}	(-)	1.45	Ref. [223, 224]	1.45	Note (1)	2.0	Ref. [221]
Friction							
μ	(-)	0.1	Ref. [207]	0.1	Ref. [207]	0.1	Ref. [207]

(1) Assumed from the IM7/8552 carbon/epoxy material system

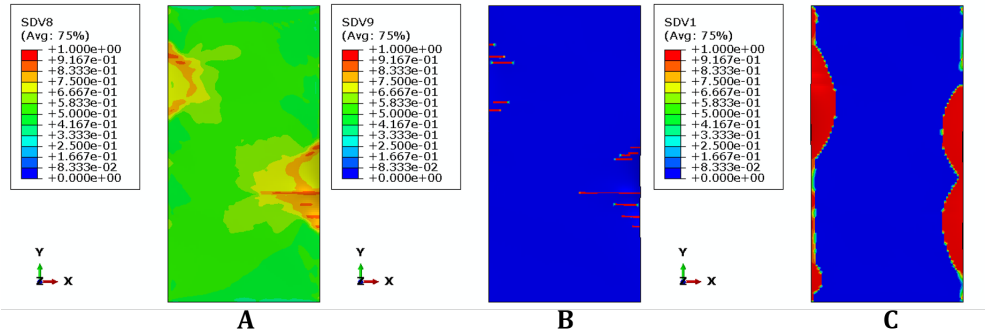

Figure 3.16: Damage extent at ultimate load in the unnotched compression simulation: A) fibre damage in a 0° ply (d_1), B) matrix damage in a 90° (d_2), C) interface damage (d). The specimen presented in this figure corresponds to the $[90/0/\text{-}45/45]_{3s}$ IM7/8552 laminate.

In general, at the point of maximum load the fibre damage in the 0° plies localizes in the vicinity of the hole and propagates perpendicular to the applied load (Fig. 3.20.A); the matrix damage in the 90° plies extends across the width of the specimen (Fig. 3.20.B); and interface damage is limited to the ligaments next to the hole (Fig. 3.20.C).

3.2.3 Open-hole compression

Figs. 3.21-3.23 show the experimental results for open-hole compressive strengths and the predictions obtained with the proposed modelling strategy for the same material systems previously considered. For IM7/8552, the relative errors are below 4.4% and the mean error is 1.9%. For T800/M21 material system, the relative errors for the two lay-ups are below 12.8% and the mean error is 7.6%. The predictions for IM7/8552 material system are significantly improved compared with the predictions obtained by Bessa [14] (maximum error of 16.5% and mean error of 11.6%). Here, the fracture toughness for longitudinal compression used was determined by Catalanotti et al. [222]. This value is lower than the one used by Bessa [14] which explains why the errors obtained are, on average, around 10% lower. The experimental results for open-hole compression for the L2 T800/M21 lay-up that uses thicker ply blocks shows a pronounced size effect that is not predicted very accurately by the model.

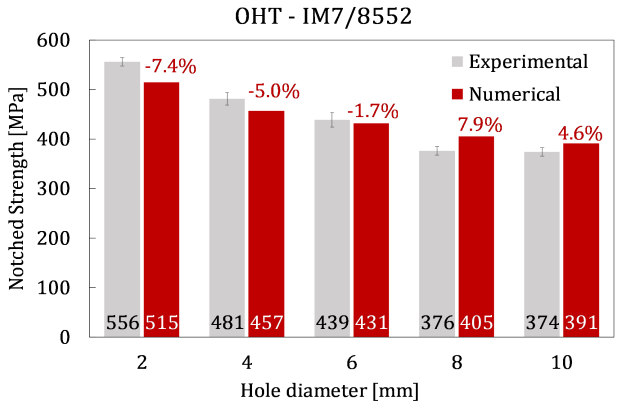

Figure 3.17: Comparison between the numerical and experimental results for the open-hole tensile strength of an IM7/8552 carbon/epoxy quasi-isotropic laminate [12]. The hole diameter-to-width ratio is $2R/W = 1/6$. The standard error related to the experimental test results is presented.

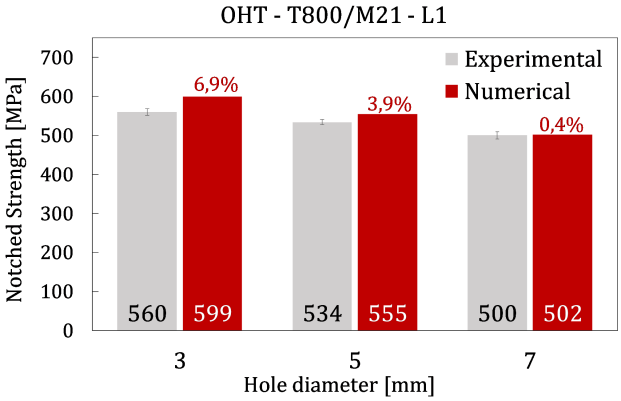

Figure 3.18: Comparison between the numerical and experimental results for the open-hole tensile strength of an T800/M21 carbon/epoxy quasi-isotropic laminate (L1) [13]. The hole diameter-to-width ratio is $2R/W = 1/4$. The standard error related to the experimental test results is presented.

This lower consistency in the predictions may be due to the fact that the material was not fully characterized and therefore, some assumptions on the material properties had to be made by the authors, particularly on the longitudinal compressive strength and fracture toughness for longitudinal compression of the unidirectional ply.

Across the materials and lay-ups considered, the OHC response has the general features that, at the point of maximum load, damage localizes at the vicinity of the hole as shown in Fig. 3.24: fibre damage in the 0° plies extends across the width of the specimen (Fig. 3.24.A), matrix damage in the 90° plies localizes in the vicinity of the hole and propagates perpendicularly to the applied load (Fig. 3.24.B), and interface damage is limited to the area of the hole (Fig. 3.24.C).

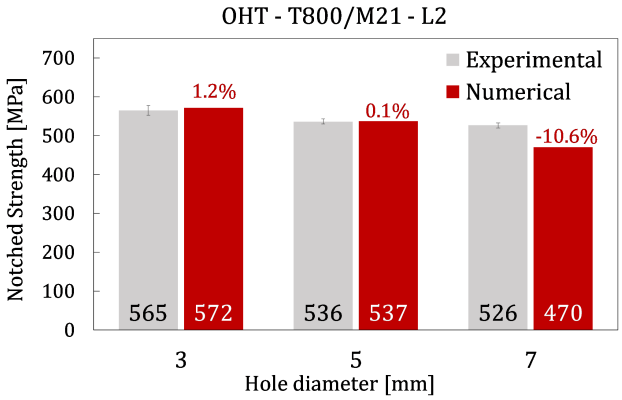

Figure 3.19: Comparison between the numerical and experimental results for the open-hole tensile strength of a T800/M21 carbon/epoxy quasi-isotropic laminate (L2) [13]. The hole diameter-to-width ratio is $2R/W = 1/4$. The standard error related to the experimental test results is presented.

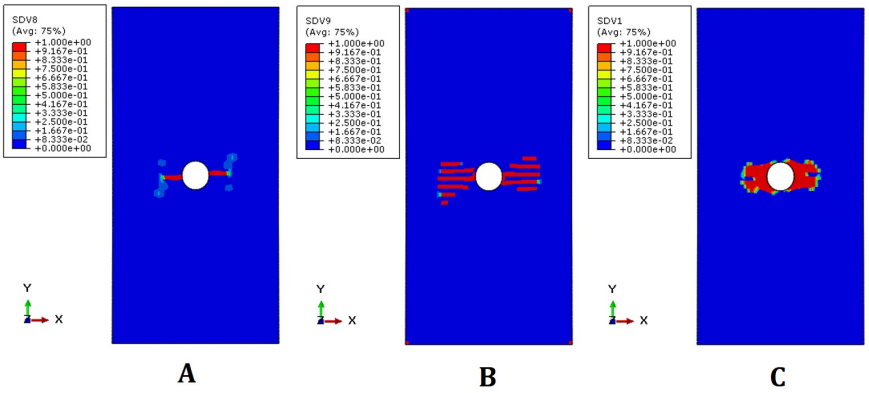

Figure 3.20: Typical damage extent at ultimate load in an open-hole tension simulation: A) fibre damage in a 0° ply (d_1) , B) matrix damage in a 90° ply (d_2), C) interface damage (d). The specimen presented in this figure corresponds to the $[90/0/\text{-}45/45]_{3s}$ IM7/8552 laminate with a hole diameter of $d = 6$mm.

3.2.4 Filled-hole compression

Filled-hole compression simulations are analysed with more detail since the pressure applied by the bolt can be significant, and therefore, accounting for frictional effects and the effect of the through-thickness stress in the formulation becomes critical. It is important to note that, even though the previous versions of the models were not particularly suitable for test cases where the triaxility of stresses is not negligible, some engineering solutions proposed by several authors [208, 209, 212, 213] can be used to improve the accuracy in the presence of though-thickness stresses. It is, therefore, interesting to compare four modelling strategies (S1 through S4). Note that S3 and S4 are based on the work presented in this paper:

- **S1** - Intralaminar damage is simulated using the user-written material subroutine described in Refs. [47–49] and interlaminar damage is simulated using built-in ABAQUS cohesive elements [229];

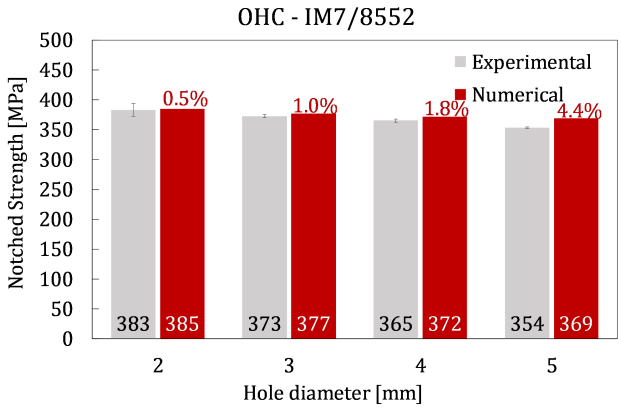

Figure 3.21: Comparison between the numerical and experimental results for the open-hole compressive strength of an IM7/8552 carbon/epoxy quasi-isotropic laminate [14]. The hole diameter-to-width ratio is $2R/W = 1/6$. The standard error related to the experimental test results is presented.

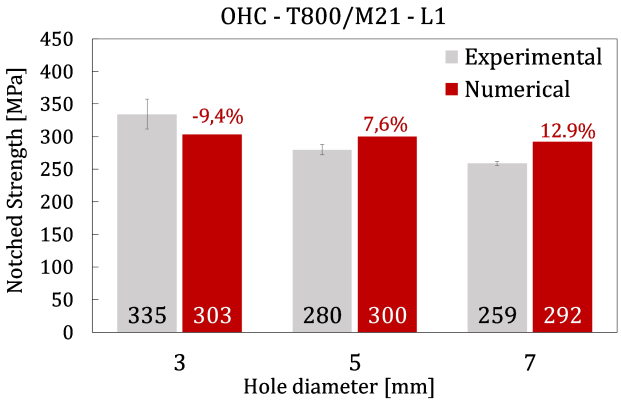

Figure 3.22: Comparison between the numerical and experimental results for the open-hole compressive strength of an T800/M21 carbon/epoxy quasi-isotropic laminate (L1) [13]. The hole diameter-to-width ratio is $2R/W = 1/4$. The standard error related to the experimental test results is presented.

- **S2** - Intralaminar damage is simulated using the user-written material subroutine described in Refs. [47–49] and interlaminar damage is simulated using built-in ABAQUS cohesive elements [229]. Engineering solutions proposed by Turon and co-authors [212, 213] and by Cui et al. [208] are used to calculate some of the properties of the cohesive elements to ensure proper energy dissipation in mixed-mode loadings and to artificially account for the effects of pressure and friction. These solutions are summarized in Appendix C;

- **S3** - Intralaminar damage is simulated using the user-written material subroutine described in Section 3.1.1 and interlaminar damage is simulated using built-in ABAQUS cohesive elements [229]. The same engineering solutions [208, 212, 213] used in S2 are used here. These solutions are also summarized in Appendix C;

- **S4** - Intralaminar damage is simulated using the user-written material sub-

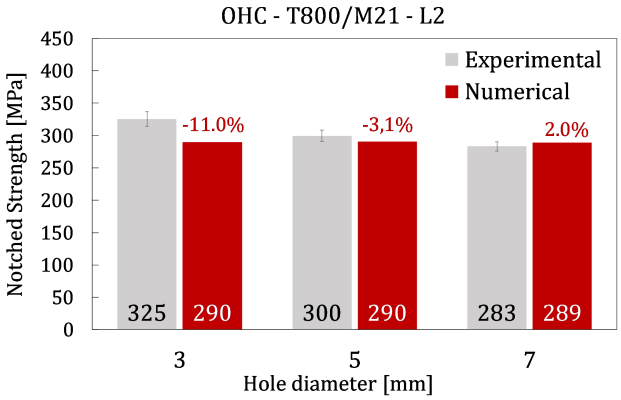

Figure 3.23: Comparison between the numerical and experimental results for the open-hole compressive strength of a T800/M21 carbon/epoxy quasi-isotropic laminate (L2) [13]. The hole diameter-to-width ratio is $2R/W = 1/4$. The standard error related to the experimental test results is presented.

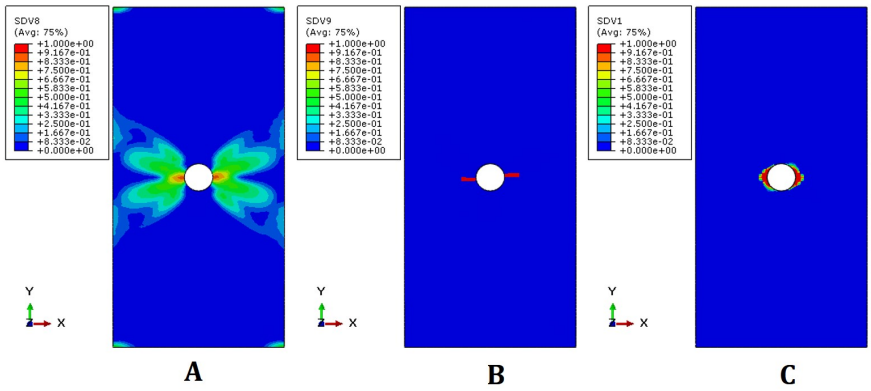

Figure 3.24: Typical damage extent at ultimate load in an open-hole compression simulation: A) fibre damage in a 0° ply (d_1), B) matrix damage in a 90° ply (d_2), C) interface damage (d). The specimen presented in this figure corresponds to the $[90/0/\text{-}45/45]_{3s}$ IM7/8552 laminate with a hole diameter of $d = 4$mm.

routine described in Section 3.1.1 and interlaminar damage is simulated using the user-written material subroutine described in Section 3.1.2, i.e., the S4 is the application of the new formulation presented in this paper.

Two simulations are performed with two different T700/M21 lay-ups: 44/44/11 where 44.4(4)%, 44.4(4)% and 11.1(1)% of the plies are 0°, ±45° and 90°, respectively, and 11/44/44 where 11.1(1)%, 44.4(4)% and 44.4(4)% of the plies are 0°, ±45° and 90°, respectively. Note that 11/44/44 stands for a 90° rotation of 44/44/11. The stacking sequences of the laminates, the experimental filled-hole compression strengths and load-displacement curves are Airbus proprietary and are therefore not presented in absolute terms. However, their absence does not affect the key observations and conclusions of this section. The stress-displacement relations and the errors between the experimental and the normalized numerical notched strengths obtained are presented in Fig. 3.25. To better understand the consequences of each modelling strategy and to assess the most suitable one, the results of each simula-

tion are analysed in detail. Given the stacking sequence, laminate 44/44/11 will be referred to as the "hard laminate" and laminate 11/44/44 will be referred to as the "soft laminate".

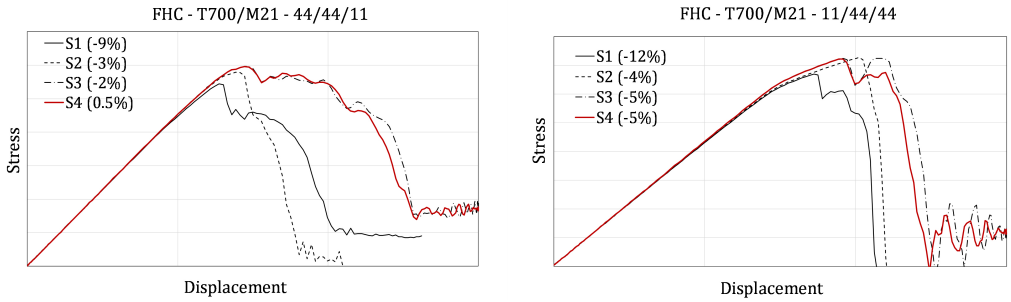

(a) (b) S2

Figure 3.25: Filled-hole compression numerical stress-displacement curves for a) the hard laminate (44/44/11) and b) the soft laminate (11/44/44) for the four modelling approaches S1 though S4. The legend provides the % difference between the model and experimental ultimate strength. Note that the x- and y-axes in A and B are not the same.

- **S1**: Using the original modelling strategy, the ultimate strength for the hard and soft laminates are both slightly underpredicted by -9% and -12% respectively (see Fig. 3.25). More importantly, the model is not able to capture the post peak response and predicts that an abrupt, catastrophic failure will occur as shown in Fig. 3.25. In the hard laminate, failure is dominated by fibre failure (Fig. 3.26a.A and 3.27a.A) and, in the soft laminate, delamination develops around the hole and quickly propagates through the width of the specimen as shown in Fig. 3.26a.C.
- **S2**: Using the modelling strategy S2, the mode II fracture toughness of the cohesive elements is increased as a function of the bolt preload. However, the pressure is not constant over all elements. In fact, the though-thickness stress is only negative under the bushings as shown in Fig. 3.28 and therefore, increasing the fracture toughness in all cohesive elements might result in an underprediction of the extent of delamination. In this case, failure is dominated by fibre compressive failure (Figs. 3.26b.A and 3.27b.A) and delamination plays a less relevant role than in S1 (Figs. 3.26b.C and 3.27b.C).
- **S3**: Using the modelling strategy S3, the predicted filled-hole compressive ultimate strengths increase towards the experimental values. Similarly to modelling strategy S2, the fracture toughness of the cohesive elements is equally increased and delamination might, therefore, be over-suppressed. Failure is progressive for two reasons. Firstly because delamination is partly suppressed, and secondly because the softening law for longitudinal compression was altered based on the experimental findings of Moran et al. [200], and therefore, even though damage in the 0° is extensive, the 0° plies do not fail completely as shown in Figs. 3.26c.A and 3.27c.A.
- **S4**: Finally, using the modelling strategy proposed in this work, the strengthening effect of pressure is more accurately represented since it is friction induced and not simply represented based on an empirical engineering solution.

In the hard laminate, damage extension is similar to the one predicted using modelling strategy S3 because delamination does not play an important role in the failure of the specimen (Figs. 3.26c.C and 3.26d.C). However, for the soft laminate, unlike in S3, delamination propagates through the width of the specimen and its extent is similar to the one predicted using modelling strategy 1 (Figs. 3.27a.C and 3.27d.C). It should be noticed that, even though the elements might be fully damaged, they are still able to carry load through friction.

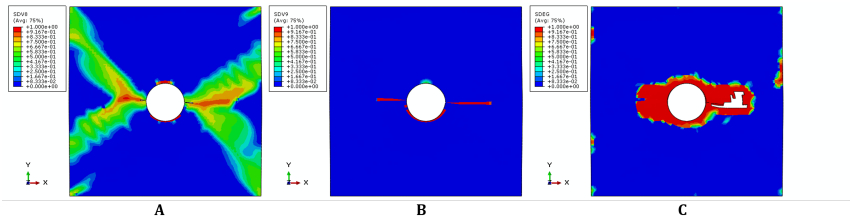

(a) S1

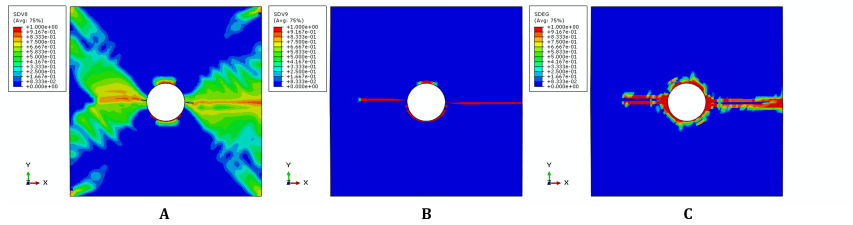

(b) S2

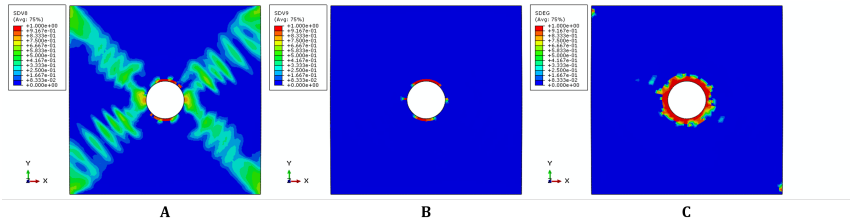

(c) S3

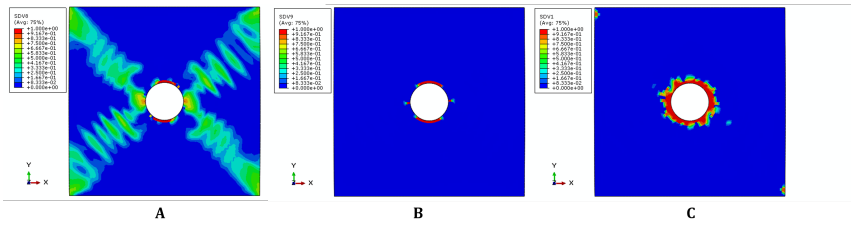

(d) S4

Figure 3.26: Predicted damage at ultimate load in 44/44/11: A) fibre damage in a 0° ply (d_1), B) matrix damage in a 90° ply (d_2), C) interface damage (d).

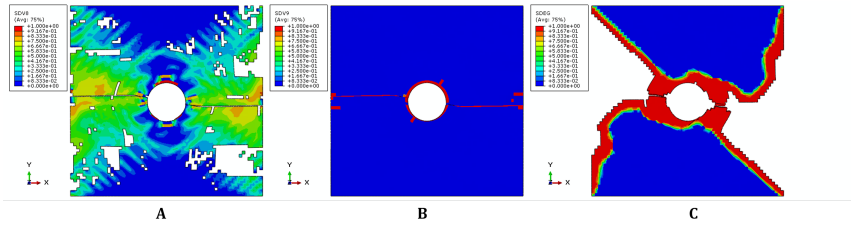

(a) S1

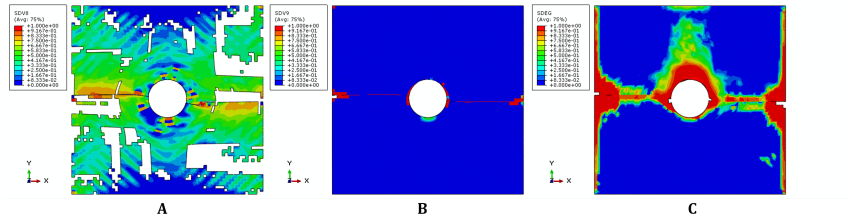

(b) S2

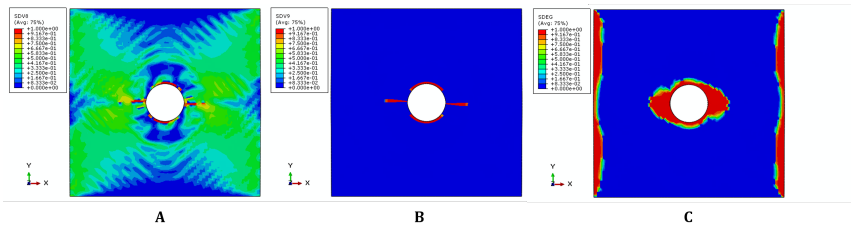

(c) S3

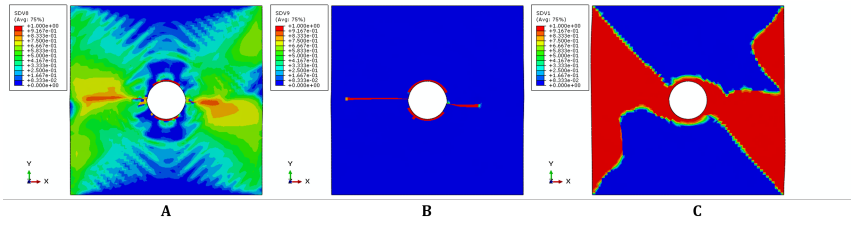

(d) S4

Figure 3.27: Predicted damage at ultimate load in 11/44/44: A) fibre damage in a 0° ply (d_1), B) matrix damage in a 90° ply (d_2), C) interface damage (d).

To further explore the predictive capabilities of modelling strategy S4, other laminates were simulated using the same methodology. Figs. 3.29 and 3.30 show the experimental results for filled hole compressive strengths and the predictions obtained with the proposed modelling strategy for six multidirectional T700/M21 laminates and one multidirectional T800/M21 laminate, respectively. The relative errors for all seven lay-ups are below 6.8% and the mean error is 2.7%. The propagation of damage and eventual final failure is a complex combination of different failure mechanisms and interactions between matrix cracking, fibre failure and delamination. Note that the set of laminates tested include four hard and three soft laminates with different percentages of 0°, 45° and 90° plies and that failure of each laminate is dominated by different failure modes. The load displacement curves

were not available, and therefore, it was not possible to verify the accuracy of the simulations in predicting the evolution of applied stress as a function of the applied displacement. Nonetheless, the ability of the model to accurately predict the filled-hole compression ultimate strength is remarkable.

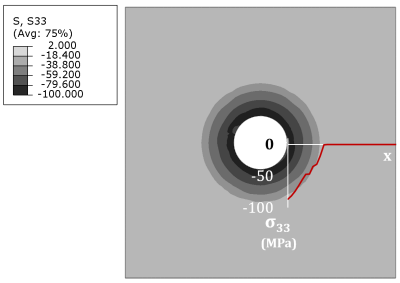

Figure 3.28: σ_{33} (in MPa) after bolt preload on the laminate of a filled hole compression specimen. σ_{33} vs x is plotted in red.

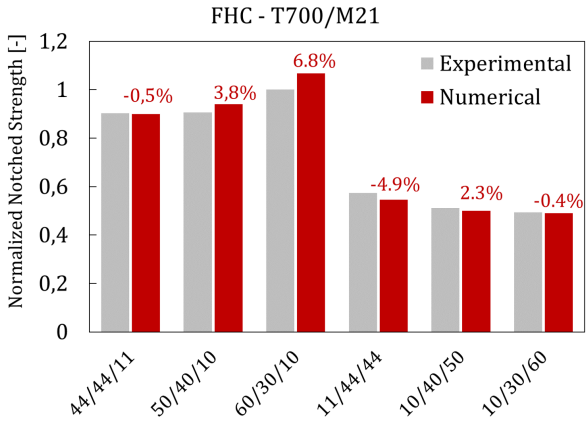

Figure 3.29: Comparison between the numerical and experimental results for the filled-hole compressive strength of six T700/M21 carbon/epoxy laminates.

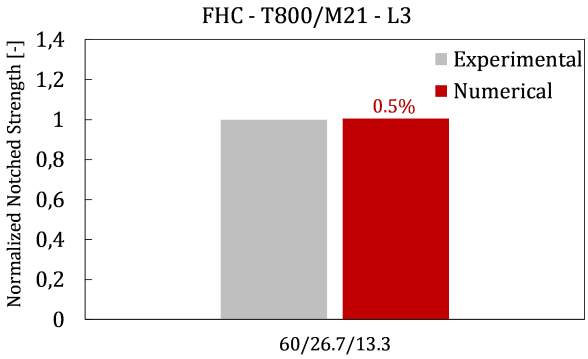

Figure 3.30: Comparison between the numerical and experimental results for the filled-hole compressive strength of one T800/M21 carbon/epoxy laminate.

3.3 Concluding remarks

A methodology to simulate fracture of composite laminates at the coupon level based on modifications of the continuum damage model proposed by Maimí et al. [47–49] and of the cohesive zone models based on the work of Turon et al. [195] and Alfano et al. [196] was proposed. The continuum damage model proposed by Maimí et al. [47–49] was enriched with a bilinear softening law for longitudinal compression more suitable to represent kinking failure, based on the experimental findings by Moran et al. [200]. Additionally, a damage activation function for longitudinal compression that accounts for the effect of though-thickness stresses based on the 3D failure criteria proposed by Camanho et al. [11] and engineering solutions to account for the effect of pressure on the longitudinal compression and in-plane shear fracture toughness were proposed. A frictional cohesive model is proposed in this work to more accurately represent delamination propagation and load carrying capability in test cases where the effect of through-thickness pressure cannot be neglected.

The methodology was thoroughly validated for various material systems and coupons with increasing level of complexity: from unnotched tension and compression, open-hole tension and compression and filled-hole compression of both soft and hard laminates. A good agreement was found between the predictions and the experimental ultimate strengths for all the test cases, oftentimes within standard error of the tests, with maximum relative error of 13%.

It is worth noting that the models developed follow the requirements typically used by the aeronautical industry, in terms of element size and mesh structure. Additionally, all the predictions were obtained using a common set of material properties and material models. These facts indicate that the work presented here is a step towards the simulation of failure of composite structures using a standard modelling strategy. Hence, this work serves as basis for modelling more complex geometries and can potentially be used for the generation of statistically-based design allowables for the most simple test cases when allied with powerful statistical tools.

Chapter 4

Analytical framework to predict the notched strength of composite laminates

Structural components are typically designed taking into account the effects of stress concentrations, which result from several sources, such as pre-defined geometrical discontinuities or discrete through-penetration in-service damage. The replacement of metallic materials by new generations of polymer composite materials in such applications is therefore partially dependent on the availability of accurate and fast strength prediction methods for the design of composite structures with stress concentrations.

Advanced Finite Element (FE) models normally result in long computing times that are not acceptable for preliminary sizing and optimization of structural details. Alternative analysis methods that mitigate the difficulties of using nonlinear FE models at the cost of using laminate-based empirical parameters have been proposed [68, 69, 230]. The most widely used analytical models use empirical "*characteristic distances*" determined from notched strength data. To eliminate the need for non-physical calibration parameters, analytical strength prediction methods should be based on independently measured material properties. To this end, Finite Fracture Mechanics (FFMs) [231, 232] provides a sound physical basis to predict the failure stress of notched structures [13, 70, 233, 234].

Camanho et al. [70] proposed a coupled FFMs model to predict the notched strength of open-hole laminate specimens. The model assumes that crack propagation results from the simultaneous fulfilment of a stress-based criterion and an energy-based criterion. The criterion can be written as a system of two equations with two unknowns: the remote notched strength $\bar{\sigma}^{\infty}$ and the crack extension at failure l. To solve it, only two independent material properties are required: the laminate unnotched strength, X^L, and the laminate mode I fracture toughness, $\mathcal{K}_{Ic}$. In this model and unlike other analytical models [68, 69] does not require the determination of a "*characteristic distance*" from a baseline specimen.

However these properties still need to be experimentally determined every time the lay-up of the laminate changes, making preliminary design and optimization of composite structures still too costly in terms of testing requirements. It is therefore clear that a method that takes the laminate layers as the basic building blocks and uses the orthotropic material properties related to the directions of the fibres is highly desirable. The ply properties, determined from characterization tests at the lamina level or from micro-mechanical models based on adequate homogenization techniques, can be used to feed appropriate models to predict the mechanical response of the whole laminate and to determine the required laminate properties.

One possibility is to rely on virtual tests based on advanced numerical models to predict the laminate strength and fracture toughness. By explicitly representing each ply in the FE model, it is straightforward to change the lay-up and stacking sequence, and to obtain predictions for any laminate. Nevertheless, these computations can still take too long, becoming unsuitable for the preliminary design stages at which material and lay-up screening take place. Relying instead in simple analytical solutions that are able to predict laminate properties based on the minimum number of ply properties is therefore the most attractive approach.

To predict the laminate elastic properties, Laminated Plate Theory (LPT) [15] is generally employed. The elastic properties of any given laminate can be easily obtained from the orthotropic material properties of the base unidirectional (UD) composite system. Hence, for material screening, the elastic properties of all composite systems considered in the screening process must be characterized, resulting in at least three independent characterization tests for each material: a longitudinal tensile test to determine the longitudinal Young's modulus (E_1), a transverse tensile test to determine the transverse Young's modulus (E_2) and the Poisson's ratio (ν_{12}), and a shear test to determine the shear modulus (G_{12}).

To predict the laminate strength, last-ply-failure (LPF) analyses [15] can be performed using appropriate failure criteria and empirical degradation factors. This is generally regarded as an effective approach, mostly due to its simplicity, as complex progressive degradation schemes and damage formulations suitable for implementation in the Finite Element Method can be avoided. These failure criteria, either stress- or strain-based, generally require at least the knowledge of the ply strengths (or strains-to-failure) related to longitudinal tension (X_T), longitudinal compression (X_C), transverse tension (Y_T), transverse compression (Y_C) and in-plane shear (S_L), which means that at least five independent characterization tests must be performed for each material system.

For the prediction of the $\mathcal{R}$-curve or fracture toughness of laminates, no established method is currently available. However, the measurement of the fracture toughness is required by the FFMs model for every lay-up considered in the design process. For instance, to predict the strength of notched composite structures subjected to multi-axial loading where cracks can propagate at different angular positions, the $\mathcal{R}$-curve (or the fracture toughness) of the laminate needs to be measured for different lay-ups; this is a clear drawback, as it represents a large experimental program that can be avoided if the $\mathcal{R}$-curve of the laminate can be predicted using the $\mathcal{R}$-curve of the ply. To overcome this difficulty, Camanho et al. [235] defined and validated a simple analytical closed-form solution based on fracture mechanics and LPT to estimate the value of the mode I fracture toughness of balanced multidirectional laminates from the fracture toughness of the 0° plies and from the ply elastic properties. According to Camanho and Catalanotti [235], the model predictions are sufficiently accurate, especially considering its simplicity and ease of use, making it particularly suited for the early stages of material selection and lay-up optimization. It is important to note, though, that since the model is based on Linear-Elastic Fracture Mechanics (LEFM), it should not be used in material systems or lay-ups that promote severe plastic deformation before crack propagation or large delaminations at the vicinity of the notch.

The combination of LPT, reliable failure criteria and a model based on fracture mechanics to predict the fracture toughness of multidirectional laminates provides a

fast-analysis framework for preliminary sizing and optimization of composite structures based solely on material properties determined at the ply level. Nevertheless, the number of independent experimental tests needed to characterize each material system is still generally high. The objective of this chapter is to use the available analytical solutions (Section 4.1.1) as the building-blocks of a new analytical framework that is capable of predicting the notched response of carbon fibre-reinforced polymers (CFRPs) and the associated size effect using the minimum number of ply properties, reducing substantially the testing requirements and their associated costs.

To this end, an analytical framework to prediction of size effects in notched laminates using only the Young's modulus, the strength, and the $\mathcal{R}$-curve of the 0° ply is proposed in Section 4.1. For the prediction of the laminate elastic properties, the classical LPT will be replaced by an invariant-based approach to stiffness [236] that relies on the recently proposed Trace theory and Master Ply concept (Section 4.1.1.1). To simplify the laminate strength prediction, the concept of Omni Strain Failure Envelopes [236] and the Unit Circle failure criterion [16] are included, which provide an invariant-based approach to strength that greatly simplifies the macro-mechanical failure analyses of homogenized laminates (Section 4.1.1.2). Finally, a model based on fracture mechanics [235] is used to predict the $\mathcal{R}$-curve of the laminate (or its fracture toughness) from that of the 0° plies (Section 4.1.1.3). The laminate plain strength and the $\mathcal{R}$-curve can then be used with a coupled FFMs model to predict notch size effects in laminates with open holes (Section 4.1.2). The predictions for quasi-isotropic laminates of different carbon/epoxy systems are compared to experimental results from the literature (Section 4.1.3).

To account for the variability of the material properties that dominate failure and the effect of geometrical imperfections, an Uncertainty Quantification and Management (UQ&M) methodology to predict the B-value of notched composite laminates based on the analytical framework proposed in Section 4.1 is proposed (Section 4.2). The proposed Uncertainty Quantification and Management (UQ&M) methodology is validated against available experimental data and is applied to generate practical engineering design tools.

4.1 Prediction of size effects in open-hole laminates using only the Young's modulus, the strength, and the $\mathcal{R}$-curve of the 0° ply

4.1.1 Calculation of laminate properties

4.1.1.1 Trace theory and Master Ply concept

Tsai and Melo [236] recently proposed an invariant-based approach to describe the elastic properties of composite plies and laminates based on trace-normalized stiffness parameters.

The invariant-based approach proposed by Tsai and Melo [236] relies on the normalization of the stiffness components using the trace of the plane stress stiffness matrix, which is invariant with respect to the stacking sequence:

$$\mathrm{Tr}(\mathbf{Q}) = \mathrm{Tr}(\mathbf{A}) = \mathrm{Tr}(\mathbf{D}) \tag{4.1}$$

where Tr(•) stands for the trace of •. **Q** is the plane stress stiffness matrix in the material coordinate system:

$$\mathbf{Q} = \begin{bmatrix} Q_{11} & Q_{12} & 0 \\ Q_{21} & Q_{22} & 0 \\ 0 & 0 & 2Q_{66} \end{bmatrix} = \begin{bmatrix} \frac{E_1}{1-\nu_{12}\nu_{21}} & \frac{\nu_{12}E_2}{1-\nu_{12}\nu_{21}} & 0 \\ \frac{\nu_{21}E_1}{1-\nu_{12}\nu_{21}} & \frac{E_2}{1-\nu_{12}\nu_{21}} & 0 \\ 0 & 0 & 2G_{12} \end{bmatrix} \tag{4.2}$$

where E_1 and E_2 are the longitudinal and transverse Young's moduli, G_{12} is the shear modulus and ν_{12} and ν_{21} are the major and minor Poisson's coefficients, where:

$$\nu_{21} = \nu_{12}\frac{E_2}{E_1} \tag{4.3}$$

and **A** and **D** are the normalized in-plane and flexural laminate stiffness matrices of the laminate:

$$\mathbf{A} = \frac{1}{h}\int_{-h/2}^{h/2} [\overline{\mathbf{Q}}]^{(k)}\,\mathrm{d}z; \quad \mathbf{D} = \frac{12}{h^3}\int_{-h/2}^{h/2} [\overline{\mathbf{Q}}]^{(k)} z^2\,\mathrm{d}z \tag{4.4}$$

where $\overline{\mathbf{Q}}$ is the plane stress stiffness matrix in the laminate coordinate system and h is the laminate thickness. Tsai and Melo [236] observed that the stiffness components normalized by trace:

$$Q_{11}^* = \frac{Q_{11}}{\mathrm{Tr}(\mathbf{Q})}; \quad Q_{22}^* = \frac{Q_{22}}{\mathrm{Tr}(\mathbf{Q})}; \quad Q_{12}^* = \frac{Q_{12}}{\mathrm{Tr}(\mathbf{Q})}; \quad Q_{66}^* = \frac{Q_{66}}{\mathrm{Tr}(\mathbf{Q})} \tag{4.5}$$

of several CFRP systems (Tsai and Melo [236] analysed 10 in total) are approximately the same. This is particularly true for the Q_{11}^*, where a coefficient of variation around 1.5% for all 10 CFRP systems was reported. Based on these observations, Tsai and Melo [236] defined a **Master Ply** for CFRPs using the median values of the trace-normalized stiffness properties (Table 4.1):

$$E_1^* = \frac{E_1}{\mathrm{Tr}(\mathbf{Q})}; \quad E_2^* = \frac{E_2}{\mathrm{Tr}(\mathbf{Q})}; \quad G_{12}^* = \frac{G_{12}}{\mathrm{Tr}(\mathbf{Q})}; \quad \nu_{12} \tag{4.6}$$

Using the Master Ply E_1^*, E_2^*, G_{12}^* and ν_{12} (Table 4.1), the trace-normalized laminate engineering constants E_x^*, E_y^*, G_{xy}^* and ν_{xy} or laminate factors:

$$E_x^* = \frac{E_x}{\mathrm{Tr}(\mathbf{A})}; \quad E_y^* = \frac{E_y}{\mathrm{Tr}(\mathbf{A})}; \quad G_{xy}^* = \frac{G_{xy}}{\mathrm{Tr}(\mathbf{A})}; \quad \nu_{xy} \tag{4.7}$$

where $\mathrm{Tr}(\mathbf{A}) = \mathrm{Tr}(\mathbf{Q})$, can be determined for virtually any laminate using the Classical Laminated Plate Theory. Table 4.1 shows the Master Ply proposed by Tsai and Melo [15] and examples of laminate factors for several lay-ups. This concept allows the determination of the elastic properties E_x, E_y, G_{xy} and ν_{xy} of virtually any CFRP laminate using the laminate factors E_x^*, E_y^*, G_{xy}^* and ν_{xy} obtained from the Master Ply and Classical Laminated Plate Theory (e.g. Table 4.1), and one independent elastic property only: the trace $\mathrm{Tr}(\mathbf{A}) = \mathrm{Tr}(\mathbf{Q})$ of the plane stress stiffness matrix of the CFRP:

$$E_x = E_x^* \cdot \dot{\mathrm{Tr}}(\mathbf{A}); \quad E_y = E_y^* \cdot \mathrm{Tr}(\mathbf{A}); \quad G_{xy} = G_{xy}^* \cdot \mathrm{Tr}(\mathbf{A}); \quad \nu_{xy} \tag{4.8}$$

To determine the value of trace ($\mathrm{Tr}(\mathbf{A}) = \mathrm{Tr}(\mathbf{Q})$), the plane stress stiffness matrices does not need to be determined. Instead, it is sufficient to know the longitudinal Young's modulus of a 0° unidirectional laminate, E_1, or the longitudinal Young's modulus of a multidirectional laminate, E_x, and to divide it by the corresponding trace-normalized laminate factor, E_1^* or E_x^* (e.g. Table 4.1), whose coefficients of variation are within 4% for CFRPs:

$$\mathrm{Tr}(\mathbf{Q}) = \frac{E_1}{E_1^*} = \frac{E_1}{0.88}; \quad \text{Master} \quad \text{Ply} \tag{4.9}$$

$$\mathrm{Tr}(\mathbf{Q}) = \mathrm{Tr}(\mathbf{A}) = \frac{E_x}{E_x^*}; \quad \text{laminate} \quad \text{factor} \tag{4.10}$$

Table 4.1: Examples of universal laminate factors obtained from the Master Ply using LPT (after Tsai and Melo [15]).

Master Ply	$E_1^* = E_1/\mathrm{Tr}$	$E_2^* = E_2/\mathrm{Tr}$	$G_{12}^* = G_{12}/\mathrm{Tr}$	ν_{12}
[0]	0.880	0.052	0.031	0.320
Laminate factors	$E_x^* = E_x/\mathrm{Tr}$	$E_y^* = E_y/\mathrm{Tr}$	$G_{xy}^* = G_{xy}/\mathrm{Tr}$	ν_{xy}
[0/90]	0.468	0.468	0.031	0.036
[0/ ± 45/90]	0.336	0.336	0.129	0.308
[0_7/ ± 45/90]	0.662	0.175	0.070	0.310
[0_5/ ± 45_2/90]	0.518	0.208	0.109	0.423
[0_2/ ± 45/90]	0.445	0.289	0.109	0.308
[0/ ± 45_4/90]	0.217	0.217	0.187	0.552
[0/ ± 45]	0.370	0.155	0.161	0.734
[0/ ± 45/0]	0.499	0.141	0.129	0.701
[0/ ± 30]	0.510	0.074	0.129	1.220
[0/ ± 30/0]	0.611	0.072	0.104	1.079
[±12.5]	0.764	0.053	0.066	0.913

Recently Arteiro et al. [237] clearly defined the range of applicability of the Trace Theory and Master Ply concept. The authors used the Rule of Mixtures and the Halpin-Tsai models to establish the relations between the fibre volume fraction, the fibre/matrix stiffness ratios, and the trace-normalized engineering constants of unidirectional laminae and multidirectional laminates. It was concluded that, for sufficiently high longitudinal fibre/matrix stiffness ratios and for fibre volume fractions between 50% and 70%, typical of advanced CFRPs laminates, the variation of the trace-normalized longitudinal Young's modulus is within 6% for unidirectional laminae and within 1% for multidirectional laminates, thus, supporting their use for typical of aerospace-grade CFRPs.

Whereas LPT requires the knowledge of four ply elastic properties (E_1, E_2, G_{12} and ν_{12}), which need to be measured from different tests (including the complex in-plane shear test), the elastic properties of multidirectional laminates predicted using the trace can be obtained from the universal laminate factors (Table 4.1) and from the value of trace (Table 4.2), calculated from the longitudinal stiffness of the UD lamina (E_1) using the Master Ply concept. Characterization of the elastic properties of composite laminates using the trace requires just one test on a 0° coupon, simplifying considerably the number and complexity of the tests needed to be performed, for instance, in material scrutiny programs. It should be noted, though, that the calculations based on the trace are approximate. This means, for example, that, for quasi-isotropic laminates, plane isotropy is not strictly met

(i.e. G_{xy} is not exactly equal to $E_x/(2(1+\nu_{xy}))$), contrary to the predictions obtained with LPT. Nevertheless, the approximation is fairly reasonable — taking the quasi-isotropic universal laminate factors $E_x/\mathrm{Tr} = 0.336$ and $\nu_{xy} = 0.320$ results in $G_{xy}/\mathrm{Tr} = 0.128$ (≈ 0.129 in Table 4.1).

Table 4.2: Ply elastic properties and value of trace for different carbon/epoxy systems.

Material system	E_1 (MPa)	E_2 (MPa)	G_{12} (MPa)	ν_{12} (-)	Trace (MPa)
IM7/8552 [193]	171420	9080	5290	0.320	194795
T800/M21 [219]	172000	8900	5000	0.320	195455
T700/AR2527 [18]	110000	7400	4200	0.300	125000
M40JB/ThinPreg 80EP/CF [1]	222000	7010	4661	0.314	252273
T700/M21 [218]	130000	8300	4500	0.320	147727

To assess the accuracy of the Trace theory (schematically shown in Fig. 4.1), Table 4.3 compares the predictions obtained with the trace and LPT for quasi-isotropic laminates of different carbon/epoxy systems previously tested [1, 18, 193, 218, 219] (Table 4.2). It can be observed that the correlation between the predictions from the Trace theory and from LPT is remarkable. These results justify the use of the Trace theory for the prediction of the elastic properties of general laminates.

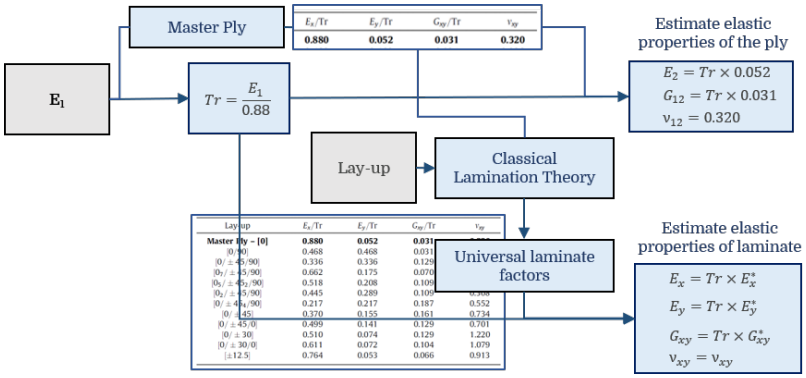

Figure 4.1: Schematic representation of the Trace theory.

4.1.1.2 Unit Circle failure criterion

Tsai and Melo [236] proposed an invariant-based approach to failure, with the aim of defining a strength property independent of laminate lay-up composition. Using a failure criterion based on a tensor polynomial defined in strain space, Tsai and Melo [236] defined an **Omni Strain Failure Envelope** for a laminate with many ply orientations by selecting the controlling ply in each orientation of the strain space.

It is noted that, in this case, the use of strain space for the representation of failure envelopes is preferred over stress space because in strain space failure envelopes are invariant [236], i.e. their shapes are independent of the presence of other plies. Superimposing the envelopes of the constituent plies forms the failure envelope for a given laminate. Hence, an inner envelope that covers all controlling plies, or Omni Strain Failure Envelope, essentially defines a material property that is

Table 4.3: Predictions of the elastic properties of quasi-isotropic laminates of different carbon/epoxy systems using LPT and the Trace theory, and relative errors (ϵ_r).

Elastic properties		IM7/8552			T800/M21		
		LPT	Trace	ϵ_r (%)	LPT	Trace	ϵ_r (%)
E_x	(MPa)	64513	65451	1.5	64401	65673	2.0
E_y	(MPa)	64513	65451	1.5	64401	65673	2.0
G_{xy}	(MPa)	24600	25129	2.1	24517	25214	2.8
ν_{xy}	(-)	0.311	0.308	−1.0	0.313	0.308	−1.7
		T700/AR2527			M40JB/ThinPreg 80EP/CF		
		LPT	Trace	ϵ_r (%)	LPT	Trace	ϵ_r (%)
E_x	(MPa)	42572	42000	−1.3	80197	84764	5.7
E_y	(MPa)	42572	42000	−1.3	80197	84764	5.7
G_{xy}	(MPa)	16306	16125	−1.1	30494	32543	6.7
ν_{xy}	(-)	0.305	0.308	0.8	0.315	0.308	−2.2
		T700/M21					
		LPT	Trace	ϵ_r (%)			
E_x	(MPa)	49782	49636	−0.3			
E_y	(MPa)	49782	49636	−0.3			
G_{xy}	(MPa)	18983	19057	0.4			
ν_{xy}	(-)	0.311	0.308	−1.0			

independent of laminate lay-up configuration, representing any laminate constructed from a given material [236]. Even though this is a conservative approach, it greatly simplifies laminate failure prediction by avoiding ply-by-ply failure analysis.

The Omni Strain Failure Envelope for a given composite material is determined from the ply elastic (E_1, E_2, G_{12} and ν_{12}) and strength properties (X_T, X_C, Y_T, Y_C and S_L) [236]. Omni Strain Failure Envelopes can be generated not only from first-ply-failure (FPF) analysis [236], using intact ply properties, but also from LPF analysis [15, 16], using degraded ply properties (e.g. Fig. 4.2)[1].

Interestingly, Tsai and Melo [16] found that the LPF Omni Strain Failure Envelopes of CFRPs are invariably controlled by the longitudinal failure of the 0° and 90° plies (e.g. Fig. 4.2). Because the analysis is conducted for LPF conditions, it is assumed that the matrix is already degraded, and, therefore, ultimate failure is governed by fibre-dominated longitudinal failure.

To make laminate failure analysis simpler, the LPF Omni Strain Failure Envelope can be approximated by a **Unit Circle** in the **normalized principal strain space** using the uniaxial tensile and compressive strains-to-failure (ε_{1T} and ε_{1C} respectively) as normalising factors (Fig. 4.3) [16]. The tensile and compressive strains-to-failure define the anchor points in the axes of the principal strain space (see Fig. 4.3).

The Unit Circle failure envelope is inscribed in the LPF Omni Strain Failure Envelope [16], resulting in a more conservative approach. However, whereas Omni Strain Failure Envelopes require complete ply characterization, the Unit Circle fail-

[1]Following Tsai and Melo [15], LPF analysis is performed applying a constant matrix degradation factor (E_m^*) used (i) to degrade the matrix Young's modulus (E_m) of the corresponding CFRP system, which is then used to determine the loss of transverse and shear moduli (E_2 and G_{12} respectively) of the composite using the micro-mechanical approach presented e.g. by Tsai and Melo [15], and (ii) to reduce the Poisson's ratio (ν_{12}) and the interaction term in the Tsai-Wu failure criterion (F_{12}^*). In addition, an exponent degradation factor (n) is used to degrade the longitudinal compressive strength due to the loss of shear modulus. All the other ply elastic and strength properties remain intact.

ure envelope can be uniquely defined from the longitudinal tensile and compressive strains-to-failure of a UD ply. Because LPF is assumed fibre-dominated, Unit Circle failure envelopes can be generated without relying on the strengths associated with matrix-dominated failure modes. Hence, ply characterization can be reduced from several tests on different lamina configurations to just two tests of a 0° coupon: longitudinal tension and longitudinal compression. The potential gains in terms of test complexity, time and cost reductions are remarkable.

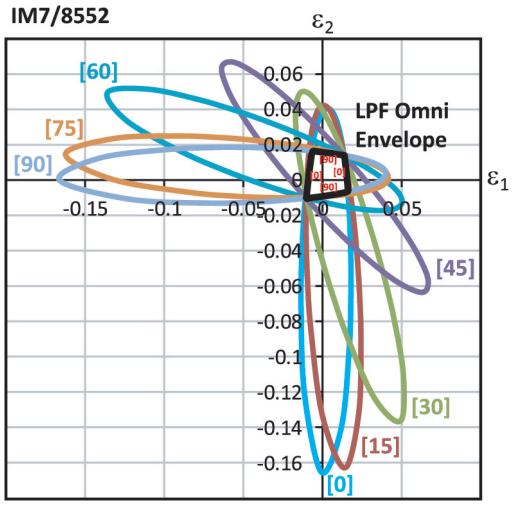

Figure 4.2: LPF (degraded) Omni Strain Failure Envelope for IM7/8552 CFRP, obtained using the Tsai-Wu failure criterion (interaction term $F_{12}^{*} = -1/2$) in strain space (after Tsai and Melo [15, 16]). In the LPF analysis, property degradation was only applied to the matrix-dominated elastic properties (E_2, G_{12} and ν_{12}), to the interaction term (F_{12}^{*}), and to the longitudinal compressive strength (X_C), using a matrix degradation factor $E_m^{*} = 0.15$ and an exponent degradation factor for the longitudinal compressive strength $n = 0.1$.

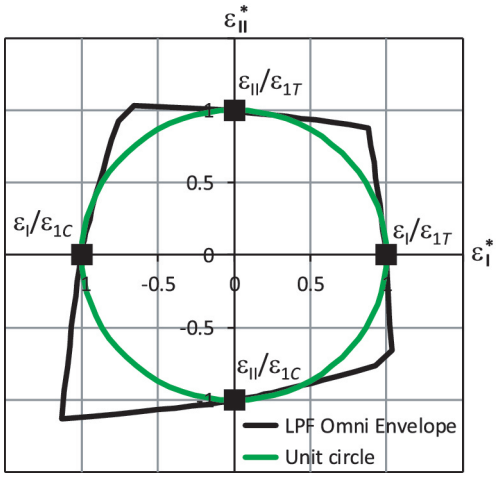

Figure 4.3: LPF Omni Strain Failure Envelope for IM7/8552 CFRP and Unit Circle failure criterion in normalized principal strain space (after Tsai and Melo [16]).

Table 4.4 shows a comparison between the failure predictions (X_T^L and X_C^L) obtained with the Unit Circle failure criterion and the experimental results reported in the literature for quasi-isotropic laminates of different carbon/epoxy systems. To

generate these predictions, only the stiffness (E_1) and the tensile and compressive strengths (X_T and X_C respectively) of the 0° lamina were used (Tables 4.2 and 4.4 respectively). The failure stresses predictions read:

$$X_T^L = \frac{X_T}{E_1} E_x \tag{4.11a}$$

$$X_C^L = \frac{X_C}{E_1} E_x \tag{4.11b}$$

where E_x is estimated using the Master ply concept and Trace theory (Section 4.1.1.1).

Table 4.4: Longitudinal ply strengths and failure predictions for quasi-isotropic laminates of different carbon/epoxy systems obtained using the Unit Circle failure criterion, and comparison with experimental results from the literature. The relative errors (ϵ_r) between predictions and experiments are also shown.

Material system	0° ply strengths (MPa)	Laminate strengths (MPa)		
		Experiments	Unit Circle	ϵ_r (%)
IM7/8552 [12, 14, 193]				
Tension	2326	845	888	5.1
Compression	1200	533	458	−14.0
T800/M21 [13, 219]				
Tension	3039	1054	1160	10.1
Compression	1669	539	637	18.3
T700/AR2527 [18]				
Tension	2300	800	878	9.7
Compression	1500	540	573	6.0
M40JB/ThinPreg 80EP/CF [1]				
Tension	2250	847	859	1.4
Compression	1052	-	402	-
T700/M21 [19, 218]				
Tension	2000	799	764	−4.4
Compression	1300	-	496	-

In general, the failure predictions are reasonably accurate. In particular, it is interesting to note that the best predictions are obtained for laminates with thinner plies (e.g. for M40JB/ThinPreg 80EP/CF, with 20 sublaminate repetitions and a ply thickness of 0.03 mm [1], the relative error is below 2%). In fact, it is important to stress that this type of analytical macro-mechanical tools, not only the Unit Circle failure criterion but also the model based on fracture mechanics used to predict the fracture toughness of balanced laminates from the fracture toughness of the 0° ply (Section 4.1.1.3), cannot distinguish between different stacking sequences (since they are valid at the homogenized laminate level), and do not account for the development of severe subcritical damage mechanisms (e.g. delamination) before ultimate failure. When a laminate is composed by very thin plies, dispersed by sublaminate repetitions, the development of subcritical damage mechanisms is very limited due to a more homogeneous through-the-thickness stress distribution. The failure conditions of these laminates are therefore closer to the fundamental assumptions of the analytical macro-mechanical models formulated at the homogenized laminate level, resulting in more accurate failure predictions.

4.1.1.3 Relation between the mode I fracture toughness of a composite laminate and that of a 0° ply

Camanho et al. [235] proposed an analytical model based on a combination of LEFM and LPT to predict the fracture toughness of balanced multidirectional laminates, $\mathcal{G}_{Ic}$, using the fracture toughness of the 0° ply, $\mathcal{G}^0_{Ic}$. The model considers a symmetric, balanced multidirectional laminate containing a crack (of generic length a) and subjected to a remote stress σ^∞ in the x-direction. For a given laminate, the ratio between the mean remote failure stress of a group of plies that represent the balanced sub-laminate (i) and the remote failure stress of the a sub-laminate composed of 0° plies [238] can be calculated from LPT using the elastic ply properties and the information about the lay-up of the laminate as:

$$\Omega_0^{(i)} = \frac{\bar{\sigma}^{(i)}}{\bar{\sigma}^0} \tag{4.12}$$

$\bar{\sigma}^{(i)}$ and $\bar{\sigma}^{(0)}$ can also be obtained from LEFM:

$$\bar{\sigma}^{(i)} = \frac{\mathcal{K}_{Ic}^{(i)}}{\chi^{(i)} Y \sqrt{\pi a}} \tag{4.13}$$

and

$$\bar{\sigma}^{(0)} = \frac{\mathcal{K}_{Ic}^{(0)}}{\chi^{(0)} Y \sqrt{\pi a}} \tag{4.14}$$

where $\mathcal{K}_{Ic}^{(i)}$ and $\mathcal{K}_{Ic}^{(0)}$ are the fracture toughness of the sub-laminate (i) and of the 0° plies. χ accounts for the laminate's orthotropy [239]

$$\chi^{(i)} = 1 + 0.1(\rho^{(i)} - 1) - 0.016(\rho^{(i)} - 1)^2 + 0.002(\rho^{(i)} - 1)^3 \tag{4.15}$$

and $\rho^{(i)}$ is given by

$$\rho^{(i)} = \frac{\left(E_x^{(i)} E_y^{(i)}\right)^{1/2}}{2G_{xy}^{(i)}} - (\nu_{xy}^{(i)} \nu_{yx}^{(i)})^{1/2} \tag{4.16}$$

$E_x^{(i)}$ and $E_y^{(i)}$ are the sublaminate's Young's Modulus in the orthotropy axes (x being is the loading direction), $G_{xy}^{(i)}$ is the sublaminate shear modulus in the orthotropy axes and $\nu_{xy}^{(i)}$ and $\nu_{yx}^{(i)}$ are the corresponding Poisson's ratios. Combining Eqs. (4.12), (4.13) and (4.14), the fracture toughness of sub-laminate (i) yields:

$$\mathcal{K}_{Ic}^{(i)} = \frac{\chi^{(i)} \Omega_0^{(i)}}{\chi^0} \mathcal{K}_{Ic}^0 \tag{4.17}$$

Assuming a self-similar crack propagation along all plies, the laminate's fracture toughness $\mathcal{K}_{Ic}^L$ is calculated as [235]

$$\mathcal{K}_{Ic}^L = \frac{\sum_{(i)}^N \mathcal{K}_{Ic}^{(i)} t^{(i)}}{t^L}, (i) \neq 90° \tag{4.18}$$

where t^L is the thickness of the laminate, $t^{(i)}$ it the thickness of the sub-laminate (i) and N is the number of sub-laminates considered. As explained by Camanho and Catalanotti [235], for the 90° plies, which do not have fibre fracture, but only

transverse cracking, the actual value of the fracture toughness of these plies should be used in Eq. 4.18; alternatively, the fracture toughness of the 90° plies can be neglected, since its value is several orders of magnitude lower than the fracture toughness of the 0° plies.

The fracture toughness of the balanced laminate can also be represented by the energy dissipated per unit area, $\mathcal{G}_{Ic}$, as:

$$\mathcal{G}_{Ic} = \frac{\left(\mathcal{K}_{Ic}^{L}\right)^2}{\acute{E}} \tag{4.19}$$

where the equivalent modulus of the laminate $\acute{E}$ is given as:

$$\acute{E} = \left(\frac{1+\rho}{2E_xE_y}\right)^{-1/2}\left(\frac{E_y}{E_x}\right)^{-1/4} \tag{4.20}$$

As can be observed from the derivation, this analytical model predicts the fracture toughness of a general fibre-dominated laminate using only the ply elastic properties and the fracture toughness of the 0° plies.

Camanho et al. [235] validated the proposed analytical model based on experiments carried out by the authors and on experimental results available in the literature. They observed that the model accurately predicts the fracture toughness of multidirectional laminates with different lay-ups using only the fracture toughness of the 0° plies and the ply elastic properties, with the largest errors occurring only for laminates that failed by a combination of fibre failure of the 0° sublaminates and delamination of the off-axis sublaminates (including complete separation of the off-axis plies) [235].

As a result, this model is considered appropriate to calculate the fracture toughness of general laminates whose failure is not controlled by delamination.

4.1.2 Finite Fracture Mechanics model

Following Ref. [70], a coupled stress and energy FFMs criterion is used in the present model to predict fracture of notched laminated plates with an uncracked central circular hole. To take the $\mathcal{R}$-curve of the laminate into account, an alternative representation of the energy equilibrium was proposed [20]. In particular, Arteiro et al. [20] showed that, by taking into account the bridging effects represented by the $\mathcal{R}$-curve in the formulation of the fracture problem, significant improvements in the predictions of the notched response of composite laminates for a wide notch size range can be obtained without requiring fitting parameters or complex FE analyses.

For a laminated plate with a central circular hole subjected to a remote stress parallel to the x-axis (Fig. 4.4), the coupled stress and energy FFMs criterion can be written as:

$$\begin{cases} \frac{1}{l}\int_{R}^{R+l} \sigma_{xx}(0,y)\,dx = X^L \\ \int_{R}^{R+l} \mathcal{G}_I(a)\,da = \int_{0}^{l} \mathcal{R}(\Delta a)\,d\Delta a \end{cases} \tag{4.21}$$

where R is the radius of the hole, l is the crack length at failure, $\sigma_{xx}(0,y)$ is the stress distribution along the ligament section perpendicular to the loading direction (along the y-axis) [240], X^L is the laminate unnotched strength, $\mathcal{G}_I(a)$ is the mode

I Energy Release Rate (ERR) of a laminated plate with a central circular hole of radius R and two symmetric cracks emanating from the hole edge (Fig. 4.4), and $\mathcal{R}(\Delta a)$ is the $\mathcal{R}$-curve, expressed in terms of the critical energy release rate.

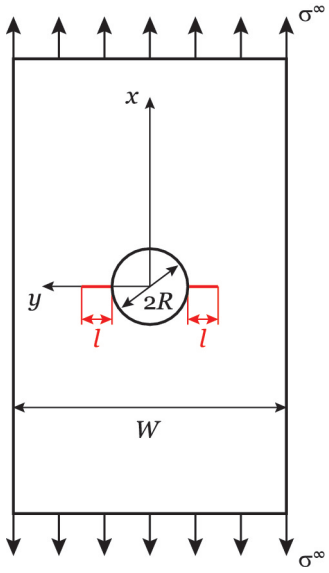

Figure 4.4: Notched plate with central circular hole.

The stress distribution along the ligament section perpendicular to the loading direction (along the y-axis, see Fig. 4.4), $\sigma_{xx}(0,y)$, can be obtained as [240]:

$$\sigma_{xx}(0,y) = \frac{K_T}{K_T^\infty}\frac{\bar{\sigma}^\infty}{2}\left[2+\left(\frac{R}{y}\right)^2+3\left(\frac{R}{y}\right)^4-(K_T^\infty-3)(5\left(\frac{R}{y}\right)^6-7\left(\frac{R}{y}\right)^8)\right] \tag{4.22}$$

where K_T^∞ denotes the stress concentration factor at the edge of the hole of an infinite plate [240]:

$$K_T^\infty = 1+\sqrt{2\left(\sqrt{\frac{E_x}{E_y}}-\nu_{xy}\right)+\frac{E_x}{G_{xy}}} \tag{4.23}$$

and K_T/K_T^∞ is the Finite-Width Correction (FWC) factor [240]:

$$\frac{K_T}{K_T^\infty} = \left\{\frac{3(1-2R/W)}{2+(1-2R/W)^3}+\frac{1}{2}\left(\frac{2R}{W}M\right)^6(K_T^\infty-3)\left[1-\left(\frac{2R}{W}M\right)^2\right]\right\}^{-1} \tag{4.24}$$

In Eq. (4.23), E_x, E_y, G_{xy} and ν_{xy} are the laminate elastic constants (predicted by LPT and Trace theory — Section 4.1.1.1); the parameter M in Eq. (4.24) is calculated as [240]:

$$M^2 = \frac{\sqrt{1-8\left[\frac{3(1-2R/W)}{2+(1-2R/W)^3}-1\right]}-1}{2(2R/W)^2} \tag{4.25}$$

The finite width correlation factor given in Eq. (4.24) is accurate for hole diameter-to-width ratios $2R/W < 0.6$ [240]. For higher hole diameter-to-width ratios, the proposed method is still applicable, but the stress distribution along the

ligament section needs to be estimated using, for example, FE simulations, which would increase the computational time needed to run the proposed framework. Nevertheless, most practical situations fall within the limit $2R/W < 0.6$, which means that the proposed approach is valid for fast computations in most applications.

The mode I ERR, $\mathcal{G}_I(a)$, is calculated as:

$$\mathcal{G}_I(a) = \frac{1}{\acute{E}} \left(\mathcal{K}_I(a)\right)^2 \tag{4.26}$$

where $\mathcal{K}_I(a)$ is the mode I Stress Intensity Factor and $\acute{E}$ is the equivalent modulus of the laminate (Eq. (4.20)). For a plate with a central circular hole of radius R and two symmetric cracks emanating from the hole edge, $\mathcal{K}_I(a)$ is given, for an isotropic plate, as:

$$\mathcal{K}_I(a) = \bar{\sigma}^{\infty} F_h F_w \sqrt{\pi a} \tag{4.27}$$

with

$$F_w = \sqrt{\sec\left(\frac{\pi R}{W}\right) \sec\left(\frac{\pi a}{W}\right)} \tag{4.28}$$

$$F_h = \sqrt{1-\lambda} f_n \tag{4.29}$$

where

$$f_n = 1 + 0.358\lambda + 1.425\lambda^2 - 1.579\lambda^3 + 2.156\lambda^4, \quad \lambda = \frac{R}{a} \tag{4.30}$$

To simplify the implementation of the $\mathcal{R}$-curve in the analytical model, the following equation can be used to fit the $\mathcal{R}$-curve:

$$\mathcal{R}(\Delta a) = \begin{cases} \mathcal{R}_{SS}\left[1 - (1 - \zeta \Delta a)^{\eta}\right] & , \Delta a \leq l_{fpz} \\ \mathcal{R}_{SS} & \Delta a > l_{fpz} \end{cases} \tag{4.31}$$

where $\mathcal{R}_{SS}$ is the steady-state value of the fracture toughness, l_{fpz} is the length of the fracture process zone and ζ and η are two parameters that are obtained fitting Eq. (4.31) to the $\mathcal{R}$-curve.

Using Eqs. (4.22), (4.26), (4.27) and (4.31) in Eq. (4.21), the coupled stress and energy FFMs criterion can be solved for l (crack extension at failure) and for the remote stress at failure, $\bar{\sigma}^{\infty}$.

When the $\mathcal{R}$-curve is not available, the coupled stress and energy FFMs criterion can still be used with a constant value of the fracture toughness, as originally proposed by Camanho et al. [70]. In this case, the energy based criterion in can be written in terms of a critical ERR, $\mathcal{G}_{Ic}$, as:

$$\begin{cases} \frac{1}{l} \int_{R}^{R+l} \sigma_{xx}(0, y)\, dy = X^L \\ \int_{R}^{R+l} \mathcal{G}_I(a)\, da = \mathcal{G}_{Ic} \end{cases} \tag{4.32}$$

The laminate mode I fracture toughness, $\mathcal{G}_{Ic}$, can be obtained from the mode I fracture toughness of the 0° ply, $\mathcal{G}^{\circ}_{Ic}$, as described in Section 4.1.1.3. To measure the mode I fracture toughness of the 0° ply, a centre-cracked specimen, for example, can be used [18, 70]. In this case, Eqs. (4.22), (4.26) and (4.27) can be used in Eq. (4.32) which can then be solved for l and $\bar{\sigma}^{\infty}$.

4.1.3 Model verification

The combination of the models described in Section 4.1.1 provides the framework to predict the laminate elastic, strength and fracture properties required to predict size effects in notched laminates from the minimum number of ply properties. The proposed methodology can be summarized as follows (see also Fig. 4.5):

1. Knowing the **longitudinal Young's modulus of the ply**, E_1, the **Master Ply concept** can be used to determine the **trace** and estimate the **ply elastic properties**. From the **trace**, and using the **universal laminate factors** (e.g. Table 4.1), the **elastic properties** of any **laminate** (or **sublaminate**) can be easily obtained.

2. Knowing the **longitudinal strength of the ply**, X, and using the **elastic properties of the laminate** determined using the Trace theory, the **Unit Circle failure criterion** is applied to predict the **laminate unnotched strength**, X^L.

3. Knowing the $\mathcal{R}$**-curve of the 0° plies**, $\mathcal{R}^0(\Delta a)$, and using the **elastic properties** of the balanced and 0° **sublaminates** determined using the trace, an **analytical model** based on fracture mechanics is employed to predict the **laminate** $\mathcal{R}$**-curve**, $\mathcal{R}(\Delta a)$.

4. The **laminate unnotched strength**, X^L, and the **laminate** $\mathcal{R}$**-curve**, $\mathcal{R}(\Delta a)$, can then be used in the **FFMs model** (Eq. (4.21)) to predict **size effects** in the **notched strength** ($\bar{\sigma}$) of the laminate.

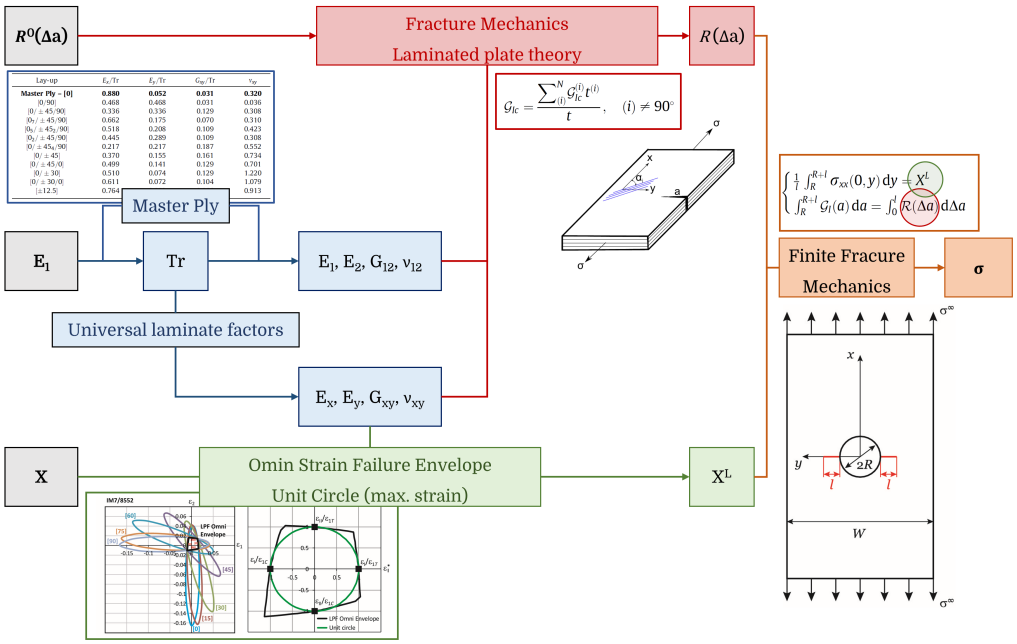

Figure 4.5: Schematic representation of the proposed combined framework to predict size effects from the minimum number of properties determined at the ply level.

This framework was implemented in the commercial software Matlab [241] and Python.

To validate the proposed framework, experimental results available in the literature for the notched strength of multidirectional laminates are compared with the predictions obtained using only **three ply properties**: the **longitudinal Young's modulus of the ply**, E_1 (data shown in Table 4.2), the **longitudinal ply strength**, X (data shown in Table 4.4), and the **$\mathcal{R}$-curve of the 0° plies**, $\mathcal{R}^0(\Delta a)$ (or, when not available, using the **fracture toughness of the the 0° plies**, $\mathcal{G}^0_{Ic}$) - data shown in Table 4.5).

Table 4.5: $\mathcal{R}$-curve (or fracture toughness) of the 0° plies for different carbon/epoxy systems.

Material	$\mathcal{R}$-curve of the 0° plies				$\mathcal{G}^0_{Ic}$ (N/mm)	Ref.
Material system	$\mathcal{R}^0_{ss}$ (N/mm)	l_{fpz} (mm)	γ (mm^{-1})	β (-)		
Tension						
IM7/8552	205	2.63	0.319	3.65	-	Ref. [23]
T800/M21	283	1.14	0.758	3.53	-	Ref. [23]
T700/AR2527	254	1.92	0.423	4.00	-	Ref. [23]
M40JB/ThinPreg 80EP/CF	-	-	-	-	61	Note (1)
T700/M21	-	-	-	-	391	Note (2)
Compression						
IM7/8552	61	1.43	0.513	4.29	-	Ref. [222]
T800/M21	-	-	-	-	37	Note (3)
T700/AR2527	-	-	-	-	43	Note (4)

(1) Back calculated from the fracture toughness of a QI laminate determined from a centre-notched tension test [18].
(2) Back calculated from the fracture toughness of a QI laminate determined from an open-hole tension test [19].
(3) Back calculated from the notched strength of a QI laminate determined from a centre-notched compression test [219].
(4) Back calculated from the notched strength of a QI laminate determined from a centre-notched compression test [24].

4.1.3.1 Open-hole tension

Figs. 4.6 – 4.10 show the comparison between the predictions for the open-hole tensile strengths obtained with the proposed framework, which is illustrated in Fig. 4.5, and the experimental results available in the literature [12, 13, 17–19] for quasi-isotropic laminates of different carbon/epoxy systems. The three ply properties of each carbon/epoxy system used in the predictions — the longitudinal Young's modulus, E_1, the longitudinal tensile strength, X_T, and the $\mathcal{R}$-curve (or fracture toughness) of the 0° plies associated with tensile fibre failure, $\mathcal{R}(\Delta a)$ (or $\mathcal{G}^0_{Ic}$) — are provided in Tables 4.2, 4.4 and 4.5, respectively. It is noted that Eq. (4.21) was used for the strength prediction of the materials whose $\mathcal{R}$-curves are available (IM7/8552, T800/M21 and T700/AR2527). Equation (4.32) was used in the open-hole tensile strength prediction of M40JB/ThinPreg 80EP/CF and T700/M21.

4.1.3.2 Open-hole compression

Figs. 4.11 – 4.13 show the comparison between the predictions for the open-hole compressive strengths obtained with the proposed framework, which is illustrated in Fig. 4.5, and the experimental results available in the literature [13, 14, 18]

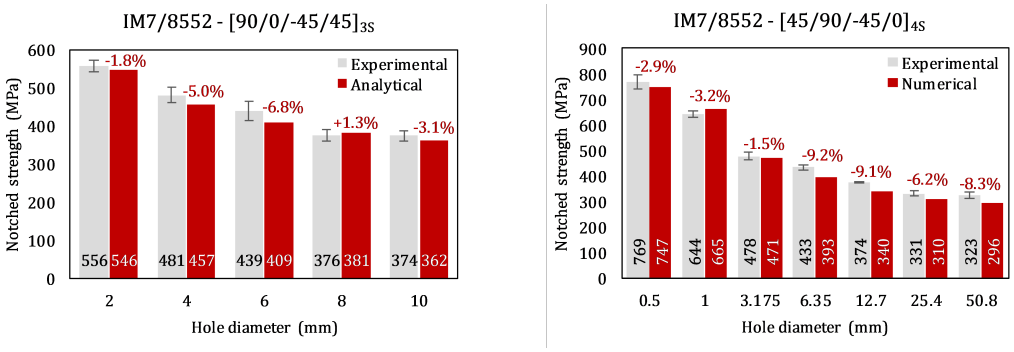

a) b)

Figure 4.6: Comparison between predictions and experimental results for the open-hole tensile strength of different IM7/8552 carbon/epoxy laminates: a) $[90/0/-45/45]_{3S}$ laminate [12]. The hole diameter-to-width ratio is $2R/W = 1/6$. , b) $[45/90/-45/0]_{4S}$ laminate [17]. The hole diameter-to-width ratios are $2R/W = 0.031$ for $2R = 0.5$ mm, $2R/W = 0.062$ for $2R = 1.0$ mm, and $2R/W = 0.2$ for $2R \geq 3.2$ mm.

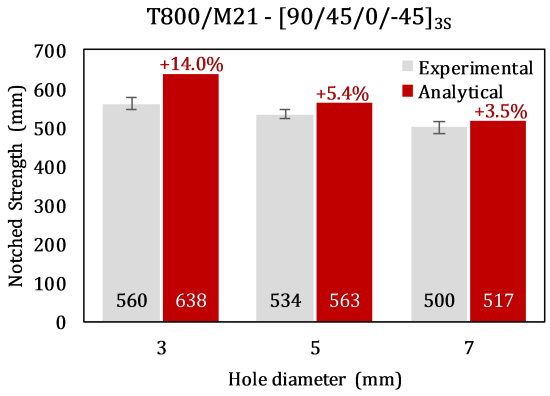

Figure 4.7: Comparison between predictions and experimental results for the open-hole tensile strength of a T800/M21 carbon/epoxy $[90/45/0/-45]_{3S}$ laminate [13]. The hole diameter-to-width ratio is $2R/W = 1/4$.

for quasi-isotropic laminates of different carbon/epoxy systems. The three ply properties of each carbon/epoxy system used in the predictions — the longitudinal Young's modulus, E_1, the longitudinal compressive strength, X_C, and the and the $\mathcal{R}$-curve (or fracture toughness) of the 0° plies associated with the formation of a kink band, $\mathcal{R}(\Delta a)$ (or $\mathcal{G}_{Ic}^0$) — are provided in Tables 4.2, 4.4 and 4.5, respectively. The predictions of open-hole compressive strength were obtained using Eq. (4.32) for and using Eq. (4.21) for IM7/8552.

4.1.3.3 Discussion

The results shown in Figs. 4.6 – 4.13 indicate that, in general, the FFMs model coupled with the invariant-based approaches to stiffness and strength and the analytical model based on fracture mechanics to estimate the laminate fracture toughness provides reasonable predictions for the open-hole tensile and compressive strengths of general carbon/epoxy laminates using only three ply properties (E_1, X_T or X_C, and $\mathcal{R}^0(\Delta a)$ or $\mathcal{G}_{Ic}^0$) and the lay-up as inputs. Typically, relative errors

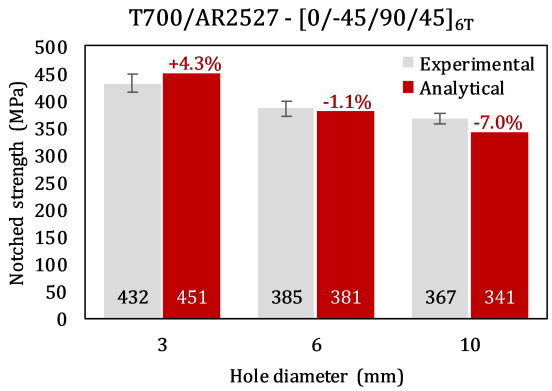

Figure 4.8: Comparison between predictions and experimental results for the open-hole tensile strength of a T700/AR2527 carbon/epoxy $[0/-45/90/45]_{6T}$ laminate [18]. The hole diameter-to-width ratio is $2R/W = 1/4$.

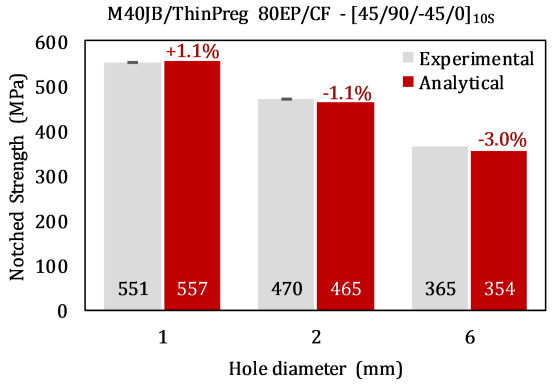

Figure 4.9: Comparison between predictions and experimental results for the open-hole tensile strength of an M40JB/ThinPreg 80EP/CF carbon/epoxy $[45/90/-45/0]_{10S}$ laminate [19]. The hole diameter-to-width ratio is $2R/W = 1/6$.

around or below 10% are obtained in the predictions of open-hole tensile strength.

However, for IM7/8552, the open-hole compressive strength (Fig. 4.11) is underpredicted by the proposed framework. This is attributed to the apparently low longitudinal compressive strength (X_C) reported in Ref. [193][2], resulting in an underprediction of the laminate compressive unnotched strength using the Unit Circle failure criterion (Table 4.4). This can also be attributed to the low values reported for the fracture toughness associated with the propagation of kink bands, not only for IM7/8552, but also for T800/M21 and T700/AR2527. In fact, it is noted that the open-hole compressive strengths are underpredicted in all three material systems (Figs. 4.11 – 4.13).

Predictions of the FFMs model can be obtained by finding its input proper-

[2]Other References in the literature (e.g. Ref. [36]) report higher values for the longitudinal compressive strength (X_C) of the same material system. For instance, using the value reported in Ref. [36], the relative errors obtained with the proposed framework for the smaller notched configurations are below 10%, increasing above 20% for the larger configurations. For consistency in the choice of the Reference used to obtain the ply elastic and strength properties of IM7/8552, the value reported in Ref. [193] is used.

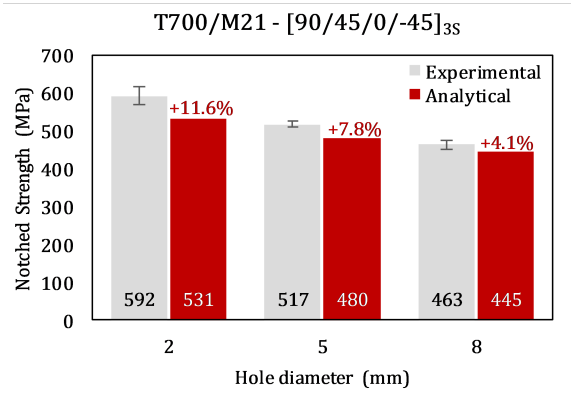

Figure 4.10: Comparison between predictions and experimental results for the open-hole tensile strength of a T700/M21 carbon/epoxy $[90/45/0/-45]_{3S}$ laminate [19]. The hole diameter-to-width ratio is $2R/W = 1/6$.

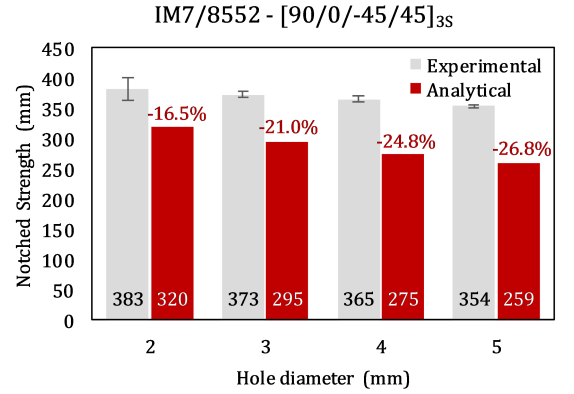

Figure 4.11: Comparison between predictions and experimental results for the open-hole compressive strength of an IM7/8552 carbon/epoxy $[90/0/-45/45]_{3S}$ laminate [14]. The hole diameter-to-width ratio is $2R/W = 1/6$.

ties (laminate strength and fracture toughness) from direct measurements at the laminate level instead of obtaining these properties using the proposed framework[3]. Since the proposed framework only requires the longitudinal properties of the UD material (for any laminate), some loss of accuracy is expected when comparing to a direct measurement of the laminate properties (see Table 4.6).

The results presented in Figs. 4.6 – 4.10 also show that the best predictions are obtained for laminates with thinner plies. It is remarkable that the predictions for the open-hole tensile strength of the M40JB/ThinPreg 80EP/CF quasi-isotropic laminate (with 20 sublaminate repetitions) differ from the experimental results by just 3% or less. And it is important to stress that these predictions were obtained using only the longitudinal Young's modulus, E_1 (Table 4.2), the longitudinal tensile strength, X_T (Table 4.4), and the fracture toughness of the 0° plies, $\mathcal{G}_{Ic}^0$ (Table 4.9).

Taking into account that the coupled framework described in the present section provides predictions of the notched strength of laminates in a few seconds, it can

[3]Trace theory to obtain the laminate elastic properties, Unit Circle failure criterion to find the laminate strength and the model based on fracture mechanics for the laminate fracture toughness.

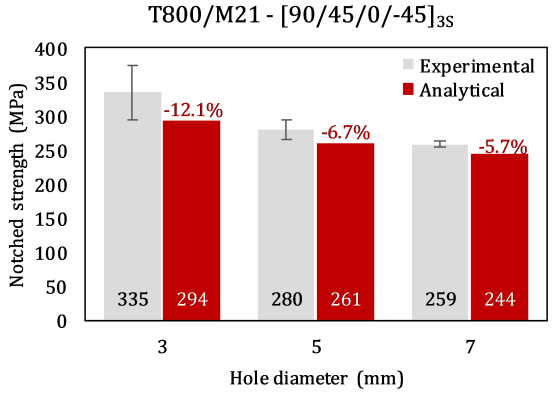

Figure 4.12: Comparison between predictions and experimental results for the open-hole compressive strength of a T800/M21 carbon/epoxy $[90/45/0/-45]_{3S}$ laminate [13]. The hole diameter-to-width ratio is $2R/W = 1/4$.

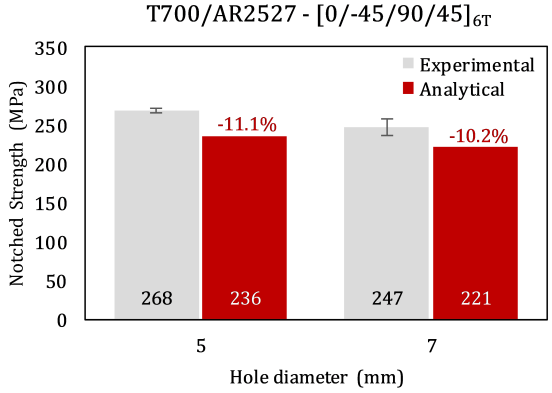

Figure 4.13: Comparison between predictions and experimental results for the open-hole compressive strength of a T700/AR2527 carbon/epoxy $[0/-45/90/45]_{6T}$ laminate [18]. The hole diameter-to-width ratio is $2R/W = 1/4$.

be used to generate design charts for notched laminates plotting the predicted (normalized) notched strengths as a function of the hole diameter-to-width ratio ($2R/W$) for different hole sizes. As mentioned in Section 4.1.2, even for hole diameter-to-width ratios $2R/W > 0.6$, the proposed method is still applicable as long as the stress distribution along the ligament section is estimated, for instance, using FE simulations. Design charts for general multidirectional laminates can, therefore, be easily and quickly obtained using only the lay-ups and three ply properties as inputs. This enables significant gains not only in terms of time to obtain the required material properties and to compute all possible laminate designs, but also in terms of costs, in particular at the stages of material screening and lay-up selection.

It should be noted, though, that the proposed framework, which is based on simple analytical models to estimate the unnotched strength and fracture toughness of general laminates and predict their notched strength based on these properties, is applicable to the cases characterized by fibre-dominated intralaminar fracture, either brittle or pull-out failure modes in tension [34], or fibre kinking or shear-driven fracture in compression [18]. This is typically the case of laminates with sufficiently thin plies [18, 34]. The strength prediction of laminates whose main

failure mechanism is delamination requires appropriate nonlinear models, which can only be solved using complex Finite Element Analyses, making the design and sizing of structures with such laminates far more complicated.

Finally, it is interesting to note that, according to the invariant-based approaches to stiffness and strength [16, 236], the elastic and strength characterization of a carbon/epoxy system just requires the knowledge of the trace (derived from the longitudinal Young's modulus, E_1), and of the longitudinal strengths (or strains-to-failure), X_T and X_C, respectively. Since using the invariant-based approach to stiffness well defined universal laminate factors can be obtained from the Master Ply concept, the trace can also be easily obtained from the measurement of the longitudinal Young's modulus of a multidirectional laminate, E_x (Table 4.1), which are much easier to test than 0° coupons. Taking into account that the invariant-based approach to strength is formulated in strain space, the longitudinal strengths (or specifically the strains-to-failure) of the 0° ply can also be obtained from a multidirectional laminate, e.g. a cross-ply laminate, which are much easier to test to failure than 0° coupons (namely in compression). In addition, to ensure test stability, the fracture toughness of the 0° plies are generally measured from cross-ply laminates (neglecting the fracture toughness of the 90° plies) [23, 222, 235, 242–245]. Therefore, the proposed coupled framework also shows potential for simpler characterization test procedures, as the complicated 0° coupons can be avoided and the characterization tests more easily performed only on cross-ply laminates.

Table 4.6: Comparison between the maximum errors for the open-hole strength predictions of the FFMs model obtained with the proposed framework using only longitudinal properties of the UD material and those obtained with the directly measured laminate properties.

Material system	Stacking sequence	Proposed framework†	Using laminate properties‡	
		max. error	max. error	Ref.
Tension				
IM7/8552	$[90/0/-45/45]_{3S}$	7%	4%	[70]
IM7/8552	$[45/90/-45/0]_{4S}$	9%	8%	[70]
T800/M21	$[90/45/0/-45]_{3S}$	14%	7%	[13]
T700/AR2527	$[0/-45/90/45]_{6T}$	7%	8%	[71]
M40JB/ThinPreg 80EP/CF	$[45/90/-45/0]_{10S}$	3%	4%	[24]
Compression				
T800/M21	$[90/45/0/-45]_{3S}$	12%	5%	[13]
T700/AR2527	$[0/-45/90/45]_{6T}$	11%	7%	[71]

† Predictions based only on the longitudinal properties of the UD material.
‡ Predictions based on directly measured laminate properties.

4.1.4 Summary

The work presented in this section demonstrated that it is possible to predict the notched strength of balanced carbon/epoxy laminates within the accuracy typically sought for preliminary design and optimization of composite structures using only three ply-based properties.

The proposed analytical framework is based on a FFMs model [70] coupled with the recently proposed invariant-based approaches to stiffness and strength [16, 236] and an analytical model based on fracture mechanics to estimate the lam-

inate fracture toughness [235]. This framework can be used to predict the notched strengths of general laminates characterized by fibre-dominated intralaminar fracture, which is typically the case of laminates with sufficiently thin plies [18, 34].

Comparisons with experimental results available in the literature show that this analytical framework is able to provide reasonable predictions for the open-hole tensile and compressive strengths of general carbon/epoxy laminates using only the lay-up and three ply properties as inputs: the longitudinal Young's modulus, the longitudinal strength, and the $\mathcal{R}$-curve of the 0° plies. Typically, relative errors around or below 10% were obtained; but more importantly, for laminates with thin plies, relative errors of 3% or less were achieved, making the proposed method particularly suitable for thin-ply laminates. Important gains in terms of material characterization, computing time and cost can be obtained using the proposed framework, in particular at the stages of material screening and lay-up selection. Moreover, the proposed coupled framework also shows great potential for simpler characterization test procedures, as the complicated 0° coupons can be avoided and the characterization tests more easily performed by taking only cross-ply laminates.

4.2 Virtual calculation of the B-value allowables of notched composite laminates

Design allowables are statistically based material parameters that account for material, geometrical, and process variability and, therefore define an acceptable stress value for a given structure, ensuring their safe and efficient use. It is of key importance to accurately determine these design allowables, however, time consuming processes such experimental testing are not ideal during preliminary design. For this reason, alternatives to fully experimental material characterization have been proposed, namely, the use of statistically based numerical and analytical models [246–249]. These models include the influence of the uncertainty related to the determination of the input parameters and their intrinsic variability on the global response of the model.

Quick analytical prediction tools, such as the one presented in Section 4.1, can serve as basis for the virtual determination of design allowables specially during the preliminary design and material selection stage of the design process. In this section, a methodology to predict the B-value (the standard design allowable used in the aeronautical industry) of notched composite laminates using the analytical framework described in Section 4.1 is proposed by taking the variability of the material properties that dominate failure and the effect of geometrical imperfections into account. The proposed Uncertainty Quantification and Management (UQ&M) methodology is validated against available experimental data and is applied to generate practical engineering design tools.

4.2.1 Estimation of the B-basis value

According to the Composite Materials Handbook (CMH-17) [251], the standard design allowable used in the aeronautical industry for fail safe structures is the B-basis [249, 251], which is defined as the 95% lower confidence bound on the tenth percentile of a specified population of measurements. This is a conservative allowable that ensures with 95% confidence that 90% of the population will have a

given property, e.g. strength, higher than the B-value allowable.

By taking the variability of the input parameters (material and geometrical) and using the analytical framework proposed in Section 4.1, the uncertainty of the input parameters can be propagated to the notched strength, i.e. a statistical distribution of the notched strength can be obtained, based on the variability of the input parameters, which can then be used to compute the statistical design allowables. To obtain the B-value for the open-hole strength, two methodologies can be used: (i) the CMH-17 approach (Section 4.2.1.1) and (ii) a Monte Carlo based approach (Section 4.2.1.2). The CMH-17 is the methodology proposed by the Composite Materials Handbook [251] and is generally employed for small populations, such as the ones typically obtained experimentally. Monte Carlo simulation is a computerized mathematical technique that allows, by repeated, nearly infinite, random sampling of the input parameters, obtaining the distribution of the population of results. Since the analytical model serving as basis for the UQ&M framework provides quick estimations of the notched strength, this method can also be employed here.

Both approaches rely on the set of material and geometrical properties and respective statistical distribution and differ in how the strength data is dealt with to determine the B-value. Note that, for a given run of the analytical model the geometrical and material properties are considered deterministic.

4.2.1.1 CMH-17 approach

The Composite Materials Handbook [251] defines different methods to determine the B-value depending on the distribution that best fits the data. As summarized in Fig. 4.14, for unstructured data, the CMH-17 approach suggests to successively test if the Weibull, normal and lognormal distributions are adequate fits to the data. If any of these distributions fits the data then the respective methods to calculate the B-basis should be used. If none of these three distributions can be assumed, nonparametric procedures should be used to determine the B-value.

To find the best fitting distribution, the CMH-17 suggests the use of the Anderson-Darling test. This test compares the Cumulative Distribution Function of the distribution of interest with that of the data, which allows the determination of a Observance Significance Level. If the calculated Observance Significance Level is greater than 0.05, it is concluded that the distribution analysed fits the data. Otherwise, the analysed distribution does not fit the data and the subsequent distribution is analysed. Once a fitting distribution is found, the B-value can be computed according to the procedures in the CMH-17 for the selected statistical distribution [251]. If none of these distributions fit the data, nonparametric procedures are used. These procedures depend on the sample size, being the Hanson-Koopmans method used for small sample sizes ($n < 28$). For large sample sizes the B-value can be computed from tabulated data in the CMH-17. Full details of the procedures are available in CMH-17 [251].

4.2.1.2 Monte Carlo simulations

The Monte Carlo Methods (MCS) rely on the repeated random sampling to obtain numerical results. To determine the B-value using this approach nearly infinite predictions of the notched strength should be obtained so that an Empirical

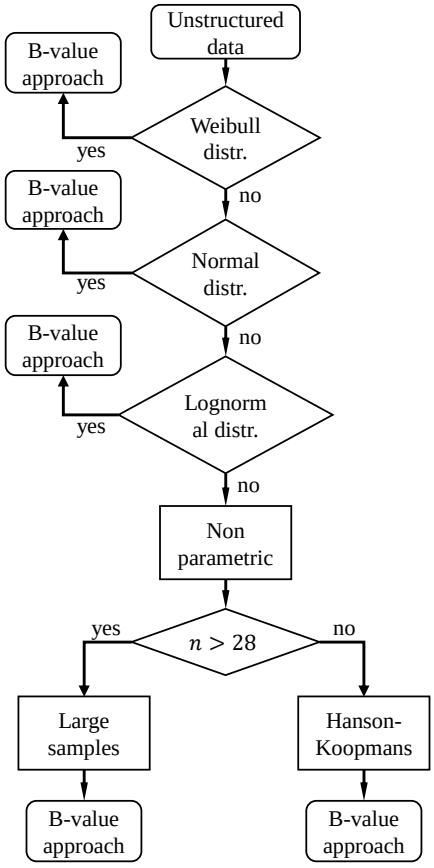

Figure 4.14: Schematic representation of the steps to calculate the B-value using the CMH-17 methodology.

Cumulative Distribution Function (ECDF) for the parameter in study can be determined. For each set of n results, where n is the sample size that should be large enough to be representative of the population, it is possible to determine the ECDF and extract the 10^{th} percentile value, $P_{10,j}$. This process is repeated N times to determine the distribution of the 10^{th} percentile. From this distribution the B-value can be computed by considering the 95% lower confidence bound [252], which corresponds to the 5^{th} percentile of the ECDF. The MCS based methodology to calculate the B-value can be summarized as follows (see Fig. 4.15):

1. Design of the experiments: the material properties and geometrical parameters are distributed according to their associated statistical distributions to define the uncertainty quantification and management matrix. Using the current analytical framework, the dimensions of the matrix are n x 5 where n are the different cases to be analysed and 5 are the model input parameters (in this case, E_1, X^L, $\mathcal{R}_{ss}$, R and W).

2. Estimation of the notched strength: for each case i the notched strength ($\bar{\sigma}_i^{\infty}$) is calculated using the analytical model described in Section 4.1.

3. Determination of the 10^{th} percentile percentile: once all the cases have been

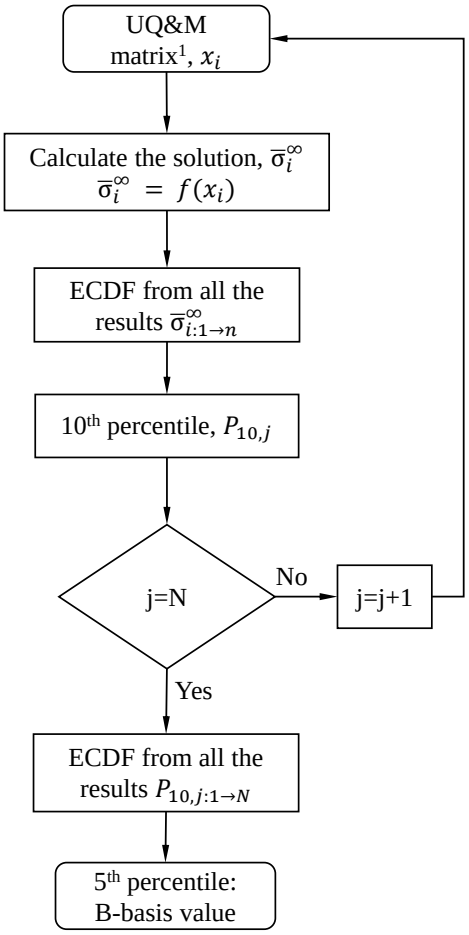

[1] UQ&M matrix dimensions are: n different cases per 5 input variables (x_i); in the first iteration $j = 1$.

Figure 4.15: Schematic representation of the steps to calculate the B-value using the Monte Carlo based methodology.

computed ($\bar{\sigma}_{i:1\to n}^{\infty}$) the ECDF of the notched strengths is used to determine the $P_{10,j}$.

4. Computation of the B-basis allowable: steps 1, 2 and 3 are repeated N times to obtain the ECDF of the 10^{th} percentile, $P_{10,j:1\to N}$, and to determine the 5^{th} percentile which corresponds to the B-basis value.

If the sample size (n) is large enough, then the 10^{th} percentile of the population can be directly approximated by the 10^{th} percentile of the sample, as the variability between the samples will be minimal. This will be explored in more detail in Section 4.2.3.2.

4.2.2 Variability of the model parameters

The analytical framework presented in Section 4.1 requires three ply material parameters to estimate the strength of a multidirectional notched laminate: the longitudinal Young's modulus, the longitudinal strength and the $\mathcal{R}$-curve of the 0° plies.

The model was validated using the mean ply properties determined experimentally, resulting in the prediction of a nominal notched strength for a given nominal dimension (hole radius and specimen width). Here, the variability associated with the determination of the ply properties and the geometry of the specimens is accounted for. The variability associated with the geometrical parameters (notch radius and specimen width) is directly related to the manufacturing process, namely the cutting methodology and respective tolerances. For this reason, the dimensions of the specimens can be assumed to follow a uniform distribution:

$$f(x) = \begin{cases} \frac{1}{b-a} & \text{for} \quad a \leq x \leq b \\ 0 & \text{for} \quad x < a \quad or \quad x > b \end{cases} \tag{4.33}$$

where $f(x)$ is the probability density function and a and b are the limits allowed by the provided tolerances.

Accounting for the variability of the longitudinal Young's modulus and the longitudinal strength is straightforward since these properties are obtained directly from the experimental tests and have an associated standard deviation. It is assumed here that these two properties follow a normal distribution with known mean and standard deviation, corresponding to the values obtained experimentally:

$$f(x) = \frac{1}{\sqrt{2\pi}s} e^{\frac{(x-\bar{x})^2}{2s^2}} \tag{4.34}$$

where $f(x)$ is the probability density function, $\bar{x}$ is the mean value and s is the standard deviation measured experimentally for the longitudinal Young's modulus and the longitudinal strength.

Accounting for the variability of the $\mathcal{R}$-curve is less clear since the $\mathcal{R}$-curves are generally not measured directly but determined from notched strengths measured experimentally. Thus, it is of key importance to define a methodology to randomly generate statistically representative $\mathcal{R}$-curves. Two methods to determine the variability of the mode I crack resistance curves from the experimental procedure proposed by Catalanotti et al. [23, 222] are described in Appendix D.

Note that, in this section, a modification was made to the analytical expression used to approximate the $\mathcal{R}$-curve presented in Eq. (4.31). Here, the following analytical expression is proposed to represent the $\mathcal{R}$-curve:

$$\begin{cases} \mathcal{R}(\Delta a) = \mathcal{R}_{ss} \left[1 - (1 - \Delta a / l_{fpz})^{\beta}\right] & \text{if} \quad \Delta a < l_{fpz} \\ \mathcal{R}(\Delta a) = \mathcal{R}_{ss} & \text{if} \quad \Delta a \geq l_{fpz} \end{cases} \tag{4.35}$$

where β is a parameter determined to obtain the best fit of the $\mathcal{R}$-curve. The proposed equation guarantees that the steady state value of the fracture toughness is reached when $\Delta a = l_{fpz}$.

4.2.3 Model verification

In this section the sample sizes required to accurately take into account geometrical and material variability within the UQ&M framework (schematically shown in Fig. 4.16) is analysed and the results are validated against available experimental data.

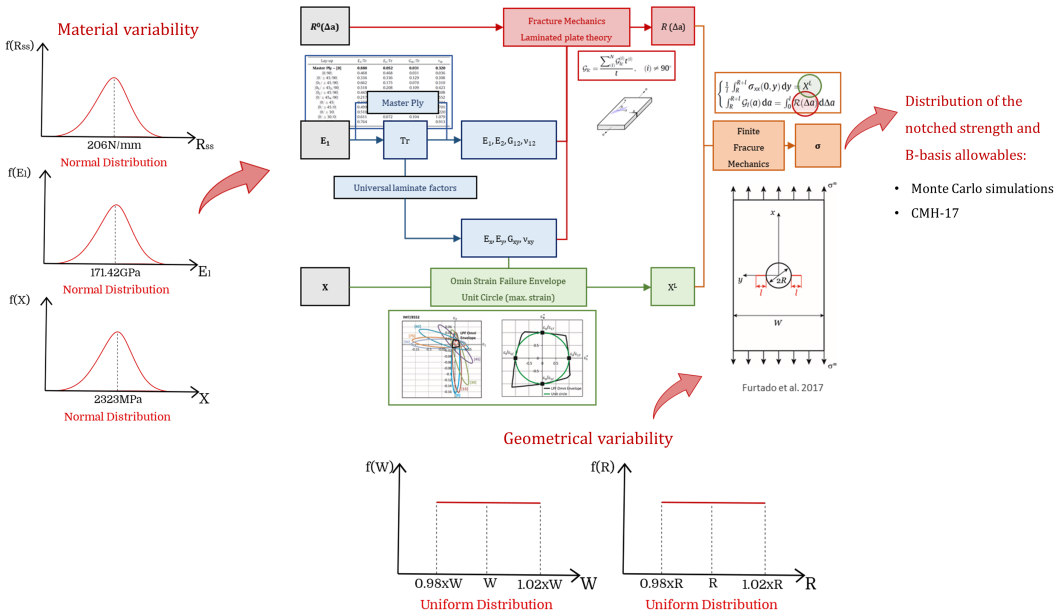

Figure 4.16: Schematic representation of the proposed UQ&M framework.

4.2.3.1 Case study

To exemplify and validate the methodology proposed to calculate the B-value of the notched strength, IM7/8552 $[90/0/\text{-}45/45]_{3s}$ quasi-isotropic laminate with a central circular hole loaded in tension was used. Hole diameter-to-width ratios of $0.05 < 2R/W < 0.6$ and hole diameters of 2, 4, 6, 8 and 10mm were considered [12].

The variability associated with the geometry of the specimens is directly related to the manufacturing process, namely the cutting methodology and respective allowed tolerances. The specimen dimensions were assumed to follow a uniform distribution with a maximum deviation of $\pm 2\%$ of the nominal value of the width and hole diameter. The material properties were assumed to follow a normal distribution with known mean and standard deviation. These properties are summarized in Table 4.7. The uncertainty related to the longitudinal Young's modulus and strength is directly related to the the mean values ($\bar{x}$) and respective standard deviation (s) determined experimentally [12] while the variability of the $\mathcal{R}$-curve was determined using the method 1 explained in Appendix D.1.1. As explained in Section D, the fitting parameters of the crack resistance curves (β and l_{fpz}) cannot be treated independently as that would potentially lead to non admissible $\mathcal{R}$-curves. For this reason, a dependence between the parameters was established as a function of $\mathcal{R}_{ss}$: l_{fpz} was considered to vary linearly with $\mathcal{R}_{ss}$ and β to be constant for the case analysed. For this reason, the crack resistance curves are simply defined as a function of $\mathcal{R}_{ss}$ as presented in Table 4.7.

4.2.3.2 Effect of the sample size on the mean notched strength and on B-basis value using the MCS method

To validate the proposed UQ&M methodology, it is important to analyse the number of simulations required to ensure an accurate determination of the output

Table 4.7: Materal material properties of the IM7/8552 material system [12]. $\bar{x}$ is the mean value and s is the standard deviation.

IM7/8552	E_1 [GPa]	X^T [GPa]	$\mathcal{R}_{ss}$ [N/mm]	l_{fpz} [mm]	β [-]
$\bar{x}$	171.42	2323.47	206.75	$2.7776E^{-2} \cdot \mathcal{R}_{ss} - 3.0598$	2.9027
s	2.38	127.45	23.64	-	-

parameters. Since the framework proposed is fully analytical, a very large number of simulations can be performed, however, it is of key importance to ensure that the open-hole strength (mean and B-basis) are determined efficiently, i.e. performing the minimum number of simulations required to obtain accurate and statistically consistent results.

The methodology to determine the B-basis using MCS is described in Section 4.2.1.2. This methodology requires the computation of $n \times N$ number of simulations to determine the B-value. This may lead to a very high number of simulations, rendering the methodology computationally expensive. However, it is possible to determine the B-basis based on a smaller number of simulations if we consider $N = 1$ and have a sample size (n) sufficiently large to be representative of the population of results. With this methodology, the B-basis can be approximated by the 10^{th} percentile of the sample, therefore, reducing the number of required simulations.

To determine the minimum sample size that ensures this representativeness, the sample size was varied between 10 and 100,000. For each sample size 10 random samples were obtained to compute both the average and standard deviation of the mean open hole strength ($\bar{\sigma}^{\infty}$) and the respective B-basis (P_{10}). The results of the convergence analysis on the average open-hole tensile strength and the B-basis allowable are shown in Fig. 4.17 and Table 4.8.

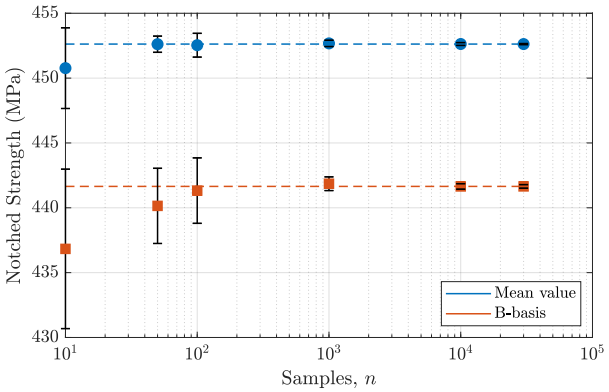

Figure 4.17: Average open-hole tensile strength and the 10th percentile from $N = 10$ simulations determined from different number of samples n.

As shown in Fig. 4.17 and Table 4.8, the variability of both the mean open-hole tensile strength and the B-basis allowable decrease with the increase of the sample size. However, it is worth noting that the computational cost increases proportionally to the sample size. For a sample size of 10,000 the Coefficient of Variation (CoV) of both the mean open-hole tensile strength and B-basis is very

Table 4.8: Mean value and standard deviation of the average open-hole tensile strength ($\bar{\sigma}^{\infty}$) and B-value (P_{10}) according to the number of samples when $N = 10$.

Samples, n	$\bar{\sigma}^{\infty}$		P_{10}	
	$\overline{\sigma^{\infty}}$ [MPa]	$s_{\sigma^{\infty}}$ [MPa]	$\overline{P_{10}}$ [MPa]	$s_{P_{10}}$ [MPa]
10	450.77	3.11	436.83	6.15
50	452.61	0.62	440.15	2.90
100	452.54	0.91	441.33	2.52
1000	452.68	0.24	441.86	0.53
10000	452.63	0.11	441.65	0.21
30000	452.62	0.04	441.64	0.13
100000	452.62	0.03	441.64	0.05

low, 0.02% and 0.05%, respectively. For a sample size of 30,000, which has a three times increase in the computational time, an insignificant reduction in the CoV for the mean strength and B-basis is obtained (to 0.01% and 0.03% respectively). For this reason, a sample size of 10,000 was considered to be large enough to represent the population of results and ensure a good compromise between the accuracy and computational cost. The calculation of the B-basis allowable using MCS can be done in a computationally efficient way by estimating the notched strength 10,000 times (with $N = 1$) and determining the 10^{th} percentile of the sample as this number of samples is considered representative of the whole population. This methodology will be considered for the determination of the B-basis allowables using Monte Carlo simulations in the following sections.

4.2.3.3 Effect of the sample size on the B-basis using the CMH-17 approach

In this section, a comparison between the B-basis determined using the CMH-17 approach (see Section 4.2.1) is compared with the results obtained using Monte Carlo simulations. The CMH-17 approach is particularly useful since it takes into account the size of the population and the distribution that most accurately represents the data to determine the B-basis and therefore, a good estimate of this parameter can be obtained using a small number of data points.

In Fig. 4.18 the B-basis allowable for open-hole tensile strength determined using the CMH-17 methodology for different sample sizes is shown and compared with the value obtained using the MCS approach. For each sample size, 100 simulations based on different randomly generated samples were performed so that the average value for the B-basis and its dispersion could be obtained.

As the sample size increases, the B-value determined with the CMH-17 approach becomes less conservative and the confidence interval is reduced, as larger samples are considered more representative of the population. In Table 4.9 the results of the B-value are also shown for different sample sizes. In addition, the methodologies from the CMH-17 applied for each sample are shown, as different distributions best fit the data depending on the sample considered. Hereafter, a sample size of 25 is considered to determine the B-basis allowable using the CMH-17 approach, as it ensures a good B-basis estimation and it is a reasonable sample size that can potentially be used in experimental campaigns.

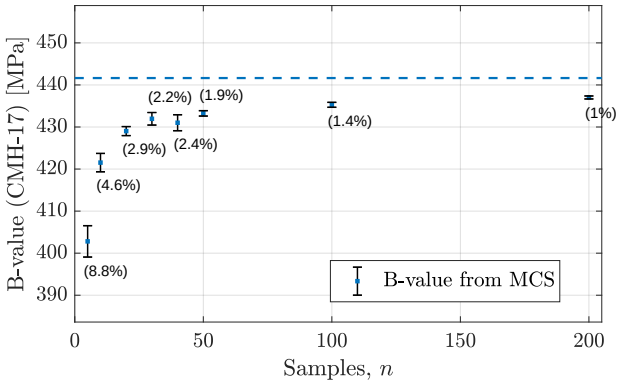

Figure 4.18: Comparison of the b-value obtained from the CMH-17 approach with its 95% interval of confidence, for different sample sizes (n) and the B-value obtained from MCS (dashed line).

Table 4.9: Results for the B-basis determination using the CMH-17 methodology. W, N, LN and NP stand for Weibull, Normal, Lognormal and Non parametric distributions, respectively.

Samples, n	W	N	LN	NP	$\bar{B}$ [MPa]	s_B [MPa]	IC_B [$\pm$ MPa]	error %
5	92	8	0	0	411.35	17.992	3.5696	6.858
10	93	3	0	0	428.77	9.5808	1.9008	2.9152
15	88	3	0	0	431.84	8.0774	1.6026	2.2193
20	94	2	0	0	434.78	4.2685	0.84686	1.553
25	94	2	0	0	435.92	4.3825	0.86948	1.2953
30	91	4	0	5	438.17	7.051	1.3989	0.78675
40	94	3	0	3	437.74	3.4001	0.67458	0.88285
50	92	5	0	3	437.24	3.2488	0.64456	0.99621
100	78	5	0	17	438.76	2.7482	0.54525	0.65224
150	91	1	0	8	439.43	1.5205	0.30167	0.50112

4.2.3.4 Validation of the UQ&M framework

A comparison between the experimental results presented in Ref. [12] and the predictions using the proposed framework is shown in Fig. 4.19. Both the open-hole tensile strengths computed using the nominal values of the material and geometrical properties and the results obtained when these properties are considered stochastic are included. The latter methodology allows the determination of the average value for open-hole tensile strength for each geometry and its expected variability.

As expected, the nominal notched strength and the mean open hole strength determined using the proposed framework are approximately the same, which ensures the consistency of the uncertainty quantification framework developed. The results shown in Fig. 4.19 indicate that the proposed framework is capable of accurately predicting the open-hole tensile strength. The maximum error obtained for this case study was 12% which, taking into account that this is an analytical formulation with a very reduced computational cost, is very reasonable.

As the developed framework is aimed at the determination of the B-basis allowable for open hole strength, the comparison between the B-basis obtained experimentally and determined analytically with the two presented methods is shown in Fig. 4.20. For consistency, as five specimens were tested experimentally [12], the same sample size was considered to compute the B-value allowable with the CMH-17

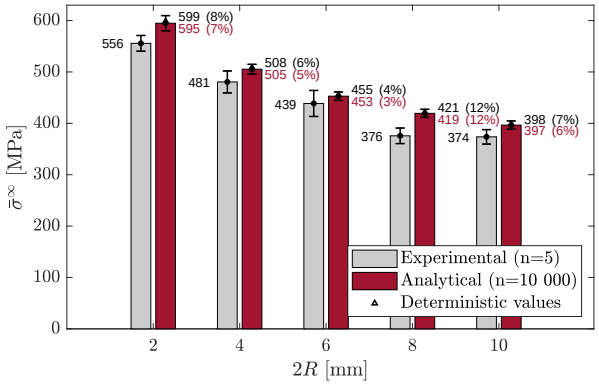

Figure 4.19: Comparison between the mean open hole strength of experimental results [12] and the analytical results of five different $2R$ and a fixed ratio $2R/W = 1/6$, where $\bar{\sigma}^{\infty}$ is the notched strength, R the radius of the hole and W the width.

approach. This allows a direct comparison between the experimental B-basis and the one obtained numerically. Nevertheless, the results with a sample size of 25 are also shown. To ensure that the results obtained did not result in outliers, ten B-basis calculations were performed for each geometry. For the Monte Carlo simulations approach a larger number of simulations is always required to ensure the representativeness of the population, therefore, the sample size was kept at 10,000.

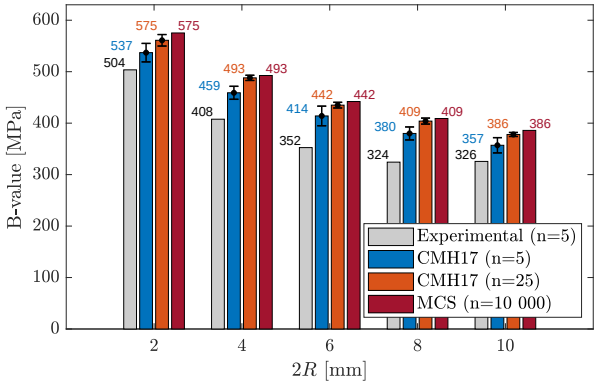

Figure 4.20: Comparison between the B-value obtained experimentally ($n = 5$), with the CMH-17 ($n = 5$ and $n = 25$) and with the MCS method ($n = 10,000$).

As shown in Fig. 4.20, for the same sample size ($n = 5$), the B-value determined with the CMH-17 approach is similar to that obtained experimentally, which reflects not only the ability of the framework to accurately compute the open hole strength of a given configuration, but also its ability to propagate the uncertainty of the input parameters to the open hole strength. The B-basis obtained with the MCS approach is always less conservative than the one obtained with the CMH-17 approach due to the larger sample size, which is reflected in the results shown in Fig. 4.20 and Fig. 4.18.

4.2.4 Applications

4.2.4.1 Design charts for open hole tension

Taking into account that the analytical UQ&M framework developed enables the quick estimation of the notched strength of laminated composites and the respective B-basis allowables, it can be used to generate design charts and compare the performance of different lay-ups and materials in a preliminary stage of the design process.

Following Camanho et al. [70], design charts that relate the diameter-to-width ratio to the notched tensile strength of specimens with diameters 2, 6 and 10mm were generated. Monte Carlo simulations with $n = 10,000$ were used to generate the average notched strength distribution of each point and compute the mean value and respective B-basis allowable, as defined in Section 4.2.3.2 (Fig. 4.21). To calculate the B-value, the CMH-17 approach could also have been used without significant loss of accuracy as shown in Fig. 4.22 for a specimen with a hole diameter of 6mm, however, given the computational efficiency of the model, performing Monte Carlo simulations is not a particularly limiting approach.

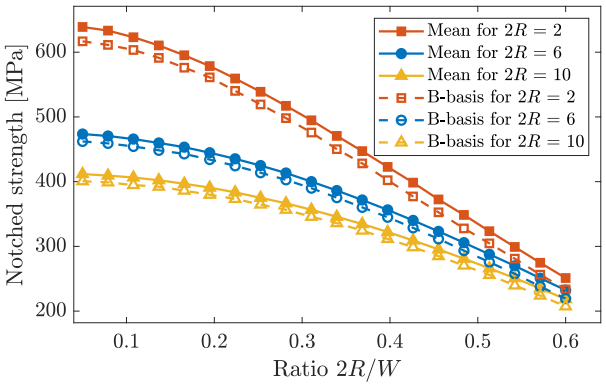

Figure 4.21: Design chart of the mean and B-basis value of the open hole strength calculated by means of MCS for different $2R$ and $2R/W$ ratios.

Experimentally generating statistically representative design charts is unreasonable given the number of specimens, specimen configurations, lay-ups and materials required to populate them. The analytical UQ&M framework here proposed can help overcome this limitation and assist engineers during the design process given its simplicity and efficiency.

4.2.4.2 Influence of the loading direction on the open hole strength

The framework was developed to work as a fast design tool that is capable to predict the notched strength of a laminate in the most varied cases. In this section, the variation of the loading direction and its effect on the open hole tensile strength is explored. The design of a laminate for a given structure is usually optimized for a given loading direction, however, it is not acceptable to have a laminate whose strength is very high in one direction but any misalignment in the load, which most certainty occurs in real usage, leads to a high reduction of its strength. Therefore,

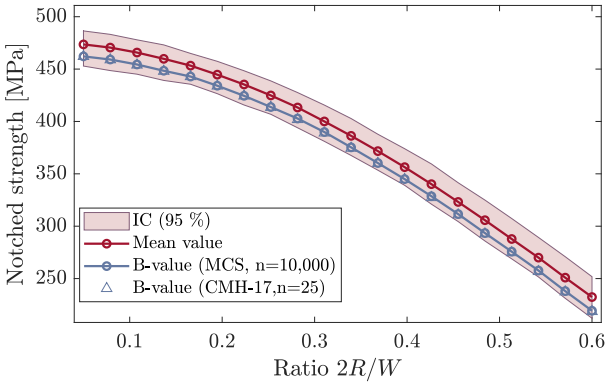

Figure 4.22: Design chart of the mean and B-basis value of the open hole strength calculated with the MCS and the CMH-17 approaches for $2R = 6$ mm.

being able to rapidly predict the notched strength in multiple loading scenarios is an useful design tool. The variation of the mean open hole strength as a function of the load direction and the respective 95% confidence interval and predicted B-basis value based on MCS ($n = 10,000$) and on the CMH-17 ($n = 25$) are shown in Fig. 4.23. This analysis was done for the baseline configuration (open-hole tensile specimen with a width of 36 mm and a diameter of 6 mm).

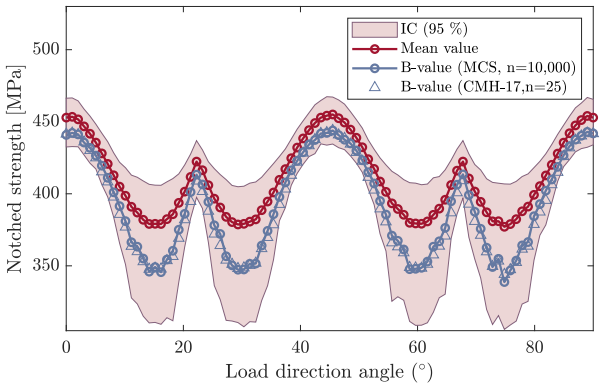

Figure 4.23: Notched strength variation with the loading direction for an IM7/8552 open-hole tensile specimen with a width of 36 mm and a diameter of 6 mm.

Since the laminate in study is quasi-isotropic (Section 4.2.3.1), the notched strengths at 0°, 45° and 90° are equal. However the strength is reduced for any other loading direction. For this particular configuration, the reduction of strength due to the variation of the loading direction is small, being the lowest notched strength equal to 377.1 MPa, and the maximum (corresponding to 0°, 45° and 90°) is equal to 455.0 MPa. Additionally, it is observed that small variations around the principal loading direction (0°) have a small effect on the notched strength. Regarding the B-basis allowable, the CMH-17 and MCS approach provide very similar results. It is interesting to note that the difference between the B-basis and the mean value for the open hole strength is not constant throughout the angle space. This difference

is highest when the average strength is lowest, which creates a wider span of the B-basis allowable between its maximum and minimum. This can be explained by the fact that for those loading directions the variability of the material and geometrical parameters leads to a higher variability of the notched strength and, therefore, a reduced B-basis allowable.

4.2.4.3 Large damage capability

The proposed framework was developed with the aim of predicting the open-hole strength of laminate structures, however, it is general enough to be able to predict the strength of different notched geometries, provided the stress distribution and energy release rate are known for those geometries and loading conditions. As it is well known, the tensile strength of composite laminates in the presence of through-thickness notches is significantly affected by size, being the smallest geometries strength-dominated and large ones toughness-dominated [20]. Therefore, the analysis tools must be able to account this distinct material behaviours when computing the notched strength. Following Arteiro et al. [20] the developed framework is used to predict the large damage capability of the laminate in study, considering a centre notched plate under tension loading (Fig. 4.24).

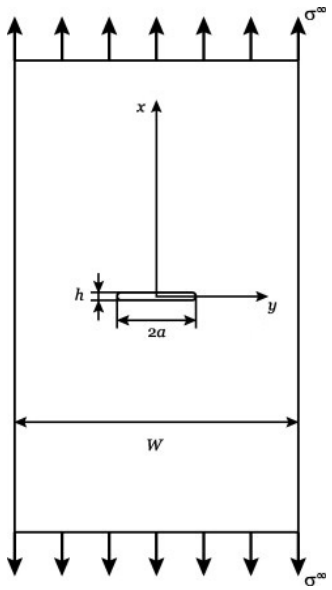

Figure 4.24: Centre notched plate configuration [20].

In Fig. 4.25, the mean notched strength and respective B-basis allowable of centre notched plates with a constant plate width-to-notch lentgth ratio ($W/2a$) equal to 7.5 with different notch sizes are shown. The notches were considered to have a constant tip radius of 0.5 mm ($h = 1$ mm). For the smaller geometries the traditional methods that only consider the steady state value of the fracture toughness in their formulation are able to predict the notched strength, however, for larger specimens and large damage capability analysis the introduction of the $\mathcal{R}$-curve in the modelling strategy is of utmost importance [20]. This is taken into account in the present framework, which increases the reliability of the modelling

strategy. It is possible to see in Fig. 4.25 that both the mean notched strength and its respective B-basis allowable follow the same trends, being the difference between both parameters similar throughout the analysed space.

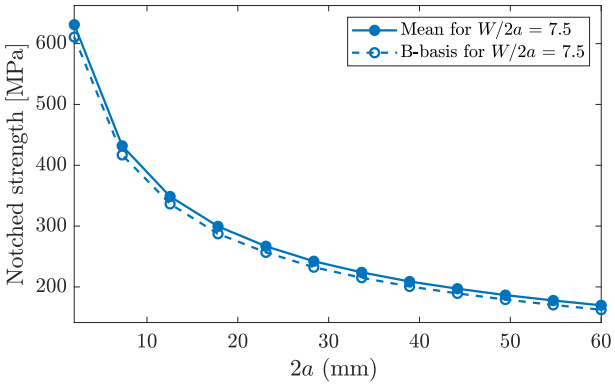

Figure 4.25: Design chart of the mean and B-basis value of the notched strength calculated by means of MCS ($n = 10,000$) for centre notched plates.

4.3 Concluding remarks

In this chapter, an analytical framework based on a FFMs model [70] coupled with an invariant-based approach to stiffness and strength [16, 236] and an analytical model based on fracture mechanics to estimate the laminate fracture toughness [235] is proposed. This framework can be used to predict the notched strengths of general laminates characterised by fibre-dominated intralaminar fracture using only three ply properties as inputs: the longitudinal Young's modulus, the longitudinal strength, and the $\mathcal{R}$-curve of the 0° plies. Relative errors around or below 10% were obtained for all the laminates and open-hole geometries analysed. The proposed framework proved to be particularly accurate for laminates with thin plies, for which relative errors of 3% or less were obtained.

The proposed analytical framework was coupled with the statistical tools required to take into account the variability of both the material and geometrical parameters and propagate this uncertainty to the notched strength, therefore allowing the quick estimation of B-basis allowable. The proposed framework was validated successfully, ensuring a maximum error around 10%, which is very reasonable given the analytical formulation of the model. Additionally, the framework is used to develop statistical-based design charts for notched specimens, tools that are useful for design engineers and would otherwise be infeasible to attain as they require a large number of testing or time consuming simulations to be performed.

The coupled framework provides a fast-analysis model for preliminary sizing and optimization of composite laminates based solely on material properties determined at the ply level. Important gains in terms of material characterization, computing time and cost can be obtained using the proposed framework, in particular at the stages of material screening and lay-up selection.

Part IV

Mechanics of thin-ply laminates

Chapter 5

The effect of ply thickness on the intralaminar fracture toughness

The previous chapters presented new analysis models, developed at different scales, that are of critical importance for the introduction of new, non-conventional composite materials in aerospace structures. With the support of the analysis models previously developed, this chapter will address one fundamental question related to size effects on ultra-thin composite laminates: does the intralaminar fracture toughness of the 0° plies depend on their thickness?

Indeed, size effects are ubiquitous in composite laminates, stemming from the variability of the strength of the reinforcing fibres [254], from the effect of ply thickness on the local fields at the tip of fibre-matrix debonds [3, 255], and from the development of a subcritical fracture process zone in notched laminates [12, 34, 256].

The recent development of tow-spreading techniques, which are able to produce thin plies, with thickness comprised between 20μm and 100μm, resulted in a considerable number of studies focused on the mechanics of deformation and failure of thin-ply laminates, and on the potential advantages of these materials over standard-grade laminates [1, 6, 18, 26].

These studies have shown that thin-ply composites suppress microcracking, delamination and splitting under different loading conditions [1, 6, 18, 19, 26]. This strengthening effect that inhibits the excessive growth of subcritical cracks in off-axis plies within a laminate is a consequence of the *in-situ* effect, which is characterized by the increase of the ply transverse and shear strengths when a ply is constrained by plies with different fibre orientations within a laminate. This effect was first detected experimentally for transverse tension and in-plane shear by Parvizi et al. [27], and further analysed by other authors [28–33]. Recently, Arteiro et al. [4] demonstrated, using computational micromechanics, the existence of an *in-situ* effect for transverse compression.

The effect of ply thickness on the intralaminar (or translaminar) fracture toughness associated with longitudinal failure has also been studied [24, 257–259]. Teixeira et al. [257] addressed the effect of ply thickness on the intralaminar fracture toughness of fibre-reinforced laminated composites and concluded that it significantly depends on the thickness of the 0° plies, and should therefore be treated as an *in-situ* property and not as an absolute material property. The authors argued that this ply thickness effect was due to the increase of the length of the pulled-out fibres and and not to other types of damage such as fibre-matrix splitting, delamination or diffuse damage. As a result, Teixeira et al. [257] and Chen et al. [260] defended that the intralaminar fracture properties used in analytical and numerical ply-level

damage propagation models (mesomodels) used for design and damage-tolerance analyses should vary as a function of the thickness.

Costa Fernandes [258] and Frossard [259] also reported a strong ply thickness effect on the intralaminar fracture toughness. In both studies, the energy release rate at initiation and during propagation were found to scale linearly with the ply thickness. Similarly to Teixeira et al. [257], the authors [258, 259] attributed this ply thickness effect to the change of pull-out length: the thicker the plies, the greater the pull-out length of the 0° plies and therefore, the higher the energy dissipated during crack propagation.

Arteiro [24] determined the apparent crack resistance curves of two material grades of spread tow fabric using double edge notch tension tests and the methodology proposed by Catalanotti et al. [23]. A higher apparent fracture toughness of the thicker material grade was measured, however, Arteiro [24] attributed this effect to the blunting effect of the damage mechanisms that precede intralaminar fracture, in particular longitudinal splits and not to an intrinsically higher fracture toughness of the thicker plies.

Taking into account the importance of the intralaminar fracture toughness on the accuracy of the strength predictions provided by both analytical and numerical methods, and the contradictory opinions found in literature, the objective of this work is to elucidate if this property depends on the ply thickness.

The effect of ply thickness on the effective intralaminar fracture toughness is studied by determining the crack resistance curves associated with longitudinal failure following the methodology proposed by Catalanotti et al. [23]. Afterwards, a detailed numerical analysis is performed to assess if the mode I fracture toughness associated with fibre failure used in numerical ply level damage propagation models should be scaled as function of the ply thickness.

5.1 Experimental work

The crack resistance curves for longitudinal tension of the three material systems were obtained following the methodology proposed by Catalanotti et al. [23], which is based on the size effect law, i.e., on the relation between the size of the specimens and their notched strength $\overline{\sigma}^{\infty}(w)$. The material selection, specimen manufacturing, test details and experimental results are reported hereafter.

5.1.1 Material selection and manufacturing

Three UD prepreg tapes with 75g/m^2, 134g/m^2 and 268g/m^2 were used to study the effect of ply thickness on the intralaminar fracture toughness. The UD prepreg tapes were produced from T700 carbon fibres and M21 epoxy resin. Cross-ply laminates with the same nominal thickness of 2.5mm were produced (see Table 5.1). The plates were cured in an autoclave following the manufacturer-specified cure procedure: 120min at 180°C and at 7bar. Three double edge notched tension (DENT) specimens per geometry were produced and cut to the nominal nominal dimensions (see Table 5.2). The fibre volume fractions V_f of each material system

were estimated using the Rule of Mixtures:

$$V_f = \frac{E_1 - E_m}{E_f - E_m} \tag{5.1}$$

where E_1 is the effective longitudinal stiffness of a unidirectional ply, E_f is longitudinal Young's modulus of the fibres and E_m is the Young's modulus of the matrix. E_1 was measured experimentally for the three material systems, E_f was provided by the material supplier and it is equal to 230GPa and E_m was assumed to be constant and equal to 5GPa. The volume fractions obtained are presented in Table 5.1.

Table 5.1: Lay-ups of the specimens manufactured from Hexcel T700/M21 UD 268gsm, 134gsm and 75gsm material systems.

Ref.	Material	V_f [%]	Lay-up
H268	T700/M21 UD 268gsm from Hexcel	69.73	$[90/0]_{3\$}$
H134	T700/M21 UD 134gsm from Hexcel	60.09	$[90/0]_{5\$}$
H75	T700/M21 UD 75gsm from Hexcel	62.88	$[90/0]_{8\$}$

Table 5.2: Geometry of the double edge notch tension specimens.

Geometry	Length [mm]	Width $2w$ [mm]	Crack length a_0 [mm]	Nr. Specimens
A	250	10	3	3
B	250	20	6	3
D	250	40	12	3
E	250	50	15	3

5.1.2 Test details and data reduction method for the $\mathcal{R}$-curve

The size effect law associated with tensile failure was determined experimentally testing geometrically similar double edge notched tension cross-ply specimens (see Fig. 5.1). All tests were performed under displacement control, at a speed of 1mm/min. The specimens were tested in an INSTRON 4208 electro-mechanical universal testing machine equipped with a 300kN load cell. Hydraulic grips were used to hold the specimens in the loading frame.

According to Catalanotti et al. [23], the driving force curves $\mathcal{G}_I$ at the ultimate remote stress are tangent to the $\mathcal{R}$-curve, which means that the ultimate remote stresses $\overline{\sigma}^{\infty}$ can be calculated solving the following system of equations:

$$\begin{cases} \mathcal{G}_I(\Delta a) = \mathcal{R}(\Delta a) \\ \frac{\partial \mathcal{G}_I(\Delta a)}{\partial \Delta a} = \frac{\partial \mathcal{R}(\Delta a)}{\partial \Delta a} \end{cases} \tag{5.2}$$

According to Refs. [239, 261] the energy release rate in mode I of a two-dimensional orthotropic body for a crack propagating in the y direction (perpendicularly to the loading direction, x) is given by:

$$\mathcal{G}_I = \frac{1}{\acute{E}} \mathcal{K}_I^2 \tag{5.3}$$

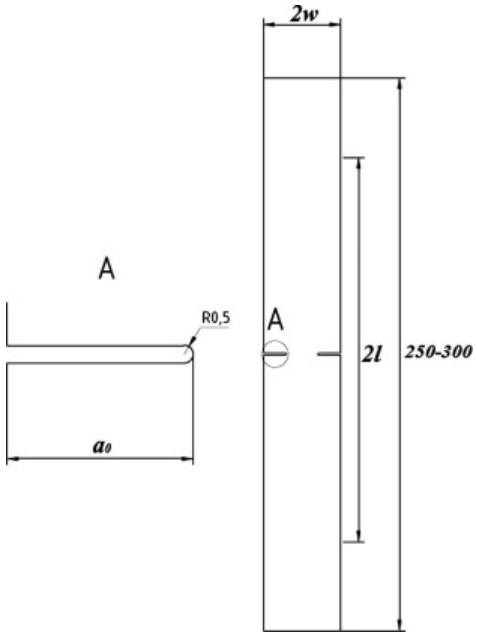

Figure 5.1: Technical draw of the specimen. [23]

where $\mathcal{K}_I$ is the mode I stress intensity factor and $\acute{E}$ is the equivalent elastic modulus:

$$\acute{E} = \left(\frac{1+\rho}{2E_xE_y}\right)^{-1/2}\left(\frac{E_y}{E_x}\right)^{-1/4} \tag{5.4}$$

and ρ is an in-plane orthotropy parameter:

$$\rho = \frac{(E_xE_y)^{1/2}}{2G_{xy}} - (\nu_{xy}\nu_{yx})^{1/2} \tag{5.5}$$

For sufficient long DENT specimens with $w/l \leq 0.5$ the stress intensity factor $\mathcal{K}_I$ is given by:

$$\mathcal{K}_I = \overline{\sigma}^{\infty}\sqrt{w}\kappa(\alpha,\rho) \tag{5.6}$$

where $\overline{\sigma}^{\infty}$ is the notched remote stress, w is half the width of the specimen, l is half the free length of the specimen and κ is a correction factor that depends on the geometry and orthotropy of the specimens. Following Catalanotti et al. [23], κ reads:

$$\kappa(\alpha,\rho) = \sqrt{\tan\frac{\pi\alpha}{2}}\sum_{i=1}^{M}\sum_{j=1}^{N}\Phi_{ij}\alpha^{i-1}\rho^{j-1} \tag{5.7}$$

where α is the notch length-to-width ratio $\alpha = a/w$ and Φ_{ij} is the element of the matrix $\mathbf{\Phi}$ of indexes i and j, and M and N are the number of rows and columns of $\mathbf{\Phi}$, respectively:

$$\mathbf{\Phi} = \begin{bmatrix} 1.7482487564 & -0.053754159533 & 0.0040142704949 & -9.8480085881E-4 \\ -0.76896688866 & -0.0068632911438 & 0.0029984681658 & -0.00010108691939 \\ 0.85633404777 & 0.23922363475 & -0.023289123198 & 0.00062358861997 \\ -0.67470597429 & -0.25334178248 & 0.022297779266 & -0.00056784694513 \\ 0.18495379886 & 0.084067007027 & -0.0068989066533 & 0.00016783852495 \end{bmatrix} \tag{5.8}$$

Replacing Eq. (5.6) in Eq. (5.3), the energy release rate reads:

$$\mathcal{G}_I(\Delta a) = \frac{1}{\acute{E}} w(\overline{\sigma}^{\infty})^2 \kappa^2(\alpha_0 + \frac{\Delta a}{w}, \rho) \tag{5.9}$$

where α_0 is the initial notch length-to-width ratio $\alpha_0 = a_0/w$. Combining Eq. (5.3) and (5.2), $\mathcal{R}(\Delta a)$ yields:

$$\mathcal{R}(\Delta a) = \frac{1}{\acute{E}} w(\overline{\sigma}^{\infty})^2 \kappa^2(\alpha_0 + \frac{\Delta a}{w}, \rho) \tag{5.10}$$

For a constant w/l and a_0/w and knowing that, by definition the $\mathcal{R}$-curve is size independent ($\frac{\partial \mathcal{R}}{\partial w} = 0$), differentiating Eq. (5.10) with respect to w yields:

$$\frac{\partial}{\partial w}(w(\overline{\sigma}^{\infty})^2 \kappa^2) = 0 \tag{5.11}$$

Given the size effect $\overline{\sigma}^{\infty}(w)$ is known, Eq. (5.11) can be solved for $w(\Delta a)$, which can then be replaced in Eq. (5.10). The size effect law is determined by testing geometrically similar double edge crack specimens, i.e. with the same width-to-crack length a_0/w ratio and different widths w and applying one of three linear regressions proposed in Ref. [262] that best fits the experimental data: i) bilogarithmic regression, ii) linear regression I, or iii) linear regression II. The regressions and the $\mathcal{R}$-curve parameters (length of the fracture process zone, l_{fpz}, and the fracture toughness at propagation $\mathcal{R}_{ss}$) are shown in Table 5.3. Note that $\kappa_0 = \kappa(\alpha_0)$ and $\acute{\kappa}_0 = \partial\kappa/\partial\alpha(\alpha_0)$.

Table 5.3: Regressions and the $\mathcal{R}$-curve parameters [23].

Regression	Formula	Fitting parameters	$\mathcal{R}_{ss}$	l_{fpz}
Bilogarithmic	$ln(\overline{\sigma}^{\infty}) = ln\frac{M}{\sqrt{N+w}}$	M, N	$\frac{\kappa_0^2}{\acute{E}} M^2$	$\frac{\kappa(\alpha_0)}{2\acute{\kappa}_0} N$
Linear regression I	$\frac{1}{(\overline{\sigma}^{\infty})^2} = Aw + C$	A, C	$\frac{\kappa_0^2}{\acute{E}} \frac{1}{A}$	$\frac{\kappa(\alpha_0)}{2\acute{\kappa}_0} \frac{C}{A}$
Linear regression II	$\frac{1}{w(\overline{\sigma}^{\infty})^2} = A\frac{1}{w} + C$	A, C	$\frac{\kappa_0^2}{\acute{E}} \frac{1}{C}$	$\frac{\kappa(\alpha_0)}{2\acute{\kappa}_0} \frac{A}{C}$

Catalanotti et al. [23] also suggested that it is useful and more convenient to express the $\mathcal{R}$-curve analytically. In this work, the $\mathcal{R}$-curve is expressed as:

$$\begin{cases} \mathcal{R}(\Delta a) = \mathcal{R}_{ss}\left[1 - (1 - \Delta a/l_{fpz})^{\beta}\right] & \text{if} \quad \Delta a < l_{fpz} \\ \mathcal{R}(\Delta a) = \mathcal{R}_{ss} & \text{if} \quad \Delta a \geq l_{fpz} \end{cases} \tag{5.12}$$

where β is a parameter that best fit the $\mathcal{R}$-curve. The $\mathcal{R}$-curve of the 0° plies can be obtained testing cross ply laminates and neglecting the fracture toughness of the 90° plies, i.e.:

$$\mathcal{R}_0 = \frac{h}{h_0} \mathcal{R}_{CP} \tag{5.13}$$

where $\mathcal{R}_0$ and $\mathcal{R}_{CP}$ are the $\mathcal{R}$-curves for the 0° plies and of the cross-ply laminate, respectively, and h and h_0 are the thickness of the laminate and the total thickness of the 0° plies respectively.

5.1.3 Experimental results

The remote stress-displacement curves obtained for each geometry and material grade are shown in Fig. 5.2 and the notched strengths obtained and respective standard deviations are summarized in Table 5.4 and Fig. 5.3a. As presented in Table 5.5, bilogarithmic regressions were used to approximate the size effect laws of the three material configurations. The $\mathcal{R}$-curves obtained for the 0° plies are shown in Fig. 5.3b and the respective parameters used to approximate the curve to an analytical expression are presented in Table 5.5.

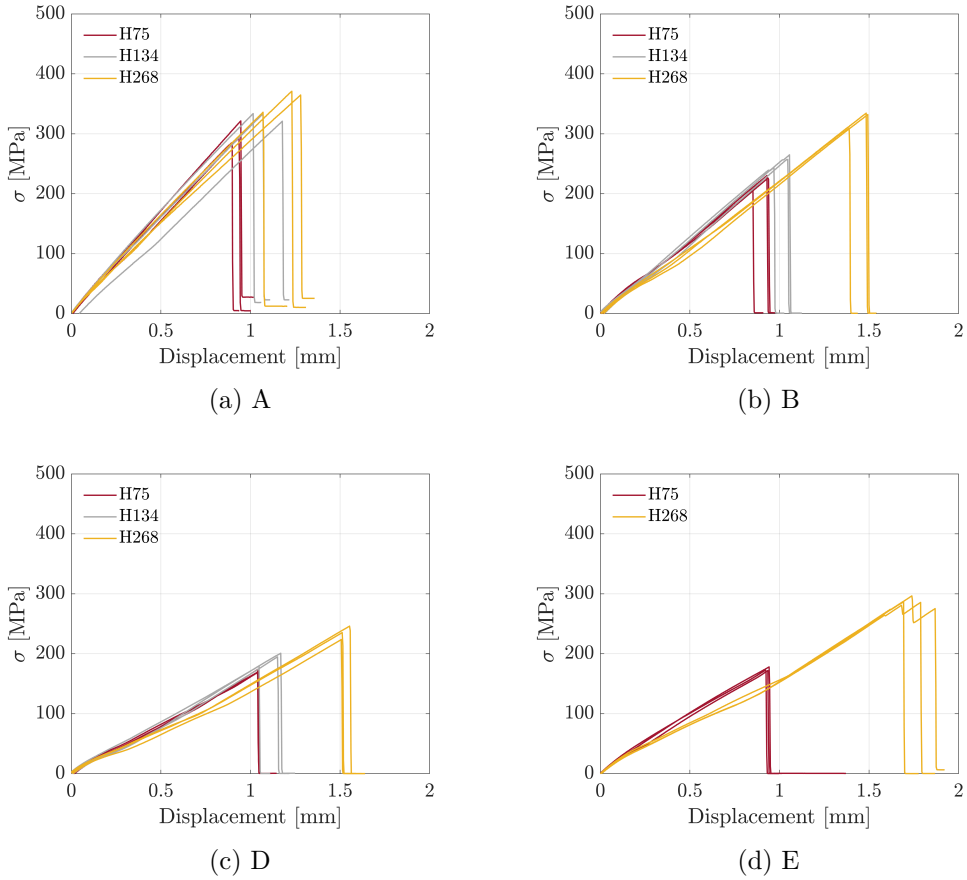

(a) A (b) B

(c) D (d) E

Figure 5.2: Load displacement curves of the double edge notch tension tests of H268, H134 and H75 material systems.

All the specimen configurations exhibited a linear response up to failure, except the largest geometry of H268. For this configuration, small load drops are clearly visible at loads close to ultimate failure, which suggests the appearance of subcritical damage in the vicinity of the notches. Fibre dominated failure was observed in all the specimens, where the cracks propagated perpendicularly to the loading direction. To have an insight of the damage extension inside the specimens, two configurations per UD material system (A and D) were analysed using X-ray imaging. As shown in Fig. 5.5, H75 samples show limited split cracks and transverse cracks in both geometries, however, subcritical damage can be observed in the other two material configurations, particularly on H268 samples. As suggested in

Refs. [18, 19, 24], since thicker plies have lower transverse strengths, the thicker 0° plies promote longitudinal split cracking at the vicinity of the notch, resulting in a stress redistribution that blunts the notch, leading to higher notched strengths. This increase in notched strength will in turn lead to the determination of a higher apparent mode I fracture toughness. As reported in Refs. [257–259] and shown in Fig. 5.4, the measured effective fracture toughness increases linearly with the ply thickness.

Table 5.4: Double edge notched tension strengths obtained for H268, H134 and H75 carbon/epoxy material systems. The initial crack length-to-width ratio is a_0/w=3/5.

		H268		H134		H75	
Ref.	2w [mm]	Mean [MPa]	Std. [MPa]	Mean [MPa]	Std. [MPa]	Mean [MPa]	Std. [MPa]
A	10	339.09	17.99	317.81	7.85	289.83	19.51
B	20	308.53	11.74	243.75	10.76	208.85	11.75
D	40	225.34	11.40	184.28	9.16	164.59	1.30
E	50	220.05	4.64	-	-	136.11	3.93

Table 5.5: Parameters of the regressions used to determine the mean $\mathcal{R}$-curves for longitudinal tension of H268, H134 and H75 material systems.

	Fitting			$\mathcal{R}$-curve parameters		
Ref	Regression	M [MPa$\sqrt{\text{mm}}$]	N [mm]	$\mathcal{R}^0_{ss}$ [N/mm]	l_{fpz} [mm]	β [-]
H268	Bilogarithmic	1241.4	7.84	252.25	2.39	2.91
H134	Bilogarithmic	871.1	2.56	131.48	0.85	2.91
H75	Bilogarithmic	720.7	1.27	83.91	0.39	2.91

The experimental results show that the apparent fracture toughness of the laminate does decrease when thin plies are used. It is questionable though if the concept of laminate fracture toughness should be used for thick plies that develop a complex network of subcritical cracks that render simplified Fracture Mechanics concepts inapplicable. Furthermore, to verify if the intralaminar fracture toughness of the 0° ply depends on the ply thickness, a numerical study is required.

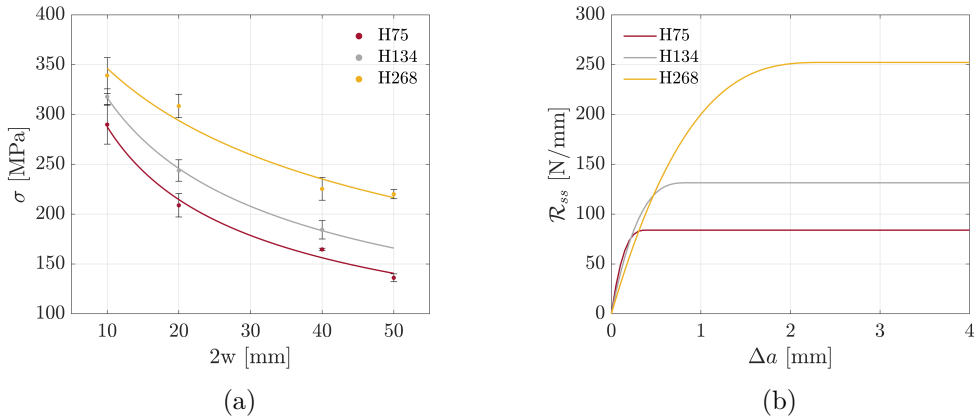

Figure 5.3: a) Size effect law and b) $\mathcal{R}$-curves for longitudinal tension (0° plies) of H268, H134 and H75 material systems.

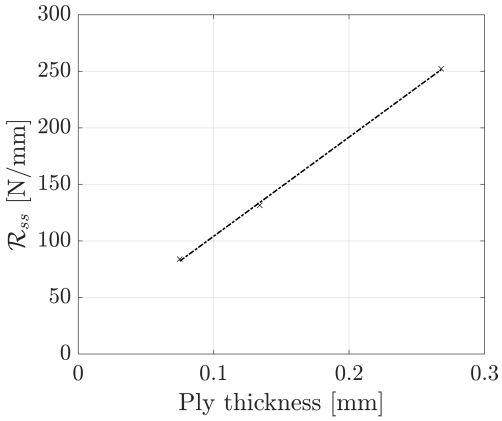

Figure 5.4: Steady state value of the longitudinal fracture toughness as a function of the ply thickness.

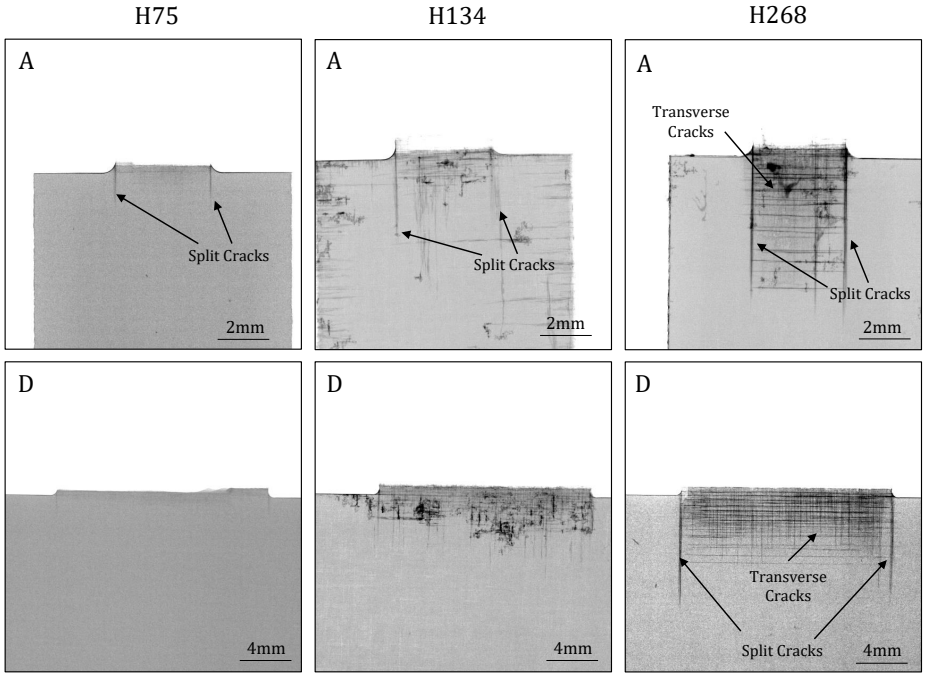

Figure 5.5: X-rays: extent of damage of representative A and D specimens of H75, H134 and H268 material systems.

5.2 Numerical analysis

In this section, a numerical analysis on the double edge notch tensile specimens is performed. The analysis focuses on the thinner and thicker material configurations, H75 and H268, respectively. First, the stress triaxiality in the double edge notch cross-ply specimens is evaluated to assess whether any significant effect of the laminate configuration on the stress distribution and consequent damage development has been overlooked. Secondly, the failure of the double edge notch specimen is simulated using a continuum damage model to predict fibre failure and transverse cracking and a cohesive zone model to represent delamination onset and propagation. The simulations are used to verify if the intralaminar fracture toughness is indeed an *in-situ* property that scales with the ply thickness.

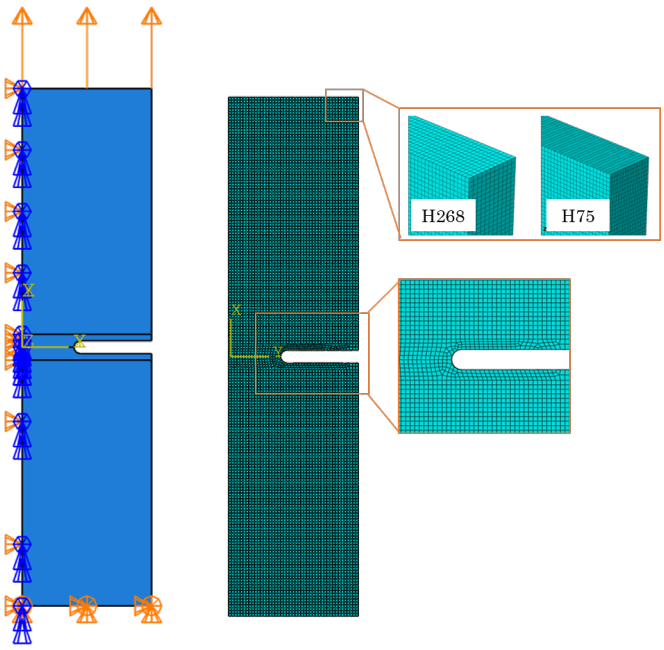

Figure 5.6: Boundary conditions and mesh used to simulate the double edge notch tension specimens.

5.2.1 Effect of stress triaxiality on the 0° plies

It has been reported by several authors [263–266] that the longitudinal tensile strength of carbon fibre reinforced polymer UD composites generally decreases with increasing compressive normal stresses acting on the transverse directions, σ_{22} and σ_{33}, with a change in failure mode from disperse axial splitting to a brittle local failure. This effect of the compressive normal stresses σ_{22} and σ_{33} on longitudinal fibre failure should be taken into account when comparing the mechanical behaviour of the two laminate configurations and to assess the validity of the testing methodology. In this work, to assess the effect of stress triaxiality on the low grade and high grade laminate configurations, linear elastic finite element simulations were performed.

The DENT Finite Element models used one 8-node linear brick reduced integration element (C3D8R) per ply thickness, t. The laminate was clamped on the

lower end, while on the other a displacement (through the definition of an appropriate smooth step amplitude) is applied to all nodes at the boundary. A mesh of $0.22\times0.22\times$t mm^3 was used for ply elements (see Fig. 5.6). Symmetry conditions along the XZ plane (where X is the loading direction and Z is the thickness direction) were defined to reduce the computational effort. At this stage, linear elastic simulations were performed and no plasticity or damage onset and propagation criteria was included in the finite element models. The material properties used are presented in Table 5.7.

One simulation per material configuration and geometry was performed and the third invariant of transversely-isotropic composite materials proposed by Camanho et al. [11] was computed to evaluate the stress triaxiality during loading:

$$I_3 = \sigma_{22} + \sigma_{33} \tag{5.14}$$

where σ_{22} and σ_{33} are the stress in the transverse and thickness directions, respectively. The third invariant was computed for all the elements and interpolated for the whole area of the ply. A schematic illustration of the third invariant on a representative 0° ply is shown in Fig. 5.7. To allow a better visualization of the stress state in the 0° ply, three vertical lines were placed in three distinct areas of the specimen: the ligament section, the notch tip and the notched section. The yellow and red lines correspond to the third invariant computed for the high-grade (H268) and low-grade (H75) laminates respectively. Regardless of the material configuration and geometry, the third invariant is positive in the whole area of the 0° plies and therefore, the stress triaxiality does not affect fibre failure for the studied configurations. Moreover, even though a slight disparity of the stress triaxiliaty at the notch tip was observed for the smaller geometries, the stress distribution in the 0° plies is very similar for the high and low-grade configurations.

From this analysis it was concluded that the 0° plies of both laminates are subjected to equivalent stress states and, therefore, the stress triaxiality should not affect the failure mechanisms differently in the two material configurations.

5.2.2 Simulation of failure of the double edge notch specimens

To verify if the intralaminar fracture toughness is indeed an *in-situ* property, the double edge notch tension specimens of H75 and H268 material systems were simulated for two scenarios. The first one corresponds to the hypothesis that the intralaminar fracture toughness is a function of the ply thickness, as proposed by several authors [257, 260]. The second scenario will test the hypothesis that the fracture toughness does not scale with the ply thickness, and that the higher apparent fracture toughness results from blunting the notch with subcritical failure mechanisms. As a result, three sets of numerical simulations were performed:

- H75: simulation of the H75 specimens using the fracture toughness associated with longitudinal failure determined experimentally for the H75 material system, $\mathcal{G}_{1+} = 83$N/mm;

- H268-83: simulation of the H268 specimens using the fracture toughness associated with longitudinal failure determined experimentally for the H75 material system, $\mathcal{G}_{1+} = 83$N/mm;

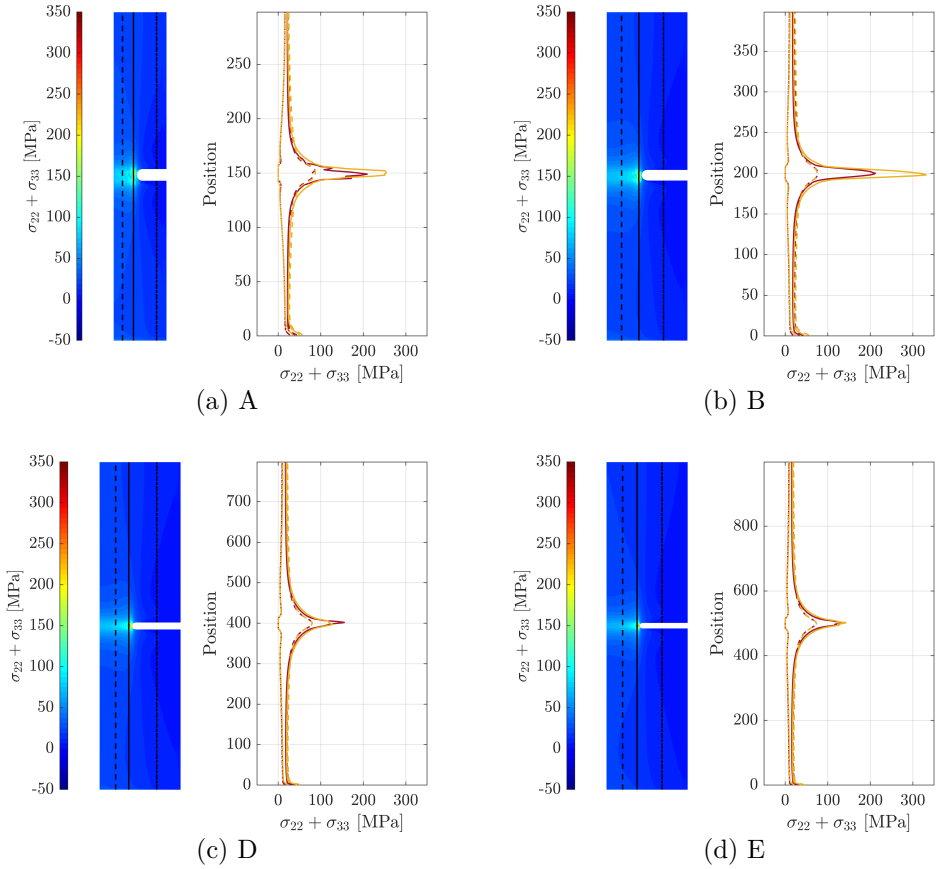

Figure 5.7: Third invariant $I_3 = \sigma_{22} + \sigma_{33}$ in a 0° ply in the geometries A, B, D and E. I_3 is represented in red for H75 and yellow for H268.

- H268-252: simulation of the H268 specimens using the fracture toughness associated with longitudinal failure determined experimentally for the H268 material system, $\mathcal{G}_{1+} = 252\text{N/mm}$.

The virtual test matrix is shown in Table 5.6. The details of the methodology and material models used are described in the following points.

5.2.2.1 Modelling strategy

The modelling strategy used to simulate the failure of the double notched specimens is presented hereafter. The same DENT Finite Element models used for the analysis on the effect of stress triaxiality were used here (see Section 5.2.1). Note that a structured mesh where the edges of the elements follow the fibre direction was used so that fibre splitting could be accurately captured.

5.2.2.1.1 Intralaminar damage

Intralaminar damage is simulated using the continuum damage model presented in Chapter 3. The continuum damage model predicts the following intralaminar failure mechanisms: longitudinal tensile failure, longitudinal compressive failure and transverse failure. A linear-elastic response followed by bi-linear softening and a

linear-elastic response followed by linear softening is assumed under longitudinal and transverse loading respectively, while a non-linear elasto-plastic response followed by linear softening is considered for in-plane shear.

Table 5.6: Summary of the numerical simulations performed.

		Softening law for longitudinal tension			
Ref.	Geometries	X_T [MPa]	f_{XT} [-]	$\mathcal{G}_{1+}$ [kJ/m^2]	f_{GT} [-]
H75	A, B, D, E	2182 [267]	0.2	83 [268]	0.5
H268-83	A, B, D, E	2299 [267]	0.2	83 [268]	0.5
H268-252	A, B, D, E	2299 [267]	0.2	252 [268]	0.5

Table 5.6 shows the parameters used in the softening laws for longitudinal tension used in the different sets of simulations. The remaining material properties of the two material systems are presented in Tables 5.7-5.9. Note that the longitudinal tensile strength measured for the high-grade material is 5% higher than that of the low-grade material, which is justified by the higher fibre volume fraction estimated for this material (see Table 5.1). The ply strengths related to matrix failure (transverse tensile strength, Y_T, transverse compressive strength, Y_C, and in-plane shear strength, S_L) were calculated as a function of the ply thickness and position of the ply using the equations proposed in Appendix B. For an embedded ply, the transverse tensile strength is the maximum between the tensile strength of a thin and a thick embedded ply:

$$Y_T^{is} = \max\left\{\sqrt{\frac{8\mathcal{G}_{Ic}}{\pi t \Lambda_{22}^o}} \quad , \quad 1.12\sqrt{2}Y_T^{UD}\right\} \tag{5.15}$$

were $\mathcal{G}_{Ic}$ is the transverse mode I fracture toughness, t is the ply thickness, Y_T^{UD} is the transverse tensile strength of a UD ply and Λ_{22}^o is given by [269]:

$$\Lambda_{22}^o = 2\left(\frac{1}{E_2} - \frac{\nu_{12}^2}{E_1}\right) \tag{5.16}$$

where E_1 and E_2 are the longitudinal and transverse Young's moduli, respectively, and ν_{12} is the Poisson's ratio. Similarly, the in-plane shear strength is given by the maximum between the strength of a thin and a thick embedded ply:

$$S_L^{is} = \max\left\{\sqrt{\frac{8\mathcal{G}_{IIc}K_1}{\pi t} + S_{LP}K_2} \quad , \quad \sqrt{2S_L^2 - S_{LP}K_2}\right\} \tag{5.17}$$

where $K_1 = \frac{KpG_{12}}{1+Kp}$ and $K_2 = \frac{S_{LP}}{1+Kp}$. G_{12} is in-plane shear modulus, S_{LP} is the shear stress that activates plastic flow, K_p is shear incremental stiffness under plastic flow, $\mathcal{G}_{IIc}$ is the transverse mode II fracture toughness and t is the ply thickness. The transverse compression strength reads:

$$Y_C^{is} = \frac{S_L^{is}Y_C^{UD}}{S_L^{UD}} \tag{5.18}$$

where Y_C^{UD} and S_L^{UD} are the transverse compression and in-plane shear strength of a UD ply, respectively. For an outer ply, the transverse tensile strength is given by

the maximum between the tensile strength of a thin outer ply and an UD ply:

$$Y_T^{is} = \max\Big\{1.78\sqrt{\frac{\mathcal{G}_{Ic}}{\pi t \Lambda_{22}^o}} \quad , \quad Y_T^{UD}\Big\} \tag{5.19}$$

Similarly, the in-plane shear strength is given by the maximum between the in-plane shear strength of a thin outer ply and an UD ply:

$$S_L^{is} = \max\Big\{\sqrt{\frac{4\mathcal{G}_{IIc}K_1}{\pi t} + S_{LP}K_2} \quad , \quad S_L^{UD}\Big\} \tag{5.20}$$

As in the case of the embedded ply, the transverse compression strength is given by Eq. (5.18).

5.2.2.1.2 Interlaminar damage

Interlaminar damage was simulated using the cohesive zone model implemented in ABAQUS [229]. The cohesive zone model relates the tractions, τ, to the displacement jumps, Δ, at the interfaces where crack propagation occurs. In this work, the quadratic nominal stress criterion was used for damage initiation and the Benzeggagh-Kenane fracture criterion was used for damage propagation [216]. The engineering solutions proposed by Turon and co-authors [212, 213] and by Cui et al. [208] presented in Appendix C were used to calculate some of the properties of the cohesive elements to ensure proper energy dissipation in mixed-mode loadings, and to artificially account for the effects of pressure and friction. The interfacial properties of the two material systems used are presented in Table 5.10.

Table 5.7: Ply elastic properties of H268 and H75 carbon/epoxy systems.

Elastic		H268		H75	
E_1	[MPa]	161600	Ref. [267]	146100	Ref. [267]
E_{1c}	[MPa]	101252	Ref. [268]	117930	Ref. [268]
E_2	[MPa]	9300	Ref. [267]	8700	Ref. [267]
G_{12}	[MPa]	4790	Ref. [267]	4600	Ref. [267]
ν_{12}	[-]	0.36	Ref. [267]	0.34	Ref. [267]

Table 5.8: Ply fracture toughness of H268 and H75 carbon/epoxy systems.

Fracture		H268		H75	
$\mathcal{G}_{1+}$	[kJ/m^2]	83 /252		83	
f_{GT}	[-]	0.5	Note (1)	0.5	Note (1)
$\mathcal{G}_{1-}$	[kJ/m^2]	60.0	Ref. [268]	60.0	Ref. [268]
$\mathcal{G}_{2+}$	[kJ/m^2]	0.45	Ref. [267]	0.3	Ref. [267]
$\mathcal{G}_{2-}$	[kJ/m^2]	1.209	Ref. [267]	1.209	Ref. [267]
$\mathcal{G}_6$	[kJ/m^2]	0.85	Ref. [267]	0.8	Ref. [267]

(1) Inversely identified using the DENT simulations of H75 material system

Table 5.9: Ply strengths of H268 and H75 carbon/epoxy systems.

Strength		H268		H75	
X_T	[MPa]	2299	Ref. [267]	2182	Ref. [267]
f_{XT}	[-]	0.2	Note (1)	0.2	Note (1)
X_C	[MPa]	1187.	Ref. [268]	1615.	Ref. [268]
f_{XC}	[-]	0.6	Note (2)	0.6	Note (2)
Y_T^{UD}	[MPa]	45.0	Ref. [267]	45.0	Ref. [267]
Y_T(inner)	[MPa]	144.2	Note (3)	211.2	Note (3)
Y_T(outer)	[MPa]	90.8	Note (3)	132.9	Note (3)
Y_C^{UD}	[MPa]	161.4	Ref. [268]	161.4	Ref. [268]
Y_C(inner)	[MPa]	211.9	Note (3)	301.8	Note (3)
Y_C(outer)	[MPa]	161.4	Note (3)	221.5	Note (3)
S_L^{UD}	[MPa]	82.	Ref. [267]	82.	Ref. [267]
S_L(inner)	[MPa]	107.7	Note (3)	153.3	Note (3)
S_L(outer)	[MPa]	82.	Note (3)	112.6	Note (3)
S_L^P	[MPa]	47.0	Note (4)	47.0	Note (4)
K_p	[-]	0.19	Note (4)	0.21	Note (4)

(1) Inversely identified using the DENT simulations of H75 material system
(2) Assumed
(3) Calculated following Appendix B
(4) Best fitting of shear stress-strain curve of the material

Table 5.10: Interlaminar material properties.

Elastic		H268		H75	
K_n	[N/mm^3]	10^6	Ref. [177]	10^6	Ref. [177]
Strengths					
τ_n	[MPa]	45.0	Ref. [267]	45.0	Ref. [267]
$\tau_s h$	[MPa]	82.	Ref. [267]	82.	Ref. [267]
Fracture					
$\mathcal{G}_{Ic}$	[kJ/m^2]	0.45	Ref. [267]	0.3	Ref. [267]
$\mathcal{G}_{IIc}$	[kJ/m^2]	0.85	Ref. [267]	0.8	Ref. [267]
η_{B-K}	[-]	2.0	Ref. [267]	2.0	Ref. [267]

5.2.2.2 Finite element analysis

Fig. 5.8 and Table 5.11 show the experimental and the predicted strengths of the two material systems. The damage extension at the point of maximum load of all the simulations performed is shown in Fig. 5.9, where the intralaminar damage is shown in red, and the interlaminar damage is shown in blue. Except for the smallest geometry (A), the notched strengths predicted for H75 specimens are extremely accurate with relative errors below 5%. As expected, the model predicts the development of a clean through-the-thickness crack, where fibre splitting is absent and only a small amount of transverse cracks develop on the outer 90° plies for the smaller geometries. This is in good agreement with the damage extension experimentally observed (Fig. 5.5).

As shown in Table 5.6, the H268 samples were simulated using two different softening laws associated with longitudinal failure: using the fracture toughness measured experimentally for H268 (H268-252) and using the softening law identified for the H75 material system (H268-83). While the notched strengths predicted for H268-252 strategy are highly overpredicted with relative errors ranging from 13% to 56%, the notched strengths predicted for H268-83 are in better agreement

with the experimental data, even though the relative errors still range from -3% to 20%. Extensive fibre splitting is predicted using both strategies which is in good agreement with the experimental observations (Fig. 5.5). Extensive matrix cracking of the outer 90° plies is predicted for all H268-252 geometries simulated, which is reduced in the H268-83 simulations.

Table 5.11: Experimental and numerical double edge notched tension strengths obtained for H268 and H75 carbon/epoxy material systems.

		H268: Exp		H268-83: Num		H268-252: Num	
Ref.	2w [mm]	Exp. [MPa]	Std. [MPa]	Num. [MPa]	Error (%)	Num. [MPa]	Error (%)
A	10	339.09	17.99	330.70	-2%	384.8	13%
B	20	308.53	11.74	297.8	-3%	373.7	21%
D	40	225.34	11.40	272.0	21%	351.7	56%
E	50	220.05	4.64	249.8	14%	340.4	54%
		H75: Exp		H75: Num			
Ref.	2w [mm]	Exp. [MPa]	Std. [MPa]	Num. [MPa]	Error (%)		
A	10	289.83	19.51	242.8	-16%		
B	20	208.85	11.75	211.1	1%		
D	40	164.59	1.30	172.1	5%		
E	50	136.11	3.93	143.2	5%		

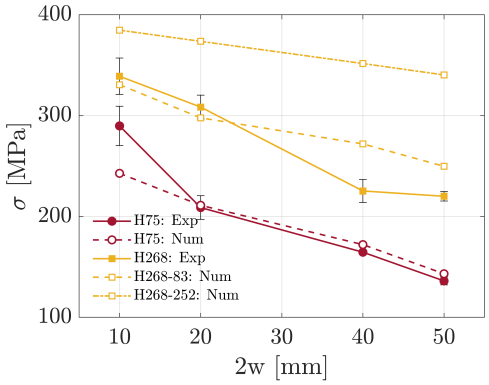

Figure 5.8: Experimental and predicted notched strengths of H75 and H268 material systems.

Note that the *in-situ* shear strength plays a particularly important role in controlling the appearance and propagation of split cracks at the vicinity of the notches. In fact, as shown in Table 5.9, the in-plane shear strengths are around 30% higher for the H75 material system compared to that of the H268 material system. This leads to the appearance of split cracks on the high-grade material that results in the redistribution of stresses and in the reduction of the stress concentration at the vicinity of the notch that are responsible for ultimate failure of the 0° plies. Contrary, for thinner plies, the stress redistribution is limited which leads to earlier failure of the laminate.

To further validate the analysis, the energy dissipated due to in-plane shear plasticity and due to in-plane damage propagation before final failure is computed for all the geometry/material configurations simulated. The goal of this analysis is to clarify whether the two laminate configurations behave similarly and/or there is a significant effect of in-plane plasticity that renders the direct comparison between the laminates inappropriate. The plastic work due to in-plane shear plasticity reads:

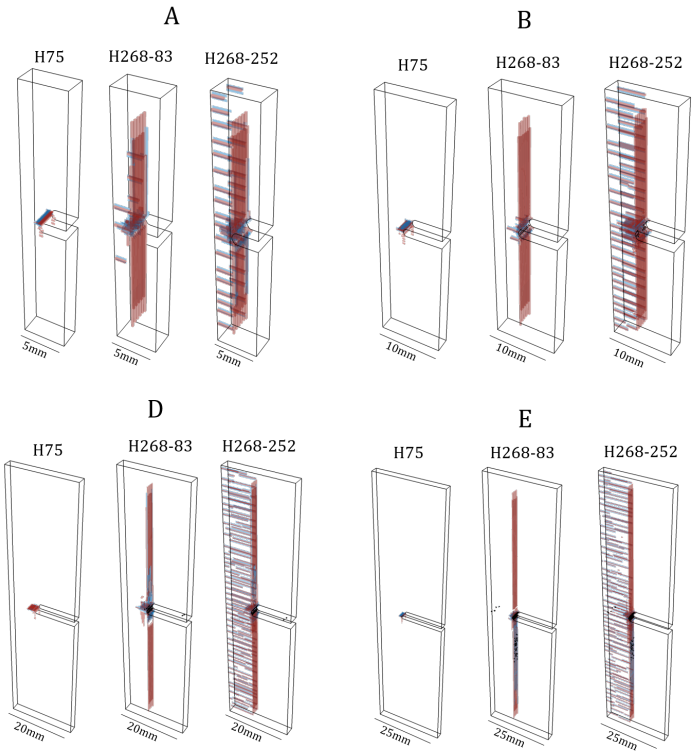

Figure 5.9: Damage extension at the point of maximum load. Intralaminar damage is shown in red and interlaminar damage is shown in blue.

$$\mathcal{G}^p = \int_0^t \int_V \sigma_{12} \dot{\gamma}_{12}^p \mathrm{d}V \mathrm{d}t \tag{5.21}$$

where σ_{12} is the in-plane shear stress, and $\dot{\gamma}_{12}^p$ is the time derivative of the plastic strain. The energy dissipated due to in-plane shear damage reads:

$$\mathcal{G}^d = \int_0^t \int_V \frac{1}{2G_{12}} \left(\frac{\sigma_{12}}{1 - d_6} \right)^2 \dot{d}_6 \mathrm{d}V \mathrm{d}t \tag{5.22}$$

where d_6 is the shear damage variable and $\dot{d}_6$ is the corresponding time derivative. The dissipated energy is shown as a function of the applied displacement in Fig. 5.10 for the four geometries simulated. For the low-grade material (H75), nearly no energy is dissipated before final failure due to in-plane damage propagation. In fact, this is in line with the damage extension shown in Fig. 5.9, where no fibre splitting is predicted. The energy dissipated due to in-plane plasticity evolves quadratically with the applied displacement up to the point of final failure of the specimen. Contrary, in the high-grade material (H268), in-plane shear damage is triggered at low applied displacement and then evolves linearly. The energy dissipated due to in-plane shear plasticity evolves quadratically in a first stage, while the split cracks develop, and then evolves linearly when the split crack length stabilizes.

The direct comparison between the energy dissipation is only valid up to the point of damage initiation, since the appearance of split cracks in the 0° plies in the

high grade material severely changes the stress state from that of the purely elasto-plastic scenario. Nonetheless, the evolution of the energy dissipated due to shear plasticity is similar between the two material configurations and even though there is up to 40% difference particularly in configurations D and E, this difference does not justify the difference in the damage mechanisms and in the notched strength reported experimentally and numerically.

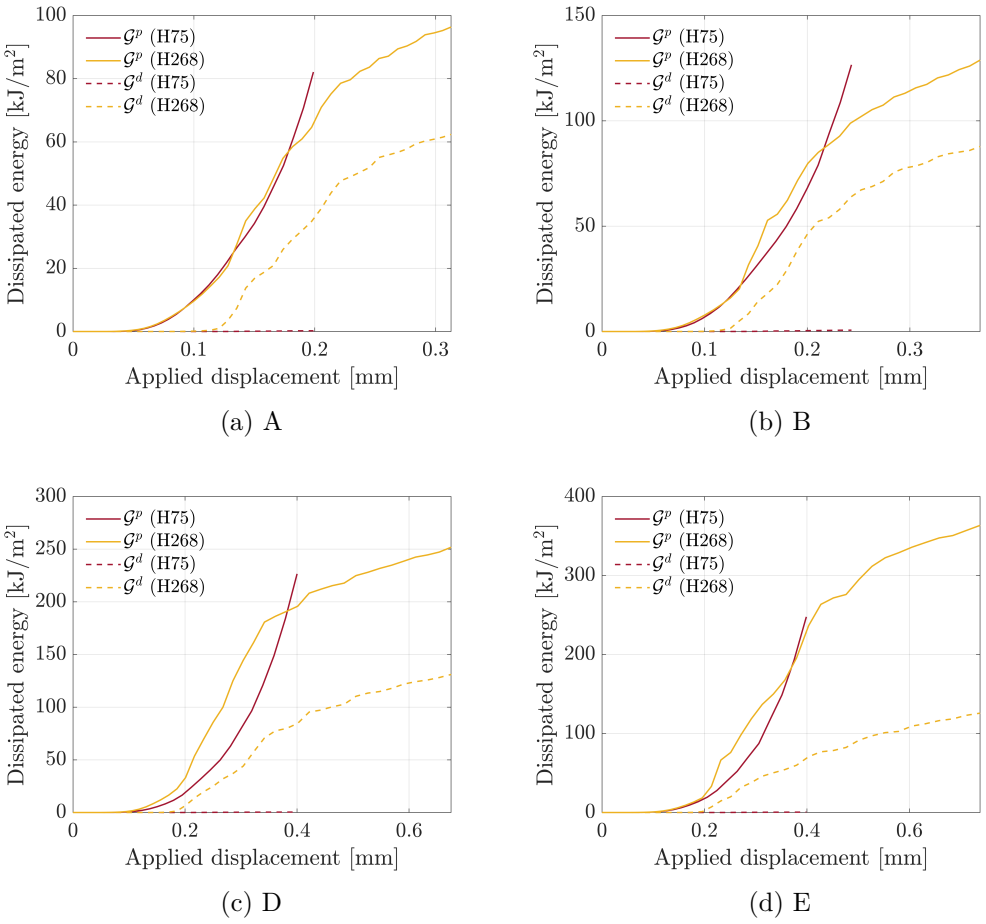

Figure 5.10: Dissipated energy due to in-plane shear plasticity $\mathcal{G}^p$ and due to shear damage propagation $\mathcal{G}^d$ as a function of the applied displacement. The dissipated energy is represented in red for H75 and yellow for H268-83.

This analysis indicates that the intralaminar fracture toughness of the 0° plies is not thickness dependant. If the combination of ply material models and modelling strategy are defined so that the model is able to capture the full extent of damage, particularly shear induced split cracking on the 0° plies, the intralaminar fracture toughness should not vary as a function of the thickness when modelling damage propagation at the ply mesoscale.

5.3 Concluding remarks

The effect of ply thickness on the effective intralaminar fracture toughness was studied by measuring the crack resistance curves associated with the longitudinal tensile failure of composite laminates with different ply thickness. Double edge notch tension specimens of the same material system and three different ply thicknesses were tested to identify the size effect law required to determine the crack resistance curves related to crack propagation. The notched strengths and the corresponding apparent intralaminar fracture toughness were shown to vary linearly as a function of the ply thickness. It was observed that the increase in notched strength as a function of the ply thickness is related to the appearance of subcritical damage around the vicinity of the notch that enables stress redistribution, and the consequent reduction of the stress concentration.

The numerical models developed demonstrated that if the notch blunting mechanisms are properly represented, the laminate strength is well predicted for a constant value of the ply intralaminar fracture toughness. This supports the hypothesis that these mechanisms are responsible for the higher strength observed in the notched laminates that use thicker plies, and that the intralaminar fracture toughness used in mesomodels should not be scaled with the ply thickness. Nevertheless, the laminate fracture toughness, which is a property used in strength prediction models developed at the laminate length scale, should be measured for different ply thickness, as this property incorporates the dissipative mechanisms that occur in the plies, as well as the modification of the initial boundary-value problem resulting from the subcritical splitting cracks.

Chapter 6

The effects of ply thickness and reinforcement configuration on the strength of composite structural details

Having elucidated the effect of the ply thickness on the fracture toughness of the 0° plies, a property of fundamental importance for the strength prediction methods, it is now necessary to study in detail the performance of thin-ply composites when used in structural details.

Extensive experimental campaigns have been carried out to evaluate the performance of thin-ply laminates for different types of loading and structural details to better understand the mechanical performance of this new type of material. It has been shown by several authors [1, 6, 18, 19, 26] that thin-ply laminated composites can suppress microcracking, delamination and splitting damage under most loading conditions and, therefore, their failure is mostly controlled by fibre failure. This strengthening effect that inhibits the excessive growth of cracks in off-axis plies within a laminate is a consequence of the *in-situ* effect, which is characterized by an increase in transverse and shear ply strengths in multidirectional laminates with the decrease of ply thickness [4, 27–33].

In the absence of geometrical discontinuities, the lack of subcritical damage in the off-axis plies and delamination within the laminate ensures the structural integrity of thin-ply laminates until the abrupt failure of the longitudinal plies occurs. Consequently, multidirectional thin-ply laminates have improved unnotched strength compared to equivalent conventional grade and thick-ply laminates [1, 6, 19].

In the presence of geometrical discontinuities or discrete damage in structures loaded in tension, the lack of progressive damage mechanisms before final failure has the inverse effect: while in conventional thick laminates, splitting and matrix cracking appear at the vicinity of the notches, promoting a local stress relaxation, in thin-ply laminates, this blunting mechanism is inhibited, which means that the stress concentration around the notch is not relaxed, leading to lower strengths [1, 6, 18–20].

The effect of ply thickness on the performance of notched laminated structures under compressive loads is less evident since opposing effects are involved. On one hand, thin-ply laminates have higher compressive strength consequence of the homogeneity of the micro-structure and, therefore, are expected to have higher compressive strength in the presence of stress concentrations. Moreover, the use of thin plies delays subcritical damage which suppresses the development of extensive matrix damage and delamination and increases the compressive stability of the

laminates [1, 24, 26]. On the other hand, similarly to notched structures loaded in tension, the delay of damage onset might inhibit stress redistribution around the notch and lead to premature brittle failure of the structures [36]. Nonetheless, these conflicting effects have been reported to generally result in an increase of the notched compressive strength with the decrease of ply thickness.

An improved performance of thin-ply laminates when subjected to bearing loads has also been reported by several authors [1, 18, 24] and it is generally attributed to the ability of thin-ply laminates to suppress the onset and propagation of damage mechanisms such as matrix cracking, delamination, fibre kinking and through-thickness shear cracks.

Several experimental campaigns to assess the effect of ply thickness on the global performance of carbon-epoxy laminated composites have been carried out and the corresponding results have been conveniently justified and validated. Despite the large number of studies previously conducted on thin-ply laminates, there is no information about the effect of geometry reinforcement and ply thickness using a given material system. With this in mind, an extensive experimental campaign was performed featuring nine equivalent multidirectional laminates made from unidirectional tapes, non-crimp fabrics and spread-tow fabrics with different fibre areal weights and the same carbon-epoxy material system. This study, will provide insight into the effect of ply thickness and the effect of type of geometry reinforcement on the damage mechanisms that dominate failure and on the ultimate strength of multidirectional laminates.

6.1 Experimental work

6.1.1 Laminate definition

Three types of T700/M21 carbon-epoxy material systems were used in this study: unidirectional prepreg tapes (UD), spread tow prepreg fabrics (STF) and non-crimp fabrics (NCF). Three UD prepreg tapes with fibre areal weight (FAW) of 75g/m^2, 134g/m^2 and 268g/m^2, two STF with FAW of 160g/m^2 and 240g/m^2 and two NCF with FAW of 134g/m^2 and 268g/m^2 were used. 0° dominated hard symmetric multidirectional laminates similar to an industry baseline laminate (H134) were selected following two criteria: first the laminates should have identical thickness, secondly, they should have similar in-plane engineering elastic properties. In line with other studies reported in the literature, the selection of laminates with similar elastic properties allows a detailed comparison of the damage mechanisms associated with failure of each laminate configuration. But, more importantly, imposing the laminate thickness to be equal to that of an industrial defined baseline allows assessing the consequences of using each material grade and geometry reinforcement for a particular application. This design constrain is more in line with the applicability mindset of the design process. The laminate stacking sequences are presented in Table 6.1.

Furtado et al. [19] and Arteiro et al. [24, 270] demonstrated that selective ply-level hybridization, where thin off-axis plies are combined with intermediate grade 0° plies, resulted in a globally enhanced notched behaviour under tensile loading without compromising the unnotched and fatigue responses. The thicker 0° plies were shown to promote longitudinal split cracking near the stress concentration

Table 6.1: Stacking sequences of the specimens manufactured. The carbon-epoxy material system used is T700/M21. The fibre areal weight (FAW) and effective FAW differ for the STF and NCF laminates, since the FAW is given by fabric layer (two plies). $ stands for "centre symmetric", i.e. the ply at the symmetry plane is not repeated.

Ref.	Type	FAW	Effective FAW	Stacking sequence
H268	UD	268g/m^2	268g/m^2	$[45/-45/0/90]_{\$}$
H134	UD	134g/m^2	134g/m^2	$[45/-45/0/45/-45/90/0]_{\$}$
H75	UD	75g/m^2	75g/m^2	$[45/-45/0/45/-45/90/0/45/-45/90/0]_{\$}$
H75-H1	UD	75/134g/m^2	75/134g/m^2	$[45/-45/45/-45/90/0_{134}/45/-45/90/0_{134}]_{\$}$
H75-H2	UD	75/268g/m^2	75/268g/m^2	$[45/-45/45/-45/90/0_{268}/45/-45/90]_{S}$
O240	STF	240g/m^2	120g/m^2	$[(45/-45)/(0/90)/(45/-45)/(0/90)]_{\$}$
O160	STF	160g/m^2	80g/m^2	$[((45/-45)/(0/90))_2/(45/-45)/(0/90)]_{\$}$
C268	NCF	268g/m^2	134g/m^2	$[(45/0)/(-45/90)/(22.5/-22.5)]_{S}$
C134	NCF	134g/m^2	67g/m^2	$[(45/0)/(-45/90)/(45/0)/(-45/90)/(45/0)/(-45/0)]_{S}$

points resulting in a more efficient stress redistribution along the loading direction and consequent higher notched strengths compared to equivalent thin and intermediate grade laminates. Additionally to the traditional UD, NCF and STF laminates, in this study, two hybrid laminates were defined, where thin transverse and off-axis plies are combined with intermediate grade (H75-H1) and high grade plies (H75-H2). The concept of selective ply hybridization is tested in more general loading conditions, including filled-hole and open-hole compression, which were not previously considered.

To ensure that a proper laminate characterization and that a fair comparison between the material grades and type of reinforcement could be made, the reinforcing fibres, epoxy resin, sizing and impregnation techniques used to produce the different material systems were kept constant to the greatest possible extent. The laminates were produced and cured in an autoclave following the manufacturer-specified cure procedure. Plain strength tension/compression, open-hole tension/compression, filled-hole compression and bolt bearing specimens were machined from the cured plates.

6.1.2 Comparison between the laminates

The Classical Lamination Theory was used to calculate the elastic properties of each laminate (see Table 6.3) using the ply properties shown in Table 6.2. Note that the elastic properties vary from laminate to laminate. Particularly, the Young's Modulus for longitudinal tension is substantially higher for H268 and H75-H2 compared to that of the remaining lay-ups and a variation of up to 30% (between O160 and H268 laminates) was identified. This discrepancy is due to differences in fibre volume fraction between the material grades and geometry reinforcements, inevitable differences in percentage of 0°, 90° and 45° plies and design limitations as a consequence of the inherent geometry of the spread-tow fabrics (equal number of 0° and 90° tows). Since the laminates are not directly comparable, the analysis conducted in this work will focus not only on the strengths but also on the normalized strengths. The normalization procedure per test method is reported in the following

sections.

Table 6.2: Ply elastic properties.

Mat.	E_1 [MPa]	E_{1c} [MPa]	E_2 [MPa]	G_{12} [MPa]	ν_{12} [-]
H268	161600†	101252††	9300†	4790†	0.36†
H134	139800†	114602††	8900†	4590†	0.32†
H75	146100†	117930††	8700†	4600†	0.34†
O240‡	66909	65089	66909	4780	0.097
O160‡	66229	63210	66229	4780	0.061
C268‡‡	139800	114602	8900	4590	0.32
C134†‡	146100	117930	8700	4600	0.34

† Data provided by AMADE, University of Girona [267].
†† Data obtained from the longitudinal compression tests [268].
‡ Assumed to be equal to the properties measured in Ref. [270].
‡‡ Assumed to be equal to the properties measured for H134.
†‡ Assumed to be equal to the properties measured for H75.

Table 6.3: Engineering properties of H268, H134, H75, H75-H1, H75-H2, O240, O160, C268 and C134 lay-ups. These properties were calculated using the classical lamination theory.

Laminate		E_x [MPa]	E_y [MPa]	G_{xy} [MPa]	ν_{xy} [-]
H268	Tension	65987	46957	25964	0.45
	Compression	43657	32119	17060	0.42
H134 (Bsl.)	Tension	50827	42325	23910	0.44
	Compression	43044	36113	20035	0.43
H75	Tension	53960	48267	23388	0.39
	Compression	44940	40381	19365	0.38
H75-H1	Tension	53938	47740	23069	0.39
	Compression	45340	40015	19113	0.38
H75-H2	Tension	65893	45330	21864	0.40
	Compression	46558	38020	18048	0.38
O240	Tension	44308	44308	19475	0.40
	Compression	43248	43248	18887	0.40
O160	Tension	45505	45506	19197	0.35
	Compression	43649	43648	18421	0.35
C268	Tension	66766	38997	20288	0.43
	Compression	55852	33321	17139	0.42
C134	Tension	65480	44804	21040	0.39
	Compression	54066	37553	17519	0.38

6.1.3 Test details

The specimen geometries and test details of the plain strength tension and compression, open-hole tension and compression, filled-hole compression and bolt bearing tests are presented in the following points. A schematic representation of the tests is given in Fig. 6.1.

6.1.3.1 Plain strength tension tests

Three unnotched specimens per material configuration were tested following the ASTM D3039/D3039M test standard [271]. Specimens with a nominal width (W) of 25mm and a nominal length (L) of 250mm were used. The tests were

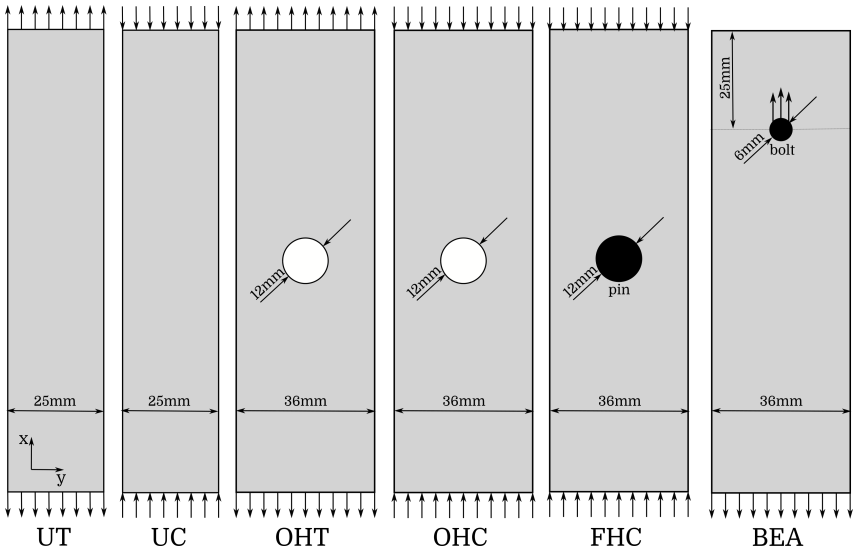

Figure 6.1: Schematic representation of the test cases.

performed under displacement control, at a speed of 1.0mm/min, in an Instron 4208 electro-mechanical universal testing machine equipped with a 200kN load cell. Aluminium end tabs were used in the unnotched specimens to avoid failure at the gripping sections. Hydraulic grips with a clamping pressure of 200bar were used to hold and apply the tensile load to the test specimen. The unnotched strengths were obtained dividing the failure load by the cross-section of the specimen:

$$X_L^T = \frac{P}{Wt} \tag{6.1}$$

where P is the maximum load and W and t are the width and thickness of the laminate. To account for the differences in stacking sequence and fibre volume fraction between the different laminates and material grades, the unnotched strengths were normalized by the longitudinal Young's modulus:

$$\sigma_N = \frac{X_L^T}{E_x} \tag{6.2}$$

6.1.3.2 Plain strength compression tests

Three unnotched specimens per material configuration were tested following the ASTM D6484/D6484M test standard [272]. Specimens with a nominal width (W) of 25mm and a nominal length (L) of 305mm were used. Only the nominal width of the samples H268 was 36mm. The compression rig was clamped using M8 bolts fastened with a torque of 8Nm. The tests were performed under displacement control, at a controlled speed of 1.0mm/min, in a servo-hydraulic MTS 810 testing machine with a load capacity of 250kN, using a 250kN load cell. The unnotched strengths were obtained dividing the failure load by the cross-section of the specimen:

$$X_L^C = \frac{P}{Wt} \tag{6.3}$$

To account for the differences in stacking sequence and fibre volume fraction between the different laminates and material grades, the unnotched strengths were

also normalized by the longitudinal Young's modulus:

$$\sigma_N = \frac{X_L^C}{E_x} \tag{6.4}$$

6.1.3.3 Open-hole tension tests

Three open-hole tension specimens per material configuration were tested following the ASTM D5766/D5766M test standard [273]. Specimens with a nominal width (W) of 36mm, a nominal length (L) of 250mm and a hole diameter of 12mm were used. The tests were performed under displacement control, at a speed of 1.0mm/min, in an Instron 4208 electro-mechanical universal testing machine equipped with a 200kN load cell. Hydraulic grips with a clamping pressure betweeen 100-200bar were used to hold and apply the tensile load to the test specimen. The unnotched strengths were obtained dividing the failure load by the cross-section of the specimen:

$$\overline{\sigma}^T = \frac{P}{Wt} \tag{6.5}$$

To account for the differences in stacking sequence and fibre volume fraction between the different laminates and material grades, the notch sensitivity of each laminate was compared by using the normalized notched strength [70]:

$$\overline{\sigma}_N = \frac{\overline{\sigma}}{X_L} \tag{6.6}$$

where $\overline{\sigma}$ is the notched strength, and X_L is the unnotched strength of the laminate. The behaviour of a notched coupon is limited by two extreme scenarios:

- **Notch sensitivity**: the normalized notched strength of the laminate is a function only of the stress concentration factor, K_T. It corresponds to a brittle behaviour and reads:

$$\overline{\sigma}_S = \frac{1}{K_T} \tag{6.7}$$

The stress concentration factor, K_T, is given as [240]:

$$K_T = R_K K_T^{\infty} \tag{6.8}$$

where the stress concentration factor of an infinite plate with a centre hole, K_T^{∞}, is given by [240]:

$$K_T^{\infty} = 1 + \sqrt{2\left(\sqrt{\frac{E_x}{E_y}} - \nu_{xy}\right) + \frac{E_x}{G_{xy}}} \tag{6.9}$$

and the finite width correlation factor, R_K, is [240]:

$$R_K = \left\{ \frac{3(1-2R/W)}{2+(1-2R/W)^3} + \frac{1}{2}\left(\frac{2R}{W}M\right)^6 (K_T^{\infty}-3)\left[1-\left(\frac{2R}{W}M\right)^2\right] \right\}^{-1} \tag{6.10}$$

and M is a geometrical parameter defined as [240]:

$$M^2 = \frac{\sqrt{1-8\left[\frac{3(1-2R/W)}{2+(1-2R/W)^3}-1\right]}-1}{2(2R/W)^2} \tag{6.11}$$

- **Notch insensitivity**: in this case the normalized notched strength of the laminate is a function of the geometry of the specimen:

$$\overline{\sigma}_I = 1 - \frac{2R}{W} \tag{6.12}$$

For $2R/W = 1/3$, $\overline{\sigma}_I = 1 - 2R/W = 2/3$ for notch insensitivity.

Since the notch sensitivity limit varies from laminate to laminate, a notch sensitivity ratio was defined as

$$\eta = \frac{\overline{\sigma}_N - \overline{\sigma}_S}{\overline{\sigma}_I - \overline{\sigma}_S} \tag{6.13}$$

η ranges from 0 to 1: the former represents notch sensitivity and the latter notch insensitivity.

The sensitivity to the loading direction in the presence of stress concentrations was assessed for the UD laminates (H75, H134, H268, H75-H1 and H75-H2) by testing off-axis open-hole tension specimens, where the stacking sequences are rotated 30°, 60° and 90°.

6.1.3.4 Open-hole compression tests

Three open-hole compression specimens per material configuration were performed following the ASTM D6484/D6484M test standard [272]. Specimens with a nominal width (W) of 36mm, a nominal length (L) of 305mm and a hole diameter of 12mm were used. The compression rig was clamped using M8 bolts fastened with a torque of 8Nm. The tests were performed under displacement control, at a controlled speed of 1.0mm/min, in a servo-hydraulic MTS 810 testing machine with a load capacity of 250kN, using a 250kN load cell. The unnotched strengths were obtained dividing the failure load by the cross-section of the specimen:

$$\overline{\sigma}^C = \frac{P}{Wt} \tag{6.14}$$

To account for the differences in stacking sequence and fibre volume fraction between the different laminates and material grades, the notch sensitivity of each laminate was compared as explained in Section 6.1.3.3.

6.1.3.5 Filled-hole compression tests

Three filled-hole compression specimens per material configuration were performed following the ASTM D6742/D6742M test standard [274]. Specimens with a nominal width (W) of 36mm, a nominal length (L) of 305mm and a hole diameter of 12mm were used. The compression rig was clamped using M8 bolts fastened with a torque of 8Nm. The tests were performed under displacement control, at a controlled speed of 1.0mm/min, in a servo-hydraulic MTS 810 testing machine with a load capacity of 100kN, equipped with a 100kN load cell. The notched strengths were obtained dividing the failure load by the cross-section of the specimen:

$$\overline{\sigma} = \frac{P}{Wt} \tag{6.15}$$

To account for the differences in stacking sequence and fibre volume fraction between the different laminates and material grades, the filled-hole compression strengths were normalized by the unnotched compression strength of the corresponding laminate:

$$\sigma_N = \frac{\overline{\sigma}}{X_C^L} \tag{6.16}$$

6.1.3.6 Bolt bearing tests

Three bolt-bearing tests per material configuration were performed following the ASTM D5961/D5961M test standard [275]. Specimens with a nominal hole diameter (D) of 6mm, end distance (e) of 25mm, width (W) of 36mm, and nominal length (L) of 215mm were used. An M6 bolt was used with washers subjected to a "finger-tight" clamping pressure, corresponding to a torque T=2.2Nm. The tests were conducted in a servo-hydraulic MTS 810 testing machine with a load capacity of 100kN, equipped with a 100kN load cell. The tests were performed under displacement control, at a controlled speed of 1.0mm/min. The end of the specimen far from the bearing hole was clamped using a bolted clamping rig with six M10 bolts fastened with a torque of 55–60Nm. The bearing stress is given by:

$$\sigma^{br} = \frac{P}{Dt} \tag{6.17}$$

where P is the load and D and t are the hole diameter and thickness of the laminate. To account for the differences in stacking sequence and fibre volume fraction between the different laminates and material grades, the bolt bearing strengths were also normalized by the unnotched compression strength of the corresponding laminate:

$$\sigma_N = \frac{\sigma^{br}}{X_C^L} \tag{6.18}$$

6.1.4 Digital image correlation set-up

The digital image correlation (DIC) technique was used in this study to evaluate the in-plane displacement and strain fields and detect strain concentrations corresponding to surface cracking in the unnotched and open-hole tension specimens during loading. Before testing, the surface of the specimens were cleaned using sandpaper and acetone and the specimens were sprayed with black and white ink to generate a random distribution of granular dots required by the DIC system.

The MatchID® software was used for the acquisition and the post-processing of the images. A single Manta G-505 camera from Allied Vision equipped with a Nikon AF 200mm f/4 D ED IF Micro lens was used to capture the images during loading. During the test, the optical system was positioned perpendicular to the surface of the specimens and a light system was used to ensure an even lighting of the specimen.

A performance analysis tool was used to carry out the proper selection of the DIC setting parameters including subset size, subset step, strain window, correlation criterion, shape function, and piece-wise polynomial order for the strain reconstruction. A suitable balance in between spatial resolution and accuracy was achieved for all tested materials.

Table 6.4: Mean strength, standard deviation and standard error obtained for the nine material configurations.

Lam		PST	PSC	OHT	OHC	FHC	BEA INI	BEA MAX
H268	Mean [MPa]	759	488	373	254	289	847	1060
	Std. dev. [MPa]	19.4	36.4	17.6	4.1	7.7	48.2	20.3
	Std. error [MPa]	11.2	21.0	10.2	2.4	4.5	27.8	11.7
H134	Mean [MPa]	653	581	302	252	310	912	1116
	Std. dev. [MPa]	32.1	6.3	2.1	10.2	31.6	20.4	16.7
	Std. error [MPa]	18.5	3.6	1.2	5.9	18.3	11.8	9.7
H75	Mean [MPa]	802	603	333	263	322	1102	1225
	Std. dev. [MPa]	12.6	31.0	6.6	6.1	4.0	75.4	17.8
	Std. error [MPa]	7.3	17.8	3.8	3.5	2.33	42.9	10.3
H75-H1	Mean [MPa]	844	602	339	264	341	-	-
	Std. dev. [MPa]	12.1	42.7	38.5	8.3	10.3	-	-
	Std. error [MPa]	7.0	24.7	22.2	4.8	5.9	-	-
H75-H2	Mean [MPa]	951	665	429	281	349	-	-
	Std. dev. [MPa]	13.4	44.8	15.7	9.7	23.8	-	-
	Std. error [MPa]	7.7	25.9	9.1	5.6	13.7	-	-
O240	Mean [MPa]	686	531	321	255	260	903	1100
	Std. dev. [MPa]	46.0	25.2	10.4	20.5	9.8	25.7	27.6
	Std. error [MPa]	25.6	14.5	6.0	11.9	5.6	14.8	15.9
O160	Mean [MPa]	719	566	334	232	306	914	1140
	Std. dev. [MPa]	21.4	26.3	1.5	17.8	8.4	6.2	50.9
	Std. error [MPa]	12.3	15.2	0.8	10.3	4.9	3.6	29.4
C268	Mean [MPa]	-	605	416	279	315	860	1081
	Std. dev. [MPa]	-	4.5	20.1	10.9	33.8	48.2	32.0
	Std. error [MPa]	-	2.6	16.9	6.3	19.5	27.5	18.5
C134	Mean [MPa]	946	664	371	291	323	995	1116
	Std. dev. [MPa]	29.1	14.3	29.4	5.7	13.3	30.0	60.0
	Std. error [MPa]	16.8	8.4	11.6	3.3	7.7	17.3	34.6

6.2 Experimental Results

This experimental study is focused on the i) effect of ply thickness in UD, STF and NCF multidirectional laminates, ii) effect of geometry reinforcement by comparing similar grade laminates (intermediate grade and thin-ply), and iii) study of the effect of selective ply hybridization with intermediate (previously studied for a limited number of cases [19, 270]) and high grade material. The results are presented per test configuration and a final discussion is presented in Section 6.3. The conclusions drawn and presented here are based on the analysis of the load displacement curves and corresponding laminate strengths, damage extent visible on post mortem samples and, when available, the strain field in the outer plies during loading obtained using DIC. The main results of the performed tests are shown in Table 6.4.

6.2.1 Plain strength tension

The stress displacement curves obtained are shown in Fig. 6.2, the unnotched strength of each laminate is presented in Table 6.4 and Fig. 6.3 and the representative *post mortem* samples are shown in Fig. 6.4.

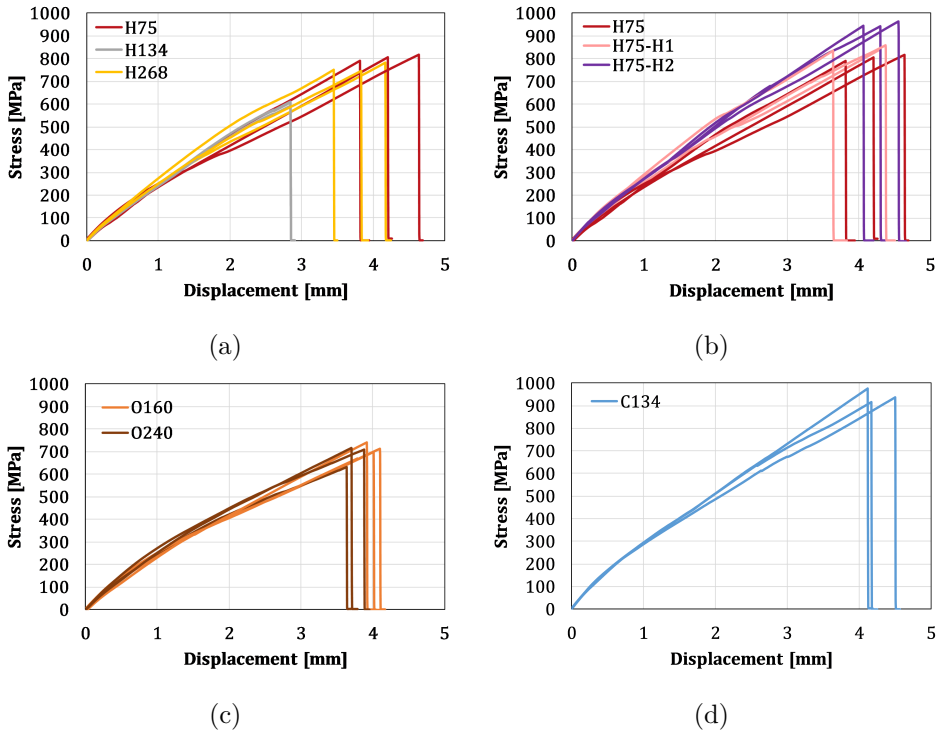

Figure 6.2: Plain strength tension stress-displacement curves of the a) H75, H134 and H268, b) H75, H75-H1 and H75-H2, c) O160 and O240 and d) C134 laminates.

6.2.1.1 Unidirectional tape

The strength of the H134 laminate obtained is 13% lower than the unnotched strength of the corresponding high-grade material (H268) configuration, which highly contradicts the results previously reported in the published literature. However, no evidence that suggests the invalidity of the tests was detected. Even though the authors suspect the cause to be related to some manufacturing defect of these specimens, the strength of the H134 laminate is shown for the sake of completeness but will not be further commented on. The reader should address this information with care.

Consistently with literature, the unnotched tensile strength of UD thin-ply laminate (H75) is 9% higher than that of corresponding high grade laminate (H268) even though the H268 laminate is stiffer in the loading direction than the H75 laminate. Thin-ply laminates have been shown to suppress subcritical damage up to the point of ultimate failure, keeping its structural integrity and being able to withstand higher loads than a comparable high-grade laminate. This effect is clearly shown in Fig. 6.5 which shows the surface longitudinal strain field and longitudinal strain measured along the edges of a representative specimen of the H268 and H75 laminates at 80%, 90% and 98% of the ultimate stress. Loss of correlation in early stages of the test was observed for the high grade laminate (Fig. 6.5b) likely due to out-of-plane displacement, caused by delamination propagation. Conversely, no transverse cracks in the outer plies were observed for the thin-ply laminate loaded up to 98% of the ultimate load. The same evidence can be observed in Fig. 6.4, which shows representative unnotched specimens post mortem. H75 developed a brittle

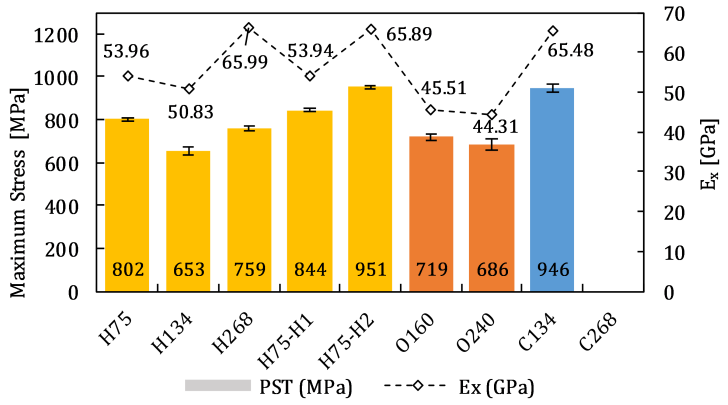

(a)

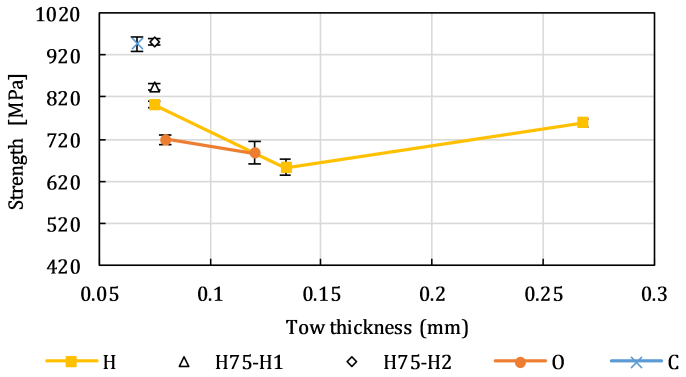

(b)

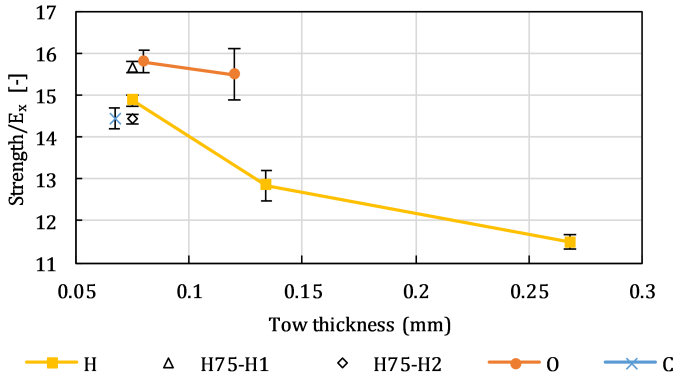

(c)

Figure 6.3: a) Summary of the ultimate unnotched tensile strengths of the nine laminates tested, b) unnotched tensile strengths as a function of the ply thickness and c) normalized tensile strength (by the longitudinal Young's modulus) as a function of the ply thickness.

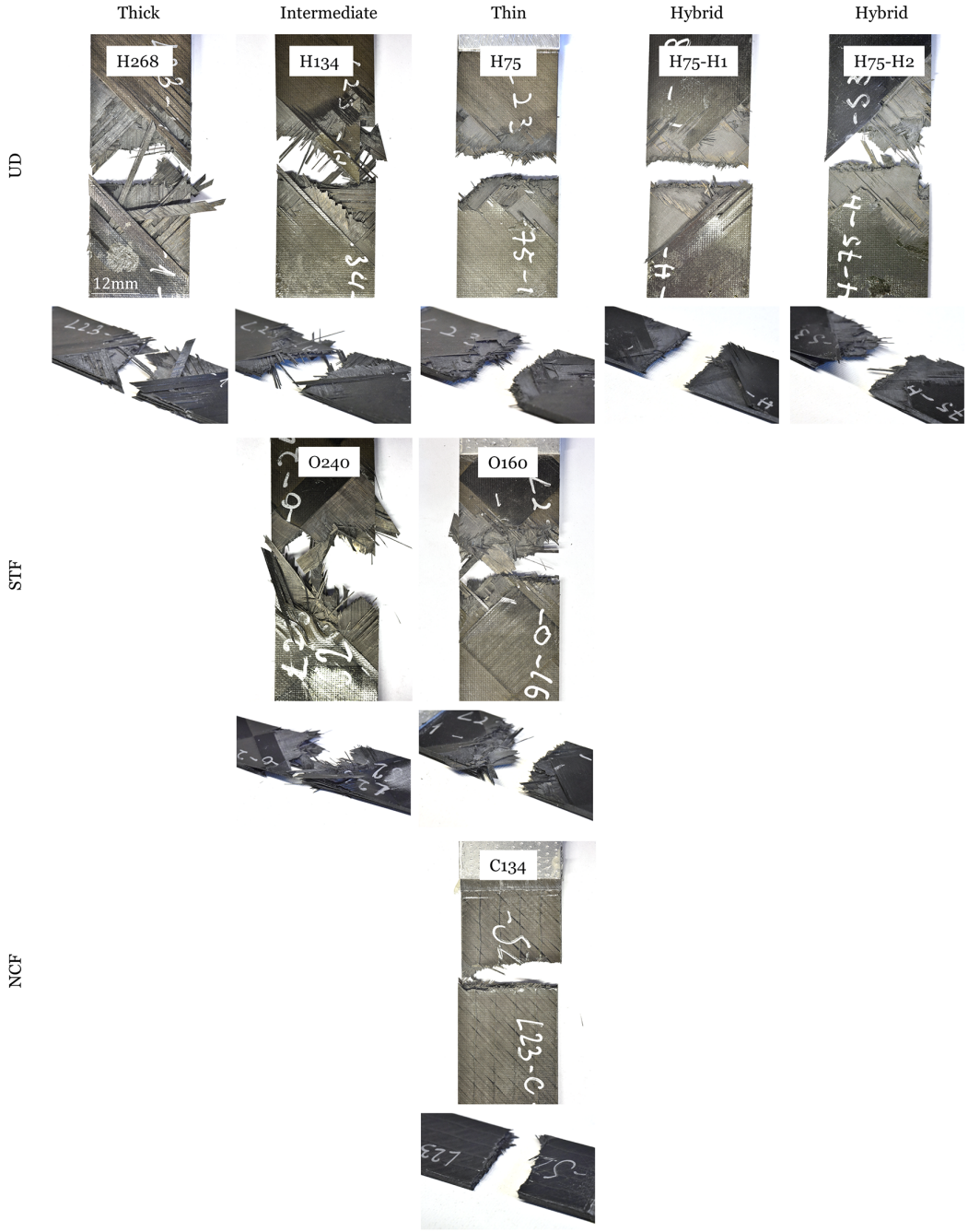

Figure 6.4: Fracture planes of representative unnotched tension specimens after testing.

type of net-section failure perpendicular to the loading direction, with limited fibre pull-out and splitting cracks while the H268 laminate shows severe fibre splitting cracks in the outer 45° plies and evidence of free-edge delamination. The appearance of premature damage affects the structural integrity of the high-grade laminate and leads to its early collapse, while in the low grade laminate subcritical damage is suppressed up to ultimate failure, allowing it to withstand higher loads.

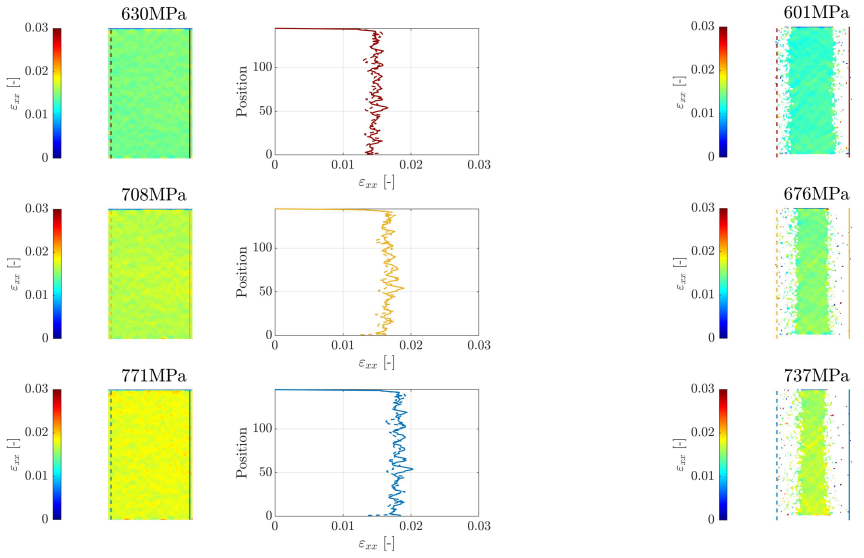

(a) H75 (b) H268

Figure 6.5: Surface longitudinal strain field and longitudinal strain measured along the edges of a representative specimen of the a) H75 and b) H268 laminates at 80%, 90% and 98% of the ultimate stress (in red, yellow and blue, respectively).

Analysing the effect of the selective hybridization on the unnotched tensile strength, as observed in Refs. [19, 24, 270], the use of high-grade and intermediate 0° plies in a low-grade laminate does not compromise the structural integrity of the unnotched structures under tensile loading. Even though the strength of hybrid laminates (H75-H1 and H75-H2) is higher than that of the corresponding non-hybrid laminate (H75), the normalized unnotched strength by the longitudinal Young's modulus of the three laminates is similar (see Fig. 6.3c) so it can simply be concluded that this type of selective ply hybridization does not compromise the tensile strength of smooth coupons. As shown in Fig. 6.6, no transverse cracks in the outer 45° ply were detected at 98% of the ultimate load of the hybrid and non-hybrid thin-ply laminate configurations. This suggests that the presence of thicker 0° plies does not affect the damage suppression capabilities of the thin off-axis plies.

6.2.1.2 Spread-tow fabric

Laminates made from spread-tow fabrics of two distinct grades were tested. As previously reported in [19, 24] for quasi-isotropic laminates, a less clear ply thickness effect can be identified for spread tow multidirectional laminates than for UD multidirectional laminates. In fact, the mean unnotched tensile strength of the thinner configuration, O160, is only 4% higher than the corresponding intermediate grade

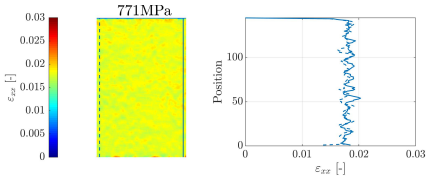

(a) H75

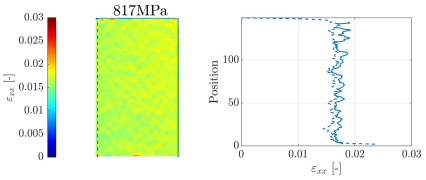

(b) H75-H1

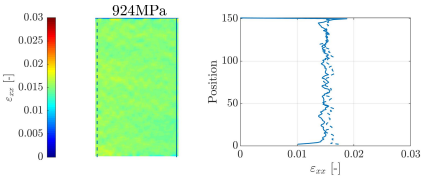

(c) H75-H2

Figure 6.6: Surface longitudinal strain field and longitudinal strain measured along the edges of a representative specimen of the a) H75, b) H75-H1 and c) H75-H2 laminates at 98% of the ultimate stress.

material, O240. Both laminates show complex fracture sections, where splitting, fibre pull-out and delamination between the layers can be clearly identified (Fig. 6.4). As shown in Fig. 6.7, transverse cracks at the free edge of the outer plies were detected for the two laminate configurations, even though they develop at lower percentage of the maximum stress for the intermediate grade configuration.

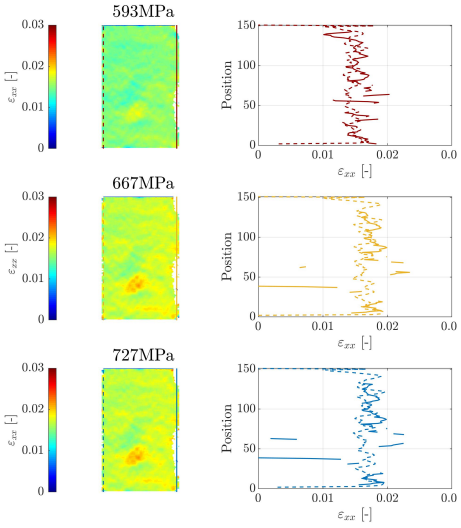

(a) O160

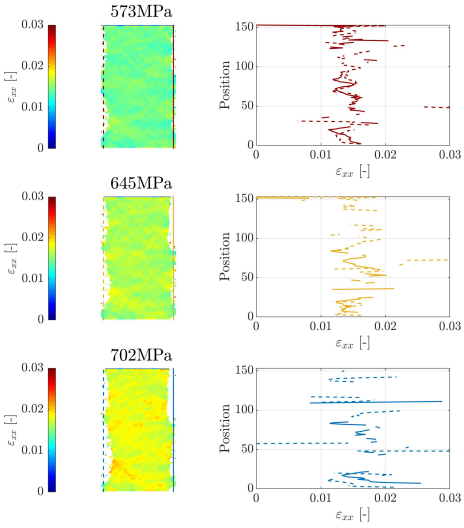

(b) O240

Figure 6.7: Surface longitudinal strain field and longitudinal strain measured along the edges of a representative specimen of the a) O160 and b) O240 laminates at 80%, 90% and 98% of the ultimate stress (in red, yellow and blue, respectively).

6.2.1.3 Non-crimp fabric

The low-grade non-crimp fabric laminate, C134, shows a similar failure section to the H75 laminate (Fig. 6.4): fibre dominated brittle type of net-section failure

mode, with nearly no observable damage at the ply level. The absence of subcritical damage justifies the high unnotched strength obtained for this material system. The corresponding intermediate grade NCF, C268, was not tested under tension, hence the effect of ply thickness on the unnotched tensile strength cannot be assessed. As a reference, Furtado et al. [19] studied the effect of ply thickness on quasi isotropic laminates and concluded that the low-grade laminate exhibited 10% higher unnotched tensile strength when compared to the intermediate grade laminate.

6.2.2 Plain strength compression

The stress displacement curves obtained are shown in Fig. 6.8, the unnotched strength of each laminate is presented in Table 6.4 and Fig. 6.9 and the representative *post mortem* samples are shown in Fig. 6.10.

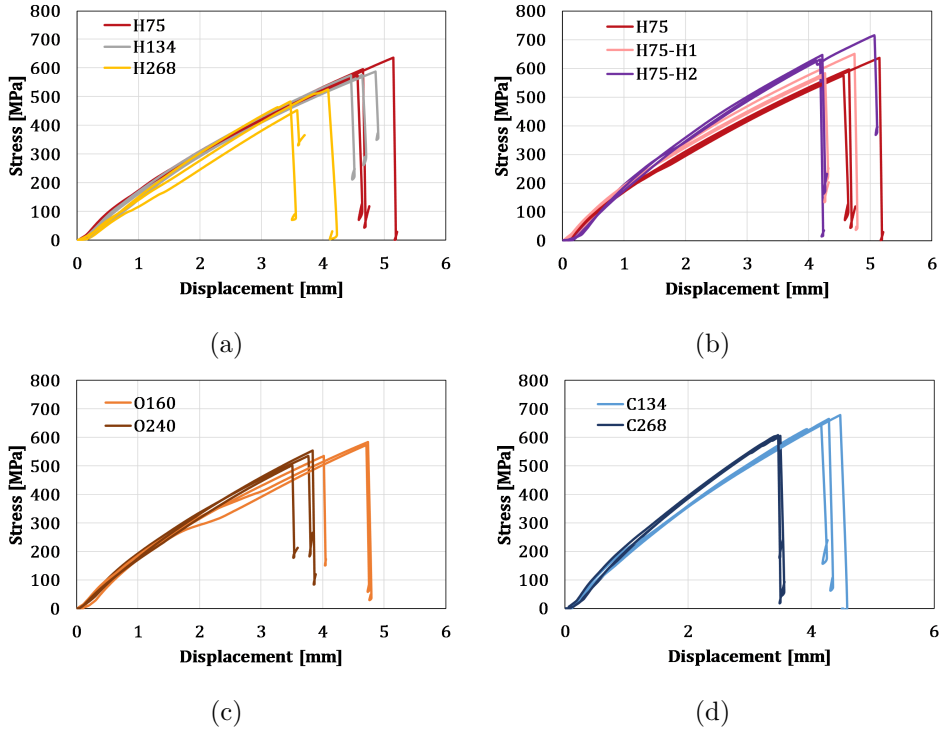

Figure 6.8: Plain strength compression stress-displacement curves of the a) H75, H134 and H268, b) H75, H75-H1 and H75-H2, c) O160 and O240 and d) C134 and C268 laminates.

6.2.2.1 Unidirectional tape

The low grade and intermediate grade laminates (H75, H75-H1, H75-H2 and H134) exhibited a net-section failure mode, characterized by a combination of fibre kinking and wedge transverse fracture, whereas the H268 specimens also showed evidence of early delamination and some surface split cracking (see Fig. 6.10).

As shown in Fig. 6.9a, the compressive strength of the smooth specimens decreases with the increase of ply thickness. H75 laminate exhibited 4% and 24% higher plain compressive strength than the H134 and H268 laminates respectively. The small improvement of the unnotched strength of the H75 laminate over the H134

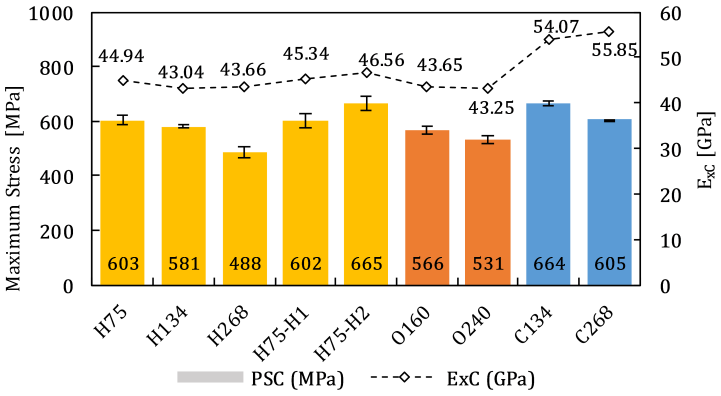

(a)

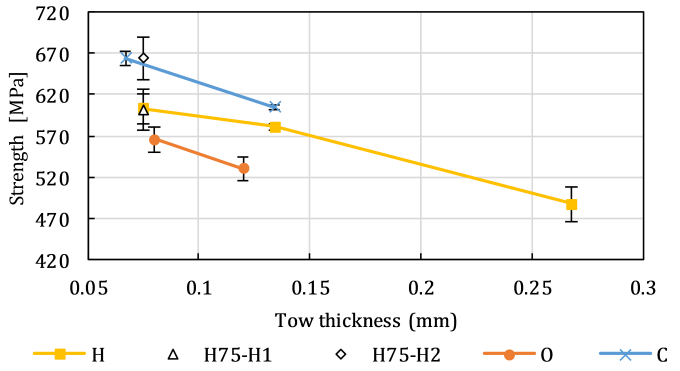

(b)

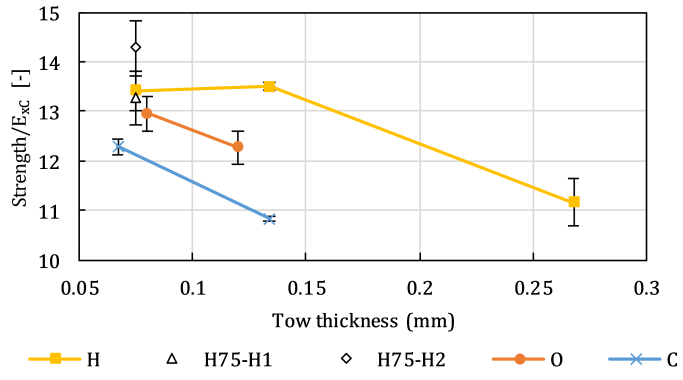

(c)

Figure 6.9: a) Summary of the ultimate unnotched compressive strengths of the nine laminates tested, b) unnotched compressive strengths as a function of the ply thickness and c) normalized compressive strength (by the longitudinal Young's modulus) as a function of the ply thickness.

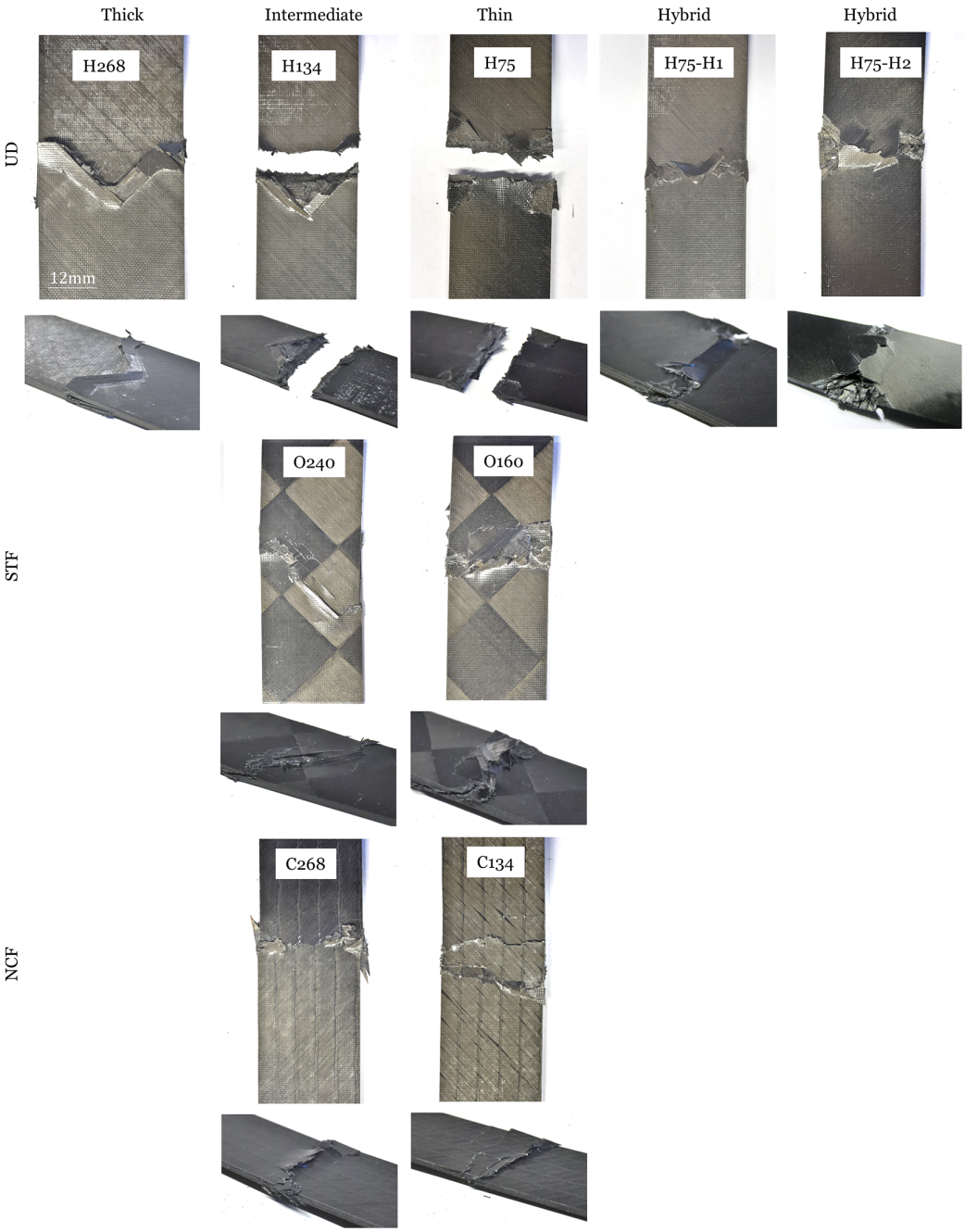

Figure 6.10: Fracture planes of representative unnotched compression specimens after testing.

laminate was concluded not to be statistically representative. In fact, the normalized strength by the longitudinal compressive stiffness (Fig. 6.9c) is approximately the same and, moreover, both laminates developed very similar brittle failure surfaces, suggesting that ultimate fracture is mainly controlled by failure of the longitudinal plies. Conversely, the reduction of compressive strength exhibited by the high grade laminate (H268) is particularly pronounced. It is clear that the use of high grade UD plies triggers premature delamination and matrix cracks in the off-axis plies prior to ultimate failure, which severely compromises the load carrying capability of the laminates loaded in compression.

As shown in Fig. 6.9, the use of intermediate grade or high grade 0° plies does not affect the strength of smooth specimens under compression. In fact, the compressive strength of H75-H1 and H75-H2 laminates are 0.2% and 10% higher than the strength of the corresponding non-hybrid laminate. Given the scatter of the data points, typical of compressive test results of composite laminates, the mean unnotched compressive strengths of the hybrid and non-hybrid thin-ply laminates were concluded to be statistically equal. Nonetheless, even though the use of thicker off-axis plies negatively affects the load carrying capability of multidirectional laminates under compression, due to the lower *in-situ* strengths and consequent early development of subcritical damage, using thicker 0° plies does not affect the compressive unnotched strength of the laminates since final failure is mainly controlled by the compressive strength of the 0° plies.

6.2.2.2 Spread-tow fabric

The failure section of both low and intermediate grade specimens (O160 and O240) is characterized by a combination of complex damage mechanisms including fibre kinking, wedge transverse fracture, delamination between the fabric layers and surface split cracking on the outer 45° plies (see Fig. 6.10). Similarly to Arteiro et al. [270], evidence of a ply thickness effect was detected for spread tow fabrics: the laminate O160 exhibited a compressive unnotched strength 7% higher than the laminate O240. However, this effect is less pronounced than that observed by Arteiro [24], who reported an 18% improvement on the unnotched compressive strength of a low grade STF laminate when compared to an intermediate grade STF laminate. Arteiro et al. [270] attributed this effect to the higher uniformity and lower fibre waviness/crimp angles of the spread-tow yarns of the 160g/m^2 STF, and consequent delay of micro-instabilities in the fibre direction.

6.2.2.3 Non-crimp fabric

The failure section of both low and intermediate grade specimens (C134 and C268) is characterized by a complex combination of damage mechanisms including fibre kinking and wedge transverse fracture (see Fig. 6.10). No signs of early delamination and split cracking were identified. A clear ply thickness effect was also detected for non-crimp fabric laminates, where the thin-ply laminate (C134) exhibited a 10% increase in the unnotched compressive strength when compared to the corresponding intermediate grade laminate (C268). However, it is important to note that the lower unnotched compressive strength of the C268 laminate can in part be attributed to the presence of higher mismatch angles of 67.5° between the 90° and 22.5° plies in this laminate, which can trigger delamination propagation and

consequently affect the stability of the laminate.

6.2.3 Open-hole tension

The stress displacement curves obtained are shown in Fig. 6.11, the unnotched strength of each laminate is presented in Table 6.4 and Fig. 6.12 and the representative *post mortem* samples are shown in Fig. 6.13.

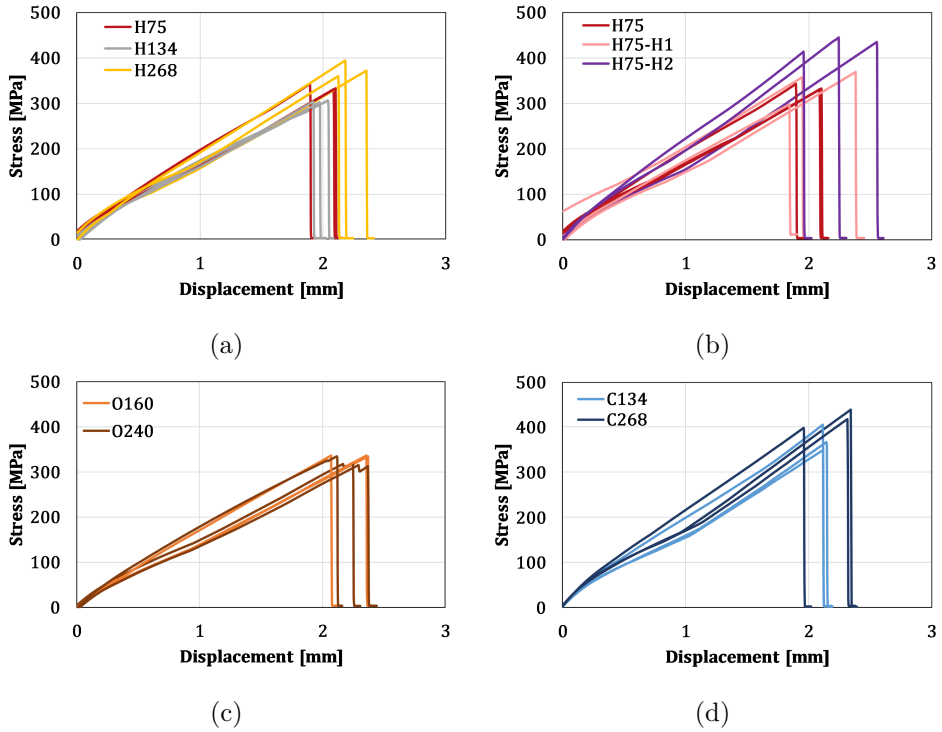

Figure 6.11: Open-hole tension stress-displacement curves of the a) H75, H134 and H268, b) H75, H75-H1 and H75-H2, c) O160 and O240 and d) C134 and C268 laminates.

6.2.3.1 Unidirectional tape

The H75 laminate exhibited a brittle type of net-section failure mode, where transverse cracking, matrix/fibre split cracks and delamination are nearly absent (see Fig. 6.13). Additionally, as shown in Fig. 6.14c, no strain localization near the hole can be identified up to 98% of the maximum load. As previously reported in Refs. [1, 6, 19, 24] for thin-ply laminates, macroscopic cracks originating from the edge of the hole clearly develop and propagate in a plane perpendicular to the loading direction, regardless of the ply orientation. The H134 specimens presented a more diffuse failure mode. Even though damage mostly propagates perpendicularly to the loading direction, triangular shaped delaminations and splitting cracks tangent to the free edge of the hole can be observed in the outer 45° layers. The H268 specimens presented a more complex failure mode dominated by matrix failure and fibre pull-out. Extensive fibre splitting and triangular shaped delamination in all off-axis plies can be observed. This is an indication that the off-axis plies have failed and separated from the 0° plies prior to the ultimate failure of the specimen

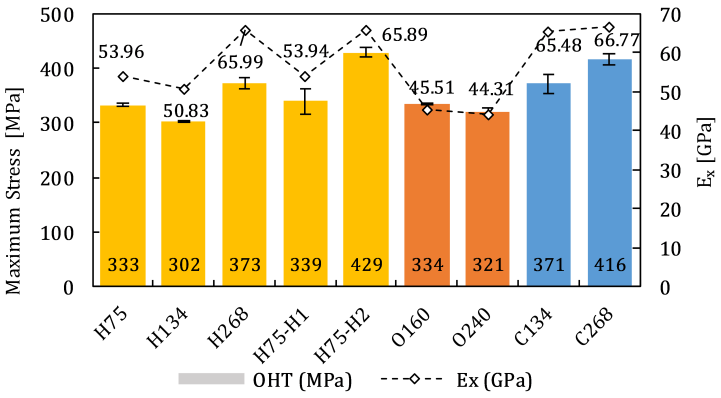

(a)

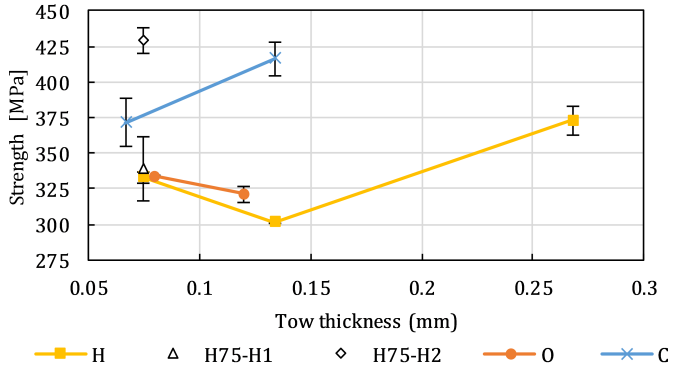

(b)

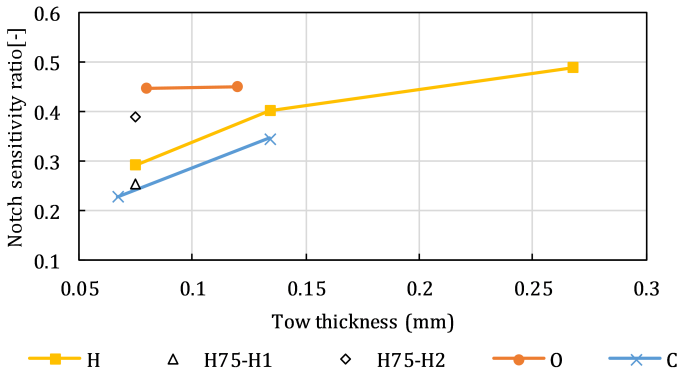

(c)

Figure 6.12: a) Summary of the notched tensile strengths of the nine laminates tested, b) notched tensile strengths as a function of the ply thickness and c) notch sensitivity ratio as a function of the ply thickness.

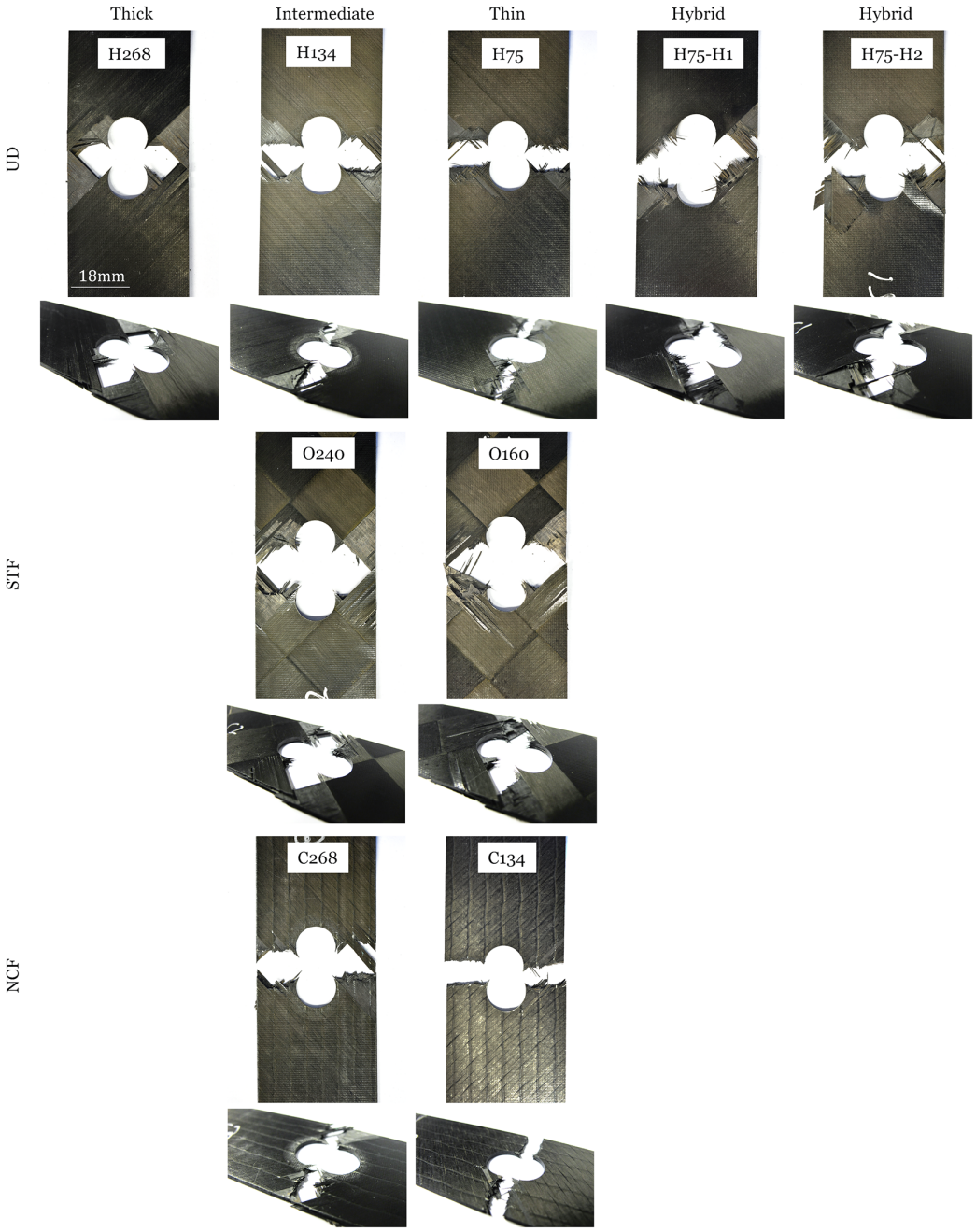

Figure 6.13: Fracture planes of representative open-hole tension specimens after testing.

and therefore, that the specimens loose their structural integrity before final failure [1, 19, 24]. This is clearly visible in Fig. 6.14a, where the appearance of transverse cracks was detected at loads as low as 80% of the ultimate load, together with transverse cracks/delamination near the free-edge. As previously suggested [18, 276] and as shown in Fig. 6.12c, the notch sensitivity decreases with the increase of ply thickness. This is the result of the damage suppression capability typically observed in thin-ply laminates, which inhibits stress redistribution. Nevertheless, it should be noted that the damage suppression leads to a closer first and last ply failure loads, which, for instance, improves fatigue behaviour [1, 6, 19]. This can potentially lead to an increase in the design stress used for notched configurations.

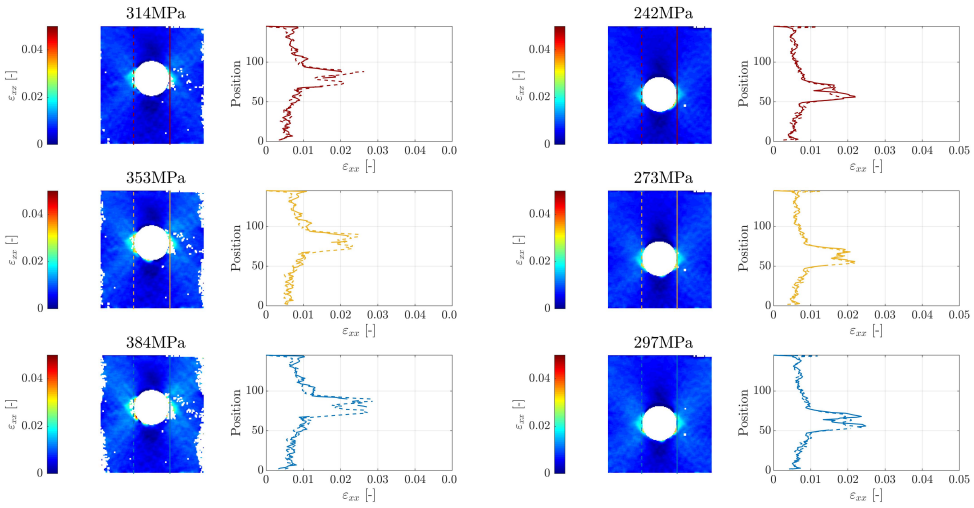

(a) H268 (b) H134

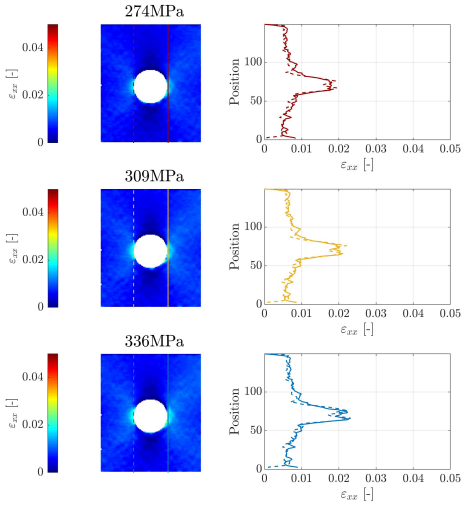

(c) H75

Figure 6.14: Surface longitudinal strain field and longitudinal strain measured along the edges of the hole of a representative specimen of the a) H268, b) H134 and c) H75 laminates at 80%, 90% and 98% of the ultimate stress (in red, yellow and blue, respectively).

The hybrid laminates showed a more diffuse failure mode, similar to the in-

termediate grade laminate (see Fig. 6.13). Triangular shaped delamination and splitting cracks tangent to the free edge of the hole can be observed in some 45° layers, however, no strain localization was observed before final failure (see Fig. 6.15) and failure seems to still be dominated by fracture of the longitudinal plies. Despite presenting different failure sections, H75-H1 exhibited a similar notched strength and similar notch sensitivity to the H75 laminate. H75-H2 laminate shows a 29% increase in notched strength and significantly lower notch sensitivity when compared to the H75 laminate. Furtado et al. [19] concluded that the use of thicker 0° plies embedded in a laminate with thin off-axis plies triggered the appearance of split cracks in the 0° plies. These promote stress redistribution around the hole, without compromising the integrity of the off-axis plies, which results in an increase on the tensile notched strength when compared to the respective non-hybrid laminates. In this work, this strengthening effect does not seem to be as clearly demonstrated. No clear evidence of split cracking on the 0° plies was observed from the analysis of the broken specimens and all specimens were tested up to failure, hence no information regarding the damage state up to that point is available. An analysis on standard specimens with width to hole diameter ratios of $W/d = 6$ and a study of the size effect on the notched strength on these laminates could further clarify the effect of ply hybridization on the notched strength.

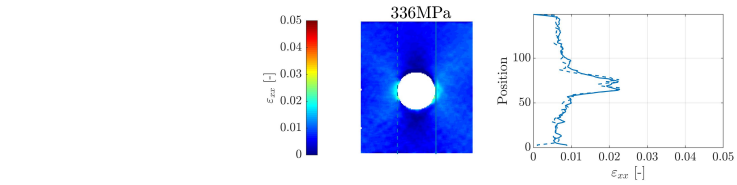

(a) H75

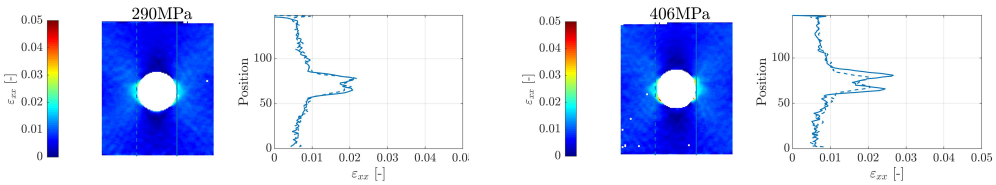

(b) H75-H1 (c) H75-H2

Figure 6.15: Surface longitudinal strain field and longitudinal strain measured along the edges of the hole of a representative specimen of the a) H75, b) H75-H1 and c) H75-H2 laminates at 98% of the ultimate stress.

6.2.3.2 Spread-tow fabric

As shown in Fig. 6.13, both spread tow fabric laminates show a fibre-dominated pull-out failure mode after testing, where fibre/matrix splitting and triangular shaped delamination between some spread tow plies can be observed. As shown in Fig. 6.16, during loading, strain localization near the hole is observed for both configurations, however, they appear in an earlier stage for the intermediate grade configuration, accompanied by out of plane displacement that suggests delamination propagation around the hole. However, despite slight differences in damage propagation, contrary to the results reported by Furtado et al. [19] but following the tendency identified

by Arteiro at el. [270], no significant ply thickness effect in the spread tow fabric laminates was detected: both the notched strength and notch sensitivity of the two material configurations is equivalent as shown in Fig. 6.12.

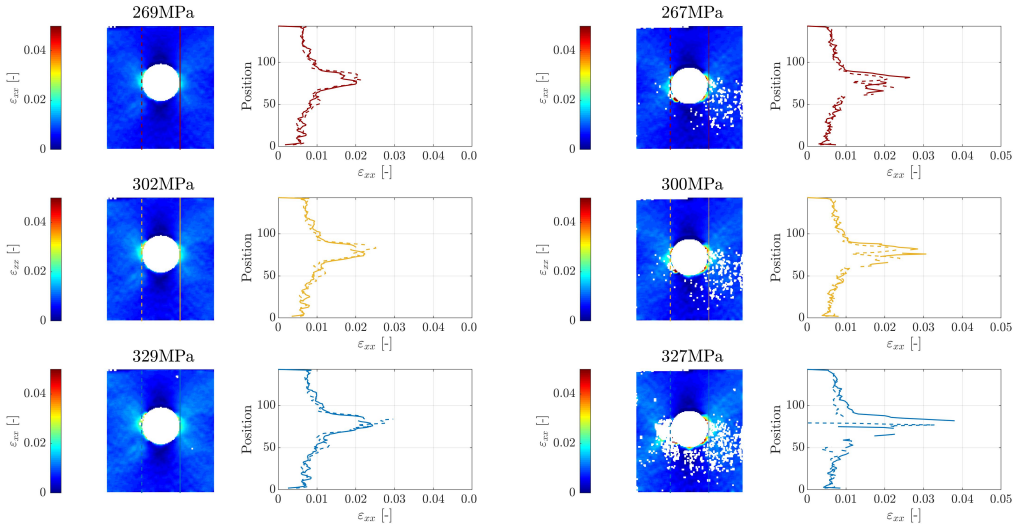

(a) O160 (b) O240

Figure 6.16: Surface longitudinal strain field and longitudinal strain measured along the edges of the hole of a representative specimen of the a) O160 and b) O240 laminates at 80%, 90% and 98% of the ultimate stress (in red, yellow and blue, respectively).

6.2.3.3 Non-crimp fabric

As shown in Fig. 6.13 and similarly to H75 specimens, a brittle net-section type of failure mode characterize the failure of the C134 specimens. In fact, no strain discontinuity was observed during loading in the vicinity of the hole. As shown in Fig. 6.17, in C268 specimens, cracks around the hole develop early, at loads lower than 80% of the ultimate failure load. These justify the higher notched strength obtained for this configuration. The development of subcritical damage near notches has been shown to reduce the stress concentration in that region, increasing the load carrying capability of the structure. The ply thickness effect determined for this material configuration is in line with the ply thickness effect reported by other authors [6, 18, 19, 24] for notched structures loaded in tension. The notch sensitivity ratio was computed for both laminates. Note that since the unnotched tensile strength of the C268 laminate was not available, the strength of the C134 laminate was considered to estimate the notch sensitivity ratio (Fig. 6.12c). Nonetheless, in line with the UD laminates, the notch sensitivity decreases with the increase of ply thickness.

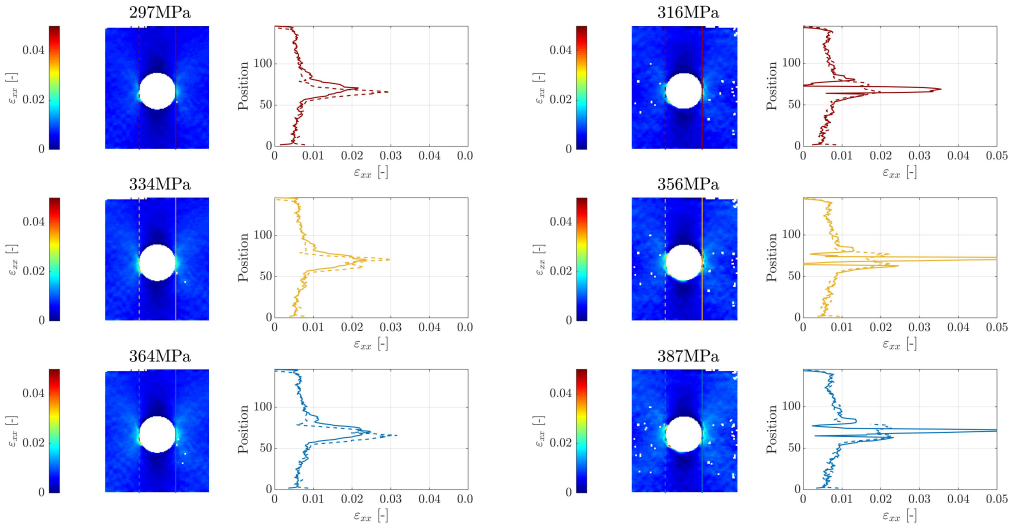

(a) C134 (b) C268

Figure 6.17: Surface longitudinal strain field and longitudinal strain measured along the edges of the hole of a representative specimen of the a) C134 and b) C268 laminates at 80%, 90% and 98% of the ultimate stress (in red, yellow and blue, respectively).

6.2.3.4 Off-axis open-hole tension

The sensitivity to the loading direction in the presence of stress concentrations of the UD laminates was assessed by testing off-axis open-hole tension specimens, where the stacking sequences are rotated 30°, 60° and 90°. The notched strength vs off-axis angle are summarized in Table 6.5 and Fig. 6.18. This analysis is particularly important for the hybrid laminates: the intermediate grade and high grade 0° plies that have been shown to promote fibre splitting, and to be beneficial to improve the notched behaviour of thin-ply laminates are gradually converted into thick off-axis plies as the laminate rotates, which can trigger matrix cracking and, therefore, compromise the mechanical performance of the laminates. Note that the notch sensitivity ratio was not determined for the rotated laminates since the unnotched strength was not measured experimentally.

As shown in Fig. 6.18, regarding the ply grade, the low-grade and intermediate grade laminates (H75 and H134) have similar sensitivity to the loading direction. Even though the laminates are 0° dominated, the loading direction has little influence on the notched strength of these laminates (the strength decreases around 10%). Contrary, the high-grade laminate is less robust as the notch strength decreases up to 30% which can compromise its interest for some more general applications, especially considering that the design strength should be lower than the ultimate strength since the laminate is already damaged at relatively low applied loads.

For the hybrid laminates, the H75-H1 laminate has similar robustness to the H75 laminate for this notch configuration. For this notched geometry, the intermediate grade 0° plies do not seem to promote fibre splitting and consequently do not lead to the higher notched strength as expected and previously reported by other authors [19, 24, 270]. Similarly, its sensitivity to the loading direction is not compromised. The robustness of the laminate should be tested for other notched

Table 6.5: Mean strength, standard deviation and standard error obtained of the open-hole off-axis tests.

Lam		0°	30°	60°	90°
H268	Young's Modulus [GPa]	65.99	68.83	56.82	46.96
	Mean strength [MPa]	373	368	311	260
	Std. deviation [MPa]	17.6	3.2	28.7	15.0
	Std. error [MPa]	10.2	1.86	16.6	8.66
H134	Young's Modulus [GPa]	50.83	58.34	52.31	42.32
	Mean strength [MPa]	302	320	305	284
	Std. deviation [MPa]	2.1	6.7	13.1	4.2
	Std. error [MPa]	1.2	3.9	3.4	5.5
H75	Young's Modulus [GPa]	53.96	58.73	55.18	48.27
	Mean strength [MPa]	333	334	301	302
	Std. deviation [MPa]	6.6	5.9	9.5	5.2
	Std. error [MPa]	3.8	3.4	5.5	5.2
H75-H1	Young's Modulus [GPa]	53.94	58.26	54.45	47.74
	Mean strength [MPa]	339	345	298	315
	Std. deviation [MPa]	38.5	10.1	7.3	52.7
	Std. error [MPa]	22.2	5.8	4.2	30.4
H75-H2	Young's Modulus [GPa]	65.89	60.79	50.50	45.55
	Mean strength [MPa]	429	318	248	238
	Std. deviation [MPa]	15.7	2.1	2.7	22.7
	Std. error [MPa]	9.1	1.2	1.5	13.1

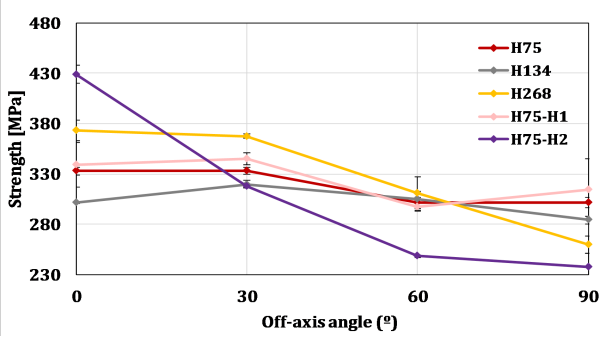

Figure 6.18: Notched strength as a function of the loading direction.

configurations.

Conversely, the H75-H2 laminate has a very high sensitivity to the loading direction (the notched strength decreases 45% as the laminate is rotated). The low grade 0° plies, that contribute to the high notched strength at 0°, gradually become thick off-axis and 90° plies with low resistance to the appearance of transverse cracks as the laminate is rotated. Hybrid laminates are therefore interesting for applications where the loading direction is highly oriented, but it should be taken into account that even small deviations in the loading direction can severally compromise the performance of the structures.

6.2.4 Open-hole compression

The stress displacement curves obtained are shown in Fig. 6.19, the unnotched strength of each laminate is presented in Table 6.4 and Fig. 6.20 and the representative *post mortem* samples are shown in Fig. 6.21.

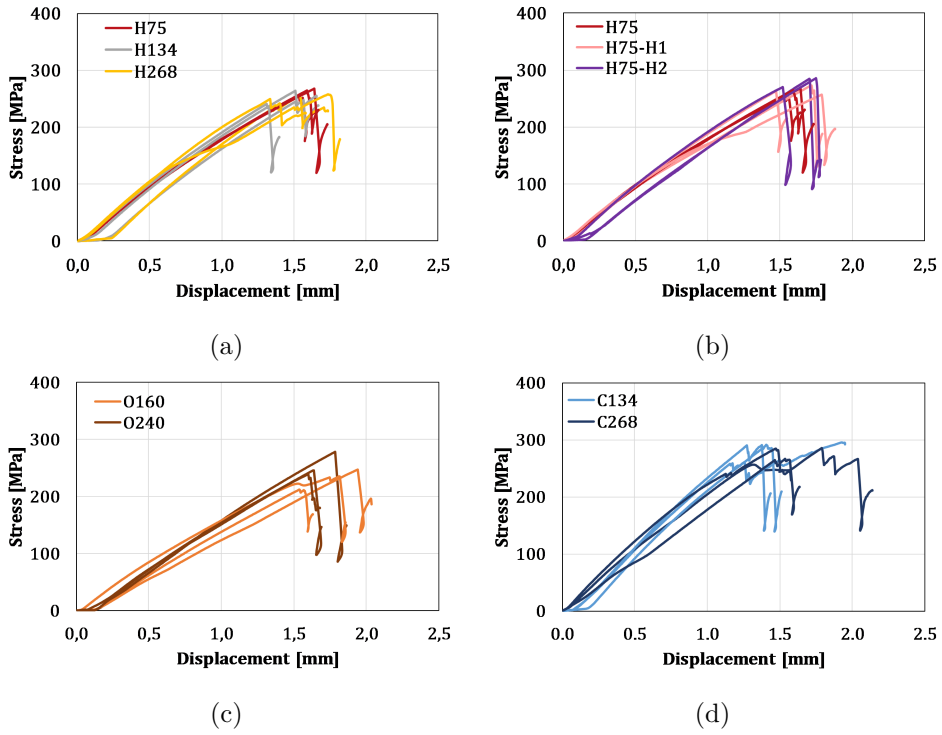

Figure 6.19: Open-hole compression stress-displacement curves of the a) H75, H134 and H268, b) H75, H75-H1 and H75-H2, c) O160 and O240 and d) C134 and C268 laminates.

6.2.4.1 Unidirectional tape

As shown in Fig. 6.20, nearly no effect of the ply thickness under notched compression was detected. In fact, the notched strength of the low-grade laminate and high-grade laminates are only 4% and 1% higher than that of the baseline laminate (H134), respectively. Additionally, nearly no considerable discrepancy in notch sensitivity was detected for the low and intermediate grade laminates. The high grade laminate exhibited a significantly lower sensitivity to the presence of stress concentrations, however, this can also be related to the lower unnotched strength reported for this material. All the non-hybrid laminates exhibited a similar type of net-section failure mode characterized by a combination of fibre kinking and transverse fracture. All samples were tested up to ultimate failure and, therefore, the damage evolution was not analysed. Following the lack of ply thickness effect exhibited for these material systems, the selective ply hybridization did not significantly affect the notch compressive strength and notch sensitivity of the open-hole compression specimens.

6.2.4.2 Spread-tow fabric

Arteiro et al. [270] tested two symmetric laminates of 160g/m^2 and 240g/m^2 spread tow fabrics under open-hole compression and reported that the lower grade laminate exhibited a 7.4% higher notched strength when compared to that of the intermediate grade laminate. The author reported that failure of the thin-ply laminate was dominated by fibre kinking while a more complex combination of damage mechanisms, where fibre kinking, wedge transverse fracture and fibre splitting was observed for the intermediate grade laminate. The improved compressive response

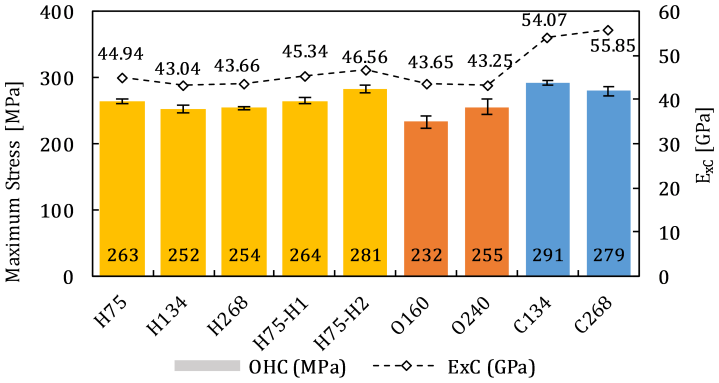

(a)

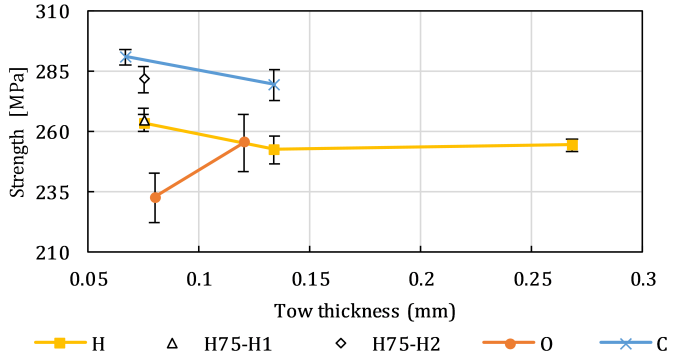

(b)

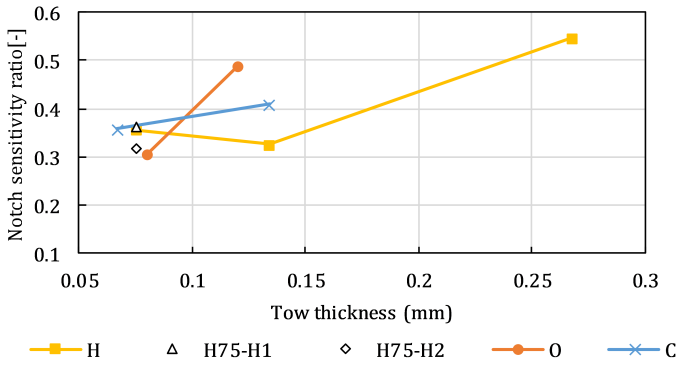

(c)

Figure 6.20: a) Summary of the notched compressive strengths of the nine laminates tested, b) notched compressive strengths as a function of the ply thickness and c) notch sensitivity ratio as a function of the ply thickness.

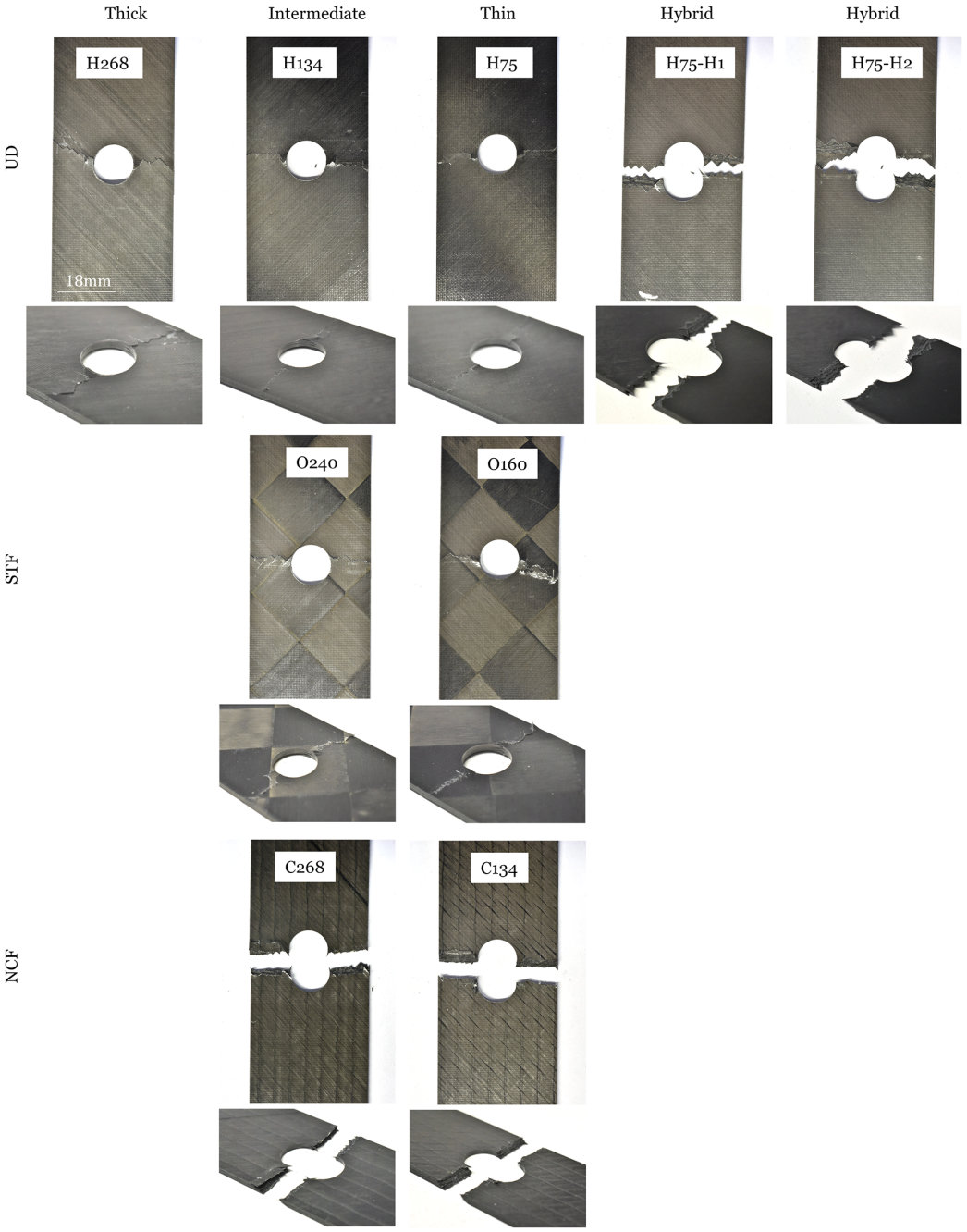

Figure 6.21: Fracture planes of representative open-hole compression specimens after testing.

of the thin-ply laminate was attributed to the better uniformity of the tows and consequent lower fibre waviness and smaller crimp angles which delay micro-instabilities in the fibre direction.

In this study, an inverse trend was observed, where the mean notched strength of the thin-ply laminate is 9% lower than the notched strength of the intermediate grade laminate (see Fig. 6.20). However, given the scatter of the experimental results, the mean notched strengths were concluded not to be statistically different (by means of the Welch T-test, with a p-value of 0.05). As shown in Fig. 6.21, the fracture surfaces of the two specimen configurations are similar, exhibiting a combination of fibre kinking and wedge transverse fracture. Given the inconsistency of the results reported in this study and those reported by Arteiro et al. [270], the ply thickness effect of spread-tow fabric laminates under notched compression should be further clarified, for instance by means of analysing the size effect [34, 35, 277] (i.e. the change in notched strength as a function of the hole diameter for constant width-to-hole diameter ratios) for the two configurations.

6.2.4.3 Non-crimp fabric

Arteiro et al. [18] studied the effect of the ply thickness on the compressive notched response of non-crimp fabric laminates. The authors concluded that, similarly to structures loaded in tension, when intermediate grade plies are used, damage develops around the notch in earlier stages of the test. However, the effect of ply thickness on the notched compressive strength was unclear, given the scatter of the experimental results and of the contradictory results obtained for different specimen sizes.

In this study and as shown in Fig. 6.20, even though the notched strength of the low grade laminate is 4% higher than that of the intermediate grade laminate, the difference is not statistically representative. The strain field of the outer plies was not evaluated for this test configuration and therefore, it was not possible to assess the damage extension at the notch vicinity before final failure. However, following the results for notched tension of the non-crimp fabric laminates (Fig. 6.17) and Ref. [18], it is likely that more extensive subcritical damage develops near the notch in the intermediate grade laminate. However, the notched compressive strength of the laminates is not affected. It should be taken into account that the maximum mismatch angle is different in the intermediate grade and thin-ply laminate (67.5° vs 45°, respectively).

6.2.5 Filled-hole compression

Typically, there is an enhancement of the filled hole strength vs the open-hole compression strength of a specimen with the same dimensions because there is an additional load path through the bolt/pin. This reduces the load that is carried around the hole and consequently reduces the stress concentration at the vicinity of the hole. The filled hole strength is influenced by the fastener-hole clearance, laminate stiffness, friction between the bolt and laminate surfaces, bolt preload, bolt material, among others [278]. In this work, only pin filled-hole compression tests were performed. The notched strength of each laminate is presented in Table 6.4 and Fig. 6.24 and the stress-displacement curves are shown in Fig. 6.22. Note that in some curves, a plateau is visible at around 150MPa. Since the stiffness of the

specimen is not altered and the ultimate strength of these specimens reaches values similar to those of the remaining specimens of the same configuration, this plateau was attributed to end crushing of the top of the specimens/initial slippage and the tests were considered valid.

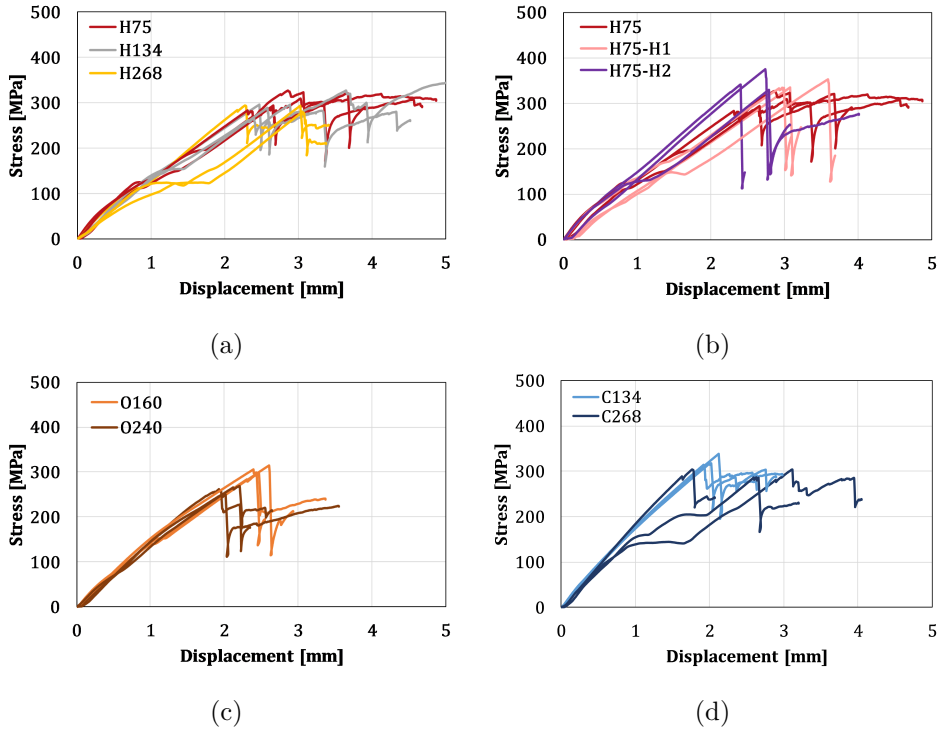

Figure 6.22: Filled-hole compression stress-displacement curves of the a) H75, H134 and H268, b) H75, H75-H1 and H75-H2, c) O160 and O240 and d) C134 and C268 laminates.

6.2.5.1 Unidirectional tape

All the laminate configurations exhibited compressive failure across the centre of the hole, characterized by 0° ply dominated kinking. Limited split cracks in the outer plies and delamination between the plies are also visible. Representative *post mortem* specimens are shown in Fig. 6.23. As shown in Fig. 6.24, even though the strength of the low grade (H75) and intermediate grade (H134) laminate are similar, the filled-hole compression strength of the high grade laminate (H268) is 10% lower than that of the low grade laminate. Since failure of this type of specimens is controlled by localized compressive failure, this decrease can be attributed to the fact that the compressive strength of the high-grade laminate is significantly lower than that of the remaining laminates, since failure is mainly controlled by matrix cracking and delamination.

For the hybrid laminates, in line with the remaining test results, the H75-H1 laminate has similar behaviour to the H75 laminate for this test configuration, with a 6% increase in maximum strength. The H75-H2 laminate exhibited a 8% increase in notched strength. However, it is interesting to note that, for both hybrid configurations, the maximum strength corresponds to the first load drop, while for the thin-configuration, the maximum load is generally taken after load pick up

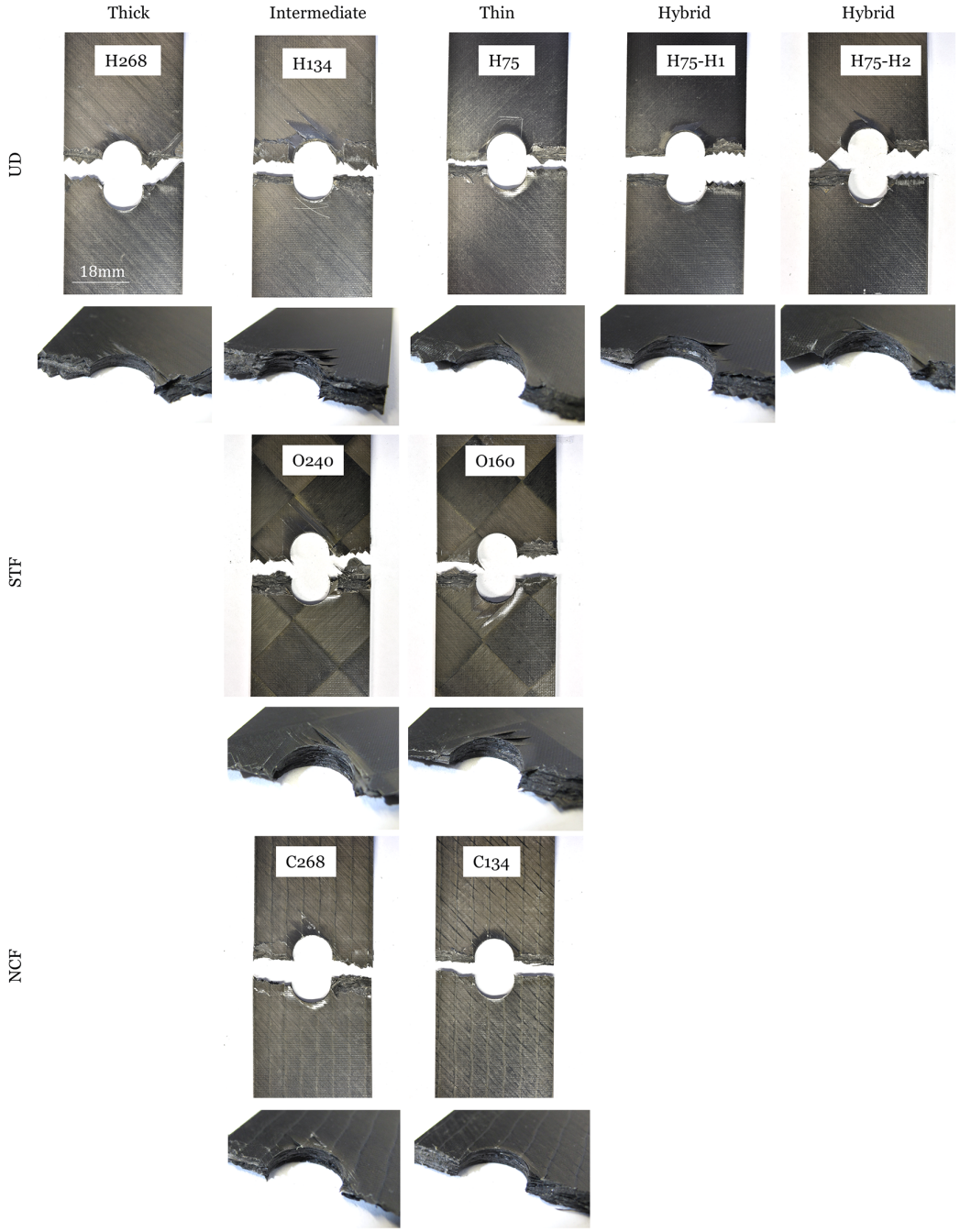

Figure 6.23: Fracture planes of representative filled-hole compression specimens after testing.

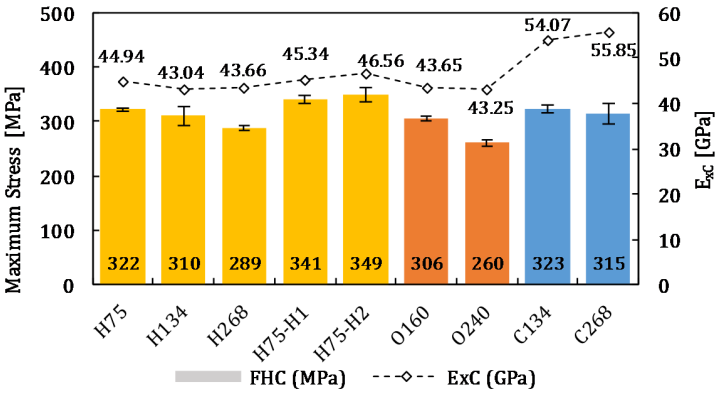

(a)

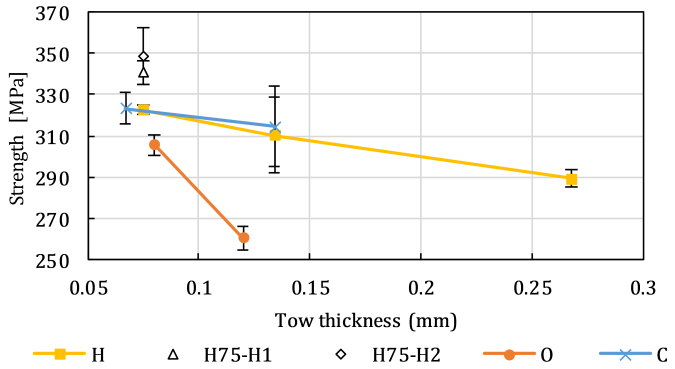

(b)

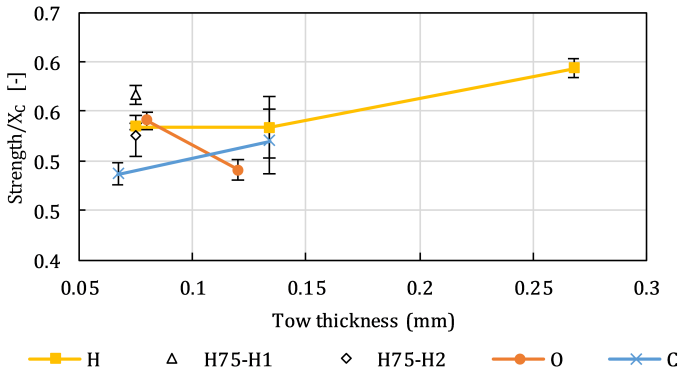

(c)

Figure 6.24: a) Summary of the filled-hole compressive strengths of the nine laminates tested, b) filled-hole compressive strengths as a function of the ply thickness and c) normalized compressive strength (by the unnotched compressive strength) as a function of the ply thickness.

consequence of the crushing ahead of the pinned area (Fig. 6.22b). This suggests that, in fact and similarly to the results reported by Arteiro et al. [24, 270] for other hybrid configurations, the thicker 0° plies provide additional stability to the laminate ahead of the pinned area while the thin-off axis plies delay the onset and propagation of matrix-dominated damage, resulting in an improved resistance. More tests for other filled-hole geometry configurations should be performed to further clarify this effect.

6.2.5.2 Spread-tow fabric

Both spread tow fabric laminates exhibited compressive failure across the centre of the hole, characterized by 0° ply dominated kinking with clear fibre split cracks in the outer 45° plies and delamination between the spread-tow layers. Representative *post mortem* specimens are shown in Fig. 6.23. Contrary to the remaining test cases, a ply thickness effect for the spread-tow fabric laminates was detected under filled-hole compression. In fact, the intermediate grade laminate (O240) exhibited a 20% lower ultimate strength than the thin-ply laminate (O160). Since final failure is mainly controlled by localized compressive failure, this decrease in ultimate strength can be partly attributed to the fact that the compressive strength of the intermediate-grade laminate is lower than that of the thin-ply laminate. Contrary to the UD and NCF laminates, for this reinforcement geometry, the load does not further increase after the first load drop. This can be consequence of the fact that the laminates are less 0° dominated than the remaining laminates and therefore, have worse compressive stability.

6.2.5.3 Non-crimp fabric

Both non-crimp fabric laminates also exhibited compressive failure across the centre of the hole, characterized by 0° ply dominated kinking. Representative *post mortem* specimens are shown in Fig. 6.23. The notched strength of both laminates is the same. Both material grades present very similar behaviour and strengths, not taking into account the non-linearities around 150MPa for the C268 laminate that were attributed to end crushing. The post mortem analysis of the specimens show very similar damage mechanisms for both laminate configurations, however, more pronounced cracking in the outer 45° plies is observed for the higher grade laminate. It is interesting to note that, although the C268 laminate presents a lower unnotched compressive strength, the same is not observed in the FHC and OHC tests, resulting in higher normalized strengths.

6.2.6 Bolt bearing

The stress-displacement curves are presented in Fig. 6.25. The definition of bearing stress is still unclear depending on the author and application. Several bearing strengths can be defined, including:

- First non-linearity: this is a conservative value of the bearing load carrying capability. It generally corresponds to the damage initiation/first ply failure and the load usually increases before final failure of the specimen.

- First load drop: the bearing stress at this point is governed by the propagation of matrix shear cracks and fibre kinking corresponding to the last-ply failure.
- Ultimate strength: corresponds to the collapse of the joint and is typically followed by a large load drop. Characterized by high permanent deformation of the hole and extensive damage near the bolt region.

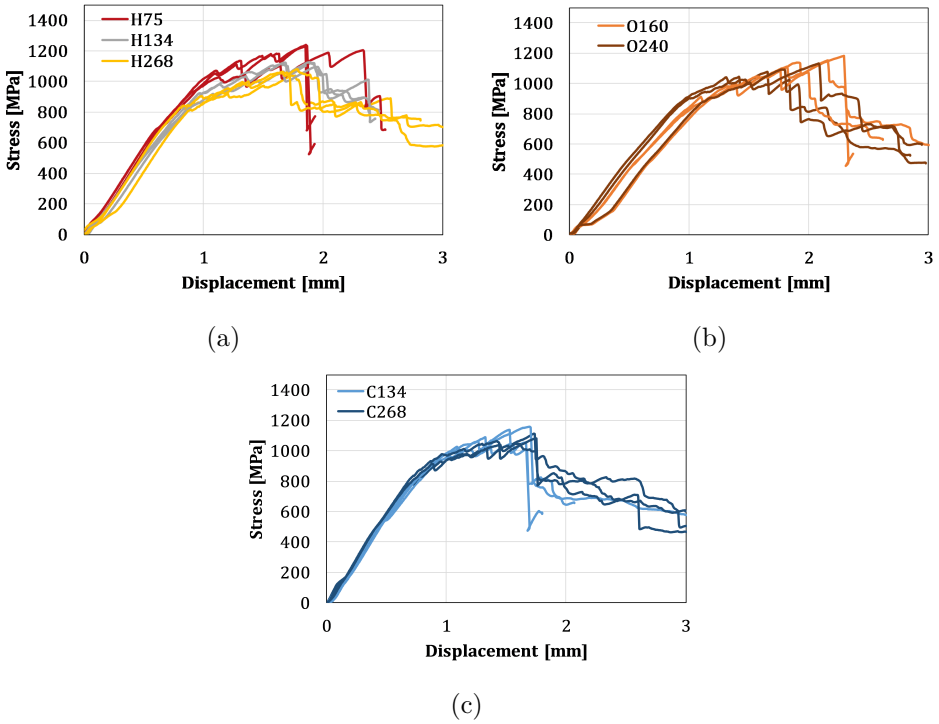

Figure 6.25: Bearing stress-displacement curves of the a) H75, H134 and H268, b) O160 and O240 and c) C134 and C268 laminates.

In this work, the first load drop and ultimate strength are defined. The bearing strengths of each laminate is presented in Table 6.4 and Fig. 6.27.

6.2.6.1 Unidirectional tape

All the specimens exhibited bearing failure modes as expected, characterized by localized compressive damage at the vicinity of the loaded hole. Representative *post mortem* specimens are shown in Fig. 6.26. As the ply thickness increases, the more complex are the failure sections, characterized by more extensive delamination in the vicinity of the hole, matrix cracks and fibre splitting in the outer plies. As shown in Fig. 6.27, with the increase in ply thickness, both the bearing load corresponding to the first load drop and the ultimate bearing load decrease significantly. In fact, the thin-ply laminate exhibited a 21% and 10% higher initiation and maximum bearing stress when compared to the baseline laminate (H134), respectively. In agreement with this, the thick-ply laminate exhibited a 7% lower strength corresponding to the first load drop and 5% lower ultimate strength than the baseline. As previously reported by other authors [1, 18], thin-ply laminates have improved bearing resistance, both to damage initiation and to damage growth when compared

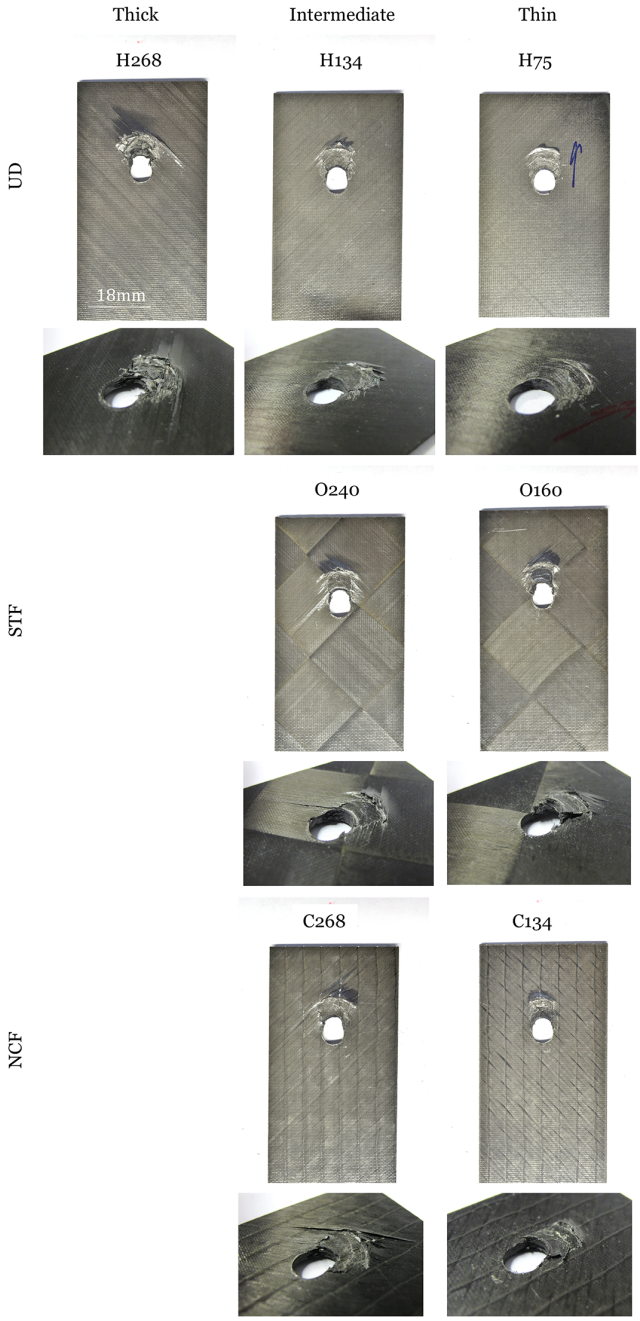

Figure 6.26: Fracture planes of representative bolt-bearing specimens after testing.

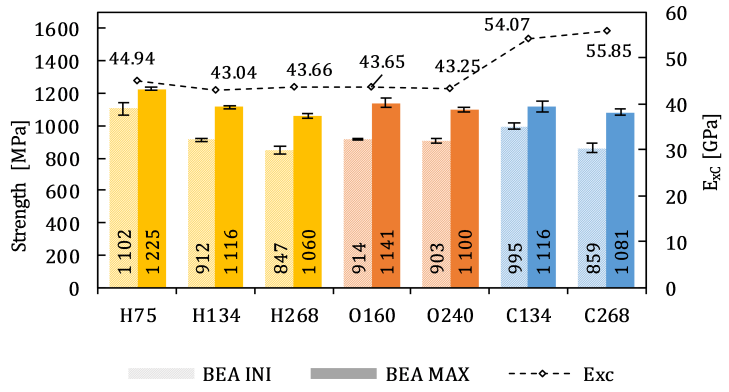

(a)

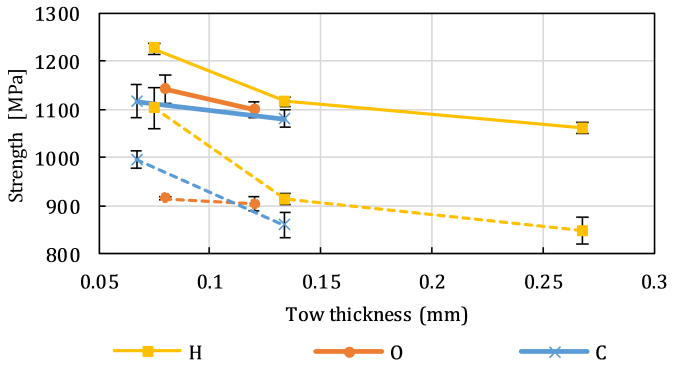

(b)

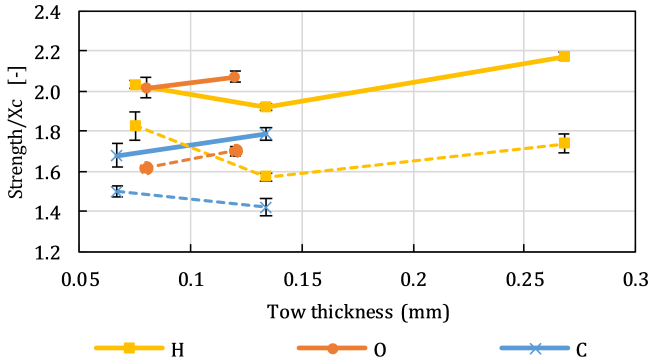

(c)

Figure 6.27: a) Summary of the bearing strengths of the nine laminates tested, b) bearing strengths as a function of the ply thickness and c) normalized bearing strengths (by the unnotched compressive strength) as a function of the ply thickness.

to standard and thick-ply laminates. This improvement is attributed to the damage suppression capability of thin-ply laminates, consequence of higher *in-situ* strengths, and more efficient ply constraining.

The bearing resistance of the hybrid laminates was not assessed in this study. However, as reference, Arteiro et al. [24, 270] showed that combining intermediate grade 0° plies with thin transverse and off-axis plies resulted in an improved bearing resistance compared to that of an equivalent thin-ply laminate. The thin off-axis plies delay the onset and propagation of matrix-dominated damage and the thicker 0° plies provided additional stability to the laminate below the bolt/washer assembly resulting in an improved bearing resistance, also confirmed in the filled-hole compression tests carried out in this study (Section 6.2.5.1).

6.2.6.2 Spread-tow fabric

Both spread tow fabric laminates exhibited bearing failure modes, characterized by localized compressive damage at the vicinity of the loaded hole. Representative *post mortem* specimens are shown in Fig. 6.26. No relevant difference between the failure modes (Fig. 6.26) of the laminates was observed. Since the governing failure mechanisms of the two configurations are similar, the bearing response is equivalent. It is worth noting that the effective ply thickness of both material grades is less disparate than the ply thicknesses used in previous studies [1, 18] and both fabrics were obtained by tow spreading which ensures good homogeneity of the plies [24].

6.2.6.3 Non-crimp fabric

As shown in Fig. 6.26, the specimens of both material grades exhibited bearing failure modes, characterized by localized compressive damage at the vicinity of the loaded hole. The intermediate grade laminate exhibited a slightly more complex damage surface, where split cracks in the outer plies were more clearly visible. As shown in Fig. 6.27, the thin-ply laminate (C134) exhibited 16% higher stress at the first load drop but equivalent ultimate bearing strength.

6.3 Discussion

In this section, a summary of the more relevant conclusions is presented. The effect of the ply thickness, the effect of ply thickness hybridization and the effect of the ply reinforcement configuration on the global response of the material is presented in Sections 6.3.1, 6.3.2 and 6.3.3, respectively.

6.3.1 Effect of ply thickness on the global response of the material

6.3.1.1 Unidirectional tape

Generally speaking, the low grade material (H75) exhibited brittle failure under tension and compression, with little evidence of premature damage prior to ultimate failure (only assessed under tensile loading from the strain field in the outer plies). The intermediate grade laminate (H134) presented some evidence of premature damage at the free edge in the smooth coupons loaded in tension and

at the vicinity of the hole in notched specimens. The high-grade laminate (H268) showed matrix dominated failure under tension and compression, with clear evidence of early delamination and matrix cracking under tensile loading.

As shown in Fig. 6.28, an overall improvement of the material behaviour with the decrease of ply thickness was observed with two exceptions: no ply thickness effect was detected for notched specimens loaded in compression (OHC) and, as previously reported in literature, the high-grade laminate (H268) exhibit a higher notched tensile strength when compared with low-grade laminate (H75). However, evidence of premature damage was reported for the tensile case. Moreover, H268 laminate presented a high sensitivity to the loading direction, which can compromise the performance of the laminate for some applications.

As expected and as presented in Fig. 6.28b (OHT), the thinner material configuration presented a higher notch sensitivity under tensile loading, i.e. a more brittle behaviour. In fact, as previously mentioned, the suppression of premature damage inhibits the stress redistribution and leads to a lower strength of the laminate. However, it should also be taken into account that the unnotched tensile strength of the intermediate grade laminate (H134) is particularly low, and consequently, its notch sensitivity ratio might be over predicted.

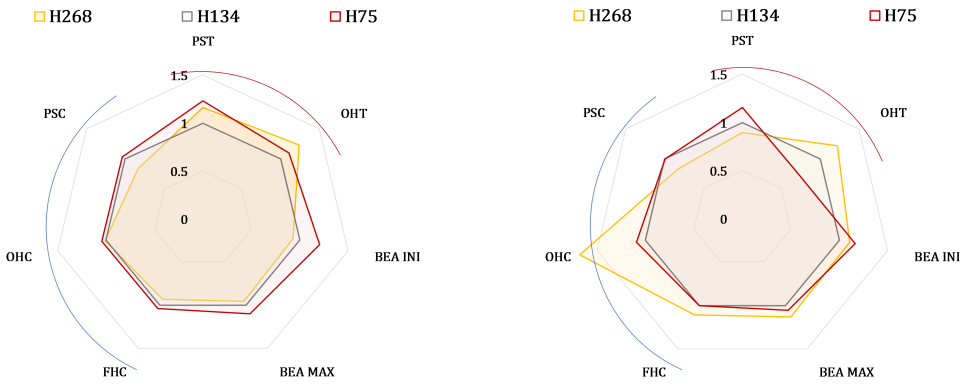

Figure 6.28: a) Strengths and b) normalized strengths of the non-hybrid laminates made from unidirectional tape. Note that PST and PSC are normalized by the tensile and compressive longitudinal Young's moduli, respectively, BEA MAX, BEA INI and FHC are normalized by the PSC and the notch sensitivity ratio is presented for OHT and OHC. H134 is used as baseline.

Even though the behaviour under fatigue loading was not studied in this work, it is important to take into account that thin-ply laminates, being able to suppress the appearance of early damage even when subjected to high loads, have clear advantages under cyclic loading [6, 19].

6.3.1.2 Spread-tow fabric

As shown in Fig. 6.29, regarding the ultimate strengths, nearly no ply thickness effect on the material response was detected, except under filled-hole compression. For all the test configurations, both thin and intermediate grade laminates exhibited similar complex fracture sections where splitting, fibre pull-out and some

delamination between the plies are visible. Under tension, premature damage was detected for both material grades but it developed in earlier stages of the tests in the high-grade laminate.

As previously pointed out [24], the material grades used in this study have quite similar effective ply thickness and were both obtained by tow spreading which guarantees good uniformity of the plies. A more pronounced thickness effect is expected for thinner and thicker spread tow fabrics, particularly if, as a result, the crimp angles and waviness of the tows significantly increase.

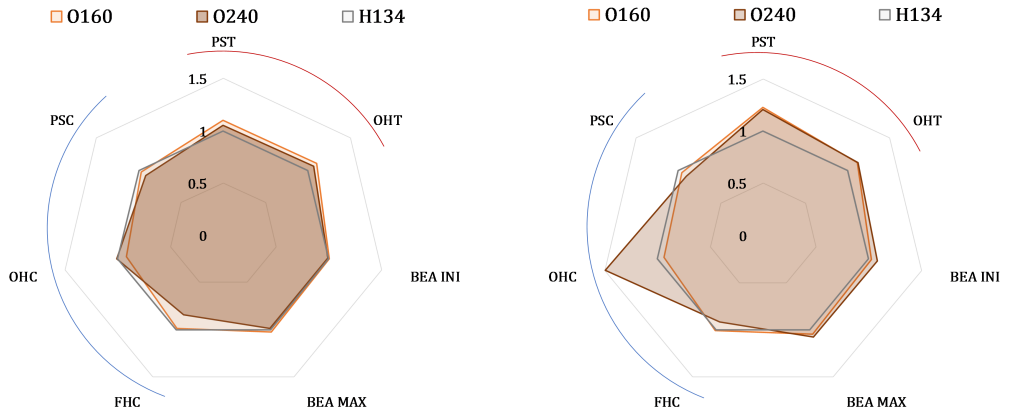

(a) (b)

Figure 6.29: a) Strengths and b) normalized strengths of the spread tow fabric laminates. Note that PST and PSC are normalized by the tensile and compressive longitudinal Young's moduli, respectively, BEA MAX, BEA INI and FHC are normalized by the PSC and the notch sensitivity ratio is presented for OHT and OHC. H134 is used as baseline.

6.3.1.3 Non-crimp fabric

The C134 laminate exhibited more brittle failure sections, similar to those of the H75 laminate. The corresponding intermediate grade laminate (C268) also exhibited fibre dominated failure but some evidence of fibre splitting, pull-out and little evidence of delamination was also detected. As shown in Fig. 6.30, overall the low-grade laminate (C134) exhibited higher ultimate strengths than the corresponding intermediate grade laminate (C268) except for the notched tension strength due to the appearance of subcritical damage at the vicinity of the notch in the latter. As reported in Refs. [6, 18, 19, 24], in structures with stress concentrations loaded in tension, the appearance of cracks at the vicinity of the notch leads to stress redistribution and consequent increase of the ultimate strength. The thin-ply laminate (C134) has an overall more consistent behaviour, even though the effect of ply thickness is not highly pronounced for this reinforcement geometry. It is important to take into account that the stacking sequence may have a significant influence on the performance, since the C268 laminate has a higher mismatch angle between plies than the C134 laminate. As typically observed, the intermediate grade laminate is more insensitive to the presence of stress concentrations (see OHC and OHT in Fig. 6.30b). However, it should be taken into account that premature damage develops

around the notch for this material grade (only evaluated in this study under OHT) which can have negative repercussions under fatigue loadings.

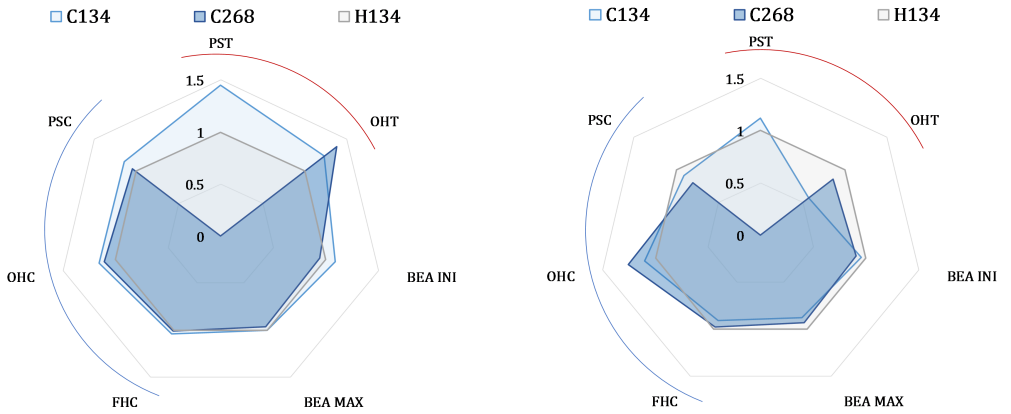

(a) (b)

Figure 6.30: a) Strengths and b) normalized strengths of the non-crimp fabric laminates. Note that PST and PSC are normalized by the tensile and compressive longitudinal Young's moduli, respectively, BEA MAX, BEA INI and FHC are normalized by the PSC and the notch sensitivity ratio is presented for OHT and OHC. H134 is used as baseline.

6.3.2 Effect of ply hybridization on the global response of the material

The non-hybrid and corresponding hybrid laminates all exhibited similar brittle failure under tension and compression. As shown in Fig. 6.31, contrary to Furtado et al. [19] and Arteiro et al. [24, 270] findings, the strengthening effect of selective hybridization with intermediate grade plies was not as clearly demonstrated. In fact, the non-hybrid (H75) and the H75-H1 hybrid laminate exhibited very similar performances in all the test cases. Conversely, an overall improvement of the strengths was obtained for H75-H2, particularly under notched tension (OHT). However, it is also important to note that the H75-H2 laminate is highly sensitive to the loading direction when compared to H75, which can compromise its behaviour in some structural applications.

The bearing performance of the hybrid laminates was not studied here. Arteiro et al. [270] reported that the use of blocked 0° plies effectively delayed the onset and propagation of localised compressive damage when compared to the use of dispersed 0° plies. It was concluded that the thicker 0° plies provide additional stability in the bolted area that resulted in an overall improvement of the bearing response. A similar behaviour would be expected for the laminate configurations presented in this study.

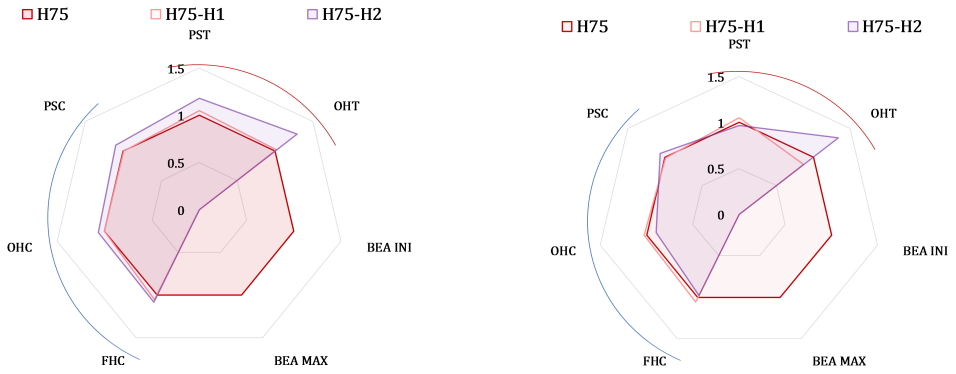

(a) (b)

Figure 6.31: a) Strengths and b) normalized strengths of the hybrid laminates made from unidirectional tapes. Note that PST and PSC are normalized by the tensile and compressive longitudinal Young's moduli, respectively, BEA MAX, BEA INI and FHC are normalized by the PSC and the notch sensitivity ratio is presented for OHT and OHC. H75 is used as baseline.

6.3.3 Effect of the reinforcement configuration on the global response of the material

6.3.3.1 Thin-ply laminates

In this section, a comparison between the mechanical performance of the thin-ply laminates made of unidirectional tape (H75), spread-tow fabric (O160) and non-crimp fabric (C134) is made (see Fig. 6.32). Generally speaking, H75 and C134 laminates presented a brittle failure in all test configurations with nearly no evidence of premature damage prior to ultimate failure. The UD laminate exhibited an overall more consistent behaviour, particularly when accounting for the different laminate configurations, i.e. the normalized strengths (see Fig. 6.32b). The non-crimp fabric laminate (C134) exhibited higher plain strength and notched strength, but slightly worse mechanical performance in bolted/pinned connections. The spread-tow fabric laminate exhibited complex failure sections with diffuse damage in all test configurations and slightly lower strengths than the UD laminate in all test configurations. However, taking into account the design constrains (the % of 0°/90° and +45°/-45° is the same given the ply morphology), the global performance of the laminates is particularly interesting, especially considering it is easier to handle during manufacturing than UD laminates.

6.3.3.2 Intermediate grade laminates

The mechanical performance of the intermediate grade laminates (H134, C268 and O240) is analysed in this section (see Fig. 6.33). The UD laminate presented a semi-brittle failure section, characterized by diffuse damage where some delamination and fibre splitting were visible after final failure. The O240 laminate exhibited more complex failure sections typically observed in spread tow fabric laminates, consequence of the cross-ply reinforcement configuration.

Consistently with the thinner material grade, the UD laminate exhibited an

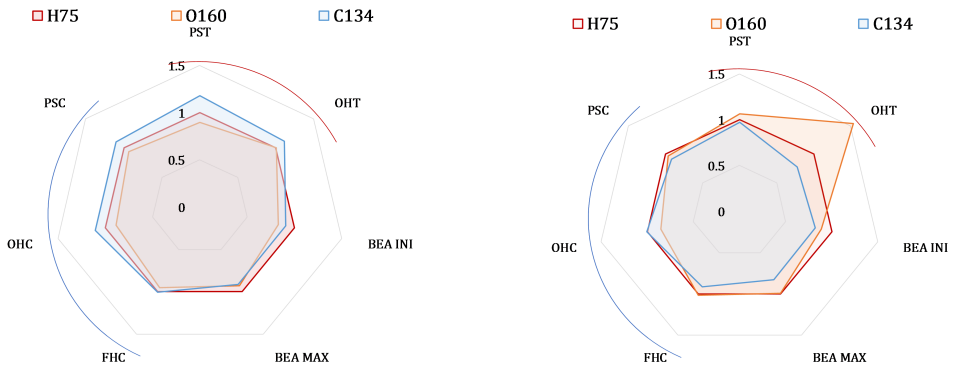

Figure 6.32: a) Strengths and b) normalized strengths of the thin-ply laminates. Note that PST and PSC are normalized by the tensile and compressive longitudinal Young's moduli, respectively, BEA MAX, BEA INI and FHC are normalized by the PSC and the notch sensitivity ratio is presented for OHT and OHC. H75 is used as baseline.

overall more consistent behaviour. However, it is important to take into account that the unnotched tensile strength of the UD laminate (H134) is particularly low, and consequently, the notch sensitivity ratio might be over predicted. The non-crimp fabric laminate exhibited an overall better performance and particularly higher notched tensile strength. Note that the notch sensitivity ratio of the C268 laminate was performed assuming that the unnotched tensile strength of the laminate was equal to that of the C134 laminate. Similarly to the thinner configuration, the spread-tow fabric laminate exhibited complex failure sections with diffuse damage in all test configurations. Despite the design constrains (the % of 0°/90° and +45°/-45° is the same given the ply morphology), the spread tow fabric laminate exhibited a similar behaviour to that of the industry defined baseline.

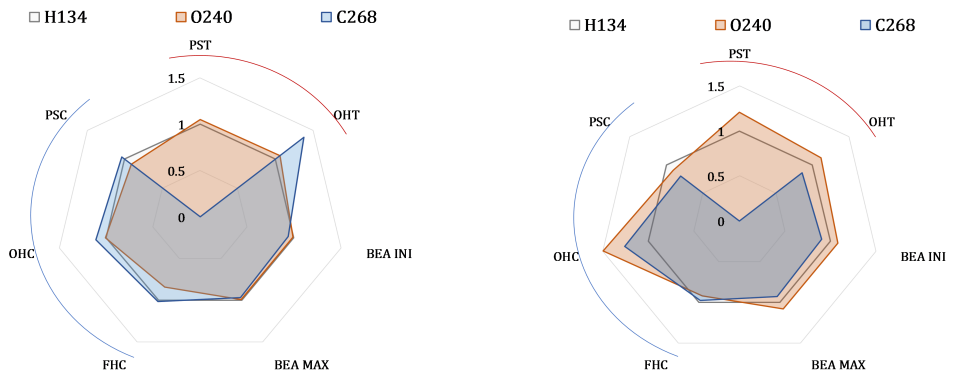

Figure 6.33: a) Strengths and b) normalized strengths of the intermediate grade laminates. Note that PST and PSC are normalized by the tensile and compressive longitudinal Young's moduli, respectively, BEA MAX, BEA INI and FHC are normalized by the PSC and the notch sensitivity ratio is presented for OHT and OHC. H134 is used as baseline.

6.4 Concluding remarks

An extensive experimental test campaign was performed, featuring nine equivalent 0° dominated hard multidirectional laminates made from unidirectional tapes, non-crimp fabrics and spread-tow fabrics with fibre areal weights ranging from 67g/m^2 to 268g/m^2 and the same carbon-epoxy material system. Standard structural details including plain strength tension/ compression, open-hole tension/ compression, filled-hole compression and bolt-bearing specimens were tested up to failure with the goal of clarifying i) the effect of ply thickness, ii) the effect of selective ply thickness hybridization and iii) the effect of type of geometry reinforcement on the damage mechanisms that dominate failure and on the ultimate design strengths of multidirectional laminates. The main conclusions of this study are:

- Regarding the manufacturing process:
  - Given the material configuration (cross-ply layers), laminate and structure design using STF is less flexible than using UD tapes and NCF (note that prepregs with different mismatch angles can already be manufactured). However, STF and NCF present clear advantages during the lay-up process since bi-angle prepreg handling is easier and the lay-up process is more efficient.
- Regarding the effect of ply thickness:
  - An overall improvement of the material behaviour with the decrease of ply thickness in the UD laminates (75g/m^2, 134g/m^2 and 268g/m^2) was observed. Even though the behaviour under fatigue loading was not studied in this work, it is important to take into account that thin-ply laminates, being able to suppress premature damage even when subjected to high loads, have clear advantages under cyclic loading.
  - Nearly no ply thickness effect was identified for STF (160g/m^2 and 240g/m^2). Both laminates presented very similar strengths which makes the higher-grade material more interesting in terms of manufacturing. The STF material grades used in this study have quite similar effective ply thickness and were both obtained by tow spreading which guarantees good uniformity of the plies. A more pronounced thickness effect is expected for thinner and thicker STFs, particularly if, as a result, the crimp angles and waviness of the tows increase significantly.
  - Regarding the NCF laminates (134g/m^2 and 268g/m^2), the effect of ply thickness is less evident than for the UD laminates given the difference in mismatch angles but, overall, the thin-ply laminate exhibited higher strengths (except for notched tensile strength due to the appearance of subcritical damage at the vicinity of the notch).
- Regarding the effect of ply hybridization:
  - Nearly no effect of ply thickness hybridization was detected when intermediate grade (134g/m^2) 0° plies are combined with thin off-axis plies, under the different loading configurations.

  - An overall improvement of the strengths when high-grade (268g/m^2) 0° plies are combined with thin off-axis plies was observed when compared to the corresponding non-hybrid laminate. However, a high sensitivity to the loading direction in the presence of stress concentrations was observed. The high grade 0° plies, that contribute to the high notched strength at 0°, gradually become thick off-axis and 90° plies with low resistance to the appearance of transverse cracks as the laminate is rotated. Hybrid laminates are therefore interesting for applications where the loading direction is highly oriented, but it should be taken into account that even small deviations in the loading direction can severally compromise the performance of the structures.

- Regarding the effect of reinforcement configuration:
  - The UD laminates exhibited an overall more uniform behaviour, particularly when accounting for the different laminate configurations, i.e. the normalized strengths.
  - The STF laminates exhibited complex failure sections with diffuse damage and slightly lower strengths than the UD laminates in all test configurations. However, it should be noted that, given the design constrains (the % of 0°/90° and +45°/-45° is the same given the ply morphology) the global performance of the laminates is particularly interesting and similar to the baseline considered.
  - The NCF laminates exhibited a similar behaviour in the unnotched and open-hole test cases to that of the UD laminates, but slightly worse mechanical performance in bolted/pinned connections.
  - Spread-tow non-crimp and textile fabrics did not show especial susceptibility to early failure either in the presence or not of geometrical discontinuities. Due to their added flexibility in terms of manufacturing and processing, the replacement of unidirectional tapes by spread-tow non-crimp and textile fabrics can be seen as an economical solution that does not compromise the structural response, ensuring the weight benefits of composite materials at lower processing costs and opening the possibility of integrating new, more efficient manufacturing processes.

While the mechanical behaviour and damage mechanisms of thin-ply laminates have been exhaustively studied, there are still many opportunities to fully exploit the characteristics of thin plies and to explore their applicability. With the information presented here, where the main characteristics of failure of structural details manufactured using thin-ply laminates with different reinforcement geometries have been elucidated, it is now possible to explore new design opportunities using thin plies.

Part V

Nano-reinforced interfaces

Chapter 7

Interlaminar fracture toughness of thin-ply laminates reinforced by carbon nanotubes

It was demonstrated in the previous chapters that thin-ply laminates have and improved mechanical behaviour when compared with standard grade materials for several design drivers. One of the reasons for this improvement is the fact that thin-ply composites delay the onset of free-edge delamination due to the more favourable stress distribution resulting from the use of thinner plies; however, the effect of using thin plies on the interlaminar fracture toughness associated with delamination propagation still needs to be fully understood. Furthermore, the possible synergies between thin-ply laminates and recently developed techniques to reinforce the interfaces between composite plies needs to be studied in detail.

One of such techniques consists of using nanostructured composite materials, where nanoparticles such as carbon nanotubes are used alongside microscale fibre composite laminates. The main idea behind this combination is to improve the matrix dominated properties of traditional composites. In fact, carbon nanotubes introduce additional energy dissipating mechanisms that have the potential to enhance the interlaminar fracture toughness and therefore be used to improve the interfacial properties of composite laminates.

Recently, composite laminates composed of carbon fibre-epoxy plies nano-stitched together with vertically aligned carbon nanotube arrays have been developed. It was shown that this innovative process guarantees a good dispersion of carbon nanotubes and improves both interlaminar and, consequently, intralaminar composite strength and toughness [8, 10, 110–112].

Garcia et al. [8] conducted an experimental program to assess the influence of including CNT in the interface on the mode I and mode II interlaminar fracture toughness. Double cantilever beam (DCB) and four point bending end notched flexure (4ENF) tests were performed in a unidirectional CFRP reinforced with 60-150 μm high CNT arrays. In this preliminary study, it was concluded that the inclusion of CNT does not influence the resulting thickness of the specimens after curing and that the mode I and mode II fracture toughness were improved by a scale of 1.5-2.5 and 3 times, respectively, by the inclusion of CNTs. This improvement was reported to be a consequence of both interlayer toughening through plastic deformation and crack bridging. In fact, Scanning Electron Microscope (SEM) analysis of the fracture surface of reinforced DCB specimens showed z-oriented CNTs on both the crack surfaces suggesting bridging of the crack by the aligned CNTs.

Falzon et al. [10] also compared the fracture toughness of nano-stitched and unreinforced interfaces by performing DCB and ENF tests and determining the mode

I and mode II crack resistance curves ($\mathcal{R}$-curves), respectively. Mode I tests showed an increase in the average fracture toughness between 31%-61%, and mode II tests showed an increase of 161% but a very large scatter in the results was reported.

Lewis [110] performed short beam shear tests [127] to study the influence of nano-stitching on the interlaminar shear strength (ILSS). Quasi-isotropic lay-ups reinforced with 5-65μm CNT in every interface were tested. Even though samples with seven different CNT heights were tested, no relevant difference was reported between the reinforced configurations since, regardless of the initial height, the forests were compressed to around $5\mu m$ in the interface. The average improvement in ILSS over the unreinforced baseline was 8.75±0.5%. Moreover, the CNT reinforcement was shown to be effective enough to deviate delamination propagation from the interfaces to within the plies even though this results in a very limited strength improvement.

Other forms of through-thickness reinforcement that rely on bridging as the main toughening mechanism such as stitching, z-pinning and weaving have proved to increase the through-thickness properties, however, the in-plane properties usually decrease due to damage and misalignment of the reinforcing fibres caused by the reinforcement's geometry. Following Garcia et al. [8] study, Guzmán de la Villoria et al. [111] carried out an experimental campaign to prove that the nano-reinforcement had no such degrading effect due to the un-obstructive nature of the interface reinforcement in the adjacent plies. The experimental test campaign included open-hole compression, bolt bearing and L-shape tests. For bolt-bearing, the major reported improvement was not the increase in ultimate failure but the delay/suppression of sub-critical interlaminar damage giving the material a 30% increase in the load corresponding in the load corresponding to damage onset (first load drop). For open-hole compression, both a 14% increase of ultimate strength and the suppression of sub-critical damage near the hole was reported. For the L-shapes tests, the reported improvement was also the suppression of sub-critical damage that resulted in a 26% increase in the ultimate deflection of the specimen and a correspondent 30.7% increase in the energy required to break the specimen.

The experimental campaign reported in Ref. [111] suggests that the in-plane properties are not degraded by the presence of CNT in the interfaces and actually benefit from their presence. Their presence contributes to the suppression of interlaminar damage in some loading cases, lay-ups and geometries and can result in the improvement of the design strengths.

More recently, Kalfon-Cohen et al. [21], attempted for the first time to combine thin-ply laminates with nano-reinforced interfaces. The goal of this experimental campaign was to understand what are the improvements on the interlaminar strength and toughness that could be obtained by reinforcing thin-ply laminates with CNTs compared to baseline conventional grade laminates. Short beam shear tests were performed on three quasi-isotropic laminate configurations: a conventional grade laminate (162gsm), a thin-ply laminate (54gms) and a nano-reinforced thin-ply laminate, where the middle plies of the specimens where reinforced with $20\mu m$ tall carbon nanotubes. A synergetic strength effect of nano-stitching and thin-ply lamination was found: the use of thin-ply increased the strength by 10% and the selective reinforcement of the interfaces further increased it by 5%. Moreover, as shown in Fig. 7.1, a complete suppression of delamination planes of the nano-reinforced interfaces was found, which confirms the effectiveness of the rein-

forcement technique. A 15% increase of the mode I and mode II fracture toughness of the nano-reinforced interfaces was numerically estimated based on finite element analysis of the short beam shear samples, performed using the models described in Chapter 3. However proper characterization of the interfaces is still required to confirm this numerical assessment.

In this study, the mode I, mode II and mixed-mode crack resistance curves associated with crack propagation in nano-reinforced thin-ply interfaces are experimentally determined. Following Kalfon-Cohen et al. [21], 54gsm thin-ply HTS40/Q-1112 carbon fibre-epoxy material system reinforced with 20μm aligned carbon nanotubes are used. The experimental procedure and test results are presented in Section 7.1. A numerical study on the effect of ply thickness and the effect of reinforcing the interfaces with carbon nanotubes on a composite subcomponent is also performed. The case study and numerical results are presented in Section 7.2.

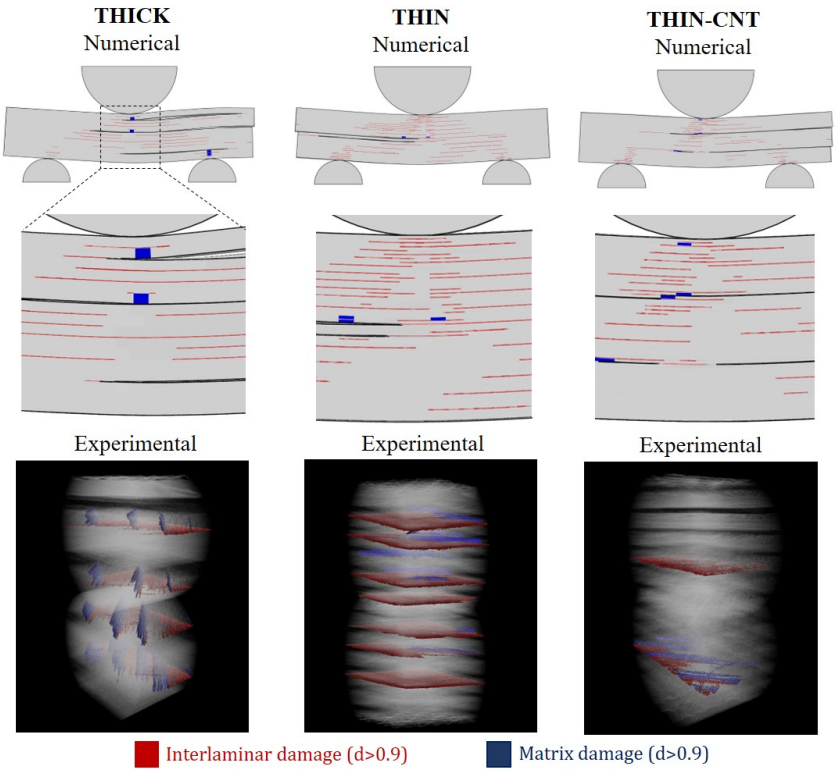

Figure 7.1: Segmented Synchrotron Radiation Computed Tomography (SRCT) images of *post mortem* short-beam shear samples and the corresponding finite element results of the simulated specimens. Delamination is shown in red and matrix cracks are shown in blue. For the nano-reinforced sample (THIN-CNT), the middle fifteen interfaces are reinforced with vertically aligned carbon nanotubes [21].

7.1 Experimental work

7.1.1 Test Setup and data reduction method

The ASTM standards [113, 114] proposed to measure the mode I and mode II interlaminar fracture toughness are based on Linear Elastic Fracture Mechanics (LEFM) which main hypothesis is that the nonlinear deformation at the crack front is small in comparison to any of the specimen's dimensions. The method has been largely applied to fibre reinforced polymers, however, the determination of the fracture toughness and crack resistance curves using these methods rely on the accurate measurement of the crack length, which can be particularly difficult for mode II and mixed mode tests. Moreover, the main hypothesis that the non-linear deformation at the crack front, and the bridging mechanisms that may be present along the wake of the crack, have a negligible effect might not apply for all material systems, including those that have nano-reinforced interfaces.

J-integral closed-form solutions for interlaminar fracture tests have been proposed for mode I [115–118], mode II [119–122] and mixed mode [123–126] but the ASTM standard methods are still usually preferred over these solutions. In this work, the solutions proposed by Paris and Paris [279], Stigh et al. [122] and Sarrado et al. [126] are used. These J-integral closed-form solutions, rely on the determination of the rotation angle of the load introduction points, instead of the crack length. This increases the complexity of the instrumentation, however, reduces the uncertainty of the results related to the determination of that crack length and greatly simplifies the data post processing. NA3-30 capacitive dielectric liquid-based inclinometers from SEIKA Mikrosystemtechnik GmbH were used to control the rotation angles at the load introduction points. Even though this information is not required to calculate the J-integral, the crack length was monitored from the photos of the cross-section of the specimens recorded with a Canon EOS 550D camera. The load, displacement and rotation angles were recorded with a frequency of 20Hz and the crack length was monitored from the photos of the cross-section of the specimens recorded every 0.5s. A schematic representation of the experimental setup and instrumentation is shown in Fig. 7.2. The particular data reduction methods and instrumentation for each type of test are explained in the following sections.

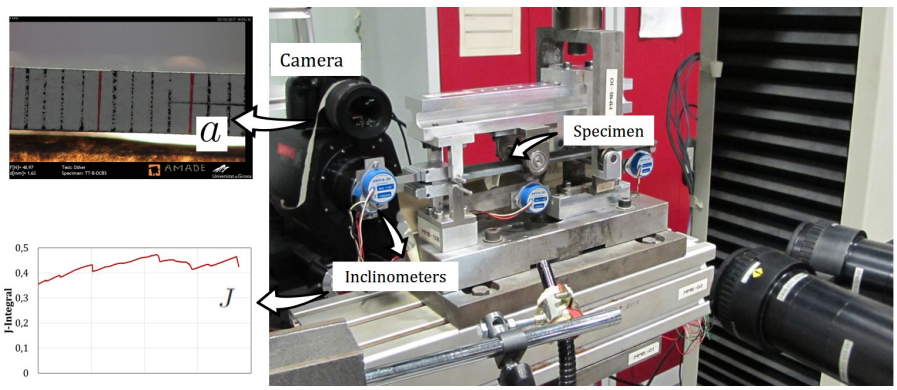

Figure 7.2: Schematic representation of the experimental setup and information obtained from the tests

7.1.1.1 Mode I tests

The double cantilever beam (DCB) specimens were tested on a MTS Insight equipped with a 10kN load cell under displacement control at a speed of 5mm/min. Two inclinometers were used to monitor the rotation angles at the load introduction points, θ_A and θ_C. The test setup is shown in Fig. 7.3 and the dimensions of the samples are presented in Table 7.1.

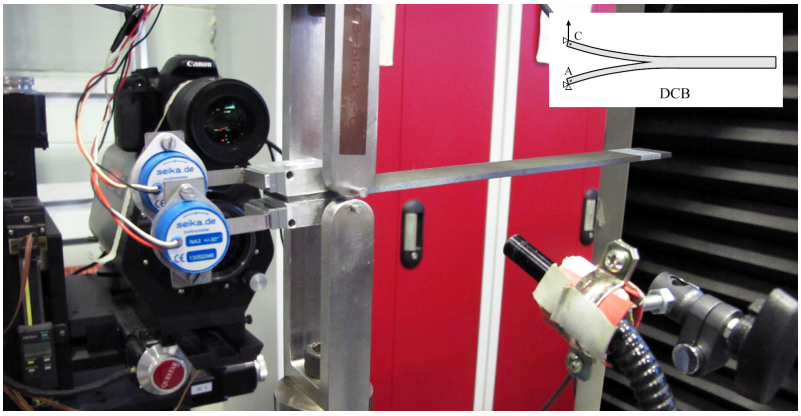

Figure 7.3: Experimental setup of the double cantilever beam tests

The J-integral for mode I was calculated as proposed by Paris and Paris [279]:

$$J = 2\frac{P}{b}\theta \tag{7.1}$$

where P is the applied load, b is the width of the specimen and θ is the angle at the load introduction point. In this work, the rotation angles at both the upper and lower load introduction points of the DCB specimen were recorded. The angles are defined as positive counter clockwise.

Table 7.1: Nominal dimensions of the DCB samples. L, b, 2h, a_0, c are the length (or half span for ENF and MMB), width and thickness of the specimen, length of the precrack and lever arm length, respectively.

Ref	L (mm)	b (mm)	2h (mm)	a0 (mm)	c (mm)
DCB	250	25	3	37	-
ENF	60	25	3	42	-
MMB	75	25	3	45	59.4

7.1.1.2 Mode II tests

The end notched flexure (ENF) specimens were tested on a MTS Insight equipped with a 10kN load cell under displacement control at a speed of 1mm/min. Three inclinometers were used to monitor the rotation angle at the load introduction points, θ_A, θ_B and θ_D. The test setup is shown in Fig. 7.4 and the dimensions of the samples are presented in Table 7.1. The determination of the mode II crack resistance curves requires the crack propagation to be stable. For the ENF tests, the crack propagation is stable for a_0/L higher than approximately 0.7, where L is the

half span and a_0 is the initial crack length. The span used was 120mm, rather than the 100mm suggested by the ASTM standard, to increase the crack propagation area and therefore, a initial crack length of 42mm had to be used to ensure a stable crack propagation during the test.

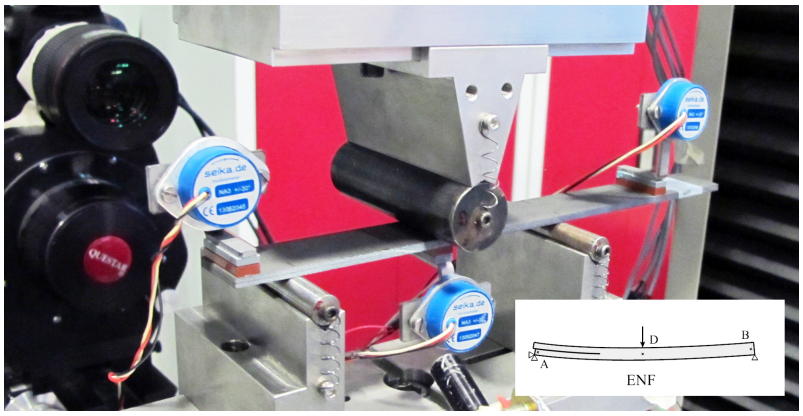

Figure 7.4: Experimental setup of the end notched flexure tests.

The J-integral for mode II is calculated as proposed by Stigh et al. [122]:

$$J = \frac{P}{2b}(\theta_A - 2\theta_D + \theta_B) \tag{7.2}$$

where P is the applied load, b was the width of the specimen and θ_A, θ_B and θ_D are the angles at the load introduction points (see Fig. 7.4). As before, the angles are defined as positive counter clockwise.

7.1.1.3 Mixed-mode tests

The mixed mode bending (MMB) specimens were tested on a MTS Insight equipped with a 10kN load cell under displacement control at a speed of 0.5mm/min. Four inclinometers were used to monitor the rotation angle at the load introduction points, θ_A, θ_B, θ_C and θ_D. The test setup is shown in Fig. 7.5 and the dimensions of the samples are presented in Table 7.1. The distance between supports was set to 150mm to increase the crack propagation area, and the initial crack length was set to 45mm. The MMB lever arm was determined following the ASTM standard, depending on the specimen thickness and material properties. The aimed mixed-mode ratio was 50%.

The J-integral for mixed mode bending was calculated as proposed by Sarrado et al. [126]:

$$J = \frac{P}{b}\left[\left(\frac{1}{2} - \frac{c}{2L}\right)\theta_A + \left(\frac{1}{2} + \frac{c}{2L}\right)\theta_B + \frac{c}{L}\theta_C - \left(1 + \frac{c}{2L}\right)\theta_D\right] \tag{7.3}$$

where P is the applied load, b is the width of the specimen and θ_A, θ_B, θ_C and θ_D are the rotation angles (in radians) at the load introduction points (see Fig. 7.5), defined as positive counter clockwise.

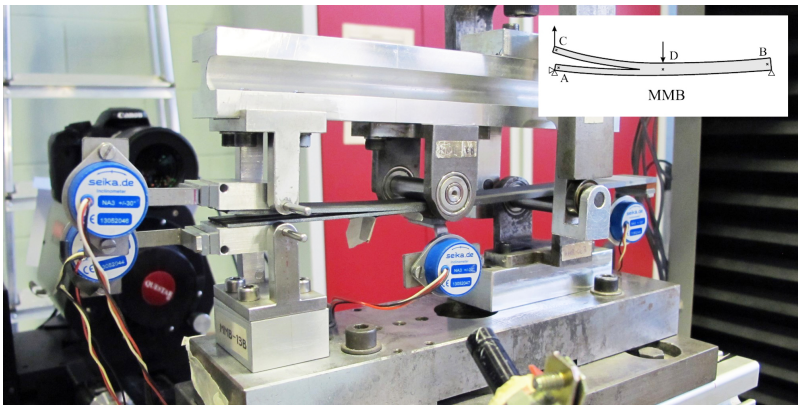

Figure 7.5: Experimental setup of the mixed mode bending tests.

7.1.2 Specimen preparation

20μm height aligned carbon nanotube (A-CNT) forests were grown on 30mm x 120mm silicon wafer substrates using the Chemical Vapor Depositon process. The final stage of the process included a water-assisted delamination step that allows the CNT forests to be easily removed from the silicon wafers. 54gsm thin-ply HTS40/Q-1112 carbon fibre-epoxy prepreg was used. Baseline and Nanoreinforced unidirectional [0_{30}/d/0_{30}] laminates were manufactured, where d is the middle plane where the teflon insert is located. The middle two plies were layed-up with a mismatch angle of 4° to minimize fibre nesting, so the effective lay-up used was [0_{29}/2/d/-2/0_{29}]. The nano-stitched samples were manufactured including a 30mm x 120mm CNT forest in the middle interface as described in Ref. [110] and shown in Fig. 7.6: a) the silicon wafer is inverted onto the prepreg, b) pressure is applied to the wafer and finally c) the wafer is removed. A 60mm long and 0.025mm thick PTFE insert was introduced in the mid-plane of each plate to create the precrack. The panels were cured in an autoclave according to the manufacturer specifications: 30min at 80°C at 0 bar followed by 90min at 130°C at 7bar. The specimens were cut from the plates using diamond coated disk. Before testing, the surface of the specimens was cleaned using sandpaper and acetone and one side of the samples was painted white and marked at every millimetre so that the crack length could be monitored. Table 7.2 summarizes the specimens manufactured.

Table 7.2: Description of the ply thickness and stacking lay-up of each set of samples. The dimensions L, b and 2h are the nominal dimensions.

Ref	Lay-up	Nanostitched int.	Ply t (μm)	L (mm)	b (mm)	2h (mm)
TT-B	[0_{29}/2/d/-2/0_{29}]	-	54	250	25	3
TT-R	[0_{29}/2/d/-2/0_{29}]	Middle	54	250	25	3

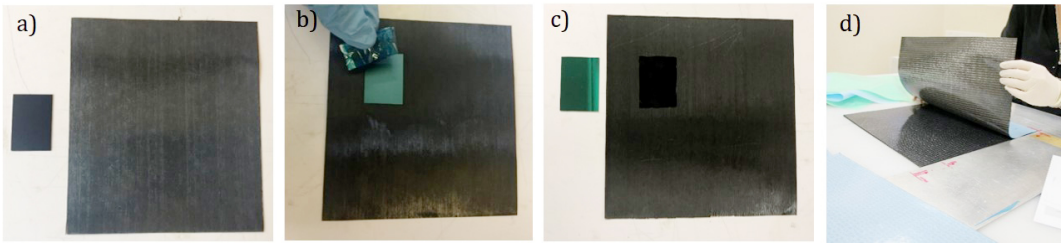

Figure 7.6: Transfer process: a) the silicon wafer is inverted onto the prepreg, b) pressure is applied to the wafer and finally c) the wafer is removed d) a new ply is layed up.

7.1.3 Experimental test results

7.1.3.1 Mode I test results

The load-displacement curves of the DCB tests are shown in Fig. 7.7. The specimens all showed a linear elastic behaviour up to the point of maximum load, where the load dropped sharply. The specimens were not precracked and consequently the cracks start propagating from in the area near the teflon insert. The vicinity of the teflon insert is typically a resin rich area and the corresponding crack is likely not as sharp as a the crack tip resulting from propagation. The first load drop observed after the peak load in every test is partially attributed to the crack geometry and resin content. Even tough the point of maximum load might yield unrealistically high values of the fracture toughness, it was used to calculate this property so that a comparison between the two material configurations can be made.

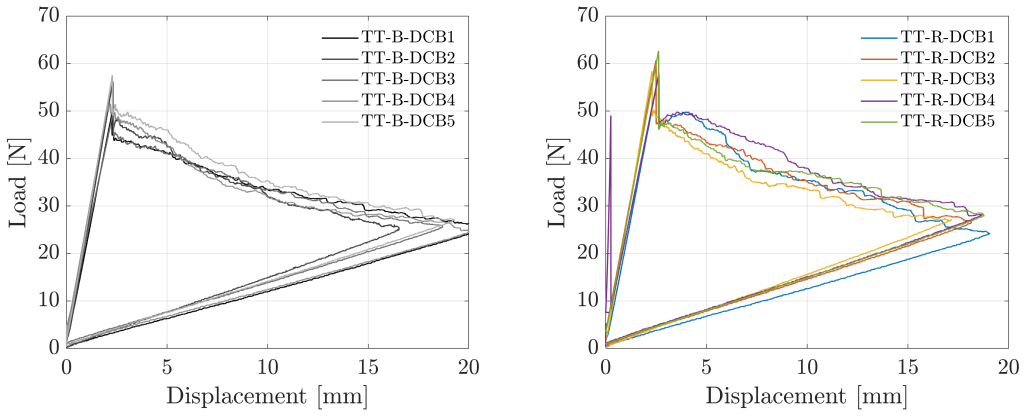

(a) TT-B-DCB (b) TT-R-DCB

Figure 7.7: Load-displacement curves of TT-B-DCB TT-R-DCB samples.

From the load and rotation angles at the load introduction points obtained for each specimen, the mode I J-integral was determined following Eq. (7.1) and plotted as a function of the crack length. The results are shown in Fig. 7.8. Note that the steady state values for the fracture toughness were not reached for the applied displacement. In fact, a significant amount of fibre bridging was observed both configurations as shown in Fig. 7.9.

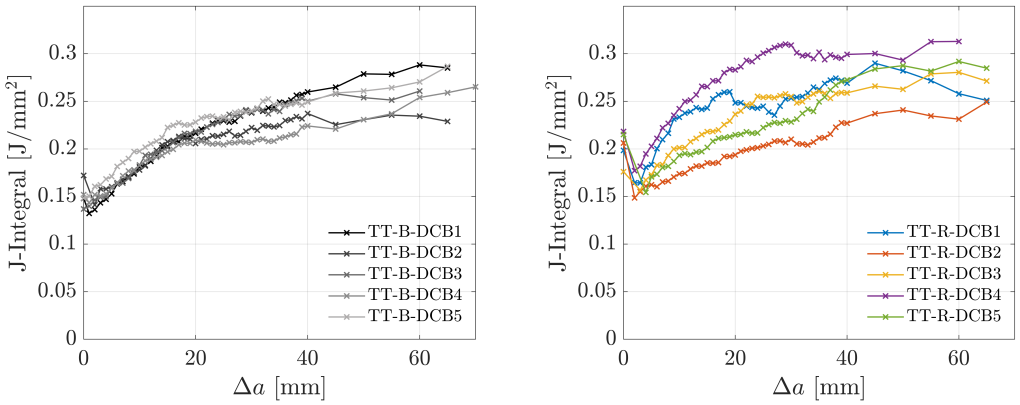

(a) TT-B-DCB (b) TT-R-DCB

Figure 7.8: Mode I crack resistance curves of TT-B-DCB TT-R-DCB samples.

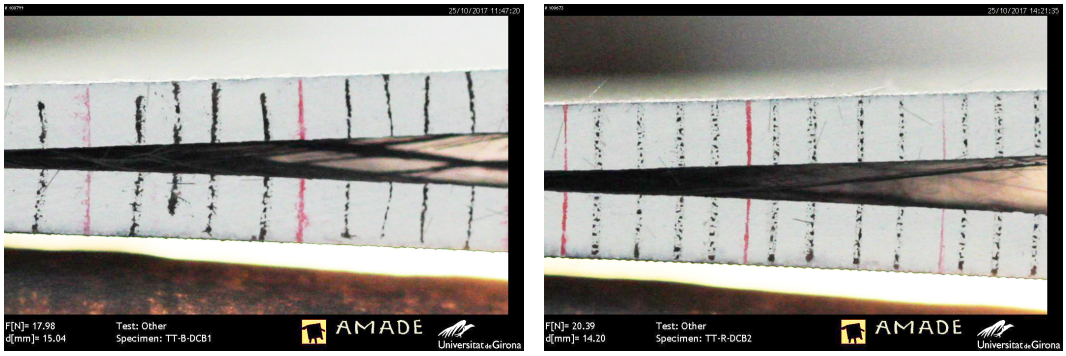

(a) TT-B-DCB (b) TT-R-DCB

Figure 7.9: Fibre bridging of TT-B-DCB and TT-R-DCB samples.

The average $\mathcal{R}$-curves for both configurations are shown in Fig. 7.10a. The average initiation value of the fracture toughness of the reinforced samples is 34% higher than that of the baseline configuration but the average mode I fracture toughness during propagation is only 10% higher than that of the baseline and the error bars nearly overlap. The higher inconsistency of the crack propagation of the reinforced samples compared to the baseline samples is clearly highlighted in Figs. 7.8 and 7.10a. In fact, it is plausible that for some samples, the crack migrates to an unreinforced region, namely the intralaminar region. This process might increase or decrease the measured fracture toughness. On one hand, if a crack migrates to the intralaminar region where CNTs are not present the measured fracture toughness should be supposedly lower. However, this can lead to an increased crack tortuosity and a more significant fibre bridging effect, which should lead to a higher apparent measured fracture toughness. The crack surface of the broken samples was analysed as shown in Fig. 7.11. From previous scanning electron microscopy analysis on broken samples, it was concluded that darker matte areas (highlighted with a white contour in Fig. 7.11) correspond to carbon nanotube rich areas and lighter glassy areas correspond to resin/fibre rich areas where carbon nanotubes are not visible (see Fig. 7.12). In Fig. 7.11, it can be observed that in the reinforced samples the

area near the teflon insert is clearly a CNT rich area but as the crack progresses, the percentage of CNT rich area decreases significantly. This suggests that in the beginning of the test, the crack propagates through the reinforced area, and then progressively shifts away from this area into the unreinforced intralaminar region. This explains why the initiation value of the fracture toughness of the reinforced samples is 34% higher while during crack propagation, only a 10% improvement was found.

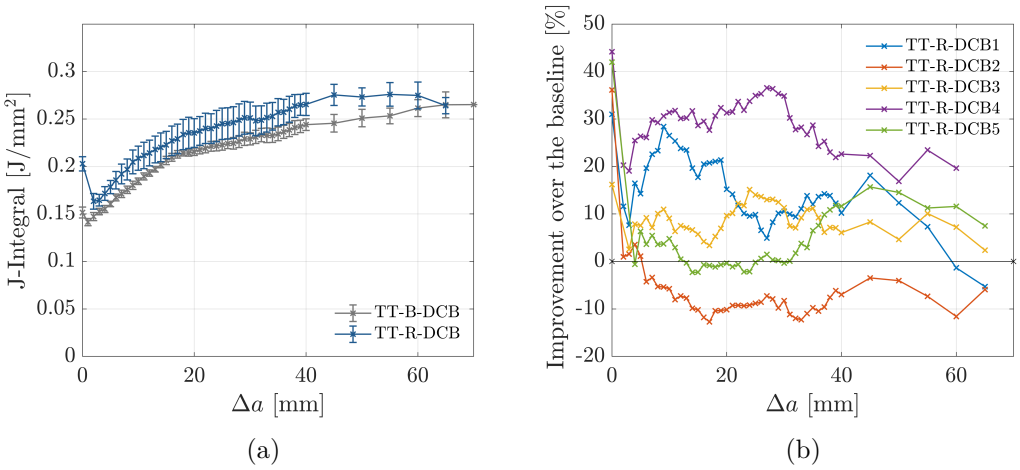

Figure 7.10: a) Average mode I crack resistance curves of TT-B-DCB and TT-R-DCB samples. b) improvement over the baseline of each TT-R-DCB sample.

In Fig. 7.10b, the improvement of the mode I fracture toughness of the reinforced samples over the average toughness of the baseline samples is plotted as a function of the crack length. The inconsistency is one more highlighted since the improvements over the baseline range from -10% to +35% depending on the sample. However, no significant difference between the crack surfaces to justify the different improvements are observed.

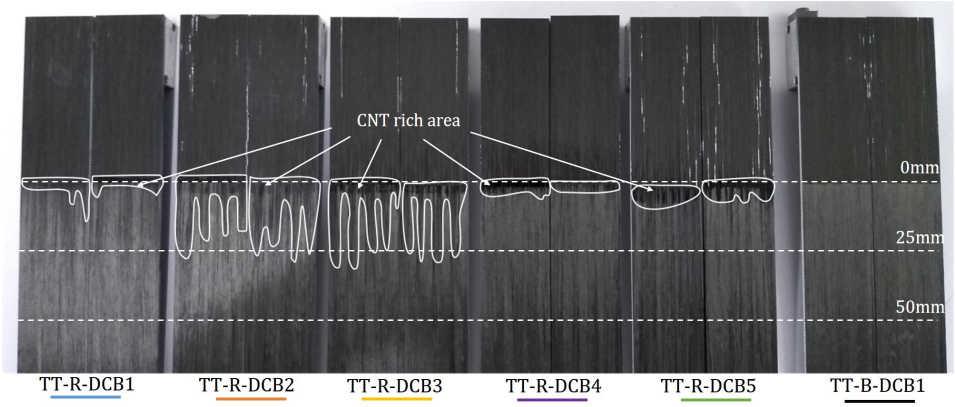

Figure 7.11: Crack surfaces of TT-R-DCB1 - TT-R-DCB5 and TT-B-DCB1 samples. The CNT rich crack surfaces are highlighted with a white contour.

7.1.3.2 Mode II test results

Despite the modification of in the test setup (see Section 7.1.1.2), initial tests revealed that the crack propagation was still unstable for the selected a_0/L ratio. In fact, similarly to the mode I tests, if the samples are not precracked, the crack propagates from a resin rich area near the teflon insert, which is not as sharp as the crack tip resulting from crack propagation, and therefore, the load drops suddenly after crack initiation. For this reason, all the samples were precracked 2mm in mode I using a wedge. The tests performed on the baseline samples were all stable as shown in Fig. 7.13a. However, as shown in Fig. 7.13b the reinforced samples were all unstable, even though there were precracked using the same methodology. Three out of the six samples still propagated up to around 5mm, point when the measured fracture toughness drops and the crack propagated unstably. For this reason, the reinforced samples were tested twice: once after precrack and once after unstable propagation. After unstable propagation, the crack position was marked and the sample was shifted so the same initial crack length $a_0 = 42$mm was used. The first round of tests will be referred to as #1 and the second as #2. As shown in Fig. 7.13c and contrary to the #1 tests, the #2 tests of the reinforced samples were stable and significantly more consistent.

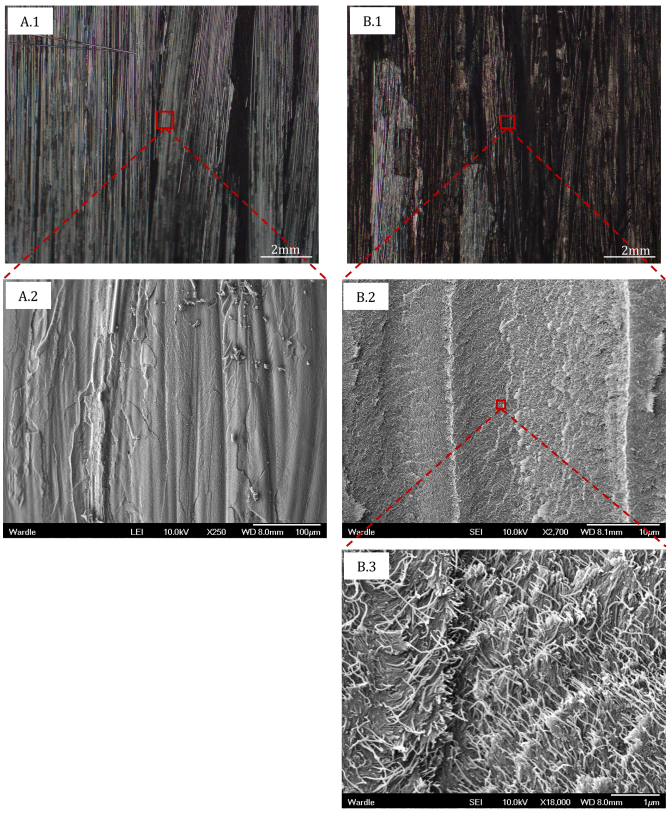

Figure 7.12: SEM analysis of the crack surfaces of a A) glassy dark region corresponding to intralaminar crack propagation and a B) dark matte region, corresponding to a CNT rich crack surface.

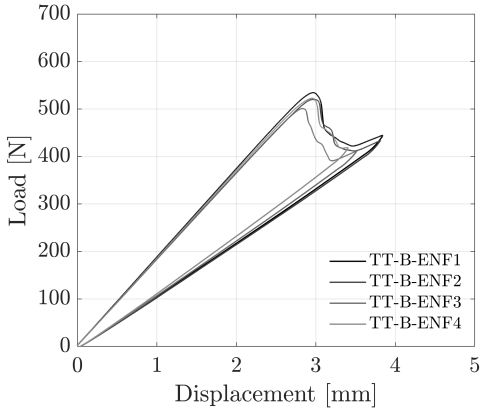

(a) TT-B-ENF

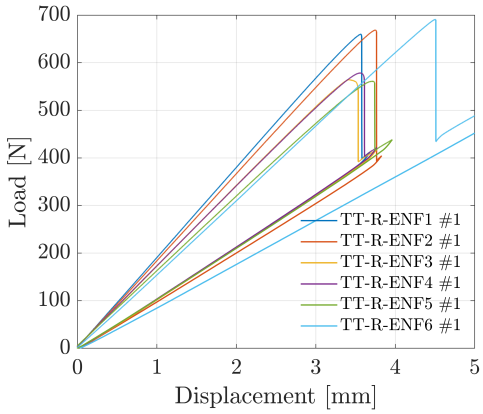

(b) TT-R-ENF #1

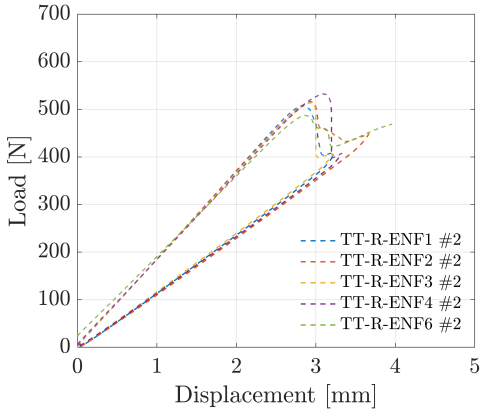

(c) TT-R-ENF #2

Figure 7.13: Load-displacement curves of TT-B-ENF TT-R-ENF samples.

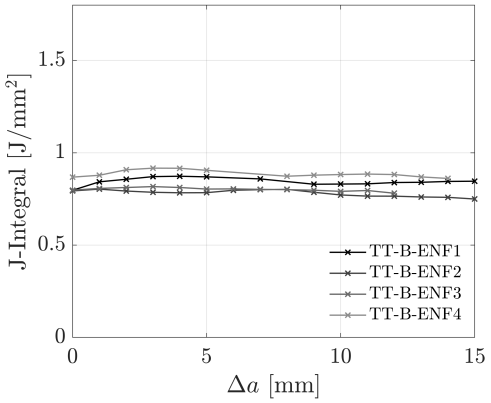

(a) TT-B-ENF

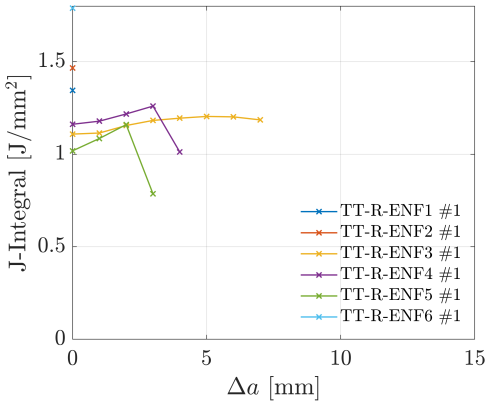

(b) TT-R-ENF #1

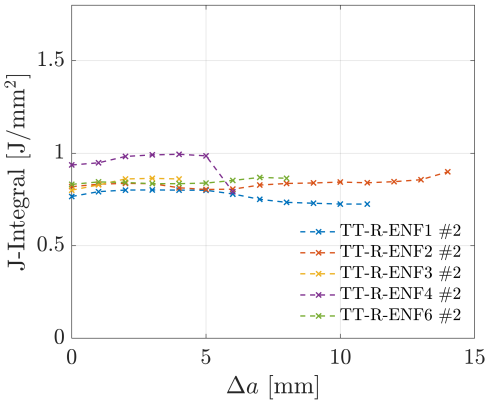

(c) TT-R-ENF #2

Figure 7.14: Mode II crack resistance curves of TT-B-ENF TT-R-ENF samples.

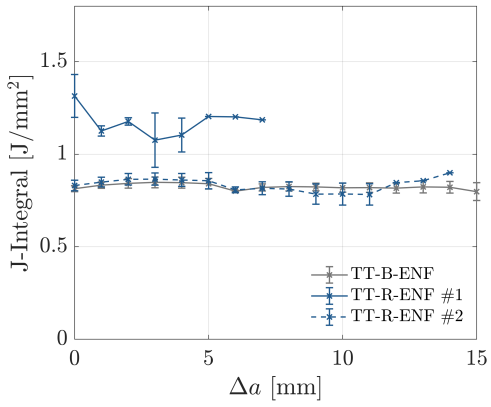

(a)

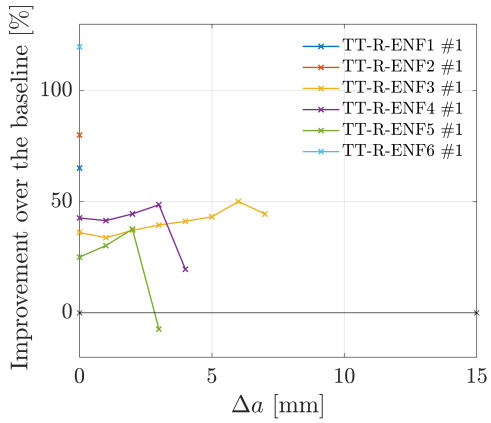

(b)

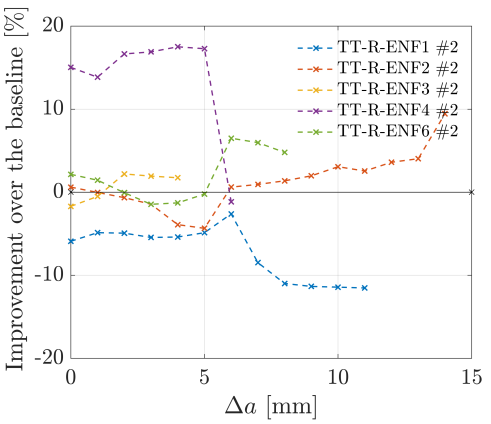

(c)

Figure 7.15: a) Average mode II crack resistance curves of TT-B-ENF, TT-R-ENF #1 and TT-R-ENF #2 samples. b) improvement over the baseline of each TT-R-ENF #1 and c) TT-R-ENF #2 samples.

From the load and rotation angles at the load introduction points obtained for each specimen, the mode II J-integral was determined following Eq. (7.2) and plotted as a function of the crack length. The results are shown in Fig. 7.14. Comparing the $\mathcal{R}$-curves from TT-R-ENF #1 and #2 (Figs. 7.14b and 7.14c) it is clear that the fracture toughness of #1 tests is higher and the tests were often more unstable than that of #2 tests. The average $\mathcal{R}$-curves for both configurations are shown in Fig. 7.15a. From Fig. 7.15a, it can be concluded that in fact, the fracture toughness of the reinforced samples (#1) is around 40% higher than that of the baseline while #2 test results show no improvement. This suggests that, the crack propagates in a CNT rich area, until it shifts away to an area where crack propagation is less limited. This was confirmed by analysing the crack surface of the samples in Fig. 7.16. Similarly to what was observed in the mode I samples, the area near the teflon insert is clearly a CNT rich area. Particularly, in the first 5mm after the precrack, the density of areas where the CNTs are visible is significantly larger than the remaining area further from the crack tip. Moreover, there is nearly no CNT rich areas visible in the area corresponding to the second round of tests (#2). This suggests that in the beginning of the test, the crack propagates through the reinforced area, and then progressively shifts away from this area into the unreinforced intralaminar region.

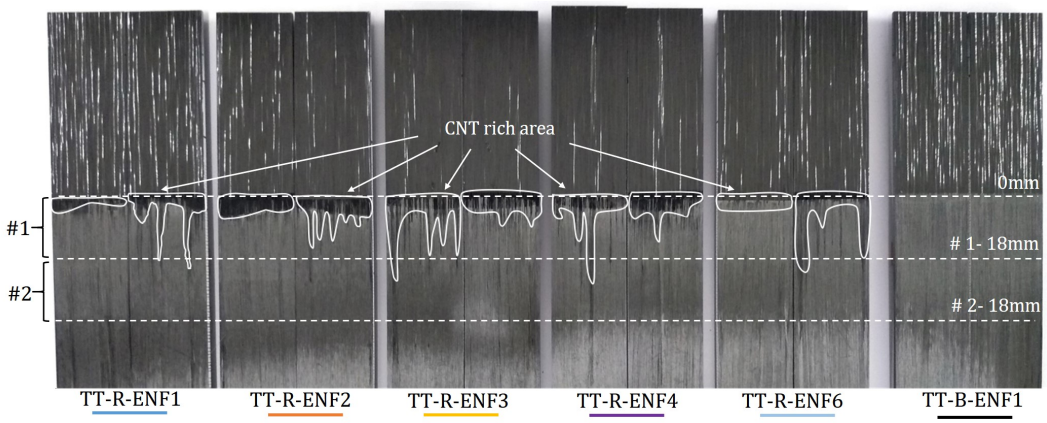

Figure 7.16: Crack surfaces of TT-R-ENF1 - TT-R-ENF6 and TT-B-ENF1 samples. The CNT rich crack surfaces are highlighted with a white contour.

7.1.3.3 Mixed-mode test results

Similarly to the mode II samples, from preliminary tests it was concluded that crack propagation unstable if the samples were not precracked. For this reason, all the samples were precracked 2mm in mode I using a wedge. The load-displacement curves obtained are shown in Fig. 7.17. Similarly to mode I and mode II samples, the baseline (TT-B) load-displacement curves are significantly more consistent than those of the reinforced samples (TT-R).

From the load and rotation angles at the load introduction points obtained for each specimen, the mixed-mode J-integral was determined following Eq. (7.3) and plotted as a function of the crack length. The results are shown in Fig. 7.18. The average $\mathcal{R}$-curves for both configurations are shown in Fig. 7.19a. The average mixed-mode fracture toughness of the reinforced configuration is not statically higher than that of the baseline even though some clearly have an increased frac-

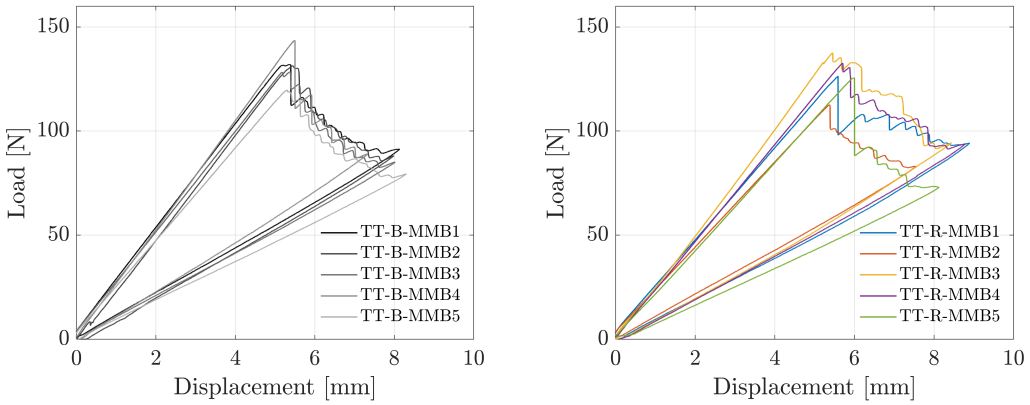

(a) TT-B-MMB (b) TT-R-MMB

Figure 7.17: Load-displacement curves of TT-B-MMB TT-R-MMB samples.

ture toughness as shown in Fig. 7.19. In fact, the improvement over the baseline range from -18% to 30% depending on the sample. This clearly highlights the higher inconsistency of the crack propagation of the reinforced samples compared to the baseline samples.

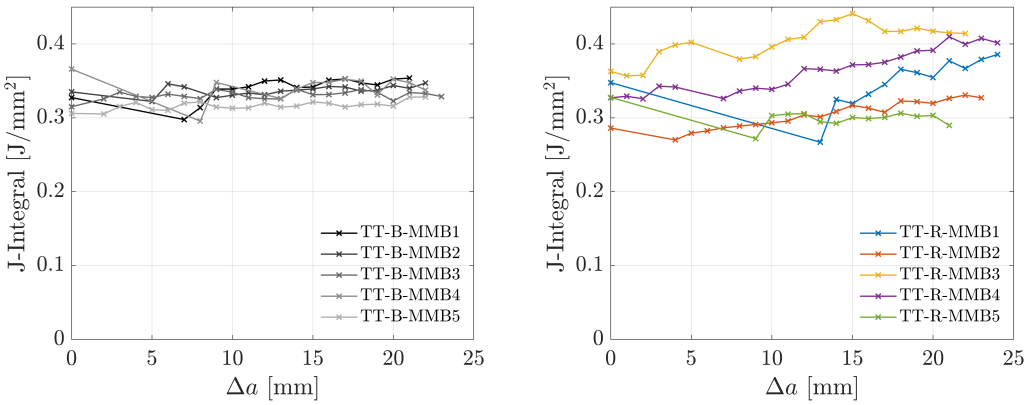

(a) TT-B-MMB (b) TT-R-MMB

Figure 7.18: 50% mixed mode crack resistance curves of TT-B-MMB TT-R-MMB samples.

Fig. 7.20 shows the crack surfaces of TT-R-MMB1 - TT-R-MMB5 and TT-B-MMB1 samples. This analysis revealed that, in the TT-R-MMB3 and TT-R-MMB4 samples, the cracks propagated through the CNT rich interfaces more often than in the remaining samples. This is consistent with the higher improvement on the fracture toughness reported for those samples.

7.1.4 Statistical analysis

A Welch's T-test or unequal variances T-test, was performed to test the hypothesis that TT-B and TT-R populations have significantly different mean mode I, mode II and mixed-mode fracture toughness or if the differences observed are more likely due to random error (sampling errors).

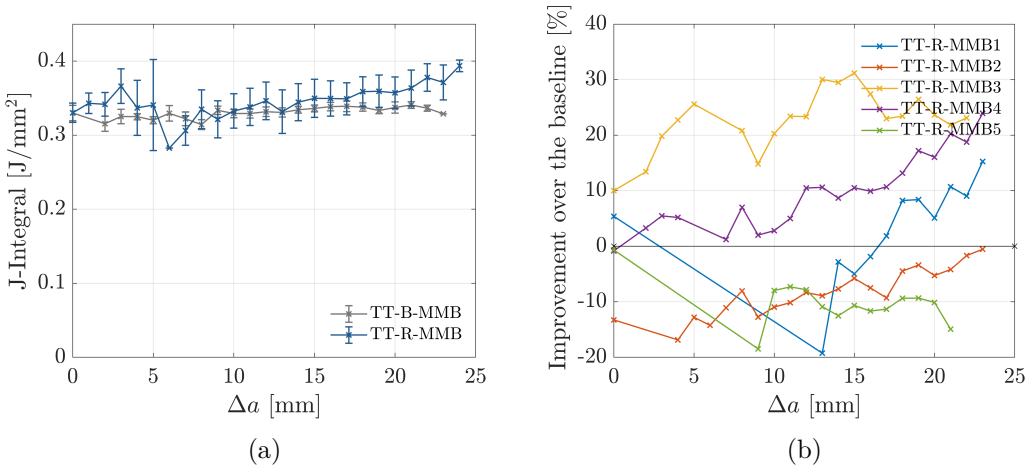

Figure 7.19: a) Average mixed-mode crack resistance curves of TT-B-MMB and TT-R-MMB b) improvement over the baseline of each TT-R-MMB samples.

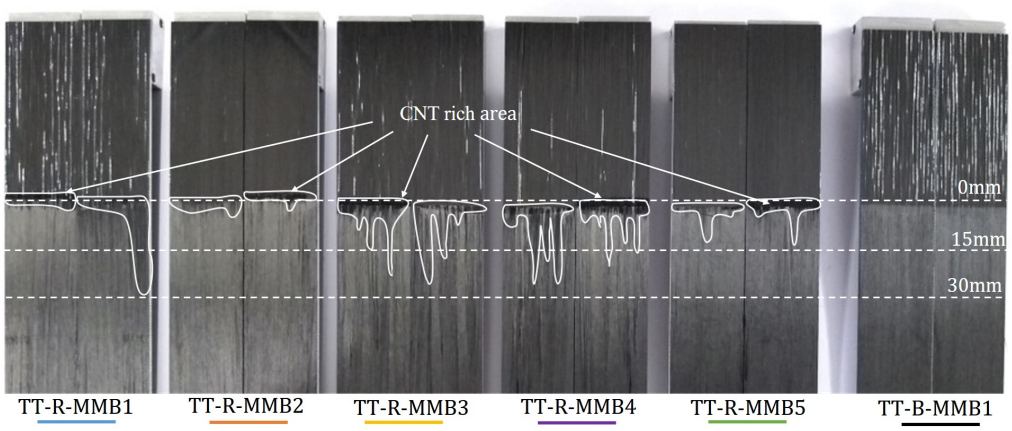

Figure 7.20: Crack surfaces of TT-R-MMB1 - TT-R-MMB5 and TT-B-MMB1 samples. The CNT rich crack surfaces are highlighted with a white contour.

The Welch's T-test is a two-sample hypothesis-testing technique that can be used to test the equality of two populations means. It is an adaptation of Student's t-test, that is more reliable when the two samples have unequal variances and unequal sample sizes. To use it, the following assumptions have to be made: i) all populations involved follow a normal distribution and ii) the samples are randomly selected and independent of one another.

The null hypothesis assumes that the population means are equal. The probability value (p-value) ranges from 0 to 1 and is used in the context of null hypothesis testing in order to quantify the idea of statistical significance of evidence. The threshold value of the the level of significance used was $\alpha = 0.05$, which means that if the p-value determined for a given set of samples is lower than 0.05 ($p - value < \alpha$), the null hypothesis can be rejected, i.e. the mean fracture toughness is not statistically equal for the two configurations.

Since the fracture toughness is a function of the crack length, the p-value was also calculated as a function of the crack length. For the sake of clarity, the level of confidence $(1 - \alpha)$ and $1 - p$ are plotted in Fig. 7.21. If $1 - p > 1 - \alpha$, the null

hypothesis is rejected: the mean fracture toughness is not statistically equal for the two configurations. From this analysis, the following can be concluded:

- As shown in Fig. 7.21a, there is >95% confidence that the initiation value of the mode I fracture toughness of the reinforced samples is higher than that of the baseline samples. However, there is no statistical difference between the fracture toughness of the two configurations during crack propagation.
- As shown in Fig. 7.21b, there is >95% confidence that the initiation value of the mode II fracture toughness of the reinforced samples is higher than that of the baseline configuration. However, as shown in Fig. 7.21c, no significant difference between the fracture toughnesses was found the second time the samples were tested.
- The is no statistical evidence that the 50% mixed mode fracture toughness is higher than that of the baseline samples.

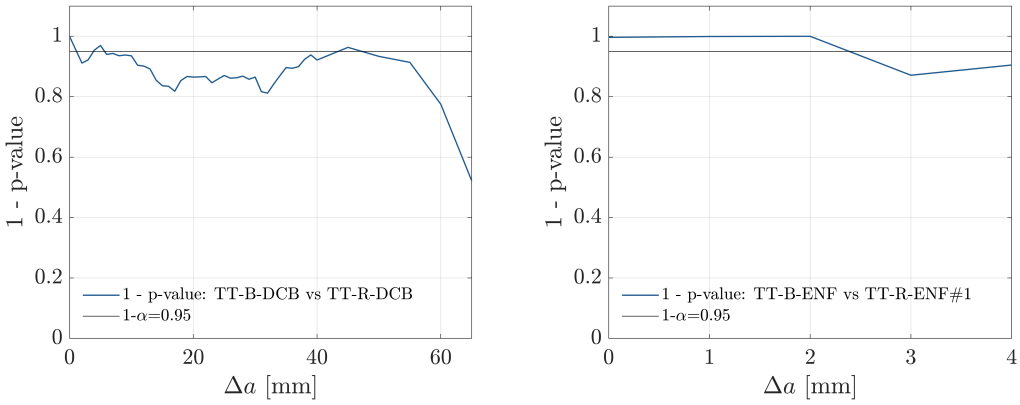

(a) DCB

(b) ENF #1

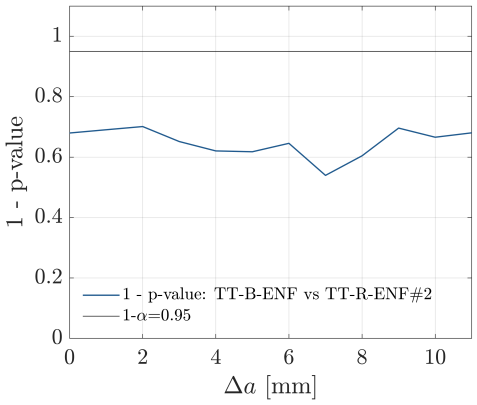

(c) ENF #2

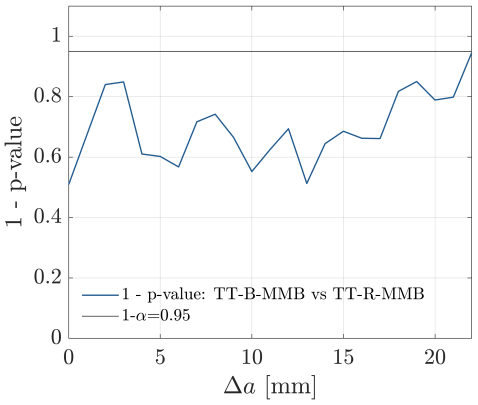

(d) MMB

Figure 7.21: 1-pvalue as a function of the crack length.

7.1.5 Discussion

The effect of the presence of carbon nanotubes in the interfaces of thin-ply laminates on the mode I, mode II and mixed mode interlaminar fracture toughness

was studied testing 54gsm thin-ply HTS40/Q-1112 carbon fibre-epoxy laminates reinforced with 20μm aligned carbon nanotubes in the interface. The test results of the reinforced configuration are less consistent than those of the baseline. It is clear from the test results that the inclusion of carbon nanotubes makes crack propagation less stable since the crack migrates to a non-reinforced area that is more prone to delamination (namely the intralaminar region) as the crack length increases. This means that the crack resistance curves measured are not directly related to the CNT rich interface but to a combination between reinforced and unreinforced regions. Only the improvement related to the initiation value of the fracture toughness could be measured. A 30% and a 40% improvement on the mode I and mode II initiation value of the fracture toughness, respectively, was determined.

If the cracks migrate to non-reinforced areas during crack propagation, this type of reinforcement might not be particularly successful in configuration and loading conditions where interlaminar crack growth is progressive. However, for in-plane loadings, where failure is usually catastrophic and when interfaces are mostly subjected to mode II and mixed mode loading conditions, the presence of the CNTs can potentially delay subcritical damage in the interfaces, as concluded by Guzmán de la Villoria et al. [111] and Kalfon-Cohen et al. [21]. The type of nano-reinforcement at hand could be particularly interesting as a selective reinforcement in areas with stress concentrations such open-holes, bolted joints or components with ply drops where delamination resistance is critical.

7.2 Case study

Aerospace composite structures are often made of skins with co-cured stringer and stiffeners. Given the mismatch in bending stiffness and the discrete transition of the thickness (ply drops) that result in stress concentrations, the structural integrity of such components is generally limited by delamination near the stiffener flange. For this reason, the local reinforcement of the structure interfaces in the thickness transition regions is expected to improve the design of such components.

A numerical study on the effect of ply thickness and the the effect the reinforcing interfaces with carbon nanotubes in a skin-stiffener component is performed. A simple specimen consisting of a stringer flange bonded onto a skin loaded in tension was considered. Three skin-stiffeners designs made from HTS40/Q-1112 were defined following Ref. [280]: L1, L2 and L4, where the ply thickness are one, two and four times that of the nominal ply thickness of the prepreg (see Table 7.3). With the purpose of determining the effect of using carbon nanotubes as a reinforcement in these structures, three additional skin-stiffener configurations, where every interface is nano-stitched, were studied: L1-CNT, L2-CNT and L4-CNT. The dimensions of the specimens are presented in Table 7.4 and Fig. 7.22.

The modelling strategy used in this study was previously used and validated in Ref. [21]. The details are presented in Section 7.2.1 and the outcomes of the analysis are presented in Section 7.2.2.

Table 7.3: Stacking sequences of the skin stiffener.

Reference	Ply thickness	Skin	Stiffener
L4 and L4-CNT	0.216mm	$[0/45/90/-45/45/-45/0]_S$	$[45/90/-45/0/90]_S$
L2 and L2-CNT	0.108mm	$[0/45/90/-45/45/-45/0]_{2S}$	$[45/90/-45/0/90]_{2S}$
L1 and L1-CNT	0.054mm	$[0/45/90/-45/45/-45/0]_{4S}$	$[45/90/-45/0/90]_{4S}$

Table 7.4: Geometry of the skin stiffener.

Reference	Ply thickness	Nr. of Plies	Length	Width	a	b
L4 and L4-CNT	0.216mm	28	150mm	25mm	42mm	50mm
L2 and L2-CNT	0.108mm	48	150mm	25mm	42mm	50mm
L1 and L1-CNT	0.054mm	96	150mm	25mm	42mm	50mm

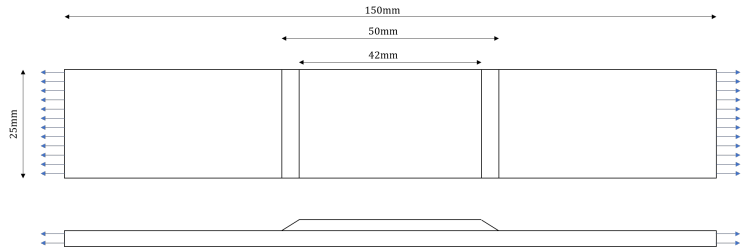

Figure 7.22: Schematic representation of the skin stiffener.

7.2.1 Modelling strategy

The skin-stiffener models used one 8-node linear brick reduced integration element (C3D8R) per ply thickness, t, and cohesive elements (COH3D8) between the plies. X-symmetry conditions were defined in the middle of the specimen and a displacement (through the definition of an appropriate smooth step amplitude) was applied to all nodes at the boundary. A mesh of $0.5\times0.5\times$t mm^3 and of $0.5\times0.5\times0.001$ mm^3 was used for ply elements and for the cohesive elements, respectively (see Fig. 7.23).

Intralaminar damage is simulated using the continuum damage model presented in Chapter 3. As explained in Chapter 3, the continuum damage model is able to predict all the intralaminar failure mechanisms. A linear-elastic response followed by bi-linear softening and a linear-elastic response followed by linear softening was used under longitudinal and transverse loading respectively, while a non-linear elasto-plastic response followed by linear softening was used for in-plane shear. The material properties are presented in Tables 7.5. The ply strengths related to matrix failure (transverse tensile strength, Y_T, transverse compressive strength, Y_C, and in-plane shear strength, S_L) were calculated as a function of the ply thickness and position of the ply using the close-form solutions proposed in Appendix B.

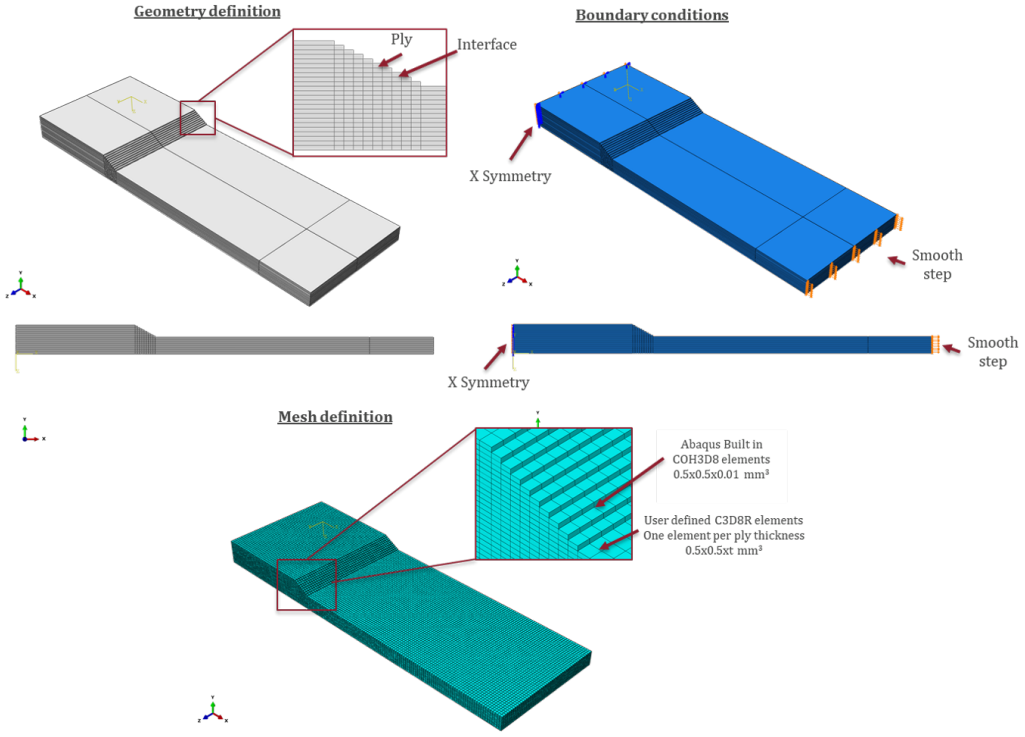

Figure 7.23: Finite element model of the skin-stiffener.

Table 7.5: Ply properties of the HTS40/Q-1112 carbon/epoxy system.

Elastic			*Fracture*			*Strength*		
E_1	[MPa]	98000	$\mathcal{G}_{1+}$	[kJ/m^2]	133.3	X_T	[MPa]	1471
E_2	[MPa]	8460	$\mathcal{G}_{1-}$	[kJ/m^2]	61	X_C	[MPa]	970
G_{12}	[MPa]	3607	$\mathcal{G}_{2+}$	[kJ/m^2]	0.26	Y_T	[MPa]	56
ν_{12}	[-]	0.32	$\mathcal{G}_{2-}$	[kJ/m^2]	1.38	Y_C	[MPa]	178
			$\mathcal{G}_6$	[kJ/m^2]	0.83	S_L	[MPa]	83.

Interlaminar damage was simulated using the cohesive zone model implemented in ABAQUS [229]. The quadratic nominal stress criterion was used for damage initiation and the Benzeggagh-Kenane fracture criterion was used for damage propagation [216]. The engineering solutions proposed by Turon et. al. [212, 213] and by Cui et al. [208] presented in Appendix C were used to calculate the mode I and mode II interlaminar strengths to ensure proper energy dissipation in mixed-mode loadings, and to artificially account for the effects of pressure and friction. As previously considered by Kalfon-Cohen [21], and following the findings presented in Section 7.1.3, the carbon nanotubes were assumed to improve the fracture of the interfaces by a factor of 30% and 40% in mode I and mode II, respectively. The interfacial properties of the two material configurations systems used are presented in Table 7.6. The baseline material configurations corresponds to the L1, L2 and L4 simulations and the reinforced material configurations corresponds to the L1-CNT, L2-CNT and L4-CNT simulations.

Table 7.6: Interface properties of the HTS40/Q-1112 carbon/epoxy system.

Baseline								
Penalty			*Fracture*			*Strength*		
K	[N/mm^3]	10^6	$\mathcal{G}_{Ic}$	[kJ/m^2]	0.26	τ_N	[MPa]	31
			$\mathcal{G}_{IIc}$	[kJ/m^2]	0.83	τ_{sh}	[MPa]	55
			η_{B-K}	[-]	2.0			
Reinforced								
Penalty			*Fracture*			*Strength*		
K	[N/mm^3]	10^6	$\mathcal{G}_{Ic}$	[kJ/m^2]	0.338	τ_N	[MPa]	35
			$\mathcal{G}_{IIc}$	[kJ/m^2]	1.162	τ_{sh}	[MPa]	66
			η_{B-K}	[-]	2.0			

7.2.2 Numerical results

The load-displacement curves of the six simulations are presented in Fig. 7.24 and the loads corresponding to delamination onset and ultimate failure are summarized in Table 7.7. As it is loaded in tension, i) the specimen bends due to the variation in stiffness of two parts of the structure, ii) delamination is triggered between in the 0°/45° interface between the skin and the stiffener, iii) the delamination plane grows, iv) until the structure fails. Only the delamination growth in the non-deformed configuration is represented in Fig. 7.24, for the sake of simplicity. Regardless of the ply thickness, since the ultimate load is dominated by intralaminar failure, the ultimate failure load is not affected by the presence of carbon nanotubes. However their use delays the onset of delamination by 15%. In fact, delamination starts in point A for the non-reinforced configurations and in point B for the reinforced configurations. This presents a significant improvement in the damage onset load of the stiffened structures, as initially expected.

Table 7.7: Load at delamination onset and failure load of the six laminate configurations.

Reference	Delamination onset [kN]	Improvement	Ultimate load [kN]	Improvement
L4	19.2 (Point A)	-	27.3 (Point C)	-
L4-CNT	22.1 (Point B)	15%	27.5 (Point C)	1%
L2	19.3 (Point A)	-	33.7 (Point D)	-
L2-CNT	22.2 (Point B)	15%	34.8 (Point D)	3%
L1	19.3 (Point A)	-	39.8 (Point E)	-
L1-CNT	22.2 (Point B)	15%	40.1 (Point E)	1%

Regarding the effect of ply thickness, even though there is no difference in the load corresponding to delamination onset, there is a 45% and 22% improvement of the ultimate strength of the thin (L1) and intermediate grade (L2) specimens when compared to the baseline thick-ply design (L4). This increase can be partly attributed to the different bending stiffness of the thin, intermediate and thick specimen configurations. This is clearly demonstrated in Fig. 7.25 where the vertical displacement of the nodes in the upper surface of the specimen (see Fig. 7.26) is plotted as a function of the x-coordinate of the nodes: the bending stiffness of the specimen progressively increases from L4 to L2 and to L1. This consequently results in higher tensile and compressive stresses in the upper and lower plies in the thicker

specimen configuration for the same applied displacement. This effect, combined with the lower *in-situ* strengths, leads to earlier ultimate failure of L4, followed by L2 and L1.

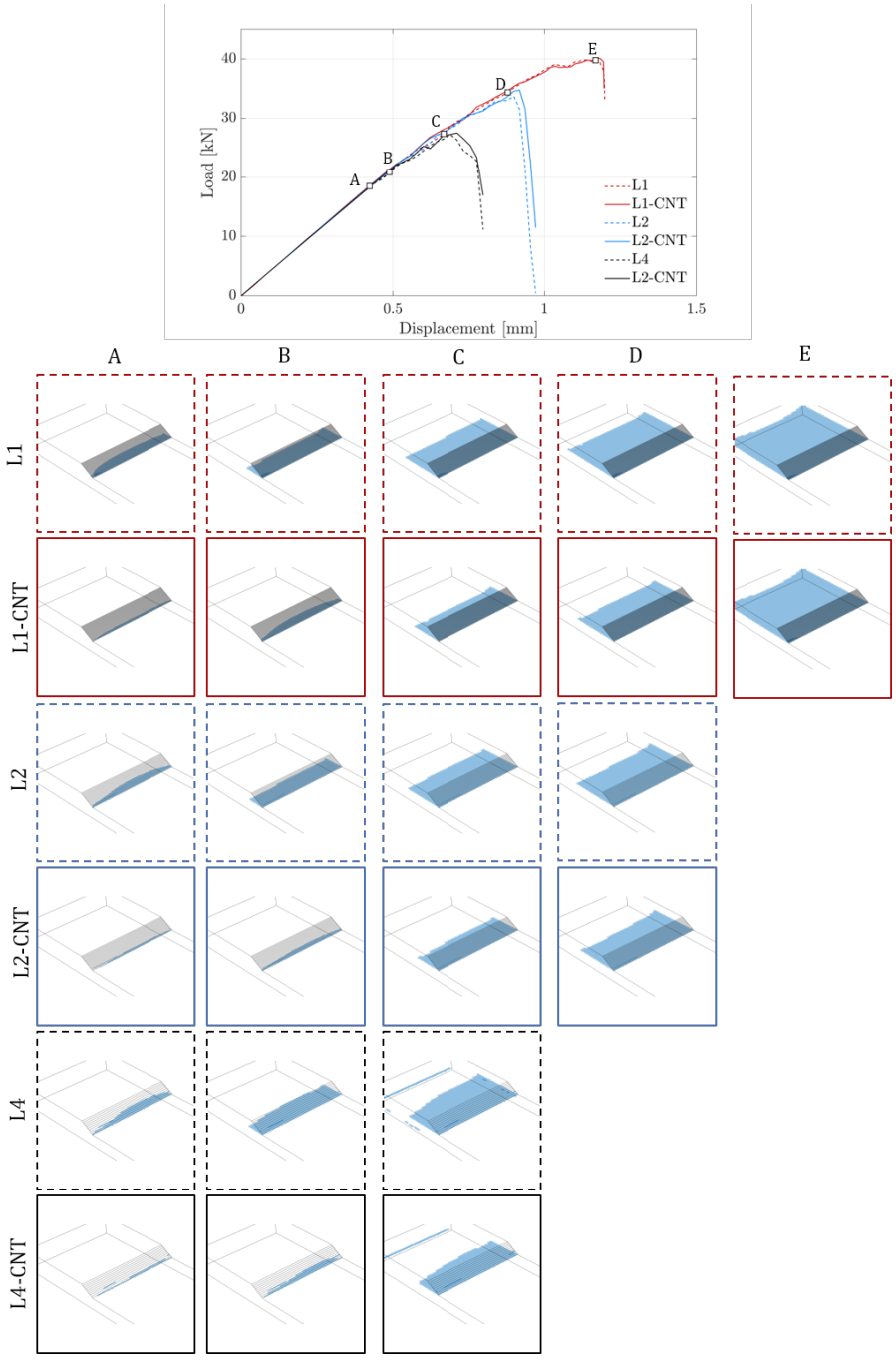

Figure 7.24: Load-displacement curves of the six specimen configurations and delamination evolution (in blue) as a function of the applied load.

The improvement resulting from the use of thinner plies reported here seems to be at least partly related to the design of the specimens and therefore the reduction of strength related to the thick-ply configuration could potentially be minimized

with a more careful definition of the stacking sequences. However, it is also important to take into account that the use of thin-plies brings clear advantages in terms of design space and therefore, if stacking sequence optimization procedures are used, structures made from thinner plies will always have advantages in term of performance simply because the design space is increased.

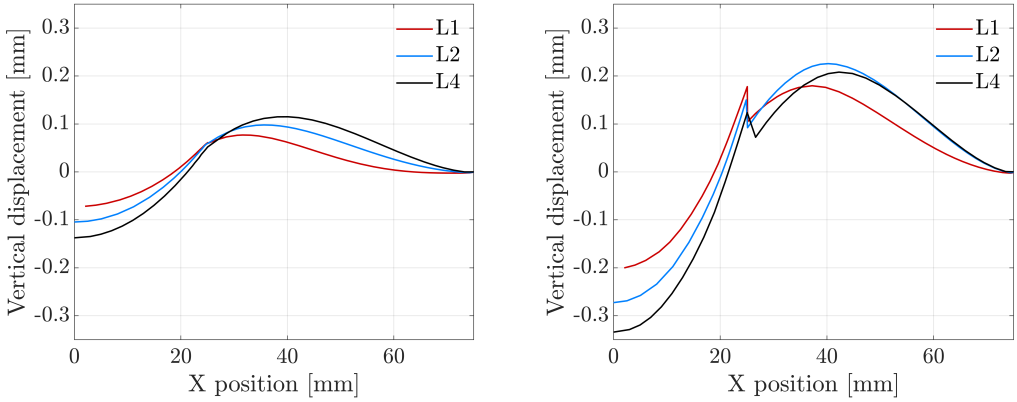

(a) $u_1 = 0.28$mm (b) $u_1 = 0.51$mm

Figure 7.25: Vertical displacement of the nodes in the upper surface of the specimen (see Fig. 7.26) pre (a) and post (b) delamination onset.

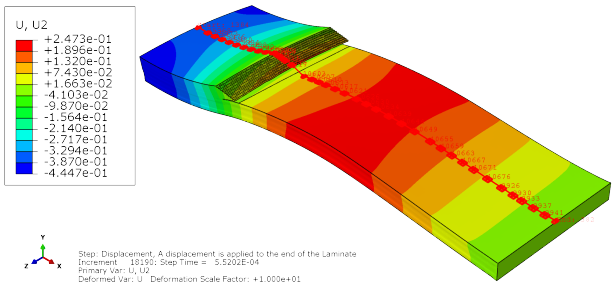

Figure 7.26: Nodes in the upper surface of the specimens where the vertical displacement was determined.

7.3 Concluding remarks

The effect of the presence of carbon nanotubes in the interfaces of thin-ply laminates on the mode I, mode II and mixed-mode interlaminar fracture toughness was studied testing 54gsm thin-ply HTS40/Q-1112 carbon fibre-epoxy laminates reinforced with 20μm aligned carbon nanotubes in the middle interface. In the nano-reinforced samples, the crack migrated to the intralaminar region after crack initiation, regardless of the test configuration. This suggests that the fracture toughness of the nano-reinforced interfaces is higher than that of a non-reinforced material, however, also indicates that only the improvement related to the initiation value of the fracture toughness could be measured. A 30% and a 40% improvement

on the mode I and mode II initiation value of the fracture toughness, respectively, was determined.

Since the cracks migrate to non-reinforced areas during crack propagation, this type of reinforcement will likely be more relevant in structures for which the design strength is limited by delamination initiation, e.g. panels with a co-cured or co-bonded stiffeners. To test this hypothesis, a numerical study on the effect of ply thickness and the effect of reinforcing the interfaces with carbon nanotubes was performed. Three equivalent skin-stiffener designs based on 0.054mm (thin), 0.108mm (intermediate) and 0.216mm (thick) plies and an additional three specimens with the same stacking sequences where the interfaces were reinforced with carbon nanotubes were considered.

Regardless of the ply thickness, since the ultimate load was controlled by intralaminar failure, the ultimate failure load was not affected by the presence of carbon nanotubes. However their use delayed the onset of delamination by 15% which significantly improves the damage onset strength of the stiffened specimens.

Even though no difference in the load corresponding to delamination onset for the different designs was found, a 45% and 22% improvement of the ultimate strength of the thin and intermediate grade specimens when compared to the baseline thick-ply design was observed. This improvement resulting from the use of thinner plies was found to be partly related to the defined stacking sequences. However, it should be taken into account that the use of thin-plies increases the design space. For this reason, stacking sequences can be better optimized for a given application and therefore, structural performance could significantly benefit from their use.

Part VI

Conclusions and future work

Chapter 8

Conclusions and future work

The main conclusions of the work presented in this thesis and potential research topics directly related to the developed work are presented in this chapter.

8.1 Conclusions

8.1.1 Analysis models to predict failure of composite laminates

Two different methodologies were proposed and implemented in this thesis: a finite element based methodology to simulate composite laminates at coupon level, compatible with industrial requirements, and an analytical framework to predict the notched strength of general laminates characterized by fibre-dominated intralaminar fracture.

To simulate the intralaminar behaviour, a modified version of the continuum damage model proposed by Maimí et al. [47–49] was developed. The model was enriched with a bilinear softening law for longitudinal compression more suitable to represent kinking failure. Additionally, a damage activation function for longitudinal compression that accounts for the effect of though-thickness stresses based on a 3D failure criteria and engineering solutions to account for the effect of pressure on the longitudinal compression and in-plane shear fracture toughness were proposed. To simulate the interlaminar behaviour, a frictional cohesive model was used to more accurately represent delamination onset and propagation in test cases where the effect of through-thickness pressure cannot be neglected.

The proposed methodology was thoroughly validated for various material systems of interest to the aeronautical community and coupons with increasing level of complexity: unnotched tension and compression, open-hole tension and compression and filled-hole compression of both soft and hard laminates. It was concluded that a very good agreement was found between the predictions and the experimental ultimate strengths for all the test cases, oftentimes within the standard error of the tests, and with industry compatible computation times.

It is worth noting that the models developed follow the requirements typically used by the aeronautical industry, in terms of element size and mesh structure and that all the predictions were obtained using a common set of material properties and material models. These facts indicate that the methodology presented here is a step towards the simulation of failure of composite structures using a standard modelling strategy. Hence, this work serves as basis for modelling more complex geometries and can potentially be used for the generation of statistically-based design allowables.

Given their formulation, these tools can be used, not only for prediction of the ultimate failure of composite laminates, but also to identify the mechanisms leading to early failure such as delamination planes, extensive matrix cracking among others. These tools are, therefore, particularly useful to properly explain experimental observations or to assist the design of more robust structures by mitigating sources that may lead to early failure.

Even though finite element models to simulate failure of composite laminates are particularly powerful solutions given their flexibility to estimate the material behaviour of different laminates, geometries and loading conditions, their computational complexity and cost still limits their use, particularly as a preliminary design tool. Considering this limitation, an analytical framework to predict the notched strength of multidirectional laminates was proposed.

The analytical framework proposed is based on a Finite Fracture Mechanics model [70] coupled with an invariant-based approach to stiffness and strength [16, 236] and fracture mechanics based analytical model to estimate the laminate fracture toughness [235]. This framework can be used to predict the notched strengths of general laminates characterized by fibre-dominated intralaminar fracture using only three ply properties as inputs: the longitudinal Young's modulus, the longitudinal strength, and the $\mathcal{R}$-curve of the 0° plies. Relative errors around or below 10% were obtained for all the laminates and open-hole geometries analysed. It was concluded that the proposed framework is particularly accurate for laminates with thin plies, for which relative errors of 3% or less were obtained.

The proposed analytical framework was also coupled with statistical tools required to take into account the variability of the material and geometrical parameters and propagate this uncertainty to the notched strength. This process allows the determination of the statistical distribution of the notched strength and the quick estimation of B-basis allowable, which is the design parameter more commonly used in the aeronautical industry. The proposed framework was validated successfully and was used to develop statistical-based design charts for notched specimens. These tools that are useful for design engineers and would otherwise be infeasible to attain as they require a large number of testing or time consuming simulations to be performed.

The coupled framework provides a fast-analysis model for preliminary sizing and optimization of composite laminates based solely on material properties determined at the ply level. Important gains in terms of material characterization, computing time and cost can be obtained using the proposed framework, in particular at the stages of material screening and lay-up selection.

8.1.2 Mechanics of thin-ply laminates

Taking into account the importance of the intralaminar fracture toughness on the accuracy of the strength predictions provided by both analytical and numerical methods, and the contradictory opinions found in literature, an experimental/numerical study was performed to elucidate if this property depends on the ply thickness.

The apparent crack resistance curves associated with longitudinal tensile failure of carbon fibre reinforced epoxy composite systems with ply thicknesses of 0.075mm, 0.134mm and 0.268mm was determined experimentally from the size effect

law of geometrically similar double edge notch tension specimens. An increase in notched strength as a function of the ply thickness and a corresponding increase of the measured intralaminar fracture toughness was observed. However, this increase was shown to be a consequence of the appearance of split cracks in the thicker 0° plies in the vicinity of the notches.

The numerical models developed demonstrated that if the notch blunting mechanisms are properly represented, the laminate strength is well predicted for a constant value of the ply intralaminar fracture toughness. This supports the hypothesis that these mechanisms are responsible for the higher strength of the thicker plies, and that the intralaminar fracture toughness of the 0° plies is not and *in-situ* property and should not be scaled with the ply thickness when modelling damage propagation at the mesoscale.

A comprehensive study of the structural performance of nine equivalent 0° dominated hard multidirectional laminates made from unidirectional tapes, non-crimp fabrics and spread-tow fabrics with fibre areal weights ranging from 67gsm to 268gsm was also performed. Structural details corresponding to unnotched specimens, notched specimens (open-hole tension and compression), and bolted connections (filled-hole compression and bolt-bearing) were tested to failure and analysed in detail to clarify i) the effect of ply thickness, ii) the effect of selective ply thickness hybridization and iii) the effect of the type of geometry reinforcement on the damage mechanisms that dominate failure and strength of multidirectional laminates.

An overall improvement of the material behaviour with the decrease of ply thickness in the laminates made from unidirectional tapes and non-crimp fabrics was observed, except for the strength in the presence of stress concentrations (notched strength), where thin ply laminates presented a more brittle behaviour, due to the suppression of premature damage around regions with stress concentrations. Conversely, nearly no ply thickness effect was observed for the spread tow laminates, since the ply morphology based on interlaced 0° and 90° plies promotes similar damage mechanisms in both configurations. A more pronounced thickness effect is expected for thinner and thicker spread tow fabrics, particularly if, as a result, the crimp angles and waviness of the tows vary significantly.

The concept of selective ply-hybridization, where both thin off-axis plies are combined with intermediate or high grade 0° plies, was tested under general loading conditions. This type of hybridization has been shown to promote longitudinal fibre splitting near the stress concentration points and lead to the reduction of the notch sensitivity typically observed in thin-ply laminates, therefore, increasing their notched strength.

Contrary to the reported literature, nearly no effect of ply thickness hybridization was detected when intermediate grade 0° plies were combined with thin off-axis plies, under the different loading configurations. However, an overall improvement of the strengths was observed when high-grade 0° plies were combined with thin off-axis plies. A high sensitivity to the loading direction in the presence of stress concentrations was also observed. The high grade 0° plies, that contribute to the high notched strength at 0°, gradually become thick off-axis and 90° plies with low resistance to the appearance of transverse cracks as the laminate is rotated. Hybrid laminates are, therefore, more suitable for applications where large deviations from the main loading axis are not expected.

Spread-tow non-crimp and textile fabrics did not show especial susceptibility

to early failure either in the presence or not of geometrical discontinuities. Due to their added flexibility in terms of manufacturing and processing, the replacement of unidirectional tapes by spread-tow non-crimp and textile fabrics can be seen as an economical solution that does not compromise the structural response, ensuring the weight benefits of composite materials at lower processing costs and opening the possibility of integrating new, more efficient manufacturing processes.

8.1.3 Nano-reinforced interfaces

The effect of reinforcing the interfaces of a thin-ply prepreg with 20μm aligned carbon nanotubes on interlaminar fracture toughness was studied. The advancing cracks in the reinforced material were shown to migrate to the intralaminar region after crack initiation, regardless of the test configuration. Even though this crack bifurcation indicates that the fracture toughness of the nano-reinforced interfaces is higher than that of a non-reinforced interface, it also indicates that only the improvement related to the initiation value of the fracture toughness could be measured. Nonetheless, a 30% and 40% improvement on the mode I and mode II initiation values of the fracture toughness, respectively, was determined.

Since the interlaminar cracks are able to migrate to non-reinforced areas during crack propagation, this type of reinforcement will likely be more relevant in structures for which the design strength is limited by delamination initiation, e.g. panels with a co-cured stiffeners. To test this hypothesis, a numerical study on the effect of ply thickness and the effect of reinforcing the interfaces with carbon nanotubes was performed. Three equivalent skin-stiffener designs based on low, intermediate and high grade plies and an additional three specimens with the same stacking sequences, and with interfaces reinforced with carbon nanotubes were considered. Regardless of the ply thickness, since the ultimate load was controlled by intralaminar failure, the ultimate failure load was not affected by the presence of carbon nanotubes. However, their use delayed the onset of delamination by 15% and therefore, improved the design strength of the devised stiffened panels.

8.2 Future work

The constitutive model proposed to predict the elastic and inelastic behaviour of composite laminates should be further validated for material systems of interest and for more complex stacking sequences, including soft and hard laminates so that the range of applicability, mesh sensitivity and ability to accurately capture the damage mechanisms associated with failure can be properly assessed. Additionally, since the model was enriched with engineering solutions aimed at improving its ability to simulate test cases where the though-thickness stress cannot be neglected, more complex test cases where this effect is more relevant should be considered, including impact loadings and bolted joints.

The effect of the presence of defects, such as disbonds, fibre waviness, surface roughness, ill-defined stacking sequences, among other, is of utmost importance to the aeronautical industry since it can help define manufacturing procedures, reduce scrap parts and define safety factors associated with the potential presence of defected parts in a given structure. The effect of defects can also be addressed using the proposed constitutive model.

Efficient methodologies to define statistical design allowables based on finite element based solutions should also be developed. Even though, currently, these tools might not be efficient enough, the computational efficiency will improve over time and, therefore, these tools may prove crucial in a near future.

Regarding the material parameters, the definition of experimental or numerical methodologies to determine the parameters of the softening law associated with longitudinal intralaminar tensile and compressive failure is of key importance. Even though they represent physical phenomena, these parameters are particularly hard to determine experimentally given the catastrophic failure associated with fibre breakage. Optimization algorithms can potentially be used to inversely identify them based on the simulation of notched specimens.

A thorough validation of the analytical framework proposed to predict the notched strength of composite laminates with fibre dominated failure should be performed, featuring hard and soft laminates, so that a proper assessment of its validity and interest as a preliminary design tool can be made. Moreover, the proposed framework can also be extended to more complex geometries such as other notch geometries, pinned connections or for multidirectional loadings scenarios.

While the mechanical behaviour and damage mechanisms of thin-ply laminates have been exhaustively studied, there are still many opportunities to fully exploit the characteristics of thin plies and to explore their applicability. With the information presented in this thesis, where for the first time an "*apples to apples*" comparison on the main characteristics of failure of structural details manufactured using thin-ply laminates has been made, it is now possible to explore new design opportunities using thin-ply laminates. It is also important to note that the design constrains and design rules for composite materials were proposed based on the mechanical behaviour of conventional grade composite laminates. The introduction of thin-ply laminates at the industrial level, would perhaps require or, at least, benefit from their review.

The use of any material system relies on the ability to predict its behaviour. Some solutions based on mesoscale finite element modelling and simplified analytical models were proposed in this thesis and proved particularly accurate to predict failure of thin-ply composite laminates. However, other approaches to predict their failure, such as phase-field models, should be proposed and further explored, potentially at the homogenized level, taking advantage of the damage suppression capability observed in thin-ply laminates.

Regarding the use of carbon nanotubes as an interface reinforcing technique, a new testing methodology should be proposed so that the fracture toughness associated with the propagation of interlaminar cracks can be properly measured.

With respect to the utility of the reinforcement technique, it was shown numerically that the improvement of the interfacial properties can be useful in delaying delamination onset and, therefore, increase the design strength of some structures. A similar analysis should be performed experimentally to further validate the modelling methodology and assess the advantages in other configurations, ideally structural components used by the industry.

Part VII

Appendix

Chapter A

Material properties and their determination

The ply and interface properties required to populate the model proposed in Chapter 3 and suggested methods for their determination are provided in Tables A.1 and A.2. Note that some properties, despite representing physical phenomena, are particularly hard to determine experimentally. To clarify punctual assumptions done in this work, the estimation of some of the material parameters is highlighter in this section.

Even though solutions to determine the cohesive laws for longitudinal tension and compression have been proposed throughout the years [281–285], they are particularly challenging to determine experimentally and there is up to date, no standard procedure to do so. In this work, the inflection points for the softening laws for longitudinal tension and compression (f_{X_T}, f_{GT} and f_{X_C}) which represent fibre bridging and crushing, respectively, were inversely identified using an open-hole or filled-hole simulation, since there was no experimental data available.

Similarly, the biaxial tensile and compressive strengths (Y_{BT} and Y_{BC}) are also impractical to determine, since the specimens are generally expensive to manufacture and the required complicated test rigs. A summary of test methods for composites under multiaxial and out-of-plane loading conditions is given in Ref. [286]. Micromechanical models can also be used to numerically determine the material response under multiaxial stress states [287, 288]. Y_{BT} and Y_{BC} were only available for IM7/8552 [11, 50] and were assumed from the remaining material systems by considering that the ratio Y_{BT}/Y_T and Y_{BC}/Y_C is constant and equal to the ratios available for the IM7/8552 material system.

The parameter, f_{fxc}, is a frictional parameter that represents the strengthening effect of pressure on the longitudinal compressive behaviour of the ply. The concept was first introduced here and therefore, no procedure was defined to determine it. For this reason, in this work, the parameters was inversely identified from an open-hole or filled-hole simulation, depending on the material system.

Table A.1: Intralaminar material parameters and suggested method for their determination.

	Material parameter	**Methodology**
	Ply Elastic Properties	
E_1	Young's modulus for longitudinal tension	ASTM D3039 [271]
E_{1c}	Young's modulus for longitudinal compression	Ref. [289]
E_2	Young's modulus for transverse tension	ASTM D3039 [271]
G_{12}	In-plane shear modulus	ASTM D3518 [290]
ν_{12}	Major Poisson's coefficient	ASTM D3039 [271]
	Ply strengths	
X_T	Longitudinal tensile strength	ASTM D3039 [271]
f_{XT}	$f_{X_T} X_T$ is the longitudinal tensile stress at inflection point	Note (1)
X_C	Longitudinal compressive strength	Ref. [289]
f_{XC}	$f_{X_C} X_C$ is the longitudinal compression stress at inflection point	Note (1)
Y_T	Transverse tensile strength (2)	ASTM D3039 [271]
Y_C	Transverse compressive strength (2)	Ref. [291]
Y_{BT}	Biaxial transverse tensile strength	Note (1)
Y_{BC}	Biaxial transverse compressive strength	Note (1)
S_L	In-plane shear strength (2)	ASTM D3518 [290]
S_{LP}	Shear stress that activates plastic flow	Note (3)
K_P	Shear incremental stiffness under plastic flow	Note (3)
	Fracture Toughness	
$\mathcal{G}_{1+}$	Fracture toughness for long. tension	Ref. [23]
f_{GT}	Portion of $\mathcal{G}_{1+}$ dissipated up to the inflection point	Note (1)
$\mathcal{G}_{1-}$	Fracture toughness for longitudinal compression	Ref. [222]
$\mathcal{G}_{2+}$	Mode I fracture toughness for transverse tension	ASTM D5528 [113]
$\mathcal{G}_{2-}$	Mode I fracture toughness for transverse compression	Calculated (4)
$\mathcal{G}_6$	Mode II fracture toughness	ASTM D7905 [114]
	Geometrical	
t	Element thickness	Ply thickness
α_0	Fracture angle of the UD ply subjected to uniaxial transverse comp.	$\approx 53°$ [63]
	Friction	
f_{fxc}	Internal frictional parameter under long. compression	Note (1)
η_G	Internal frictional parameter under in-plane shear	Ref. [207]

(1) No standard methodology to determine this material parameter is available. The parameter is assumed or inversely identified.
(2) The references given provide methodologies to determine the UD strengths of the ply. The *in-situ* properties should be calculated in function of the ply thickness and the position in the laminate proposed in Appendix B
(3) Best fitting from the in-plane shear stress-strain curve of the ply
(4) $\mathcal{G}_{2-} = \mathcal{G}_6 / \cos(\alpha_0)$

Table A.2: Interlaminar material parameters and suggested method for their determination.

	Material parameter	**Methodology**
Penalty Stiffness		
K	Penalty stiffness	Recommended value: 10^6 N/mm^3 [177]
Strengths		
τ_n	Strength under pure mode I	ASTM D3039 [271]
τ_{sh}	Strength under pure mode II	ASTM D3518 [290]
Fracture Toughness		
$\mathcal{G}_{Ic}$	Mode I fracture toughness	ASTM D3039 [271]
$\mathcal{G}_{IIc}$	Mode II fracture toughness	ASTM D7905 [114]
η	Mixed-mode interaction parameter	ASTM D6671 [292]
Friction		
μ	Friction coefficient	Note (1)

(1) The frictional parameter can be inversely identified following Ref. [207]

Chapter B

Derivation of the *in-situ* properties

B.1 Transverse tensile and *in-situ* shear strengths

Camanho et al. [22] considered three ply configurations to calculate the transverse tensile and in-plane shear strengths: thick, thin inner and thin outer plies.

B.1.1 Thick embedded plies

In a thick ply embedded in a multidirectional laminate, a slit crack such as the one shown in Fig. B.1 will propagate firstly in the transverse direction (T), and therefore the mode I and mode II energy release rates read:

$$\mathcal{G}_I(T) = \frac{\pi a_0}{2} \Lambda_{22}^o \sigma_{22}^2 \tag{B.1}$$

$$\mathcal{G}_{II}(T) = \frac{\pi a_0}{2} \chi(\gamma_{12}) \tag{B.2}$$

where $2a_0$ is the slit crack length along the thickness, $\chi(\gamma)$ is given by:

$$\chi(\gamma_{12}) = 2 \int_0^{\gamma_{12}} \sigma_{12} d\gamma_{12} \tag{B.3}$$

and Λ_{22}^o is given by [269]:

$$\Lambda_{22}^o = 2 \left(\frac{1}{E_2} - \frac{\nu_{12}^2}{E_1} \right) \tag{B.4}$$

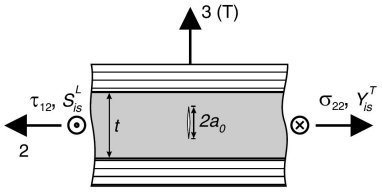

Figure B.1: Thick embedded ply [22]

Dvorak and Laws [269] proposed that the transverse tensile *in-situ* strength can be obtained by solving equation B.1 for Y_T^{is}, yielding

$$Y_T^{is} = \sqrt{\frac{2\mathcal{G}_{Ic}(T)}{\pi a_0 \Lambda_{22}^0}} \tag{B.5}$$

In the Continuum Damage model presented here and implemented in the ABAQUS user subroutine, the shear response of a given laminated composite is approximated by:

$$\sigma_{12} = \begin{cases} G_{12}\gamma_{12} & ,\gamma_{12} \leq S_{LP}/G_{12} \\ K_1\gamma_{12} + K_2 & ,\gamma_{12} > S_{LP}/G_{12} \end{cases} \tag{B.6}$$

where $K_1 = \frac{KpG_{12}}{1+Kp}$ and $K_2 = S_{LP}\left(1 - \frac{Kp}{1+Kp}\right)$, G_{12} is in-plane shear modulus, S_{LP} is the shear stress at which the plastic flow is activated and Kp is the shear incremental stiffness under plastic flow. Having defined σ_{12}, the mode II fracture toughness can be calculated replacing (B.6) in equation (B.2), yielding:

$$\begin{aligned} \mathcal{G}_{IIc}(T) &= \pi a_0 \left[\int_0^{\frac{S_{LP}}{G_{12}}} G_{12}\gamma_{12} d\gamma_{12} + \int_{\frac{S_{LP}}{G_{12}}}^{\gamma_{12}^{is}} \left(K_1\gamma_{12} + K_2\right) d\gamma_{12} \right] = \\ &= \pi a_0 \left[\left(\gamma_{12}^{is}\right)^2 \frac{K_1}{2} + \gamma_{12}^{is} K_2 - \frac{S_{LP}^2}{2G_{12}(1+Kp)} \right] \end{aligned} \tag{B.7}$$

where $K_1 = \frac{KpG_{12}}{1+Kp}$ and $K_2 = S_{LP}\left(1 - \frac{Kp}{1+Kp}\right)$.

Dvorak and Laws [269] also proposed that the a unidirectional laminate can be considered a special case of a thick ply with unconstrained outer surfaces and, therefore, the *in-situ* strengths of a thick ply can be related to those of an unidirectional thick ply. Using the classical solutions for stress intensity factors of surface cracks in unidirectional laminates [293], the mode I and mode II components of fracture toughness can also be calculated as

$$\mathcal{G}_{Ic}(T) = 1.12^2 \pi a_0 \Lambda_{22}^0 (Y^T)^2 \tag{B.8}$$

and

$$\mathcal{G}_{IIc}(T) = 2\pi a_0 \left[\gamma_L^2 \frac{K_1}{2} + \gamma_L K_2 - \frac{S_{LP}^2}{2G_{12}(1+Kp)} \right] \tag{B.9}$$

where $\gamma_L = \frac{S_L - K_2}{K_1}$.

Combining equations (B.5) and (B.8), the transverse tensile *in-situ* strength for a thick ply yields:

$$Y_T^{is} = 1.12\sqrt{2} Y_T \tag{B.10}$$

Combining equations (B.7) and (B.9), the in-plane shear strength can be obtained solving the following equation for γ_{12}^{is}:

$$(\gamma_{12}^{is})^2 \frac{K_1}{2} + \gamma_{12}^{is} K_2 = \gamma_L^2 K_1 + 2\gamma_L K_2 - \frac{S_{LP}^2}{2G_{12}(1+Kp)} \tag{B.11}$$

Knowing γ_{12}^{is} the in-plane shear strength can be obtained solving the second member of equation (B.6) for σ_{12}:

$$S_L^{is} = \sqrt{2S_L^2 - S_{LP}K_2} \tag{B.12}$$

B.1.2 Thin embedded plies

In thin plies embedded in a multidirectional laminate, a slit crack such as the one shown in Fig. B.2 will propagate in the longitudinal direction (L) since it already extended through the ply thickness and, therefore, the mode I and mode II energy release rate read [269]:

$$\mathcal{G}_{Ic}(L) = \frac{\pi t}{8}\Lambda^o_{22}\sigma^2_{22} \tag{B.13}$$

$$\mathcal{G}_{IIc}(L) = \frac{\pi t}{8}\chi(\gamma_{12}) \tag{B.14}$$

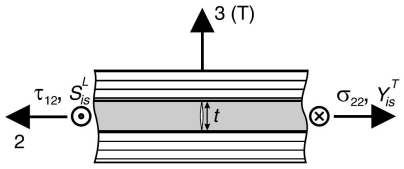

Figure B.2: Thin embedded ply [22]

The transverse tensile *in-situ* strength can be obtained by solving equation B.13 for Y_T^{is} yielding

$$Y_T^{is} = \sqrt{\frac{8\mathcal{G}_{Ic}}{\pi t\Lambda^0_{22}}} \tag{B.15}$$

Replacing equation (B.3) in equation (B.14) yields

$$\mathcal{G}_{IIc} = \frac{\pi t}{4}\left[(\gamma_{12}^{is})^2\frac{K_1}{2} + \gamma_{12}^{is}K_2 - \frac{S^2_{LP}}{2G_{12}(1+Kp)}\right] \tag{B.16}$$

which can be solved for γ_{12}^{is}. Knowing γ_{12}^{is} the in-plane shear strength can be obtained solving the second member of equation B.6 for σ_{12}:

$$S_L^{is} = \sqrt{\frac{8\mathcal{G}_{IIc}K_1}{\pi t} + S_{LP}K_2} \tag{B.17}$$

B.1.3 Thin outer plies

A thin outer ply is a special case of the thin ply for which the energy release rate is larger because the slit crack is closer to the surface of the laminate (Fig. B.3). The mode I and mode II energy release rate read:

$$\mathcal{G}_{Ic} = 1.22^2\frac{\pi t}{4}\Lambda^o_{22}\sigma^2_{22} \tag{B.18}$$

$$\mathcal{G}_{IIc} = \frac{\pi t}{4}\chi(\gamma_{12}) \tag{B.19}$$

The transverse tensile *in-situ* strength can be obtained by solving equation B.18 for Y_T^{is} yielding

$$Y_T^{is} = 1.78\sqrt{\frac{\mathcal{G}_{Ic}}{\pi t\Lambda^0_{22}}} \tag{B.20}$$

Replacing equation (B.3) in (B.19), yields:

$$\mathcal{G}_{IIc} = \frac{\pi t}{2}\left((\gamma_{12}^{is})^2\frac{K_1}{2} + \gamma_{12}^{is}K_2 - \frac{S_{LP}^2}{2G_{12}(1+Kp)}\right) \tag{B.21}$$

which can be solved for the γ_{12}^{is}. Knowing γ_{12}^{is} the in-plane shear strength can be obtained solving the second member of equation B.6 for σ_{12}:

$$S_L^{is} = \sqrt{\frac{4\mathcal{G}_{IIc}K_1}{\pi t} + S_{LP}K_2} \tag{B.22}$$

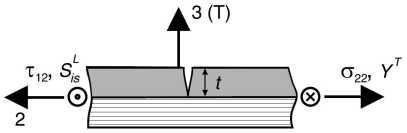

Figure B.3: Thin outer ply [22]

B.2 Transverse compressive strength

The *in-situ* transverse compressive stress Y_C^{is} is calculated imposing that the slope in the σ_{22}-σ_{12} failure envelope when $\sigma_{22} = 0$, η_L, is equal to the slope of the envelope obtained with the *in-situ* properties (see Fig. B.4). To maintain consistency between the assumptions made to derive the *in-situ* strengths and the assumed behavior of the material, the criterion used in both cases is the LaRC03-04 failure criterion [64]. The coefficient of longitudinal influence η_L can be determined experimentally but in the absence of biaxial test data, it can be estimated as [63, 64]

$$\eta_L = \frac{-S_L^{UD}\cos(2\alpha_0)}{Y_C^{UD}\cos^2(\alpha_0)} \tag{B.23}$$

and therefore, the *in-situ* transverse compressive strength Y_C^{is} can be estimated as

$$\eta_L = \eta_{L,is} \Leftrightarrow Y_C^{is} = \frac{S_L^{is}Y_C^{UD}}{S_L^{UD}} \tag{B.24}$$

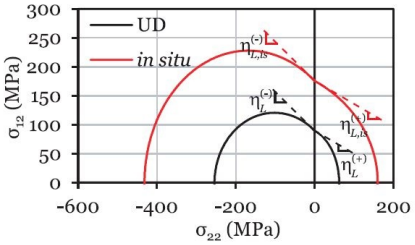

Figure B.4: σ_{22}-σ_{12} failure envelope [11]

B.3 General expression for the *in-situ* strengths

The general expression for the *in-situ* strengths are presented in this section. Note that $K_1 = \frac{KpG_{12}}{1+Kp}$ and $K_2 = S_{LP}\left(1 - \frac{Kp}{1+Kp}\right)$.

For an embedded ply:

- the ***in-situ*** **transverse tensile strength** is the maximum between the transverse tensile strength of a thin embedded ply and a thick embedded ply, i.e.:

$$Y_T^{is} = \max\left\{\sqrt{\frac{8\mathcal{G}_{Ic}}{\pi t \Lambda_{22}^o}} \quad , \quad 1.12\sqrt{2}Y_T^{UD}\right\} \tag{B.25}$$

- the ***in-situ*** **in-plane shear strength** is the maximum between the in-plane shear strength of a thin embedded ply and a thick embedded ply, i.e.:

$$S_L^{is} = \max\left\{\sqrt{\frac{8\mathcal{G}_{IIc}K_1}{\pi t} + S_{LP}K_2} \quad , \quad \sqrt{2S_L^2 - S_{LP}K_2}\right\} \tag{B.26}$$

- **the *in-situ* transverse compressive strength** Y_C^{is} is given by:

$$Y_C^{is} = \frac{S_L^{is}Y_C^{UD}}{S_L^{UD}} \tag{B.27}$$

For an outer ply:

- the ***in-situ*** **transverse tensile strength** is the maximum between:

$$Y_T^{is} = \max\left\{1.78\sqrt{\frac{\mathcal{G}_{Ic}}{\pi t \Lambda_{22}^o}} \quad , \quad Y_T^{UD}\right\} \tag{B.28}$$

- The ***in-situ*** **in-plane shear strength** is the maximum between the in-plane shear strength of a UD ply and a thin outer ply, i.e.:

$$S_L^{is} = \max\left\{\sqrt{\frac{4\mathcal{G}_{IIc}K_1}{\pi t} + S_{LP}K_2} \quad , \quad S_L^{UD}\right\} \tag{B.29}$$

- **the *in-situ* transverse compressive strength** Y_C^{is} is given by:

$$Y_C^{is} = \frac{S_L^{is}Y_C^{UD}}{S_L^{UD}} \tag{B.30}$$

Chapter C

Engineering solutions for the determination of the material properties of an interface

Cohesive finite elements require very fine meshes: the fracture process zone should include at least three cohesive elements so that delamination is accurately simulated. Turon et al. [212] proposed an engineering solution to avoid the use of such refined meshes that consists of lowering the cohesive strengths whilst keeping the fracture toughness constant to enlarge the cohesive zone and to allow a better representation of the softening behaviour at the vicinity of the crack tip. Following Refs. [212] and [213], the cohesive properties should therefore, be determined as follows:

1. Take the penalty stiffness, K, equal to 10^6 N/mm^3 [177];
2. Determine the transverse tensile strength Y_T^{UD} (ASTM D3039 [271]);
3. Determine the mode I fracture toughness $\mathcal{G}_{Ic}$ (ASTM D5528 [113]);
4. Determine the mode II fracture toughness $\mathcal{G}_{IIc}$ (ASTM D7905 / D7905M [114]);
5. Select the element size in the direction of crack propagation, l_e [212];
6. Select the number of elements in the cohesive zone, N_e, which should be at least 3 [212];
7. Calculate the strength in pure mode I as: $\bar{\tau}_N = \sqrt{\frac{9\pi E_{22}\mathcal{G}_{Ic}}{32 N_e l_e}}$ [212];
8. Calculate the effective strength in pure mode I as [212].

$$\tau_N = \min\left\{Y_T^{UD}, \bar{\tau}_N\right\} \tag{C.1}$$

It was shown that through-thickness compression increases the interlaminar shear strength of laminates and delay delamination [205–207]. Cui et al. [208] suggests that this strengthening effect is a result of an increase on mode II fracture toughness under through-thickness compression that can be expressed as:

$$\mathcal{G}_{IIc}^{ef} = \mathcal{G}_{IIc}\left(1 - \eta_G \langle -\sigma_{33} \rangle\right) \tag{C.2}$$

where $\mathcal{G}_{IIc}$ is the mode II fracture toughness, η_G a material dependent empirically derived enhancement factor, σ_{33} is the through-thickness stress and $\langle x \rangle$ is the

Mccaulay operator. [208, 209]. In situations where the applied pressure is fairly constant (e.g. in bolt bearing and filled-hole compression tests), equation C.2 can be used to artificially account for the strengthening effect on the interfaces caused by friction under shear. These enginering solutions are used in modelling stategies S2 and S3 in Chapter 3 and in Chapters 5 and 7.

Chapter D

Variability of the longitudinal mode I crack resistance curve

Catalanotti et al. [23, 222] proposed a methodology to determine the $\mathcal{R}$-curve of polymer composites reinforced by unidirectional fibres based on the size effect law, i.e the relation between the size of the specimens and their notched strength $\overline{\sigma}^{\infty}(w)$. The size effect law can be determined by experimentally testing geometrically similar double edge notch specimens, i.e. with the same width-to-crack length ratio $2w/a$ and different widths $2w$. The size effect law can be determined by finding a fitting regression that best approximates the experimental data [262] and the $\mathcal{R}$-curve parameters (length of the fracture process zone, l_{fpz}, and the fracture toughness at propagation $\mathcal{R}_{ss}$) can then be obtained as a function of these fitting parameters [23, 222, 262]. Catalanotti et al. [23] also suggested to express the $\mathcal{R}$-curve analytically. Here, the following analytical expression is proposed to represent the $\mathcal{R}$-curve:

$$\begin{cases} \mathcal{R}(\Delta a) = \mathcal{R}_{ss}\left[1-(1-\Delta a/l_{fpz})^{\beta}\right] & \text{if} \quad \Delta a < l_{fpz} \\ \mathcal{R}(\Delta a) = \mathcal{R}_{ss} & \text{if} \quad \Delta a \geq l_{fpz} \end{cases} \tag{D.1}$$

where β is a parameter determined to obtain the best fit of the $\mathcal{R}$-curve. The proposed equation guarantees that the steady state value of the fracture toughness is reached when $\Delta a = l_{fpz}$. Since the mean $\mathcal{R}$-curve is determined from the mean experimental notched strengths of the double edge notch specimens, accounting for the variability of the $\mathcal{R}$-curves implies accounting for the variability of the size effect law. Two methodologies to determine the variability of the $\mathcal{R}$-curves are proposed in the following section.

D.1 Methodology

D.1.1 Method 1

The variability is obtained by generating a large number of $\mathcal{R}$-curves accounting for the variability of the notched strength ($\bar{\sigma}^{\infty}$) of the specimens with different geometries by:

1. Randomly generating N_i strengths per each specimen geometry following a statistical distribution determined experimentally for each specimen geometry;

2. Fitting the data to one of the fitting regressions proposed in Ref. [262];

3. Determining the $\mathcal{R}$-curve parameters (l_{fpz} and $\mathcal{R}_{ss}$) as proposed in Ref. [23, 222, 262];

4. Fitting the $\mathcal{R}$-curve to the analytical expression proposed in Eq. (D.1);

5. Repeat 1-4, N times obtaining a large number of $\mathcal{R}$-curves and the distribution of the fitting parameters.

Using this methodology, a set of statistically representative crack resistance curves is obtained. With the generated $\mathcal{R}$-curves it is possible to determine the mean values and standard deviation of the three $\mathcal{R}$-curve fitting parameters (l_{fpz}, $\mathcal{R}_{ss}$ and β). However, due to the nature of the crack resistance curves, the fitting parameters cannot be treated independently as that would lead to unrealistic and potentially non-continuous $\mathcal{R}$-curves. For this reason, a relation between the parameters should be established as a function of $\mathcal{R}_{ss}$, i.e. $l_{fpz} = f(\mathcal{R}_{ss})$ and $\beta = g(\mathcal{R}_{ss})$. These functions can vary and should be analysed for each material system considered. A more detailed analysis is given in Section D.2.

D.1.2 Method 2

The variability can also be obtained from the determination of the 95% prediction bounds of the linear regression used to fit the size effect law measured experimentally. Either the whole set of experimental points or the mean strengths per specimen geometry can be used, however, the confidence intervals will be generally narrower if only the mean size effect law is used. This process allows the determination of the mean $\mathcal{R}$-curve and the two 95% confidence $\mathcal{R}$-curves. The three $\mathcal{R}$-curve parameters and the respective standard deviations can also be determined.

This method provides only three sets of $\mathcal{R}$-curve parameters and therefore, $\mathcal{R}_{ss}$, l_{fpz} and β are considered independent. This second method is simpler to apply and less computationally expensive, however, the relation between $\mathcal{R}_{ss}$ and the remaining parameters has to be assumed, so caution is required when applying this method.

D.2 Case study

The determination of the $\mathcal{R}$-curve is based on the size effect law which can be determined from the strengths of geometrically similar double edge notched specimens with different widths. Table D.1 shows the notched strengths and respective standard deviations of the double edge notch tension specimens that were used to determine the longitudinal crack resistance curve of IM7/8552 material system [23].

Table D.1: Double Edge Notched Tension Strength for IM7/8552 $[90/0]_{8s}$ [23].

Ref.	w [mm]	$\bar{x}$ [MPa]	s [MPa]
B	7.5	309	9
C	10	289	16
D	12.5	269	11
E	15	256	10

Using Method 1 described in Section D.1.1, a set of statistically representative crack resistance curves, with a known mean and standard deviation of the three fitting parameters (l_{fpz}, $\mathcal{R}_{ss}$ and β) is obtained, as shown in Fig. D.1.

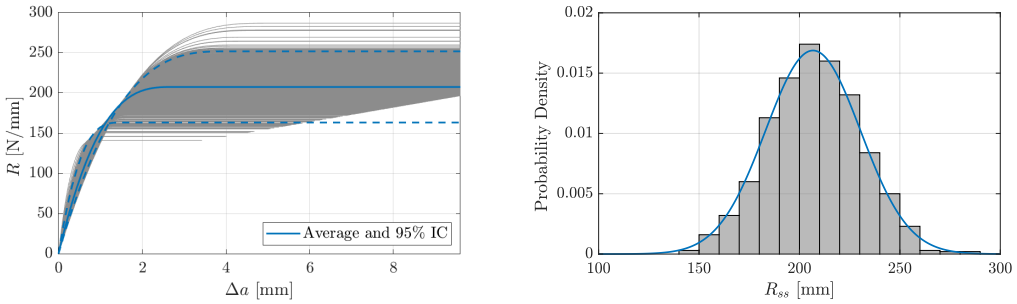

(a) (b)

Figure D.1: Schematic representation of randomly generated $\mathcal{R}$-curves using method 1 (a) and distribution of the steady state fracture toughness R_{ss} (b).

The fitting parameters of the crack resistance curves cannot be treated independently as that would potentially lead to non admissible $\mathcal{R}$-curves. For this reason, a dependence between the parameters was established as a function of $\mathcal{R}_{ss}$. As shown in Fig. D.2, it was found that l_{fpz} varies linearly with $\mathcal{R}_{ss}$ and β is almost constant for the case analysed. Therefore, the crack resistance curves can be defined as a function of $\mathcal{R}_{ss}$. $\mathcal{R}_{ss}$ is generated randomly following a normal distribution with a know mean (206.75N/mm) and standard deviation (23.64N/mm) and the other two parameters are estimated as:

$$l_{fpz} = 2.7776 \times 10^{-2} \times \mathcal{R}_{ss} - 3.0598 \qquad [\text{mm}]$$
$$\beta = 2.9027 \qquad [\text{-}]$$

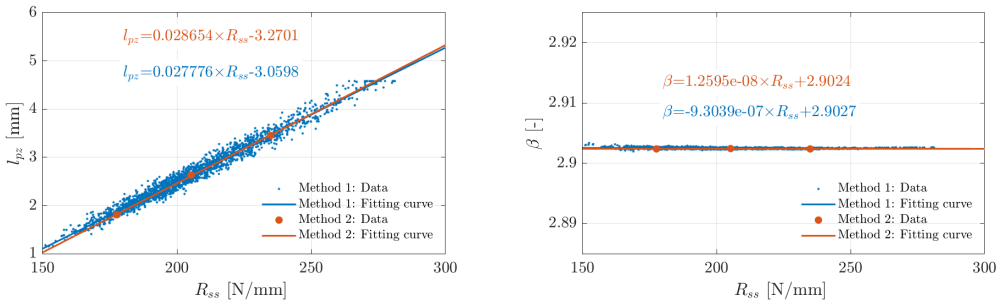

(a) (b)

Figure D.2: l_{fpz}= f($\mathcal{R}_{ss}$) (a) and β= g($\mathcal{R}_{ss}$) (b) obtained with method 1 and method 2.

Using Method 2 the variability is obtained from the determination of the 95% prediction bounds of the fitting of the size effect law. Either the whole set of experimental points or the mean strengths per specimen geometry can be used. In this study only the mean strengths were used since the full set of results was not available.

Since this method provides only three sets of $\mathcal{R}$-curve parameters, the relation between l_{fpz}, $\mathcal{R}_{ss}$ and β is undefined. However, using Method 1, it was shown that a linear functions can be used to relate $\mathcal{R}_{ss}$ to l_{fpz} and β, and so the fitting parameters of the curves can be easily determined as a function of $\mathcal{R}_{ss}$ as shown in Fig. D.2. Using this method, $\mathcal{R}_{ss}$ is generated randomly following a normal distribution with a know mean (205.26N/mm) and standard deviation (14.83N/mm) and the other two parameters are estimated as:

$$l_{fpz} = 2.8654 \times 10^{-2} \times \mathcal{R}_{ss} - 3.2701 \qquad [\text{mm}]$$
$$\beta = 2.9024 \qquad [\text{-}]$$

As shown in Fig. D.2 the fitting curves obtained with both methods show similar trends. Fig. D.3 shows the normal distribution and the corresponding average and 95% IC $\mathcal{R}$-curves obtained with both methods. Only a 1.5N/mm difference in the mean $\mathcal{R}_{ss}$ using Methods 1 and 2 was found. However, since the standard deviation obtained using Method 2 is around 40% lower than the one measured using Method 1 because the confidence bounds were determined using the mean double edge notch strengths, the normal distribution of $\mathcal{R}_{ss}$ is significantly narrower when Method 2 is used. Using the whole set of data would be preferred in Method 2.

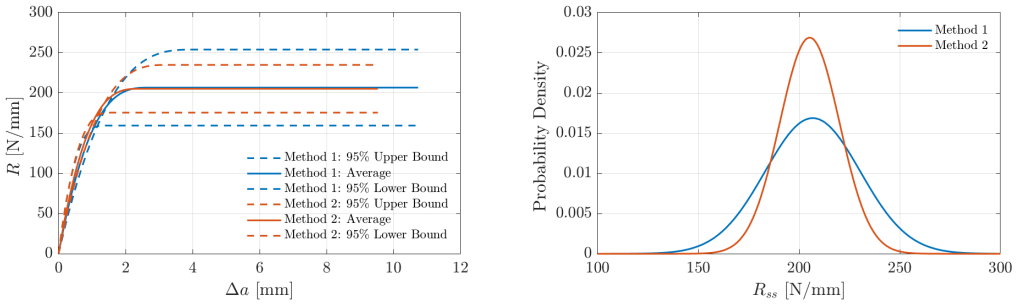

(a) (b)

Figure D.3: Average and 95% confidence bounds $\mathcal{R}$-curves (a) and predicted normal distribution of $\mathcal{R}_{ss}$ using method 1 and method 2 (b).

Bibliography

[1] R. Amacher, J. Cugnoni, J. Botsis, L. Sorensen, W. Smith, and C. Dransfeld, "Thin ply composites: Experimental characterization and modeling of size-effects," Composites Science and Technology, vol. 101, pp. 121–132, sep 2014.

[2] G. Frossard, J. Cugnoni, T. Gmür, and J. Botsis, "Mode I interlaminar fracture of carbon epoxy laminates: Effects of ply thickness," Composites Part A: Applied Science and Manufacturing, vol. 91, pp. 1–8, 2016.

[3] A. Arteiro, G. Catalanotti, A. R. Melro, P. Linde, and P. P. Camanho, "Micro-mechanical analysis of the in situ effect in polymer composite laminates," Composite Structures, vol. 116, pp. 827–840, sep 2014.

[4] A. Arteiro, G. Catalanotti, A. R. Melro, P. Linde, and P. P. Camanho, "Micro-mechanical analysis of the effect of ply thickness on the transverse compressive strength of polymer composites," Composites Part A: Applied Science and Manufacturing, vol. 79, pp. 127–137, 2015.

[5] E. V. Iarve, D. Mollenhauer, and R. Kim, "Theoretical and experimental investigation of stress redistribution in open hole composite laminates due to damage accumulation," Composites Part A: Applied Science and Manufacturing, vol. 36, no. 2, pp. 163–171, 2005.

[6] S. Sihn, R. Kim, K. Kawabe, and S. Tsai, "Experimental studies of thin-ply laminated composites," Composites Science and Technology, vol. 67, pp. 996–1008, may 2007.

[7] F. H. Gojny, M. H. G. Wichmann, B. Fiedler, and K. Schulte, "Influence of different carbon nanotubes on the mechanical properties of epoxy matrix composites – A comparative study," Composites Science and Technology, vol. 65, no. 15, pp. 2300–2313, 2005.

[8] E. J. Garcia, B. L. Wardle, and A. John Hart, "Joining prepreg composite interfaces with aligned carbon nanotubes," Composites Part A: Applied Science and Manufacturing, vol. 39, no. 6, pp. 1065–1070, 2008.

[9] J. P. Gore and A. Sane, "Flame synthesis of carbon nanotubes," Carbon Nanotubes-Synthesis, Characterization, Applications, no. 1, p. 16801, 2011.

[10] B. G. Falzon, S. C. Hawkins, C. P. Huynh, R. Radjef, and C. Brown, "An investigation of Mode I and Mode II fracture toughness enhancement using aligned carbon nanotubes forests at the crack interface," Composite Structures, vol. 106, pp. 65–73, 2013.

[11] P. P. Camanho, A. Arteiro, A. R. Melro, G. Catalanotti, and M. Vogler, "Three-dimensional invariant-based failure criteria for fibre-reinforced composites," International Journal of Solids and Structures, vol. 55, pp. 92–107, 2015.

[12] P. P. Camanho, P. Maimí, and C. G. Dávila, "Prediction of size effects in notched laminates using continuum damage mechanics," Composites science and technology, vol. 67, no. 13, pp. 2715–2727, 2007.

[13] G. H. Erçin, P. P. Camanho, J. Xavier, G. Catalanotti, S. Mahdi, and P. Linde, "Size effects on the tensile and compressive failure of notched composite laminates," Compos Struct, vol. 96, pp. 736–744, 2013.

[14] M. Bessa, "Meso-mechanical model of the structural integrity of advanced composite laminates," Master's thesis, Faculdade de Engenharia, Universidade do Porto, Porto, 2010.

[15] S. W. Tsai and J. D. D. Melo, Composite Materials Design and Testing — Unlocking mystery with invariants. Stanford: Composites Design Group, Department of Aeronautics and Astronautics, Stanford University, 2015.

[16] S. W. Tsai and J. D. D. Melo, "A unit circle failure criterion for carbon fiber reinforced polymer composites," Composites Science and Technology, vol. 123, pp. 71–78, 2016.

[17] X. Xu, M. R. W., K. Chang, and S. R. Hallett, "Unification of strength scaling between unidirectional, quasi-isotropic, and notched carbon/epoxy laminates," Compos Part A-Appl S, vol. 90, pp. 296–305, 2016.

[18] A. Arteiro, G. Catalanotti, J. Xavier, and P. P. Camanho, "Notched response of non-crimp fabric thin-ply laminates," Composites Science and Technology, vol. 79, pp. 97–114, apr 2013.

[19] C. Furtado, A. Arteiro, G. Catalanotti, J. Xavier, and P. P. Camanho, "Selective ply-level hybridisation for improved notched response of composite laminates," Composite Structures, vol. 145, pp. 1–14, 2016.

[20] A. Arteiro, G. Catalanotti, J. Xavier, and P. P. Camanho, "Large damage capability of non-crimp fabric thin-ply laminates," Composites Part A: Applied Science and Manufacturing, vol. 63, pp. 110–122, aug 2014.

[21] E. Kalfon-Cohen, R. Kopp, C. Furtado, X. Ni, A. Arteiro, G. Borstnar, M. N. Mavrogordato, I. Sinclair, S. M. Spearing, P. P. Camanho, et al., "Synergetic effects of thin plies and aligned carbon nanotube interlaminar reinforcement in composite laminates," Composites Science and Technology, vol. 166, pp. 160–168, 2018.

[22] P. P. Camanho, C. G. Dávila, S. T. Pinho, L. Iannucci, and P. Robinson, "Prediction of in situ strengths and matrix cracking in composites under transverse tension and in-plane shear," Composites Part A: Applied Science and Manufacturing, vol. 37, pp. 165–176, feb 2006.

[23] G. Catalanotti, A. Arteiro, M. Hayati, and P. P. Camanho, "Determination of the mode I crack resistance curve of polymer composites using the size-effect law," Engineering Fracture Mechanics, vol. 118, pp. 49–65, mar 2014.

[24] A. Arteiro, Structural Mechanics of Thin-Ply Laminated Composites. PhD thesis, Universidade do Porto, 2016.

[25] C. T. Herakovich, Mechanics of Fibrous Composites. Wiley, 1997.

[26] T. Yokozeki, Y. Aoki, and T. Ogasawara, "Experimental characterization of strength and damage resistance properties of thin-ply carbon fiber/toughened epoxy laminates," Composite Structures, vol. 82, no. 3, pp. 382–389, 2008.

[27] A. Parvizi, K. W. Garrett, and J. E. Bailey, "Constrained cracking in glass fibre-reinforced epoxy cross-ply laminates," Journal of Materials Science, vol. 13, no. 1, pp. 195–201, 1978.

[28] F. Chang and M. Chen, "The in situ ply shear strength distributions in graphite/epoxy laminated composites," Journal of Composite Materials, vol. 21, no. 8, pp. 708–733, 1987.

[29] K. W. Garrett and J. E. Bailey, "Multiple transverse fracture in 90° cross-ply laminates of a glass fibre-reinforced polyester," Journal of Materials Science, vol. 12, no. 1, pp. 157–168, 1977.

[30] A. Parvizi and J. E. Bailey, "On multiple transverse cracking in glass fibre epoxy cross-ply laminates," Journal of Materials Science, vol. 13, no. 10, pp. 2131–2136, 1978.

[31] D. L. Flaggs and M. H. Kural, "Experimental determination of the in situ transverse lamina strength in graphite/epoxy laminates," Journal of composite materials, vol. 16, no. 2, pp. 103–116, 1982.

[32] L. Boniface, P. A. Smith, M. G. Bader, and A. H. Rezaifard, "Transverse ply cracking in cross-ply {CFRP} laminates—initiation or propagation controlled?," Journal of composite materials, vol. 31, no. 11, pp. 1080–1112, 1997.

[33] T. A. Sebaey, J. Costa, P. Maimí, Y. Batista, N. Blanco, and J. A. Mayugo, "Measurement of the in situ transverse tensile strength of composite plies by means of the real time monitoring of microcracking," Composites Part B: Engineering, vol. 65, pp. 40–46, 2014.

[34] B. G. Green, M. R. Wisnom, and S. R. Hallett, "An experimental investigation into the tensile strength scaling of notched composites," Composites Part A: Applied Science and Manufacturing, vol. 38, no. 3, pp. 867–878, 2007.

[35] M. R. Wisnom and S. R. Hallett, "The role of delamination in strength, failure mechanism and hole size effect in open hole tensile tests on quasi-isotropic laminates," Composites Part A: Applied Science and Manufacturing, vol. 40, no. 4, pp. 335–342, 2009.

[36] J. Lee and C. Soutis, "Measuring the notched compressive strength of composite laminates: Specimen size effects," Composites Science and Technology, vol. 68, no. 12, pp. 2359–2366, 2008.

[37] H. Saito, M. Morita, K. Kawabe, M. Kanesaki, H. Takeuchi, M. Tanaka, and I. Kimpara, "Effect of ply-thickness on impact damage morphology in CFRP laminates," Journal of Reinforced Plastics and Composites, vol. 30, no. 13, pp. 1097–1106, 2011.

[38] K. Kawabe, H. Sasayama, and S. Tomoda, "New carbon fiber tow-spread technology and applications to advanced composite materials," SAMPE journal, vol. 45, no. 2, pp. 6–17, 2009.

[39] Y. Nishikawa, K. Okubo, T. Fujii, and K. Kawabe, "Fatigue crack constraint in plain-woven CFRP using newly-developed spread tows," International Journal of Fatigue, vol. 28, no. 10, pp. 1248–1253, 2006.

[40] T. Tay, S. H. N. Tan, V. B. C. Tan, and J. H. Gosse, "Damage progression by the element-failure method (EFM) and strain invariant failure theory (SIFT)," Composites Science and Technology, vol. 65, no. 6, pp. 935–944, 2005.

[41] E. Abisset, F. Daghia, and P. Ladevèze, "On the validation of a damage mesomodel for laminated composites by means of open-hole tensile tests on quasi-isotropic laminates," Composites Part A: Applied Science and Manufacturing, vol. 42, no. 10, pp. 1515–1524, 2011.

[42] V. Iarve, M. R. Gurvich, D. H. Mollenhauer, C. A. Rose, and C. G. Dávila, "Mesh-independent matrix cracking and delamination modeling in laminated composites," International journal for numerical methods in engineering, vol. 88, no. 8, pp. 749–773, 2011.

[43] F. P. der Meer, C. Oliver, and L. J. Sluys, "Computational analysis of progressive failure in a notched laminate including shear nonlinearity and fiber failure," Composites Science and Technology, vol. 70, no. 4, pp. 692–700, 2010.

[44] D. Ling, Q. Yang, and B. Cox, "An augmented finite element method for modeling arbitrary discontinuities in composite materials," International journal of fracture, vol. 156, no. 1, pp. 53–73, 2009.

[45] M. R. Wisnom, "Modelling discrete failures in composites with interface elements," Composites Part A: Applied Science and Manufacturing, vol. 41, no. 7, pp. 795–805, 2010.

[46] C. Schuecker and H. E. Pettermann, "A continuum damage model for fiber reinforced laminates based on ply failure mechanisms," Composite structures, vol. 76, no. 1, pp. 162–173, 2006.

[47] P. Maimí, P. P. Camanho, J. A. Mayugo, and C. G. Dávila, "A continuum damage model for composite laminates: Part II – Computational implementation and validation," Mechanics of Materials, vol. 39, no. 10, pp. 909–919, 2007.

[48] P. Maimí, P. P. Camanho, J. A. Mayugo, and C. G. Dávila, "A continuum damage model for composite laminates: Part I – Constitutive model," Mechanics of Materials, vol. 39, no. 10, pp. 897–908, 2007.

[49] P. Maimí, Modelización constitutiva y computacional del daño y la fractura de materiales compuestos. PhD thesis, Universitat de Girona, 2007.

[50] M. Vogler, R. Rolfes, and P. P. Camanho, "Modeling the inelastic deformation and fracture of polymer composites – Part I: Plasticity model," Mechanics of Materials, vol. 59, pp. 50–64, apr 2013.

[51] P. P. Camanho, M. A. Bessa, G. Catalanotti, M. Vogler, and R. Rolfes, "Modeling the inelastic deformation and fracture of polymer composites–Part II: smeared crack model," Mechanics of Materials, vol. 59, pp. 36–49, 2013.

[52] Y. Qiu, M. A. Crisfield, and G. Alfano, "An interface element formulation for the simulation of delamination with buckling," Engineering Fracture Mechanics, vol. 68, no. 16, pp. 1755–1776, 2001.

[53] A. Turon, P. P. Camanho, J. Costa, and C. G. Dávila, "A damage model for the simulation of delamination in advanced composites under variable-mode loading," Mechanics of Materials, vol. 38, pp. 1072–1089, nov 2006.

[54] J. H. A. Schipperen and R. De Borst, "A numerical analysis of mixed-mode delamination in carbon–epoxy prepregs," Composite structures, vol. 54, no. 4, pp. 445–451, 2001.

[55] J. Reinoso, A. Arteiro, M. Paggi, and P. P. Camanho, "Strength prediction of notched thin ply laminates using finite fracture mechanics and the phase field approach," Composites Science and Technology, vol. 150, pp. 205 – 216, 2017.

[56] C. Miehe, F. Welschinger, and M. Hofacker, "Thermodynamically consistent phase-field models of fracture: Variational principles and multi-field FE implementations," International Journal for Numerical Methods in Engineering, vol. 83, pp. 1273–1311, sep 2010.

[57] C. Miehe, M. Hofacker, and F. Welschinger, "A phase field model for rate-independent crack propagation: Robust algorithmic implementation based on operator splits," Computer Methods in Applied Mechanics and Engineering, vol. 199, pp. 2765–2778, nov 2010.

[58] R. M. Christensen, "Stress based yield/failure criteria for fiber composites," International Journal of Solids and Structures, vol. 34, pp. 529–543, feb 1997.

[59] K. Liu, "A progressive quadratic failure criterion for a laminate," Composites Science and Technology, vol. 58, pp. 1023–1032, jul 1998.

[60] L. Hart-Smith, "Predictions of the original and truncated maximum-strain failure models for certain fibrous composite laminates," Composites Science and Technology, vol. 58, pp. 1151–1178, jul 1998.

[61] C. T. Sun, J. Tao, and A. S. Kaddour, "The prediction of failure envelopes and stress/strain behavior of composite laminates: comparison with experimental results," Composites Science and Technology, vol. 62, pp. 1673–1682, sep 2002.

[62] A. Kuraishi, S. W. Tsai, and K. S. Liu, "A progressive quadratic failure criterion, part B," Composites Science and Technology, vol. 62, pp. 1683–1695, sep 2002.

[63] A. Puck, "Failure analysis of FRP laminates by means of physically based phenomenological models," Composites Science and Technology, vol. 58, pp. 1045–1067, jul 1998.

[64] C. G. Dávila, P. P. Camanho, and C. A. Rose, "Failure criteria for FRP laminates," Journal of Composite materials, vol. 39, no. 4, pp. 323–345, 2005.

[65] C. G. Dávila and P. P. Camanho, "Failure criteria for FRP laminates in plane stress," NASA TM, vol. 212663, no. 613, 2003.

[66] S. T. Pinho, L. Iannucci, and P. Robinson, "Physically-based failure models and criteria for laminated fibre-reinforced composites with emphasis on fibre kinking: Part I: Development," Composites Part A: Applied Science and Manufacturing, vol. 37, pp. 63–73, jan 2006.

[67] G. Catalanotti, P. P. Camanho, and A. T. Marques, "Three-dimensional failure criteria for fiber-reinforced laminates," Composite Structures, vol. 95, pp. 63–79, jan 2013.

[68] J. M. Whitney and R. J. Nuismer, "Stress fracture criteria for laminated composites containing stress concentrations," Journal of composite materials, vol. 8, no. 3, pp. 253–265, 1974.

[69] E. J. R. Waddoups M. E. and B. E. Kaminski, "Macroscopic fracture mechanics of advanced composite materials," J Compos Mater, no. 5, pp. 446–454, 1971.

[70] P. P. Camanho, G. H. Erçin, G. Catalanotti, S. Mahdi, and P. Linde, "A finite fracture mechanics model for the prediction of the open-hole strength of composite laminates," Composites Part A: Applied Science and Manufacturing, vol. 43, pp. 1219–1225, aug 2012.

[71] A. Arteiro, G. Catalanotti, J. Xavier, and P. P. Camanho, "Notched response of non-crimp fabric thin-ply laminates: Analysis methods," Composites Science and Technology, vol. 88, pp. 165–171, nov 2013.

[72] V. Choudhary and A. Gupta, "Polymer/carbon nanotube nanocomposites," Carbon Nanotubes-Polymer Nanocomposites, pp. 65–90, 2011.

[73] P. C. Ma, N. A. Siddiqui, G. Marom, and J. K. Kim, "Dispersion and functionalization of carbon nanotubes for polymer-based nanocomposites: a review," Composites Part A: Applied Science and Manufacturing, vol. 41, no. 10, pp. 1345–1367, 2010.

[74] M. S. Konsta-Gdoutos, Z. S. Metaxa, and S. P. Shah, "Highly dispersed carbon nanotube reinforced cement based materials," Cement and Concrete Research, vol. 40, no. 7, pp. 1052–1059, 2010.

[75] Z. Han and A. Fina, "Thermal conductivity of carbon nanotubes and their polymer nanocomposites: a review," Progress in polymer science, vol. 36, no. 7, pp. 914–944, 2011.

[76] M. Quaresimin, K. Schulte, M. Zappalorto, and S. Chandrasekaran, "Toughening mechanisms in polymer nanocomposites: From experiments to modelling," Composites Science and Technology, vol. 123, pp. 187–204, 2016.

[77] T. H. Hsieh, A. J. Kinloch, A. C. Taylor, and I. A. Kinloch, "The effect of carbon nanotubes on the fracture toughness and fatigue performance of a thermosetting epoxy polym," Journal of Materials Science, vol. 46, no. 23, pp. 7525–7535, 2011.

[78] C. A. Cooper, S. R. Cohen, A. H. Barber, and H. D. Wagner, "Detachment of nanotubes from a polymer matrix," Applied Physics Letters, vol. 81, no. 20, pp. 3873–3875, 2002.

[79] Z. Fan, K. Hsiao, and S. G. Advani, "Experimental investigation of dispersion during flow of multi-walled carbon nanotube/polymer suspension in fibrous porous media," Carbon, vol. 42, no. 4, pp. 871–876, 2004.

[80] M. H. G. Wichmann, J. Sumfleth, F. H. Gojny, M. Quaresimin, B. Fiedler, and K. Schulte, "Glass-fibre-reinforced composites with enhanced mechanical and electrical properties – Benefits and limitations of a nanoparticle modified matrix," Engineering Fracture Mechanics, vol. 73, no. 16, pp. 2346–2359, 2006.

[81] J. Qiu, C. Zhang, B. Wang, and R. Liang, "Carbon nanotube integrated multifunctional multiscale composites," Nanotechnology, vol. 18, p. 275708, jul 2007.

[82] Y. S. Song, "Multiscale fiber-reinforced composites prepared by vacuum-assisted resin transfer molding," Polymer Composites, vol. 28, pp. 458–461, aug 2007.

[83] E. T. Thostenson, J. J. Gangloff, C. Li, and J. Byun, "Electrical anisotropy in multiscale nanotube/fiber hybrid composites," Applied Physics Letters, vol. 95, no. 7, p. 073111, 2009.

[84] Y. Zhou, F. Pervin, L. Lewis, and S. Jeelani, "Fabrication and characterization of carbon/epoxy composites mixed with multi-walled carbon nanotubes," Materials Science and Engineering: A, vol. 475, no. 1, pp. 157–165, 2008.

[85] K. J. Green, D. R. Dean, U. K. Vaidya, and E. Nyairo, "Multiscale fiber reinforced composites based on a carbon nanofiber/epoxy nanophased polymer matrix: Synthesis, mechanical, and thermomechanical behavior," Composites Part A: Applied Science and Manufacturing, vol. 40, no. 9, pp. 1470–1475, 2009.

[86] M. Kim, Y. Park, O. I. Okoli, and C. Zhang, "Processing, characterization, and modeling of carbon nanotube-reinforced multiscale composites," Composites Science and Technology, vol. 69, no. 3, pp. 335–342, 2009.

[87] P. M. Ajayan and J. M. Tour, "Materials science: nanotube composites," Nature, vol. 447, no. 7148, pp. 1066–1068, 2007.

[88] J. N. Coleman, U. Khan, W. J. Blau, and Y. K. Gun'ko, "Small but strong: a review of the mechanical properties of carbon nanotube–polymer composites," Carbon, vol. 44, no. 9, pp. 1624–1652, 2006.

[89] Z. Spitalsky, D. Tasis, K. Papagelis, and C. Galiotis, "Carbon nanotube–polymer composites: chemistry, processing, mechanical and electrical properties," Progress in polymer science, vol. 35, no. 3, pp. 357–401, 2010.

[90] R. F. Gibson, "A review of recent research on mechanics of multifunctional composite materials and structures," Composite structures, vol. 92, no. 12, pp. 2793–2810, 2010.

[91] R. Van Noorden and Others, "The trials of new carbon," Nature, vol. 469, no. 7328, pp. 14–16, 2011.

[92] T. Chou, L. Gao, E. T. Thostenson, Z. Zhang, and J. Byun, "An assessment of the science and technology of carbon nanotube-based fibers and composites," Composites Science and Technology, vol. 70, no. 1, pp. 1–19, 2010.

[93] G. Mago, D. M. Kalyon, S. C. Jana, and F. T. Fisher, "Polymer nanocomposite processing, characterization, and applications," Journal of Nanomaterials, 2010.

[94] M. F. L. De Volder, S. H. Tawfick, R. H. Baughman, and A. J. Hart, "Carbon nanotubes: present and future commercial applications," science, vol. 339, no. 6119, pp. 535–539, 2013.

[95] P. Karapappas, A. Vavouliotis, P. Tsotra, V. Kostopoulos, and A. Palpetis, "Enhanced fracture properties of carbon reinforced composites by the addition of multi-wall carbon nanotubes," Journal of Composite Materials, 2009.

[96] T. Yokozeki, Y. Iwahori, S. Ishiwata, and K. Enomoto, "Mechanical properties of CFRP laminates manufactured from unidirectional prepregs using CSCNT-dispersed epoxy," Composites Part A: Applied Science and Manufacturing, vol. 38, no. 10, pp. 2121–2130, 2007.

[97] A. Godara, L. Mezzo, F. Luizi, A. Warrier, S. V. Lomov, A. W. van Vuure, L. Gorbatikh, P. Moldenaers, and I. Verpoest, "Influence of carbon nanotube reinforcement on the processing and the mechanical behaviour of carbon fiber/epoxy composites," Carbon, vol. 47, no. 12, pp. 2914–2923, 2009.

[98] G. Romhany and G. Szebenyi, "Interlaminar crack propagation in mwcnt/fiber reinforced hybrid composites," Express Polymer Letters, vol. 3, no. 3, pp. 145–151, 2009.

[99] M. Arai, Y. Noro, K. Sugimoto, and M. Endo, "Mode I and mode II interlaminar fracture toughness of CFRP laminates toughened by carbon nanofiber interlayer," Composites Science and Technology, vol. 68, no. 2, pp. 516–525, 2008.

[100] E. T. Thostenson, W. Z. Li, D. Z. Wang, Z. F. Ren, and T. W. Chou, "Carbon nanotube/carbon fiber hybrid multiscale composites," Journal of Applied physics, vol. 91, no. 9, pp. 6034–6037, 2002.

[101] W. B. Down and R. T. K. Baker, "Modification of the surface properties of carbon fibers via the catalytic growth of carbon nanofibers," Journal of Materials Research, vol. 10, no. 03, pp. 625–633, 1995.

[102] Z. Zhao, L. Ci, H. Cheng, and J. Bai, "The growth of multi-walled carbon nanotubes with different morphologies on carbon fibers," Carbon, vol. 43, no. 3, pp. 663–665, 2005.

[103] F. Cesano, S. Bertarione, D. Scarano, and A. Zecchina, "Connecting carbon fibers by means of catalytically grown nanofilaments: formation of carbon-carbon composites," Chemistry of materials, vol. 17, no. 20, pp. 5119–5123, 2005.

[104] K. L. Kepple, G. P. Sanborn, P. A. Lacasse, K. M. Gruenberg, and W. J. Ready, "Improved fracture toughness of carbon fiber composite functionalized with multi walled carbon nanotubes," Carbon, vol. 46, no. 15, pp. 2026–2033, 2008.

[105] Q. Zhang, J. Liu, R. Sager, L. Dai, and J. Baur, "Hierarchical composites of carbon nanotubes on carbon fiber: influence of growth condition on fiber tensile properties," Composites Science and Technology, vol. 69, no. 5, pp. 594–601, 2009.

[106] H. Qian, A. Bismarck, E. S. Greenhalgh, and M. S. P. Shaffer, "Carbon nanotube grafted carbon fibres: A study of wetting and fibre fragmentation," Composites Part A: Applied Science and Manufacturing, vol. 41, no. 9, pp. 1107–1114, 2010.

[107] F. An, C. Lu, J. Guo, S. He, H. Lu, and Y. Yang, "Preparation of vertically aligned carbon nanotube arrays grown onto carbon fiber fabric and evaluating its wettability on effect of composite," Applied Surface Science, vol. 258, no. 3, pp. 1069–1076, 2011.

[108] R. J. Sager, P. J. Klein, D. C. Lagoudas, Q. Zhang, J. Liu, L. Dai, and J. W. Baur, "Effect of carbon nanotubes on the interfacial shear strength of T650 carbon fiber in an epoxy matrix," Composites Science and Technology, vol. 69, no. 7, pp. 898–904, 2009.

[109] E. J. Garcia, B. L. Wardle, A. John Hart, and N. Yamamoto, "Fabrication and multifunctional properties of a hybrid laminate with aligned carbon nanotubes grown In Situ," Composites Science and Technology, vol. 68, no. 9, pp. 2034–2041, 2008.

[110] D. J. Lewis, "Interlaminar reinforcement of carbon fiber composites from unidirectional prepreg utilizing aligned carbon nanotubes," Master's thesis, Massachusetts Institute of Technology, 2016.

[111] R. Guzman de Villoria, P. Hallander, L. Ydrefors, P. Nordin, and B. L. Wardle, "In-plane strength enhancement of laminated composites via aligned carbon nanotube interlaminar reinforcement," Composites Science and Technology, vol. 133, pp. 33–39, 2016.

[112] J. Blanco, E. J. García, R. G. de Villoria, and B. L. Wardle, "Limiting mechanisms of mode I interlaminar toughening of composites reinforced with aligned carbon nanotubes," Journal of Composite Materials, vol. 43, no. 8, pp. 825–841, 2009.

[113] ASTM D5528 - 13 and ASTM D 5528, " Standard Test Method for Mode I Interlaminar Fracture Toughness of Unidirectional Fiber-Reinforced Polymer Matrix Composites," West Conshohocken, PA: ASTM International.

[114] ASTM D7905 D7905M, "Fibre reinforced plastics - Determination of interlaminar fracture toughness energy - Mode I - Gic," West Conshohocken, PA: ASTM International.

[115] J. R. Rice, "A path independent integral and the approximate analysis of strain concentration by notches and cracks," Journal of applied mechanics, vol. 35, no. 2, pp. 379–386, 1968.

[116] B. F. Sorensen, "Cohesive law and notch sensitivity of adhesive joints," Acta Materialia, vol. 50, no. 5, pp. 1053–1061, 2002.

[117] B. F. Sorensen and T. K. Jacobsen, "Determination of cohesive laws by the J integral approach," Engineering Fracture Mechanics, vol. 70, no. 14, pp. 1841–1858, 2003.

[118] F. Nilsson, "Large displacement aspects on fracture testing with double cantilever beam specimens," International journal of fracture, vol. 139, no. 2, pp. 305–311, 2006.

[119] A. J. Russell and K. N. Street, "Factors affecting the interlaminar fracture energy of graphite/epoxy laminates," Progress in science and Engineering of Composites, pp. 279–286, 1982.

[120] L. A. Carlsson, J. W. Gillespie, and R. B. Pipes, "On the analysis and design of the end notched flexure (ENF) specimen for mode II testing," Journal of composite materials, vol. 20, no. 6, pp. 594–604, 1986.

[121] K. Leffler, K. S. Alfredsson, and U. Stigh, "Shear behaviour of adhesive layers," International Journal of Solids and Structures, vol. 44, no. 2, pp. 530–545, 2007.

[122] U. Stigh, K. S. Alfredsson, and A. Biel, "Measurement of cohesive laws and related problems," in ASME 2009 international mechanical engineering congress and exposition, pp. 293–298, American Society of Mechanical Engineers, 2009.

[123] B. F. Sorensen, K. Jørgensen, T. K. Jacobsen, and R. C. Østergaard, "DCB-specimen loaded with uneven bending moments," International Journal of Fracture, vol. 141, no. 1-2, pp. 163–176, 2006.

[124] J. L. Högberg, B. F. Sorensen, and U. Stigh, "Constitutive behaviour of mixed mode loaded adhesive layer," International Journal of Solids and Structures, vol. 44, no. 25, pp. 8335–8354, 2007.

[125] K. S. Alfredsson and J. L. Högberg, "Energy release rate and mode-mixity of adhesive joint specimens," International Journal of Fracture, vol. 144, no. 4, pp. 267–283, 2007.

[126] C. Sarrado, A. Turon, J. Renart, and J. Costa, "An experimental data reduction method for the Mixed Mode Bending test based on the J-integral approach," Composites Science and Technology, vol. 117, pp. 85–91, 2015.

[127] ASTM D 2344 / D 2344M-16, "Standard Test Method for Short-Beam Strength of Polymer Matrix Composite Materials and Their Laminates," West Conshohocken, PA: ASTM International.

[128] Y. Yoon, J. Song, D. Kim, J. Kim, J. Park, S. Oh, and C. Han, "Transparent Film Heater Using Single-Walled Carbon Nanotubes," Advanced Materials, vol. 19, no. 23, pp. 4284–4287, 2007.

[129] Z. . Wu and J. N. Wang, "Preparation of large-area double-walled carbon nanotube films and application as film heater," Physica E: Low-dimensional Systems and Nanostructures, vol. 42, no. 1, pp. 77–81, 2009.

[130] D. Kim, H. Lee, J. Y. Woo, and C. Han, "Thermal behavior of transparent film heaters made of single-walled carbon nanotubes," The Journal of Physical Chemistry C, vol. 114, no. 13, pp. 5817–5821, 2010.

[131] J. Kang, H. Kim, K. S. Kim, S. Lee, S. Bae, J. Ahn, Y. Kim, J. Choi, and B. Hong, "High-performance graphene-based transparent flexible heaters," Nano letters, vol. 11, no. 12, pp. 5154–5158, 2011.

[132] K. Jiang, J. Wang, Q. Li, L. Liu, C. Liu, and S. Fan, "Superaligned carbon nanotube arrays, films, and yarns: a road to applications," Advanced Materials, vol. 23, no. 9, pp. 1154–1161, 2011.

[133] H. Jang, S. K. Jeon, and S. H. Nahm, "The manufacture of a transparent film heater by spinning multi-walled carbon nanotubes," Carbon, vol. 49, no. 1, pp. 111–116, 2011.

[134] P. Liu, L. Liu, K. Jiang, and S. Fan, "Carbon-Nanotube-Film Microheater on a Polyethylene Terephthalate Substrate and Its Application in Thermochromic Displays," Small, vol. 7, no. 6, pp. 732–736, 2011.

[135] H. Im, E. Y. Jang, A. Choi, W. J. Kim, T. J. Kang, Y. W. Park, and Y. H. Kim, "Enhancement of heating performance of carbon nanotube sheet with granular metal," ACS applied materials & interfaces, vol. 4, no. 5, pp. 2338–2342, 2012.

[136] D. Janas and K. K. Koziol, "Rapid electrothermal response of high-temperature carbon nanotube film heaters," Carbon, vol. 59, pp. 457–463, 2013.

[137] D. Jung, M. Han, and G. S. Lee, "Flexible transparent conductive heater using multiwalled carbon nanotube sheet," Journal of Vacuum Science & Technology B, vol. 32, no. 4, p. 04E105, 2014.

[138] H. Chu, Z. Zhang, Y. Liu, and J. Leng, "Self-heating fiber reinforced polymer composite using meso/macropore carbon nanotube paper and its application in deicing," Carbon, vol. 66, pp. 154–163, 2014.

[139] A. E. Aliev, N. K. Mayo, R. H. Baughman, D. Avirovik, S. Priya, M. R. Zarnetske, and J. B. Blottman, "Thermal management of thermoacoustic sound projectors using a free-standing carbon nanotube aerogel sheet as a heat source," Nanotechnology, vol. 25, no. 40, p. 405704, 2014.

[140] S. Sorel, D. Bellet, and J. N. Coleman, "Relationship between material properties and transparent heater performance for both bulk-like and percolative nanostructured networks," ACS nano, vol. 8, no. 5, pp. 4805–4814, 2014.

[141] J. J. Bae, S. C. Lim, G. H. Han, Y. W. Jo, D. L. Doung, E. S. Kim, S. J. Chae, T. Q. Huy, N. Van Luan, and Y. H. Lee, "Heat dissipation of transparent graphene defoggers," Advanced Functional Materials, vol. 22, no. 22, pp. 4819–4826, 2012.

[142] D. Janas and K. K. Koziol, "A review of production methods of carbon nanotube and graphene thin films for electrothermal applications," Nanoscale, vol. 6, no. 6, pp. 3037–3045, 2014.

[143] J. Du, S. Pei, L. Ma, and H. Cheng, "25th anniversary article: carbon nanotube-and graphene-based transparent conductive films for optoelectronic devices," Advanced Materials, vol. 26, no. 13, pp. 1958–1991, 2014.

[144] R. G. de Villoria, N. Yamamoto, A. Miravete, and B. L. Wardle, "Multi-physics damage sensing in nano-engineered structural composites," Nanotechnology, vol. 22, no. 18, p. 185502, 2011.

[145] J. Lee, I. Y. Stein, S. S. Kessler, and B. L. Wardle, "Aligned Carbon Nanotube Film Enables Thermally Induced State Transformations in Layered Polymeric Materials," ACS applied materials & interfaces, vol. 7, no. 16, pp. 8900–8905, 2015.

[146] L. Tong, X. Sun, and P. Tan, "Effect of long multi-walled carbon nanotubes on delamination toughness of laminated composites," Journal of composite materials, vol. 42, no. 1, pp. 5–23, 2008.

[147] A. H. Barber, S. R. Cohen, and H. D. Wagner, "Measurement of carbon nanotube–polymer interfacial strength," Applied Physics Letters, vol. 82, no. 23, pp. 4140–4142, 2003.

[148] M. Yu, O. Lourie, M. J. Dyer, K. Moloni, T. F. Kelly, and R. S. Ruoff, "Strength and breaking mechanism of multiwalled carbon nanotubes under tensile load," Science, vol. 287, no. 5453, pp. 637–640, 2000.

[149] M. Yu, B. I. Yakobson, and R. S. Ruoff, "Controlled sliding and pullout of nested shells in individual multiwalled carbon nanotubes," The Journal of Physical Chemistry B, vol. 104, no. 37, pp. 8764–8767, 2000.

[150] M. H. G. G. Wichmann, K. Schulte, and H. D. Wagner, "On nanocomposite toughness," Composites Science and Technology, vol. 68, no. 1, pp. 329–331, 2008.

[151] V. Mirjalili and P. Hubert, "Effect of carbon nanotube dispersion on the fracture toughness of polymers," in ICCM-17 17th International Conference on Composite Materials, pp. 27–31, 2009.

[152] V. Mirjalili and P. Hubert, "Modelling of the carbon nanotube bridging effect on the toughening of polymers and experimental verification," Composites Science and Technology, vol. 70, no. 10, pp. 1537–1543, 2010.

[153] A. Kelly, "Interface effects and the work of fracture of a fibrous composite," in Proceedings of the Royal Society of London A: Mathematical, Physical and Engineering Sciences, vol. 319, pp. 95–116, The Royal Society, 1970.

[154] H. D. Wagner, P. M. Ajayan, and K. Schulte, "Nanocomposite toughness from a pull-out mechanism," Composites Science and Technology, vol. 83, pp. 27–31, 2013.

[155] X. Chen, I. J. Beyerlein, and L. C. Brinson, "Bridged crack models for the toughness of composites reinforced with curved nanotubes," Journal of the Mechanics and Physics of Solids, vol. 59, no. 9, pp. 1938–1952, 2011.

[156] A. H. Barber, R. Andrews, L. S. Schadler, and H. D. Wagner, "On the tensile strength distribution of multiwalled carbon nanotubes," Applied Physics Letters, vol. 87, no. 20, p. 203106, 2005.

[157] A. H. Barber, I. Kaplan-Ashiri, S. R. Cohen, R. Tenne, and H. D. Wagner, "Stochastic strength of nanotubes: An appraisal of available data," Composites Science and Technology, vol. 65, no. 15, pp. 2380–2384, 2005.

[158] C. A. Klein, "Characteristic tensile strength and Weibull shape parameter of carbon nanotubes," Journal of applied physics, vol. 101, no. 12, p. 124909, 2007.

[159] L. Liu, D. Tasis, M. Prato, and H. D. Wagner, "Tensile mechanics of electrospun multiwalled nanotube/poly (methyl methacrylate) nanofibers," Advanced Materials, vol. 19, no. 9, pp. 1228–1233, 2007.

[160] N. M. Pugno and R. S. Ruoff, "Nanoscale Weibull statistics for nanofibers and nanotubes," Journal of Aerospace Engineering, vol. 20, no. 2, pp. 97–101, 2007.

[161] T. Xiao, Y. Ren, K. Liao, P. Wu, F. Li, and H. M. Cheng, "Determination of tensile strength distribution of nanotubes from testing of nanotube bundles," Composites Science and Technology, vol. 68, no. 14, pp. 2937–2942, 2008.

[162] C. Menna, C. E. Bakis, and A. Prota, "Effect of nanofiller length and orientation distributions on Mode I fracture toughness of unidirectional fiber composites," Journal of Composite Materials, vol. 50, no. 10, pp. 1331–1352, 2016.

[163] S. Fu and B. Lauke, "The fibre pull-out energy of misaligned short fibre composites," Journal of materials science, vol. 32, no. 8, pp. 1985–1993, 1997.

[164] B. Farahmand, Virtual Testing and Predictive Modeling. Springer, 2014.

[165] M. Rieth and W. Schommers, Handbook of theoretical and computational nanotechnology, vol. 10. American Scientific Publishers Los Angeles, CA, 2006.

[166] A. R. Leach, "Molecular modeling: principles and applications," Prentice Hall, Englewood Cliffs, NJ, 2001, 2001.

[167] L. E. Malvern, Introduction to the Mechanics of a Continuous Medium. No. Monograph, 1969.

[168] J. N. Reddy, An introduction to the finite element method, vol. 2. McGraw-Hill New York, 1993.

[169] J. Qu and M. Cherkaoui, Fundamentals of micromechanics of solids. Wiley Hoboken, 2006.

[170] G. I. Barenblatt, "The mathematical theory of equilibrium cracks in brittle fracture," Advances in applied mechanics, vol. 7, pp. 55–129, 1962.

[171] D. S. Dugdale, "Yielding of steel sheets containing slits," Journal of the Mechanics and Physics of Solids, vol. 8, no. 2, pp. 100–104, 1960.

[172] A. Hillerborg, M. Modéer, and P. Petersson, "Analysis of crack formation and crack growth in concrete by means of fracture mechanics and finite elements," Cement and concrete research, vol. 6, no. 6, pp. 773–781, 1976.

[173] J. C. J. Schellekens and R. De Borst, "A non-linear finite element approach for the analysis of mode-I free edge delamination in composites," International Journal of Solids and Structures, vol. 30, no. 9, pp. 1239–1253, 1993.

[174] O. Allix, P. Ladeveze, and A. Corigliano, "Damage analysis of interlaminar fracture specimens," Composite Structures, vol. 31, no. 1, pp. 61–74, 1995.

[175] Y. Mi, M. A. Crisfield, G. A. O. Davies, and H. B. Hellweg, "Progressive delamination using interface elements," Journal of composite materials, vol. 32, no. 14, pp. 1246–1272, 1998.

[176] G. Alfano and M. A. Crisfield, "Finite element interface models for the delamination analysis of laminated composites: mechanical and computational issues," International journal for numerical methods in engineering, vol. 50, no. 7, pp. 1701–1736, 2001.

[177] P. P. Camanho, C. G. Dávila, and M. F. de Moura, "Numerical Simulation of Mixed-mode Progressive Delamination in Composite Materials," Composite Materials, vol. 37, no. 16, 2003.

[178] R. de Borst, J. J. C. Remmers, and A. Needleman, "Mesh-independent discrete numerical representations of cohesive-zone models," Engineering fracture mechanics, vol. 73, no. 2, pp. 160–177, 2006.

[179] S. T. Pinho, L. Iannucci, and P. Robinson, "Formulation and implementation of decohesion elements in an explicit finite element code," Composites Part A: Applied science and manufacturing, vol. 37, no. 5, pp. 778–789, 2006.

[180] L. Iannucci, "Dynamic delamination modelling using interface elements," Computers & Structures, vol. 84, no. 15, pp. 1029–1048, 2006.

[181] F. Aymerich, F. Dore, and P. Priolo, "Prediction of impact-induced delamination in cross-ply composite laminates using cohesive interface elements," Composites science and technology, vol. 68, no. 12, pp. 2383–2390, 2008.

[182] Y. Zhang, P. Zhu, and X. Lai, "Finite element analysis of low-velocity impact damage in composite laminated plates," Materials & design, vol. 27, no. 6, pp. 513–519, 2006.

[183] M. Paggi and J. Reinoso, "An anisotropic large displacement cohesive zone model for fibrillar and crazing interfaces," International Journal of Solids and Structures, vol. 69, pp. 106–120, 2015.

[184] A. R. Melro, P. P. Camanho, and S. T. Pinho, "Generation of random distribution of fibres in long-fibre reinforced composites," Composites Science and Technology, vol. 68, no. 9, pp. 2092–2102, 2008.

[185] A. R. Melro, P. P. Camanho, F. M. A. Pires, and S. T. Pinho, "Micromechanical analysis of polymer composites reinforced by unidirectional fibres: Part {I} - Constitutive modelling," International Journal of Solids and Structures, vol. 50, no. 11–12, pp. 1897–1905, 2013.

[186] B. Fiedler, M. Hojo, S. Ochiai, K. Schulte, and M. Ando, "Failure behavior of an epoxy matrix under different kinds of static loading," Composites Science and Technology, vol. 61, no. 11, pp. 1615–1624, 2001.

[187] L. E. Asp, L. A. Berglund, and R. Talreja, "A criterion for crack initiation in glassy polymers subjected to a composite-like stress state," Composites Science and Technology, vol. 56, no. 11, pp. 1291–1301, 1996.

[188] L. E. Asp, L. A. Berglund, and P. Gudmundson, "Effects of a composite-like stress state on the fracture of epoxies," Composites Science and Technology, vol. 53, no. 1, pp. 27–37, 1995.

[189] L. E. Asp, L. A. Berglund, and R. Talreja, "Prediction of matrix-initiated transverse failure in polymer composites," Composites Science and Technology, vol. 56, no. 9, pp. 1089–1097, 1996.

[190] J. Chevalier, X. P. Morelle, C. Bailly, P. P. Camanho, T. Pardoen, and F. Lani, "Micro-mechanics based pressure dependent failure model for highly cross-linked epoxy resins," Engineering Fracture Mechanics, vol. 158, pp. 1–12, 2016.

[191] M. Handbook-MIL-HDBK, "17-3F: Composite Materials Handbook, Volume 3-Polymer Matrix Composites Materials Usage, Design, and Analysis," US Department of Defense, 2002.

[192] J. M. Whitney and R. J. Nuismer, "Stress Fracture Criteria for Laminated Composites Containing Stress Concentrations," J Compos Mater, no. 8, pp. 253–265, 1974.

[193] P. P. Camanho and M. Lambert, "A design methodology for mechanically fastened joints in laminated composite materials," Compos Sci Technol, vol. 66, pp. 3004–3020, 2006.

[194] C. Furtado, A. Arteiro, M. Bessa, B. Wardle, and P. P. Camanho, "Prediction of size effects in open-hole laminates using only the Young's modulus, the strength, and the R-curve of the 0° ply," Composites Part A: Applied Science and Manufacturing, vol. 101, 2017.

[195] A. Turon, E. V. González, C. Sarrado, G. Guillamet, and P. Maimí, "Accurate simulation of delamination under mixed-mode loading using a cohesive model with a mode-dependent penalty stiffness," Composite Structures, vol. 184, pp. 506–511, 2018.

[196] G. Alfano and E. Sacco, "Combining interface damage and friction in a cohesive-zone model," International Journal for Numerical Methods in Engineering, vol. 68, no. 5, pp. 542–582, 2006.

[197] E. V. González, P. Maimí, P. P. Camanho, A. Turon, and J. A. Mayugo, "Simulation of drop-weight impact and compression after impact tests on composite laminates," Composite Structures, vol. 94, no. 11, pp. 3364–3378, 2012.

[198] A. Soto, E. V. González, P. Maimí, F. M. de la Escalera, J. R. S. de Aja, and E. Alvarez, "Low velocity impact and compression after impact simulation of thin ply laminates," Composites Part A: Applied Science and Manufacturing, vol. 109, pp. 413–427, 2018.

[199] A. Soto, E. V. González, P. Maimí, J. A. Mayugo, P. R. Pasquali, and P. P. Camanho, "A methodology to simulate low velocity impact and compression after impact in large composite stiffened panels," Composite Structures, vol. 204, pp. 223–238, 2018.

[200] P. M. Moran, X. H. Liu, and C. F. Shih, "Kink band formation and band-broadening in fiber composites under compressive loading," Acta Metallurgica et Materialia, vol. 43, no. 8, pp. 2943–2958, 1995.

[201] Z. P. Bažant and B. H. Oh, "Crack band theory for fracture of concrete," Mater Struct, vol. 16, no. 93, pp. 155–177, 1983.

[202] C. W. Weaver and J. G. Williams, "Deformation of a carbon-epoxy composite under hydrostatic pressure," Journal of Materials Science, vol. 10, no. 8, pp. 1323–1333, 1975.

[203] T. V. Parry and A. S. Wronski, "Kinking and compressive failure in uniaxially aligned carbon fibre composite tested under superposed hydrostatic pressure," Journal of Materials Science, vol. 17, no. 3, pp. 893–900, 1982.

[204] S. Rabinowitz, I. M. Ward, and J. S. C. Parry, "The effect of hydrostatic pressure on the shear yield behaviour of polymers," Journal of Materials Science, vol. 5, no. 1, pp. 29–39, 1970.

[205] D. Cartié, P. Davies, M. Peleau, and I. K. Partridge, "The influence of hydrostatic pressure on the interlaminar fracture toughness of carbon/epoxy composites," Composites Part B: Engineering, vol. 37, no. 4, pp. 292–300, 2006.

[206] Q. Bing and C. T. Sun, "Effect of compressive transverse normal stress on mode II fracture toughness in polymeric composites," International Journal of Fracture, vol. 145, no. 2, pp. 89–97, 2007.

[207] G. Catalanotti, C. Furtado, T. Scalici, G. Pitarresi, F. P. van der Meer, and P. P. Camanho, "The effect of through-thickness compressive stress on mode II interlaminar fracture toughness," Composite Structures, vol. 182, 2017.

[208] W. Cui, M. R. Wisnom, and M. I. Jones, "Effect of through thickness tensile and compressive stresses on delamination propagation fracture energy," Journal of Composites Technology and Research, vol. 16, no. 4, pp. 329–335, 1994.

[209] X. Li, S. R. Hallett, and M. R. Wisnom, "Predicting the effect of through-thickness compressive stress on delamination using interface elements," Composites Part A: Applied Science and Manufacturing, vol. 39, no. 2, pp. 218–230, 2008.

[210] G. Catalanotti, "Prediction of in situ strengths in composites: Some considerations," Composite Structures, vol. 207, pp. 889–893, 2019.

[211] C. A. Rose, C. G. Dávila, and F. A. Leone, "Analysis Methods for Progressive Damage of Composite Structures," Tech. Rep. July, NASA Langley Research Center, Hampton, VA, United States, 2013.

[212] A. Turon, P. P. Camanho, J. Costa, and Dávila, "An engineering solution for mesh size effects in the simulation of delamination using cohesive zone models," Engineering Fracture Mechanics, vol. 74, no. 10, pp. 1665–1682, 2007.

[213] A. Turon, P. P. Camanho, J. Costa, and J. Renart, "Accurate simulation of delamination growth under mixed-mode loading using cohesive elements : Definition of interlaminar strengths and elastic stiffness," Composite Structures, vol. 92, no. 8, pp. 1857–1864, 2010.

[214] A. Turon, P. P. Camanho, J. Costa, and C. Dávila, "An Interface Damage Model for the Simulation of Delamination Under Variable-Mode Ratio in Composite Materials," NASA TP Technical Reports, 2004.

[215] E. V. González, P. Maimí, A. Turon, P. P. Camanho, and J. Renart, "Simulation of delamination by means of cohesive elements using an explicit finite element code," Computers, Materials & Continua, vol. 9, no. 1, pp. 51–92, 2009.

[216] M. L. Benzeggagh and M. Kenane, "Measurement of mixed-mode delamination fracture toughness of unidirectional glass/epoxy composites with mixed-mode bending apparatus," Composites Science and Technology, vol. 56, no. 4, pp. 439–449, 1996.

[217] P. F. Giddings, C. R. Bowen, A. Salo, H. A. Kim, and A. Ive, "Bistable composite laminates: Effects of laminate composition on cured shape and response to thermal load," Composite Structures, vol. 92, no. 9, pp. 2220–2225, 2010.

[218] C. Huchette, Sur la complémentarité des approches expérimentales et numériques pour la modélisation des mécanismes d'endommagement des composites stratifiés. PhD thesis, Université Paris 6, Paris, 2005.

[219] G. H. Erçin, Stress gradient effects in laminated composites. PhD thesis, Faculdade de Engenharia, Universidade do Porto, Porto, 2013.

[220] L. Marín, D. Trias, P. Badalló, G. Rus, and J. A. Mayugo, "Optimization of composite stiffened panels under mechanical and hygrothermal loads using neural networks and genetic algorithms," Composite Structures, vol. 94, no. 11, pp. 3321–3326, 2012.

[221] Airbus, "Internal communication," tech. rep., 2015.

[222] G. Catalanotti, J. Xavier, and P. P. Camanho, "Measurement of the compressive crack resistance curve of composites using the size effect law," Composites Part A: Applied Science and Manufacturing, vol. 56, pp. 300–307, 2014.

[223] C. M. L. Tavares, "Fracture of advanced composite materials: experimental basis for a constitutive model," tech. rep., University of Porto, Porto, Portugal, 2006.

[224] C. S. Lopes, P. P. Camanho, Z. Gürdal, P. Maimí, and E. V. González, "Low-velocity impact damage on dispersed stacking sequence laminates. Part II: Numerical simulations," Composites Science and Technology, vol. 69, no. 7, pp. 937–947, 2009.

[225] X. Xu, M. R. Wisnom, Y. Mahadik, and S. R. Hallett, "An experimental investigation into size effects in quasi-isotropic carbon/epoxy laminates with sharp and blunt notches," Composites Science and Technology, vol. 100, pp. 220–227, 2014.

[226] X. Xu, M. R. Wisnom, Y. Mahadik, and S. R. Hallett, "Scaling of fracture response in Over-height Compact Tension tests," Composites Part A: Applied Science and Manufacturing, vol. 69, pp. 40–48, 2015.

[227] F. A. Leone, "Deformation gradient tensor decomposition for representing matrix cracks in fiber-reinforced materials," Composites Part A: Applied Science and Manufacturing, vol. 76, pp. 334 – 341, 2015.

[228] O. Falcó, R. L. Ávila, B. Tijs, and C. S. Lopes, "Modelling and simulation methodology for unidirectional composite laminates in a virtual test lab framework," Composite Structures, vol. 190, pp. 137 – 159, 2018.

[229] Dassault Systèmes, ABAQUS User's Manual. 2011.

[230] J. W. Mar and K. Y. Lin, "Fracture mechanics correlation for tensile failure of filamentary composites with holes," Journal of Aircraft, vol. 14, no. 7, pp. 703–704, 1977.

[231] D. Leguillon, "Strength or toughness? A criterion for crack onset at a notch," Eur J Mech A-Solid, vol. 21, pp. 61–72, 2002.

[232] P. Cornetti, N. Pugno, A. Carpinteri, and D. Taylor, "Finite fracture mechanics: A coupled stress and energy failure criterion," Engng Fract Mech, vol. 73, pp. 2021–2033, 2006.

[233] E. Martin, D. Leguillon, and N. Carrère, "A coupled strength and toughness criterion for the prediction of the open hole tensile strength of a composite plate," Int J Solids Struct, vol. 49, pp. 3915–3922, 2012.

[234] P. Cornetti, A. Sapora, and A. Carpinteri, "Mode mixity and size effect in V-notched structures," Int J Solids Struct, vol. 50, pp. 1562–1582, 2013.

[235] P. P. Camanho and G. Catalanotti, "On the relation between the mode I fracture toughness of a composite laminate and that of a 0 ply: Analytical model and experimental validation," Engineering Fracture Mechanics, vol. 78, pp. 2535–2546, aug 2011.

[236] S. W. Tsai and J. D. D. Melo, "An invariant-based theory of composites," Composites Science and Technology, vol. 100, pp. 237–243, 2014.

[237] A. Arteiro, L. F. Pereira, M. A. Bessa, C. Furtado, and P. P. Camanho, "A micro-mechanics perspective to the invariant-based approach to stiffness," Composites Science and Technology, vol. 176, pp. 72 – 80, 2019.

[238] R. S. Vaidya and C. T. Sun, "Fracture criterion for notched thin composite laminates," AIAA journal, vol. 35, no. 2, pp. 311–316, 1997.

[239] G. Bao, S. Ho, Z. Suo, and B. Fan, "The role of material orthotropy in fracture specimens for composites," International Journal of Solids and Structures, vol. 29, no. 9, pp. 1105–1116, 1992.

[240] S. C. Tan, Stress Concentrations in Laminated Composites. Lancaster: Technomic, 1994.

[241] MathWorks, Natick, MA, USA, Matlab R2014a Documentation, 2014.

[242] S. T. Pinho, P. Robinson, and L. Iannucci, "Fracture toughness of the tensile and compressive fiber failure modes in laminated composites," Compos Sci Technol, vol. 66, pp. 2069–2079, 2006.

[243] M. J. Laffan, S. T. Pinho, P. Robinson, and L. Iannucci, "Measurement of the in situ ply fracture toughness associated with mode I fibre tensile failure in FRP. Part I: Data reduction," Compos Sci Technol, vol. 70, pp. 606–613, 2010.

[244] M. J. Laffan, S. T. Pinho, P. Robinson, and L. Iannucci, "Measurement of the in situ ply fracture toughness associated with mode I fibre tensile failure in FRP. Part II: Size and lay-up effects," Compos Sci Technol, vol. 70, pp. 614–621, 2010.

[245] G. Catalanotti, P. P. Camanho, J. Xavier, C. G. Dávila, and A. T. Marques, "Measurement of resistance curves in the longitudinal failure of composites using digital image correlation," Compos Sci Technol, vol. 70, pp. 1986–1993, 2010.

[246] F. Abdi, E. Clarkson, C. Godines, and S. DorMohammadi, "AB Basis Allowable Test Reduction Approach and Composite Generic Basis Strength Values," in 18th AIAA Non-Deterministic Approaches Conference, p. 951, 2016.

[247] Y. Zhang, J. Schutte, J. Meeker, U. Palliyaguru, N. H. Kim, and R. T. Haftka, "Predicting B-basis allowable at untested points from experiments and simulations of plates with holes," in 12th world congress on structural and multidisciplinary optimization, Braunschweig, Germany., 2017.

[248] G. Abumeri, F. Abdi, K. S. Raju, J. Housner, R. Bohner, and A. McCloskey, "Cost Effective Computational Approach for Generation of Polymeric Composite Material Allowables for Reduced Testing," in Advances in Composite Materials-Ecodesign and Analysis, InTech, 2011.

[249] P. R. Spendley, Design Allowables for Composite Aerospace Structures. PhD thesis, University of Surrey, 2012.

[250] K. Nam, K. J. Park, S. Shin, S. J. Kim, and I. Choi, "Estimation of Composite Laminate Design Allowables Using the Statistical Characteristics of Lamina Level Test Data," International Journal of Aeronautical and Space Sciences, vol. 16, no. 3, pp. 360–369, 2015.

[251] M. Handbook, "MIL-HDBK-17-1F: Composite Materials Handbook, Volume 1-Polymer Matrix Composites Guidelines for Characterization of Structural Materials."

[252] S. Chakraborti and J. Li, "Confidence interval estimation of a normal percentile," The American Statistician, vol. 61, no. 4, pp. 331–336, 2007.

[253] G. Catalanotti and P. P. Camanho, "A semi-analytical method to predict net-tension failure of mechanically fastened joints in composite laminates," Composites Science and Technology, vol. 76, pp. 69–76, mar 2013.

[254] W. A. Curtin and N. Takeda, "Tensile strength of fiber-reinforced composites: I. model and effects of local fiber geometry," Journal of composite materials, vol. 32, no. 22, pp. 2042–2059, 1998.

[255] H. Saito, H. Takeuchi, and I. Kimpara, "Experimental evaluation of the damage growth restraining in 90 layer of thin-ply cfrp cross-ply laminates," Advanced Composite Materials, vol. 21, no. 1, pp. 57–66, 2012.

[256] S. R. Hallett and M. R. Wisnom, "Experimental investigation of progressive damage and the effect of layup in notched tensile tests," Journal of Composite Materials, vol. 40, no. 2, pp. 119–141, 2006.

[257] R. F. Teixeira, S. T. Pinho, and P. Robinson, "Thickness-dependence of the translaminar fracture toughness: experimental study using thin-ply composites," Composites Part A: Applied Science and Manufacturing, vol. 90, pp. 33–44, 2016.

[258] M. F. da Costa Fernandes, "Traslaminar fracture of thinply composite laminates," Master's thesis, Faculdade de Engenharia, Universidade do Porto, Porto, 2014.

[259] G. Frossard, Fracture of thin-ply composites: effects of ply thickness. PhD thesis, École Polytechnique Fédéral de Lausanne, Suisse, 2017.

[260] B. Y. Chen, T. E. Tay, P. M. Baiz, and S. T. Pinho, "Numerical analysis of size effects on open-hole tensile composite laminates," Composites Part A: Applied Science and Manufacturing, vol. 47, pp. 52–62, 2013.

[261] D. L. C. B. Weiss and R. Stickler, "A new geometric factor formula for a center cracked plate tensile specimen of finite width," Int J Fract, vol. 55, pp. R3–R8, 1992.

[262] Z. P. Bazant and J. Planas, Fracture and size effect in concrete and other quasibrittle materials, vol. 16. CRC press, 1997.

[263] P. A. Zinoviev, S. V. Tsvetkov, G. G. Kulish, R. W. Van Den Berg, and L. J. M. M. Van Schepdael, "The behavior of high-strength unidirectional composites under tension with superposed hydrostatic pressure," Composites science and technology, vol. 61, no. 8, pp. 1151–1161, 2001.

[264] T. V. Parry and A. S. Wronski, "The effect of hydrostatic pressure on the tensile properties of pultruded cfrp," Journal of materials science, vol. 20, no. 6, pp. 2141–2147, 1985.

[265] M. J. Hinton and A. S. Kaddour, "Triaxial test results for fibre-reinforced composites: The second world-wide failure exercise benchmark data," Journal of Composite Materials, vol. 47, no. 6-7, pp. 653–678, 2013.

[266] P. Hine, R. A. Duckett, A. S. Kaddour, M. J. Hinton, and G. M. Wells, "The effect of hydrostatic pressure on the mechanical properties of glass fibre/epoxy unidirectional composites," Composites Part A: Applied Science and Manufacturing, vol. 36, no. 2, pp. 279 – 289, 2005. 7th International Conference on the Deformation and Fracture of Composites (DFC-7).

[267] "Thin ply program testing support," tech. rep., UdG, Girona, Spain, 2018.

[268] C. Furtado, R. Tavares, J. Machado, A. Arteiro, and P. P. Camanho, "Thin ply program testing support," tech. rep., INEGI, Porto, Portugal, 2018.

[269] G. J. Dvorak and N. Laws, "Analysis of progressive matrix cracking in composite laminates II. First ply failure," Journal of Composite Materials, vol. 21, no. 4, pp. 309–329, 1987.

[270] A. Arteiro, G. Catalanotti, J. Xavier, P. Linde, and P. Camanho, "A strategy to improve the structural performance of non-crimp fabric thin-ply laminates," Composite Structures, vol. 188, pp. 438 – 449, 2018.

[271] ASTM D 3039 D 3039M-14 and ASTM D 3039 / D 3039M-14, " Standard Test Method for Tensile Properties of Polymer Matrix Composite Materials," West Conshohocken, PA: ASTM International.

[272] ASTM D 6484 / D 6484M-14,, " Standard Test Method for Open-Hole Compressive Strength of Polymer Matrix Composite Laminates," West Conshohocken, PA: ASTM International, 2014, www.astm.org.

[273] ASTM D5766M-02a, ASTM D 5766/ D, " Open hole tensile strength of polymer composite laminates," West Conshohocken, PA: ASTM International.

[274] ASTM D6742 / D6742M - 02 ,, "Standard Practice for Filled-Hole Tension and Compression Testing of Polymer Matrix Composite Laminates," West Conshohocken, PA: ASTM International, www.astm.org.

[275] ASTM D5961 / D5961M - 13 ,, " Standard Test Method for Bearing Response of Polymer Matrix Composite Laminates," West Conshohocken, PA: ASTM International, www.astm.org.

[276] C. Furtado, "Optimal use of ultra-thin plies in composite structures," Master's thesis, Faculdade de Engenharia, Universidade do Porto, Porto, 2015.

[277] M. R. Wisnom, S. R. Hallett, and C. Soutis, "Scaling effects in notched composites," Journal of composite materials, 2009.

[278] A. J. Sawicki and P. J. Minguet, "Failure mechanisms in compression-loaded composite laminates containing open and filled holes," Journal of reinforced plastics and composites, vol. 18, no. 18, pp. 1708–1728, 1999.

[279] J. Anthony and P. C. Paris, "Instantaneous evaluation of J and C," International Journal of Fracture, vol. 38, no. 1, pp. R19—-R21, 1988.

[280] R. Krueger, M. K. Cvitkovich, T. K. O'Brien, and P. J. Minguet, "Testing and analysis of composite skin/stringer debonding under multi-axial loading," Journal of composite Materials, vol. 34, no. 15, pp. 1263–1300, 2000.

[281] H. A. W. Cornelissen, D. A. Hordijk, and H. W. Reinhardt, "Experimental determination of crack softening characteristics of normalweight and lightweight," Heron, vol. 31, p. 45, 1986.

[282] D. A. Hordijk, "Fracture mechanics parameters of concrete from uniaxial tensile tests as influensed by specimen length, fracture of concrete and rock," Society Experimental Mechanics, pp. 138–149, 1987.

[283] A. Bergan, C. Dávila, F. Leone, J. Awerbuch, and T. Tan, "A mode i cohesive law characterization procedure for through-the-thickness crack propagation in composite laminates," Composites Part B: Engineering, vol. 94, pp. 338–349, 2016.

[284] N. Zobeiry, R. Vaziri, and A. Poursartip, "Characterization of strain-softening behavior and failure mechanisms of composites under tension and compression," Composites Part A: Applied Science and Manufacturing, vol. 68, pp. 29–41, 2015.

[285] A. Ortega, P. Maimí, E. V. González, and D. Trias, "Characterization of the translaminar fracture cohesive law," Composites Part A: Applied Science and Manufacturing, vol. 91, pp. 501–509, 2016.

[286] R. Olsson, "A survey of test methods for multiaxial and out-of-plane strength of composite laminates," Composites Science and Technology, vol. 71, no. 6, pp. 773–783, 2011.

[287] A. Melro, Analytical and numerical modelling of damage and fracture of advanced composites. PhD thesis, Universidade do Porto, Portugal, 2011.

[288] F. P. Van der Meer, "Micromechanical validation of a mesomodel for plasticity in composites," European Journal of Mechanics-A/Solids, vol. 60, pp. 58–69, 2016.

[289] H. Koerber and P. P. Camanho, "High strain rate characterisation of unidirectional carbon-epoxy IM7-8552 in longitudinal compression," Composites Part A: Applied Science and Manufacturing, vol. 42, no. 5, pp. 462–470, 2011.

[290] ASTM D 3518 D 3518M-13 and ASTM D 3518 / D 3518M-13, "Standard Test Method for In-Plane Shear Response of Polymer Matrix Composite Materials by Tensile Test of a +- 45 Laminate," West Conshohocken, PA: ASTM International.

[291] H. Koerber, J. Xavier, and P. P. Camanho, "High strain rate characterisation of unidirectional carbon-epoxy IM7-8552 in transverse compression and in-plane shear using digital image correlation," Mechanics of Materials, vol. 42, no. 11, pp. 1004–1019, 2010.

[292] ASTM D 6671 D 6671M, " Standard Test Method for Mixed Mode I-Mode II Interlaminar Fracture Toughness of Unidirectional Fiber Reinforced Polymer Matrix Composites," West Conshohocken, PA: ASTM International.

[293] H. Tada, P. C. Paris, and G. R. Irwin, "The Stress Analysis of Cracks Handbook. The American Society of Mechanical Engineers," New York, 2000.